Decoding the development of human prenatal skin

Nusayhah Hudaa Gopee

MBBS, MRCP (UK), MRes, MSc

Submitted for the degree of Doctor of Philosophy

Biosciences Institute

Newcastle University

Supervised by

Professor Muzlifah Haniffa

Dr Emily Stephenson

December 2024

Abstract

Skin, the largest organ in the human body, is composed of diverse cell types strategically organised in defined strata and specialised appendages. Its morphogenesis is underpinned by precise spatiotemporally distributed cellular and molecular changes which remain incompletely deciphered. It is seeded by immune cells, including macrophages, early during gestation but their contribution, if any, to prenatal skin and hair follicle development is uncertain.

To investigate de novo hair follicle formation and the role of immune cells in skin development, a multi-omics atlas of human prenatal skin (7 to 17 post-conception weeks) was assembled, integrating single-cell and spatial transcriptomic data. Comparative assessments with adult skin and hair follicle datasets and cross-species analyses were performed to determine features specific to human prenatal skin. A hair-bearing skin organoid model, derived from human embryonic stem cells and induced pluripotent stem (iPS) cells, was benchmarked against prenatal skin to evaluate the faithfulness of skin organoids to in vivo skin and their utility to functionally interrogate skin morphogenesis. Findings were validated using immunofluorescence, in situ hybridization and tissue culture experiments.

The systematic charting of prenatal skin (433,961 single cells) identified the precursor cell states, differentiation trajectories and cross-compartmental cellular interactions underpinning human hair follicle neogenesis. Re-mapping of these single cells in situ, using spatial transcriptomic data, uncovered microanatomical tissue niches where immune cells co-located and cross-talked with non-immune cells, contributing to early hair follicle development, angiogenesis, neurogenesis, and scarless healing. In particular, macrophages promoted prenatal skin vascular endothelial development. Skin organoids, which lacked immune cells, concomitantly had markedly reduced quantity and heterogeneity of endothelial cells. Addition of iPS cell-derived macrophages significantly improved vascular network formation in skin organoids.

Overall, this study revealed that immune cells function as critical players in skin morphogenesis and provided a potential blueprint to enhance future skin and organoid tissue engineering.

Acknowledgements

I would like to express my sincere gratitude to my supervisors, Prof Muzlifah Haniffa for her unremitting encouragement and academic mentorship, Dr Emily Stepheson for her patient guidance and practical training, and to both for their constant support and helpful advice navigating this research project and my career in general. I would also like to thank Prof Nick Reynolds and Prof Simi Ali for their critical perspectives and insightful discussions throughout my studies.

The work presented in this thesis is part of a collaborative effort and I am thankful to all those who have contributed from the Haniffa Lab team and core facilities based in Newcastle University and Wellcome Sanger Institute. In particular, I would like to thank Dr Rachel Botting, Dr Emily Stephenson, Mohi Miah, Keval Sidhpura, Justin Englebert, and Dr Vicky Rowe for their help with tissue digestion and gene expression library preparation for single-cell data generation, Feri Torabi, Ben Rumney, and the Sanger Spatial Genomics Platform for processing samples for Visium and spatial validation experiments, Dr Chloe Admane, Dr April Foster, and Diana Adao for their work on tissue and organoid cultures and related imaging, and Dr Luca Verger and Dr Kwasi Kwakwa for their assistance with image analysis.

I am very grateful to Dr Elena Winheim for her help when re-analysing our expanded dataset, re-rerunning my original computational scripts and conducting anew assessments of cellular communication and differentiation trajectories, to Dr Vijaya Shanmugiah for carrying out regulon analysis, to Issac Goh for comparing skin organoid and in vivo skin datasets by time-encoded logistic regression, to Dr Pavel Mazin for support with data alignment and leading the spatial transcriptomic data analysis, to Dr Karl Annusver and Dr Maria Kasper for advice regarding cross-species analysis of mouse skin, and Dr Daniela Basurto-Lozada and Dr Dave Horsfall for their expertise in facilitating promotion of this work on our web portal. Special thanks go to Dr Bayanne Olabi for additional disease-related data interpretation for our published manuscript, Dr Chloe Admane for her schematic figure creation, some of which feature in this thesis, Antony Rose for readily troubleshooting my countless coding conundrums, and Dr Rachel Botting and Dr Emily Stephenson for kindly reading through my thesis draft.

My deepest appreciation extends to the patients who donated the precious samples used in this study and to my funding bodies, the NIHR Newcastle Biomedical Research Centre and UKRI

Medical Research Council. Their invaluable contributions enabled my undertaking of this research work as part of a training fellowship.

Finally, I would like to thank my parents, siblings, and nephew for being unwavering pillars of support, strength and positivity throughout, even located half a world away. To them, I am forever indebted.

Declaration

I confirm that this thesis is my own work and that I have correctly acknowledged the work of others. I certify that no part of the material presented has been previously submitted by myself for a degree or other qualification in this or any other university.

Table of contents

Abstract ..... **ii**
Acknowledgements ..... **iii**
Declaration ..... **v**
Table of contents ..... **vi**
Index of figures ..... **xiv**
List of abbreviations ..... **xviii**
Chapter 1 . Background and literature review **1**
1.1. Structure and function of human skin **1**
1.1.1 Skin anatomy 1
Epidermis 2
Basement membrane zone 3
Dermis 4
Hypodermis 5
1.1.2 Hair follicle anatomy 6
1.1.3 Functions of the skin 9
1.2 Prenatal development of human skin **11**
1.2.1 Skin embryology and derivation from germ layers 11
1.2.2 Development of hair follicles and related appendages 13
Human de novo hair follicle development 13
Formation of hair-follicle related appendages 15
Insights from animal models 15
1.3 Role of immune cells in skin **17**
1.3.1 Immune cells in healthy skin 17
Myeloid lineage cells 17
Lymphoid lineage cells 19
1.3.2 Immune cells in prenatal skin 21
1.4 Genomic technologies to study skin development **23**
1.4.1 Single-cell RNA sequencing 24
1.4.2 Spatial transcriptomics 26
1.4.3 Concept of tissue microenvironments 29
1.4.4 Application of transcriptomic technologies to investigate skin morphogenesis 30

1.5 Skin organoids to model skin and hair follicle development 32
1.5.1 The hair-bearing skin organoid model 33
1.5.2 Skin organoid recapitulation of in vivo skin 34
1.6 Research hypothesis 35
1.7 Study aims 35
Chapter 2 . Materials and methods 36
2.1 Prenatal skin tissue acquisition and ethical approval 36
2.2 Single-cell transcriptomic data generation from prenatal skin 36
2.2.1 Tissue digestion 36
2.2.2 Fluorescence-activated cell sorting 37
2.2.3 Droplet-based scRNA-seq 38
GEM generation, barcoding and reverse transcription 38
GEM cleanup and cDNA amplification 39
cDNA cleanup and quantification 40
Gene expression library construction 40
2.3 Visium spatial transcriptomic data generation from prenatal skin 42
2.3.1 Tissue cryosection and fixation 42
2.3.2 Tissue staining and imaging 42
2.3.3 Array-based spatial transcriptome profiling 43
Tissue permeabilisation and reverse transcription 43
Second strand synthesis and denaturation 44
cDNA amplification and cleanup 46
Spatial gene expression library construction 47
2.4 Single-cell transcriptomic data analysis 48
2.4.1 Pre-processing of prenatal skin scRNA-seq data for annotation 48
Alignment to human genome 48
Quality control 49
Doublet detection 49
Low quality cells 50
Maternal contamination 51
Lowly expressed genes 51
Data transformation 52
Count normalisation and log-transformation 52

Batch correction and data integration 52
Feature selection 53
Dimensionality reduction 53
Cluster identification and annotation 54
Clustering 54
Differential gene expression 55
Differential abundance testing 55
2.4.2 Alignment of prenatal skin, skin organoid and adult skin 56
Skin organoid scRNA-seq data analysis 56
Integration of prenatal skin, skin organoid and adult skin 57
Broad level alignment by distance-based analysis 57
Broad level alignment by time-encoded cell type predictions 57
Refined cell state comparison by co-embedding 58
2.4.3 Comparison of prenatal skin to tissue-specific datasets 58
2.4.4 Cross-species comparison 59
Comparison to embryonic mouse skin 59
Comparison to adult reindeer skin 60
2.4.5 Trajectory inference analysis 60
2.4.6 Analysis of cell-cell interaction 61
2.4.7 Gene set enrichment analysis 62
Fibroblasts from prenatal and adult skin 62
Early and late gestation fibroblasts from prenatal skin 63
Prenatal skin myeloid cells 63
2.4.8 Analysis of angiogenic gene profiles 64
Gene module scoring 64
Comparison of pro- and anti-angiogenic genes 64
2.4.9 Gene regulatory network analysis 65
Regulon analysis 65
Analysis of ligand-to-target gene links 66
2.5 Spatial transcriptomic data analysis 68
2.5.1 Alignment to human genome 68
2.5.2 Cell type deconvolution 68
2.5.3 Prediction of tissue microenvironments 69

2.6 Assessing vascular network in skin organoids cultured with and without macrophages 70
2.6.1 Macrophage harvesting and phenotyping 70
2.6.2 Co-culturing skin organoids with macrophages 70
2.6.3 Whole-mount immunostaining 71
2.6.4 Confocal imaging 72
2.6.5 Analysis of skin organoid confocal images 72
2.7 Scratch wound assay of fibroblasts cultured with and without macrophages 73
2.8 Validating cellular co-localisations and interactions 74
2.8.1 Multiplex RNA fluorescence in situ hybridisation 74
Tissue preparation and probe hybridisation 74
Confocal imaging 74
Image analysis for *FOXP3* signal quantification 75
2.8.2 Immunofluorescence assays of prenatal skin and skin organoid cryosections 75
Tissue preparation and immunostaining 75
Confocal imaging 76
Chapter 3 . Prenatal skin multi-omics atlas reveals cellular crosstalk and immune cell co-location during de novo hair follicle formation 77
3.1 Introduction 77
3.2 Objectives 79
3.3 Results 80
3.3.1 Annotated single cell atlas of human prenatal skin 80
Prenatal skin sampling 80
scRNA-seq data generation 80
scRNA-seq data pre-processing 81
Annotation of cell states in prenatal skin 83
Broad cell type annotations 84
Refined cell state annotations 86
Epithelial cells 86
Stromal cells 90
Endothelial cells 97
Myeloid cells 99
Lymphoid cells 102

3.3.2 Differential abundance of cell states across gestation 105
3.3.3 Alignment of prenatal skin with skin organoid and adult skin 109
3.3.4 Hair follicle formation 116
Confirmation of captured cell states 116
Histological examination 116
Multiplex in situ hybridisation 118
Comparison with human adult hair follicles 119
Inferred differentiation trajectories 124
Epithelial cell states 124
Mesenchymal cell states 133
Mesenchymal-epithelial cellular crosstalk orchestrating hair follicle development 136
Comparison between human and mouse hair follicle development 141
3.3.5 Spatial transcriptomic atlas of early human prenatal skin 148
Prenatal skin sampling 148
Spatial transcriptomic data analysis 148
Identification of tissue microenvironments 150
3.4 Section discussion 155
3.4.1 Multi-omics profiling of human prenatal skin 155
3.4.2 Evaluating the faithfulness of the skin organoid model to in vivo skin 156
3.4.3 Insights into hair follicle development 157
3.4.4 Immune and non-immune cells co-locate in prenatal skin microenvironments 159
Chapter 4 . Early dermal fibroblasts and macrophages contribute to scarless healing potential of prenatal skin 160
4.1 Introduction 160
4.2 Objectives 162
4.3 Results 163
4.3.1 Comparison of early- and late-gestation prenatal skin dermal fibroblasts 163
4.3.2 Comparison of prenatal and adult skin dermal fibroblasts 166
4.3.3 Macrophages and prenatal skin dermal fibroblast growth and scarless repair 169
Co-location of macrophage subsets with dermal fibroblasts in early prenatal skin 169
Gene set enrichment analysis of macrophage subsets 173
Cell-cell interactions between early prenatal skin fibroblasts and macrophages 174
4.3.4 Comparison between human prenatal and reindeer skin 176

4.3.5 Scratch wound healing assay 179
4.4 Section discussion 180
4.4.1 Changes in prenatal skin fibroblasts across gestation 180
4.4.2 The immune and inflammatory milieu of prenatal skin 181
4.4.3 Additional factors influencing scarless healing potential 182
Chapter 5 . Macrophages support neurogenesis and angiogenesis in prenatal skin 184
5.1 Introduction 184
5.2 Objectives 188
5.3 Results 189
5.3.1 Macrophages and early neurocutaneous development 189
Co-location of macrophages with neural cells in early prenatal skin 189
Enrichment of neural-related gene modules in TML macrophages 190
Cell-cell interactions between TML macrophages and neural cells 191
5.3.2 Macrophages and vascular development in prenatal skin 193
Co-location of macrophages with endothelial cells in early prenatal skin 193
Enrichment of angiogenesis gene modules in macrophage subsets 195
Cellular crosstalk between macrophages and vascular endothelial cells 196
5.3.3 Endothelial cells of the skin organoid model 198
Comparison of endothelial cells between skin organoid and prenatal skin 198
Endothelial cell differentiation 200
Endothelial cell differentiation in in vivo prenatal skin 200
Endothelial cell differentiation in in vitro models 203
Mechanisms for limited endothelial cells in the skin organoid model 205
Blood flow, hypoxia, growth factors and sprouting potential 205
Angiogenic signals and regulon analysis 208
5.3.4 Co-culture of skin organoids with macrophages 214
5.4 Section discussion 218
5.4.1 Support of prenatal cutaneous angiogenesis by macrophages 218
5.4.2 Vascularisation of tissue organoids 219
5.4.3 Support of peripheral nerve development by yolk sac-derived macrophages 220
Chapter 6 . Conclusion and future directions 221
6.1 Overview 221
6.2 Summary of findings and discussions 223

6.2.1 Prenatal skin multi-omics atlas reveals cellular crosstalk and immune cell co-location during de novo hair follicle formation 223
6.2.2 Early dermal fibroblasts and macrophages contribute to scarless healing potential of prenatal skin 224
6.2.3 Macrophages support neurogenesis and angiogenesis in prenatal skin 225
6.3 Strengths and weaknesses 226
6.3.1 Strengths of the current study 226
Breadth and depth of profiling 226
Spatial contextualisation 226
Benchmarking of skin organoid model 227
6.3.2 Weaknesses of the current study 227
Sampling from late gestation stages 227
Non-myeloid immune cell contributions 228
Mechanistic investigations 228
6.4 Future directions 229
Hair follicle biology 229
Molecular roadmaps to scarless repair 229
Future applications for skin organoids 230
6.5 Conclusion 231
References 232
Appendices 285
Appendix A. Ethical approval for prenatal skin tissue acquisition. 285
A1: Ethical approval for HDBR. 285
A2: Ethical approval for Cambridge University Hospitals. 295
Appendix B. Metadata for prenatal skin specimens. 298
B1: Prenatal skin specimens included in scRNA-seq dataset 298
B2: Prenatal skin specimens included in spatial transcriptomic dataset. 300
Appendix C: FACS-sorted cell proportions. 301
Appendix D. 10x Genomics Chromium Controller channel metadata. 304
Appendix E. Differentially expressed genes for broad cell types in prenatal skin. 307
Appendix F. Differentially expressed genes for refined cell states in prenatal skin. 311
F1: Epithelial cell states 311
F2: Stromal cell states 313

F3: Endothelial cell states. 318
F4: Myeloid cell states. 320
F5: Lymphoid cell states 323
Appendix G. Gene lists for gene module scoring 326
G1: Angiogenesis gene sets 326
G2: Endothelial and hypoxia gene sets 329
Appendix H. Prioritised ligands from NicheNet analysis. 332
Appendix I. Primary and secondary antibodies used in immunofluorescence assays 333
Appendix J. Experimental values for scratch wound assays 335
Appendix K. Gene set enrichment analysis results for *WNT2*$^+$ prenatal skin fibroblasts 339
K1: Early *WNT2*$^+$ fibroblasts 339
K2: Late *WNT2*$^+$ fibroblasts 340
Appendix L. Gene set enrichment analysis results for TML macrophages 341
Appendix M. Angiogenesis-related gene set enrichment analysis results for macrophages. 342
Appendix N. Additional outputs during PhD 345
N1: Related publications 345
N2: Presentations 347

Index of figures

Figure 1.1. Anatomy of the human skin. 2
Figure 1.2. Histomorphology of the human hair follicle. 7
Figure 1.3. Sub-compartmentalisation of the human hair follicle. 8
Figure 1.4. Stages of hair follicle formation. 14
Figure 1.5. Single-cell RNA sequencing experimental workflow 25
Figure 1.6. Visium spatial gene expression slide. 27
Figure 1.7. Visium spatial transcriptomic experimental workflow. 28
Figure 1.8. Differentiation protocol of the hair-bearing skin organoid model. 33
Figure 2.1. Barcoding and generation of full-length cDNA. 39
Figure 2.2. Construction of gene expression libraries for scRNA-seq. 41
Figure 2.3. Composition of primers on Visium spatial gene expression slide. 43
Figure 2.4. Spatial barcoding and generation of full-length cDNA. 45
Figure 2.5. Construction of Visium gene expression libraries. 47
Figure 2.6. Example of barcode rank plot for prenatal skin sample. 48
Figure 2.7. Doublet score histograms from Scrublet. 50
Figure 3.1. Isolation of prenatal skin cells by FACS 81
Figure 3.2. Quality control metrics. 82
Figure 3.3. Broad cell clusters in prenatal skin. 83
Figure 3.4. Annotation of broad cell types by differential gene expression. 84
Figure 3.5. Annotation of epidermal cells by differential gene expression. 87
Figure 3.6. Frequency of epithelial cell states. 88
Figure 3.7. Annotation of hair follicle epithelial cells by differential gene expression. 89
Figure 3.8. Stromal cell states in prenatal skin. 90
Figure 3.9. Frequency of stromal cell states. 91
Figure 3.10. Annotation of fibroblasts by differential gene expression. 91
Figure 3.11. Annotation of hair follicle mesenchymal cells 92
Figure 3.12. Annotation of adipocytic cells. 93
Figure 3.13. Annotation of mural cells by differential gene expression. 94
Figure 3.14. Annotation of skeletal muscle cells by differential gene expression. 95
Figure 3.15. Annotation of neural cells by differential gene expression. 96
Figure 3.16. Annotation of endothelial cells by differential gene expression. 97

Figure 3.17. Frequency of endothelial cell states. 98
Figure 3.18. Myeloid cell clusters in prenatal skin..... 100
Figure 3.19. Annotation of myeloid cells by differential gene expression..... 100
Figure 3.20. Annotation of macrophages. 102
Figure 3.21. Annotation of lymphoid cells by differential gene expression. 103
Figure 3.22. Differential abundance of broad cell types across gestation. 105
Figure 3.23. Differential abundance of refined cell states across gestation. 107
Figure 3.24. Broad cell types in integrated prenatal skin, adult skin and skin organoid data. 110
Figure 3.25. Alignment of broad cell types. 111
Figure 3.26. Broad cell groups in integrated prenatal, adult and skin organoid data. 112
Figure 3.27. Alignment of broad cell types across gestation..... 113
Figure 3.28. Refined epithelial cell states in integrated prenatal skin and skin organoid data.... 114
Figure 3.29. Refined stromal cell states in integrated prenatal skin and skin organoid data. 115
Figure 3.30. Histological changes in prenatal skin during gestation. 117
Figure 3.31. RNAscope FISH of prenatal skin hair follicles..... 118
Figure 3.32. Epithelial cell states in integrated prenatal/organoid and adult hair follicle data. .. 120
Figure 3.33. Alignment of adult hair follicles to prenatal skin/skin organoid..... 120
Figure 3.34. Comparison of prenatal and adult hair follicle matrix. 121
Figure 3.35. RNAscope FISH of perifollicular Tregs. 122
Figure 3.36. Quantification of perifollicular Tregs. 123
Figure 3.37. Immunofluorescence assay of perifollicular Tregs. 123
Figure 3.38. Inferred differentiation trajectory of hair follicle epithelial cells..... 125
Figure 3.39. Gene expression of differentiating hair follicle epithelial cells. 127
Figure 3.40. Driver genes along the IRS trajectory. 129
Figure 3.41. Driver genes along the ORS/CL trajectory. 130
Figure 3.42. Disease-causing genes in the skin organoid model. 132
Figure 3.43. Inferred differentiation trajectory of hair follicle mesenchymal cells. 133
Figure 3.44. Driver genes along the hair fibroblast trajectory..... 135
Figure 3.45. Development of hair follicle mesenchyme. 136
Figure 3.46. Hair follicle mesenchymal-epithelial cellular interactions. 137
Figure 3.47. Expression of *CXCL12* by hair follicle mesenchymal cells. 137
Figure 3.48. RNAscope FISH of mesenchymal-epithelial cellular interactions. 138
Figure 3.49. Mesenchymal-epithelial crosstalk. 139

Figure 3.50. Conservation of mesenchymal-epithelial interactions in skin organoids. 140
Figure 3.51.Expression of known genes involved in hair follicle signalling. 142
Figure 3.52. Cross-species comparison with mouse skin. 143
Figure 3.53. Comparison of broad cell types between human and mouse skin. 144
Figure 3.54. Comparison of fibroblast cell states between human and mouse skin. 144
Figure 3.55. Comparison of hair follicle mesenchymal cells between human and mouse. 146
Figure 3.56. Spatial distribution and abundance of *WNT2*$^+$ fibroblasts and *HOXC5*$^+$ early fibroblasts from skin surface. 149
Figure 3.57. Spatial microenvironments in prenatal skin. 151
Figure 3.58. Co-location of macrophages and endothelial cells by correlation analysis. 152
Figure 3.59. Co-location of pre-Dc and immune cells by correlation analysis. 153
Figure 3.60. Cell-cell interactions between pre-Dc and immune cells. 154
Figure 4.1. Gene set enrichment in early and late *WNT2*$^+$ fibroblasts. 164
Figure 4.2. Comparison of early and late *WNT2*$^+$ fibroblasts. 165
Figure 4.3. Comparison of prenatal and adult skin fibroblasts. 166
Figure 4.4. Expression of adult gene profile in prenatal skin fibroblasts. 167
Figure 4.5. Driver genes along the dermal fibroblast trajectory. 168
Figure 4.6. Co-location of *WNT2*$^+$ fibroblasts and macrophages by correlation analysis. 169
Figure 4.7. Immunofluorescence assay of *LYVE1*$^+$ macrophage and fibroblast co-location. 170
Figure 4.8. TML macrophage and fibroblast co-location. 171
Figure 4.9. Spatial distribution and abundance of *WNT2*$^+$ fibroblasts and macrophages from skin surface. 172
Figure 4.10. Immune-inhibitory gene modules enriched in TML macrophages. 173
Figure 4.11. Cell-cell interactions between *WNT2*$^+$ fibroblasts and macrophages. 174
Figure 4.12. Alignment of prenatal skin and reindeer skin fibroblasts. 177
Figure 4.13. Expression of pro-regenerative and pro-fibrotic genes in prenatal skin. 177
Figure 4.14. Alignment of prenatal skin and reindeer skin macrophages. 178
Figure 4.15. Scratch wound healing assay with and without macrophages. 179
Figure 5.1. Mechanisms of vascular development. 185
Figure 5.2. Co-location of macrophages and neural cells by correlation analysis. 189
Figure 5.3. Gene set enrichment in TML macrophages. 190
Figure 5.4. Neural-related gene modules enriched in TML macrophages. 191
Figure 5.5. Cell-cell interactions between TML macrophages and neural cells. 192

Figure 5.6. Immunofluorescence assay of perivascular macrophages. 194
Figure 5.7. RNAscope FISH of perivascular macrophages..... 194
Figure 5.8. Angiogenesis gene module scores in macrophage subsets. 195
Figure 5.9. Cell-cell interactions between macrophages and endothelial cells. 196
Figure 5.10. Refined endothelial cell states in integrated prenatal skin and skin organoid data. 198
Figure 5.11. Module scoring of endothelial marker genes. 199
Figure 5.12. Inferred differentiation trajectory of endothelial cells. 200
Figure 5.13. Driver genes along the arteriolar trajectory. 201
Figure 5.14. Driver genes along the venular trajectory. 202
Figure 5.15. Alignment of blood vessel organoid to prenatal skin..... 204
Figure 5.16. Expression of known flow-responsive genes. 205
Figure 5.17. Hypoxia gene module scores. 206
Figure 5.18. Expression of VEGFs. 207
Figure 5.19. Module scoring of tip and stalk gene sets. 207
Figure 5.20. Comparison of angiogenic signals between prenatal skin and the skin organoid... 208
Figure 5.21. Expression of angiogenic receptors. 209
Figure 5.22. Comparison of regulon activity. 210
Figure 5.23. Gene interaction network. 211
Figure 5.24. Expression of target genes. 212
Figure 5.25. Ligand to target gene links. 212
Figure 5.26. Angiogenesis in prenatal skin and skin organoids. 213
Figure 5.27. Phenotyping of iPS cell-derived macrophages. 214
Figure 5.28. Vascular network in skin organoids cultured with and without macrophages..... 215
Figure 5.29. Immunofluorescence assay of macrophage and endothelial cell co-location in skin organoids. 216
Figure 5.30. Assessing vascular network in skin organoids. 217

List of abbreviations

AGM	aorto-gonad-mesonephros
ANOVA	analysis of variance
APM	arrector pili muscle
ASDC(s)	$AXL^{+}SIGLEC6^{+}$ dendritic cell(s)
BMP	bone morphogenetic protein
BMZ	basement membrane zone
cDC1	conventional type 1 dendritic cells
cDC2	conventional type 2 dendritic cells
cDNA	complementary deoxyribonucleic acid
CL	companion layer
CNC	cranial neural crest
CS	Carnegie stage
CTS	connective tissue sheath
DABCO	1,4-Diazabicyclo[2.2.2]octane
DAPI	4′,6-diamidino-2-phenylindole
Dc	dermal condensate
DC(s)	dendritic cell(s)
DEG(s)	differentially expressed gene(s)
DEJ	dermo-epidermal junction
DNA	deoxyribonucleic acid
Dp	dermal papilla
DP	double positive
ECM	extracellular matrix
EDTA	ethylenediaminetetraacetic acid
em.	emission

ES cell	embryonic stem cell
ex.	excitation
FACS	fluorescent activated cell sorting
FBS	foetal bovine serum
FDR	false discovery rate
FGF	fibroblast growth factor
FISSEQ	fluorescent in situ sequencing
GEM(s)	gel bead(s) in emulsion
GOBP	Gene Ontology Biological Process
GRCh38	Genome reference consortium human 38
HCA	Human Cell Atlas
HDCA	Human Developmental Cell Atlas
hPSCs	human pluripotent stem cells
HSPCs	haematopoietic stem and progenitor cells
IFE	interfollicular epidermis
IFN	interferon
Ig	immunoglobulin
IgE	immunoglobulin E
IgM	immunoglobulin M
IL	interleukin
ILC(s)	innate lymphoid cell(s)
ILC1(s)	type 1 innate lymphoid cell(s)
ILC2(s)	type 2 innate lymphoid cell(s)
ILC3(s)	type 3 innate lymphoid cell(s)
iPS cell	induced pluripotent stem cell
IRS	inner root sheath

ISH	in situ hybridisation
ISS	in situ sequencing
KNN	k-nearest neighbour
LCs	Langerhans cells
LE	lymphatic endothelium
logFC	log fold change
LR	logistic regression
LTi cells	lymphoid tissue inducer cells
MAIT cells	mucosal-associated invariant T cells
MARS-seq	massively parallel RNA single-cell sequencing
MCs	Merkel cells
MERFISH	multiplexed error-robust fluorescence in situ hybridisation
MHC	major histocompatibility complex
MHCII	major histocompatibility complex class II
MMPs	matrix metalloproteinases
moDC(s)	monocyte-derived dendritic cell(s)
mRNA	messenger RNA
MSigDB	Molecular Signatures Database
NK cell(s)	natural killer cell(s)
NMF	non-negative matrix factorisation
OCT	optimal cutting temperature
OMM	organoid maturation medium
ORA	over-representation analysis
ORS	outer root sheath
PAGA	partition-based graph abstraction
PBS	phosphate buffered saline

PCA	principal component analysis
PCR	polymerase chain reaction
PCW	post-conception weeks
pDC(s)	plasmacytoid dendritic cell(s)
PDGF(s)	platelet-derived growth factor(s)
PFA	paraformaldehyde
pre-Dc	pre-dermal condensate
PSCs	pluripotent stem cells
RBC	Red blood cels
RNA	ribonucleic acid
rpm	revolutions per minute
RPMI medium	Roswell Park Memorial Institute medium
RT	reverse transcription
scRNA-seq	single-cell RNA sequencing
Scrublet	Single-Cell Remover of Doublets
scVI	Single-cell Variational Inference
SD	standard deviation
seqFISH	sequential fluorescence in situ hybridisation
SG	sebaceous gland
SMART-seq	switching mechanism at 5′ end of RNA template sequencing
SNPs	single-nucleotide polymorphisms
SSC	saline-sodium citrate
ST	Spatial Transcriptomics
Stereo-seq	spatial enhanced resolution omics-sequencing
TGF-β/ Tgf-β	transforming growth factor beta
Th	T helper

TIMPs	tissue-derived inhibitors of proteinases
TML macrophages	*TREM2*$^{+}$ microglia-like macrophages
Treg(s)	regulatory T cell(s)
Tris	tris(hydroxymethyl)aminomethane buffer
TSO	template switch oligo
UMAP	Uniform Manifold Approximation and Projection
UMI	unique molecular identifier
UV	ultraviolet
v/v	volume per volume
VEGF(s)	vascular endothelial growth factor(s)

Chapter 1 . Background and literature review

1.1. Structure and function of human skin

1.1.1 Skin anatomy

The skin is the largest organ in the human body and is formed by diverse cell types organised in anatomically defined layers and specialised units.[1,2] The epidermis constitutes the outermost layer of the skin and is separated from the underlying dermis by the basement membrane zone (BMZ) which lies at the dermo-epidermal junction (DEJ).[1,2] The DEJ has an undulating morphology resulting from the interlinking epidermal and dermal projections, termed rete ridges and dermal papillae respectively.[3] Beneath the dermis is the hypodermis or subcutaneous adipose tissue, the deepest layer of the skin which is demarcated from the rest of the body by fascia.[1,2] At the border between the dermis and the hypodermis, blood vessels form the deep vascular plexus serving the skin.[4] These vessels branch through the dermis and connect to the superficial vascular plexus which sits at the boundary between the papillary and reticular dermis and extends capillary loops into the dermal papillae but does not cross into the avascular epidermis.[4] Apart from an elaborate vascular system, the dermis also contains an intricate network of different sensory and motor nerve fibres.[1,5] Traversing through the epidermal and dermal layers, and connected to the external environment, are the skin appendages consisting of hair follicles with attached sebaceous glands (forming the pilosebaceous units) and sweat glands of eccrine or apocrine origin.[1,2] These various components of the skin are illustrated in Figure 1.1.

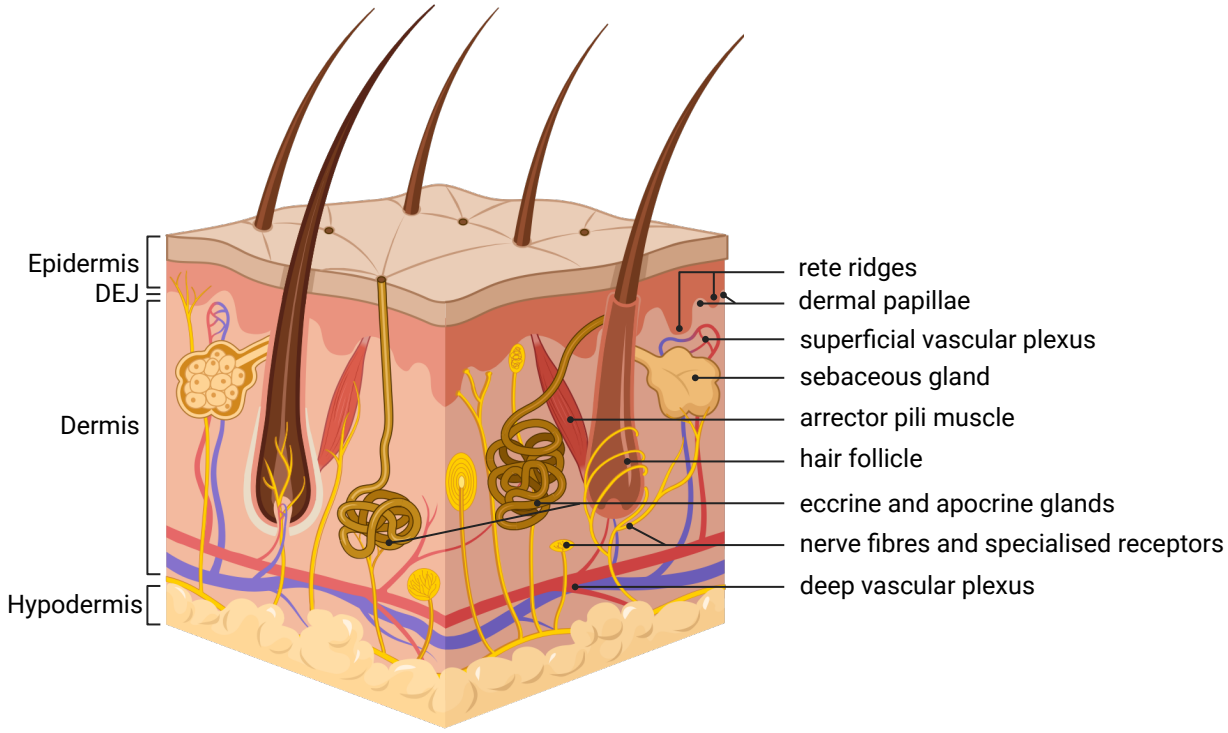

Figure 1.1. Anatomy of the human skin.

Schematic representation of human skin in cross-section depicting the distinct layers (epidermis, dermis, and hypodermis), undulating dermo-epidermal junction, and microanatomical organisation of its appendages and neurovascular supply. DEJ: dermo-epidermal junction. Created with BioRender.com.

Epidermis

The epidermis is a stratified squamous epithelium consisting of morphologically distinct cellular layers composed predominantly of keratinocytes (~95%).[1] The basal layer attached to the basement membrane, known as the stratum basale or stratum germinativum, is usually one cell thick and contains the mitotically active keratinocytes which divide to give rise to the other epidermal strata[1,2]. Divided keratinocytes detach from the basement membrane and progressively migrate outwards while undergoing terminal differentiation.[2] In the stratum spinosum (prickle cell layer) which is directly above the stratum basale, the keratinocytes first enlarge into polyhedral shapes then flatten as they move more superficially.[2] They are interconnected by abundant desmosomes - specialised membrane domains mediating intercellular adhesion coupled with linkages to the intracellular cytoskeleton[6] - which appear as 'spines' along the cell margins on microscopy. The stratum granulosum (granular cell layer) succeeds the stratum spinosum and is the most superficial

viable epidermal layer. It consists of flattened keratinocytes with lipid-containing lamellar bodies[1] and numerous intracytoplasmic granules of keratohyalin, from which this compartment derives its name.[7] The keratinocytes then lose their nuclei and cytoplasmic organelles and acquire insoluble cornified lipid envelopes through a process of cornification to form the outermost layer of the skin, the stratum corneum, prior to their eventual desquamation.[8] The migratory journey of a keratinocyte from the basal layer to being shed from the stratum corneum takes around 28 days under physiological condition.[2]

Although the layered arrangement of the epidermis is generally consistent throughout the body, regional differences exist in its overall thickness and in the cell numbers of its individual layers to adapt to specific anatomical sites. For instance, the epidermis measures less than 0.1 mm in eyelid skin compared to around 1.5 mm in the palms and soles.[2] Additionally, a fifth zone, intermediate between the strata granulosum and corneum, is present in palmoplantar skin and is termed stratum lucidum due to its translucent appearance under electron microscopy.[1]

Other constituent cells of the epidermis include melanocytes, Merkel cells (MCs) and Langerhans cells (LCs). Melanocytes are the pigment-producing cells of the skin and are primarily located in the basal layer of the epidermis, connected to the basement membrane.[9] They synthesise and store melanin pigment in intracellular organelles (melanosomes) which are transported through extended dendritic processes and transferred to keratinocytes to impart skin colour.[9] Merkel cells are considered neuroendocrine cells and are also found scattered among basal keratinocytes.[10] They are involved in tactile sensation, in close association with sensory nerve fibres, and act as mechanical transducers in response to touch.[10,11] They also produce and secrete several neuropeptides, the roles of which are not fully understood but are thought to function as potential neurotransmitters, trophic factors for keratinocytes, or presumed endocrine mediators.[10,11] Langerhans cells are the specialised antigen-presenting cells of the epidermis and are further discussed in section 1.3.

Basement membrane zone

Situated at the interface between the epidermis and the dermis is the BMZ, a complex assembly of macromolecules that extends from the intracellular compartment of basal keratinocytes, through their plasma membranes and DEJ into the upper papillary dermis.[1,12] It is composed of collagenous and non-collagenous components common to basement membranes.[12] These include type IV

collagen, laminins, nidogens, and the proteoglycan perlecan, organised in two ultrastructurally distinguishable layers, the upper lamina lucida and lower lamina densa.[12] In addition, the BMZ features several attachment structures (hemidesmosomes, anchoring filaments, and anchoring fibrils) that binds the epidermis to the dermis, providing structural integrity to the skin with optimal flexibility while permitting cross-compartment molecular and mechanical signalling.[12,13]

Dermis

Compared to the epidermis, the dermis is cellularly sparse and does not undergo sequentially ordered cellular differentiation that mirrors keratinocyte maturation.[2] However, far from being static, it is a dynamic scaffold, of primarily extracellular matrix (ECM) with embedded cellular and non-cellular components, which is continuously remodelled to maintain skin homeostasis.[14,15] The dermis is divided into two distinct areas, the superficial papillary and deeper reticular dermis, which can be distinguished microscopically based on differences in ECM arrangement and fibroblast morphology.[15,16]

The main structural element of the cutaneous ECM is collagen which comprises over 70% of the dry weight of the dermis.[1] Different subtypes of collagen arranged in distinct conformations are present in specific regions depending on functional requirement.[15] For instance, collagen type I arranged in a fibrillar pattern is abundant throughout the dermis while net-forming collagen type IV is the major constituent of the basement membrane.[14] Non-collagenous components of the ECM include elastic fibres, which confer resilience and elasticity to the skin, and a variety of glycoproteins, proteoglycans, and matricellular proteins which modulate cellular attachment, migration, proliferation and skin hydration.[2,15]

The principal cell type in the dermis are fibroblasts, a heterogeneous population, which synthesise the different molecules that make up the ECM and closely interact with the surrounding connective tissue.[1] Other dermal cells include resident immune cells, such as macrophages and mast cells, as well as transient immunocytes which circulate between the skin, circulation and lymphoid tissues.[2] The dermis also harbours the cutaneous blood vessels, lymphatics and nerve fibres as well as serving as anchorage for the various skin appendages as described above (Figure 1.1).

Hypodermis

The hypodermis, loosely arranged beneath the more rigid dermis, is made up of mostly adipocytes (fat cells), interspersed with pluripotent adipose stem cells and immune cells.[1,17,18] The fat cells are organised in lobules which are divided by fibrous septa containing rich supplies of blood and lymphatic vessels.[1,17] The subcutaneous adipose tissue is the major fat reservoir in humans, comprising approximately 80% of the total body fat content with the rest distributed around internal organs.[1] Two types of adipose tissue are recognised - white and brown; white fat is the main form associated with traditional adipose tissue functions such as energy storage, lipid and glucose metabolism and endocrine signalling whereas brown fat, which is more frequent in children, is involved in heat generation.[19] More recently further sub-categorisation of cutaneous adipose tissue into dermal and hypodermal components has been proposed in human skin, in line with observation from animal studies.[20] The dermal white adipose tissue comprises adipocytes that are present in the deep reticular dermis, particularly around hair follicles, and in the upper hypodermis with the remaining adipocytes forming the hypodermal subcutaneous fat.[20] Notably however, these regions are not physically demarcated in human skin but are thought to be functionally distinct.[20–22]

1.1.2 Hair follicle anatomy

Human hair follicles vary in size and shape depending on body location but are made up of the same essential base components which can be divided into epithelial and mesenchymal compartments.[23] In the epithelial compartment of the mature hair follicle, the keratinised hair shaft, emerging from the centre of the pilar canal, consists of a thick cortex covered by a thin single cuticle layer with a core of medulla (present in some hair types)[24] (Figure 1.2). The hair shaft is surrounded and protected by the three concentric layers of the inner root sheath (IRS); from medial (closest to the hair fibre) to lateral, this comprises the IRS cuticle, and the eponymously named Huxley's layer and Henle's layer[25] (Figure 1.2). The outermost epithelial layer of the hair follicle is the outer root sheath (ORS) which is contiguous with the basal stratum of the interfollicular epidermis.[26] Located between the ORS and Henley's layer of the IRS is the companion layer (CL), so called because of its close apposition and contact with cells in Henley's layer with which it migrates upwards during hair growth.[26,27] At the base of the hair follicle, epithelial and mesenchymal structures - the hair matrix and the dermal papilla (Dp) respectively - sit in close juxtaposition[28] (Figure 1.2). The matrix contains highly proliferative cells which produce the hair shaft, the diameter of which is determined by the number of cells in the matrix.[23] This is in turn controlled by the Dp, which is formed of closely packed specialised fibroblasts.[23] The whole hair follicle is enveloped by the other main constituent of the mesenchymal compartment, the connective tissue sheath[28] (Figure 1.2).

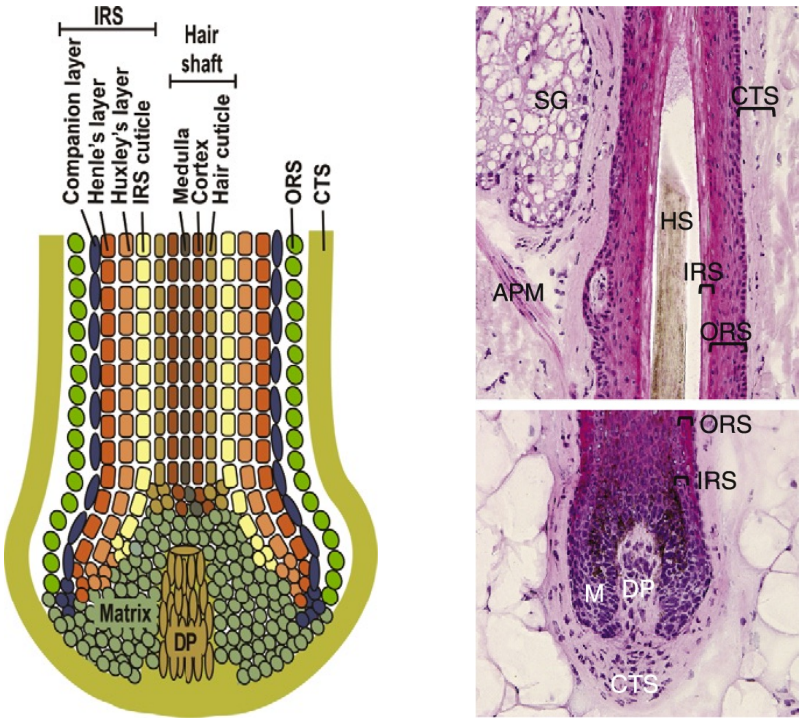

Figure 1.2. Histomorphology of the human hair follicle.

Schematic representation (left) and histological images (right) showing the concentric layers of the IRS, CL, and ORS around the central hair shaft, with the matrix and dermal papilla at the base, and the connective tissue sheath surrounding the whole hair follicle. APM: arrector pili muscle; CTS: connective tissue sheath; DP: dermal papilla; M: matrix; HS: hair shaft; IRS: inner root sheath; ORS: outer root sheath; SG: sebaceous gland. Adapted from Schneider et al.[28]

Other structures, including the arrector pili muscle and the sebaceous and apocrine glands, are attached to the hair follicle proper to form the pilosebaceous or apopilosebaceous units (Figure 1.2). The arrector pili muscle is a small band of smooth muscle which attaches the hair follicle to the dermis and enables raising of the hair when it contracts.[28] The insertion point of the arrector pili muscle forms a bulge in the ORS where the epithelial hair follicle stem cells reside.[28] Above this bulge, the sebaceous gland opens into the hair canal where it secretes sebum to lubricate the skin and hair.[29] Apocrine glands also connect to the hair canal and are restricted to the axillary, mammary, anogenital areas where they produce lipid-rich secretions with yet uncertain roles in human skin.[30]

Together, the above distinct layers and structures constitute the hair follicle as an architecturally complex mini-organ in its own right. To further facilitate its study, the hair follicle is also sub-compartmentalised into microanatomical regions, namely the infundibulum, the isthmus, the suprabulbar region and the bulb[2,28] (Figure 1.3). The infundibulum is the uppermost section, extending from the connection of the sebaceous gland into the hair canal to the epidermal surface of the skin.[2,28] The area between the sebaceous gland attachment and the arrector pili attachment at the bulge is the isthmus.[2,28] The rounded part at the base of the hair follicle containing the matrix and Dp is known as the bulb and the section above the bulb to the isthmus is the suprabulbar region.[2,28] Additional cell types, not specific to the hair follicle, also reside within it such as melanocytes in the bulb and MCs in the ORS.[23]

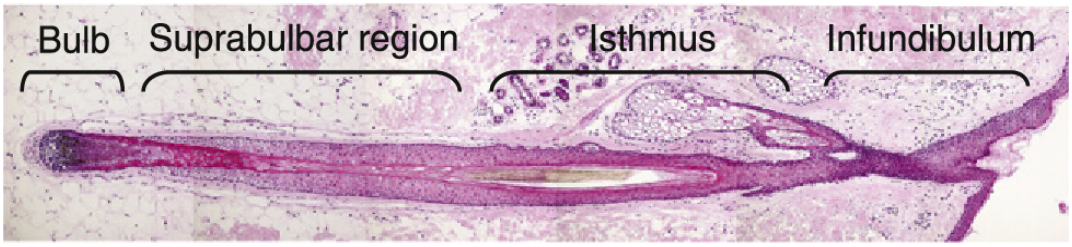

Figure 1.3. Sub-compartmentalisation of the human hair follicle.

Light microscopy image demonstrating the division of a sagittally-sectioned hair follicle into distinct regions including the infundibulum, isthmus, suprabulbar region, and bulb. Adapted from Schneider et al.[28]

All hair follicles in the human skin are established during prenatal life (described in section 1.2.2) and typically no additional ones form after birth.[23] Postnatally, the hair follicles instead cycle periodically through phases of growth (anagen), involution or regression (catagen) and resting (telogen) which terminates in production of a new hair fibre replacing the existing hair shaft which is shed (exogen).[23,24,28] The upper regions of the hair follicle, the infundibulum and isthmus, are considered permanent as they do not conspicuously change during these different phases while the lower portions are cyclically remodelled,[23,28] distinguishing postnatal hair follicle biology from its de novo formation during gestation.

1.1.3 Functions of the skin

As part of the integumentary system, the skin constitutes an interfacing barrier between the outside environment and the inside body milieu, protecting against incursion by external pathological agents, retaining vital internal elements while also allowing transcutaneous exchanges[31]. It serves as a physical barrier against mechanical insults, enabled by the tightly adjoined cells of the epidermis covered by the cornified layer and supported by the flexible, resilient dermis and cushioning hypodermis.[17,31] This physical barrier also precludes invasion by microbes, including the microorganisms that belong to the normal skin microbiota and foreign pathogens.[31,32] The keratinocytes concomitantly produce several endogenous antimicrobial peptides (cathelicidins and defensins) to defend against potential invading microorganisms,[1] in conjunction with the diverse immune cells which populate the skin layers (discussed in section 1.3.1). Physical protection by the skin also encompasses safeguarding from harmful ultraviolet (UV) radiation.[31] The keratinocytes scatter or absorb a degree of UV radiation with additional filtering from melanin pigment in melanosomes which cover the nuclei of keratinocytes to prevent genetic damage.[31,33]

The skin also acts as a permeability barrier that impedes evaporative transepidermal water loss.[32] The lamellar bodies and keratohyalin granules of the granular layer (section 1.1.1) produce and discharge several hydrophobic lipids into the intercellular spaces of the upper epidermis which obstruct the outward movement of water molecules and provide natural moisturisation to the skin.[31,32] Sebum secretion by the sebaceous glands contributes to additional waterproofing at the skin surface.[1]

As the boundary of the body in contact with the external environment, the skin operates as a critical sensory organ.[31] It is innervated by specialised encapsulated receptors and an intricate network of sensory nerve fibres which originate from the dorsal root or trigeminal ganglia and form a subepidermal neural plexus with free nerve endings crossing the DEJ into the epidermis.[1,5] The nerve fibres display varied anatomical, physical and functional properties and, together with the encapsulated receptors and complexes formed with MCs (MC-neurite complex), transduce a range of stimuli including touch, pressure, stretch, pain and heat.[5,10] Additionally, several constitutive cells of the epidermis such keratinocytes are now recognised as key participants in sensory perception.[5] They not only closely interact with afferent neurons but also possess neuron-like sensor proteins capable of detecting and transducing noxious and thermal stimuli, qualifying the entire epidermis as a sensory tissue.[5,31]

In addition to its barrier functions, the skin plays a key role in thermoregulation, effected through alterations in the blood flowing through it and regulation of sweat production.[1] Vasodilation occurs in response to a rise in body temperature, increasing the cutaneous blood flow in both the deep and superficial vascular plexuses leading to heat dissipation.[34] Conversely, cold exposure causes vasoconstriction of the skin blood vessels to reduce blood flow and heat loss to prevent lowering of body temperature and hypothermia.[34] The amount of sweat produced by the eccrine glands in the skin is controlled by peripheral and central thermoreceptors which sense changes in body temperature and by non-thermal stimuli such as exercise which can directly induce sweating.[35] The sweat is secreted onto the skin surface and its evaporation results in a cooling effect.[35]

Closely related to the thermoregulatory role of the skin, is thermal insulation imparted by its subcutaneous fat.[20] The adipocytes in the skin also contribute to lipid and glucose metabolism and energy storage by accumulating lipid droplets which can then be broken down to fuel metabolic requirements in fasted states.[19] Furthermore, the subcutaneous adipose tissue is a crucial endocrine organ secreting numerous adipocytokines which regulate various aspects of appetite and food-seeking behaviour, insulin production and steroid conversion.[19] Vitamin D is another metabolic product which is solely endogenously synthesised in the skin under the influence of sun exposure and is essential for calcium homeostasis.[36] These wide-ranging functions highlight the multi-faceted aspects of the skin as a simultaneous barrier, sensory, immune and endocrine organ.

1.2 Prenatal development of human skin

1.2.1 Skin embryology and derivation from germ layers

Prenatal cutaneous development involves several carefully coordinated stages and processes to form the architecturally complex and multi-component organ that constitutes the fully formed mature skin described in section 1.1.1. The earliest event in skin specification occurs during gastrulation in the third week of development when the three germ layers - the ectoderm, mesoderm and endoderm - are established.[37–39] The ectoderm gives rise to the eventual epidermis and its appendages while the juxtaposed mesoderm produces the stromal cells of the dermis, including fibroblasts, endothelial and mural cells, and the underlying adipose tissue and fascia.[40] At the start of organogenesis following gastrulation, part of the ectoderm overlying the notochord is induced to become the neuroectoderm which is the primordium of the entire nervous system.[39] As the neuroectoderm folds, neural crest cells dissociate from its lateral aspects and in the trunk region, migrate either ventrally to form the peripheral sensory neurons and Schwann cells or dorsally to differentiate into melanocytes[41]. In the craniofacial area, part of the dermis of head and neck skin is additionally derived from cranial neural crest (CNC) cells.[39,41]

The embryonic epidermis starts as a single basal layer of multipotent epithelial cells from the ectoderm which is then overlaid by the periderm by the fourth week after conception.[42,43] The periderm is a flat transient epithelial layer, unique to gestation, which is thought to provide protective coverage to the nascent epidermis, prevent aberrant epidermal adhesions and potentially enable substance exchange between the embryo and surrounding amniotic fluid.[44,45] Under the periderm, the developing epidermis proliferates and stratifies to form an initial intermediate layer (two to three cell thick) which matures into the spinous layer and subsequently differentiates to form the granular and cornified layers.[43,44] The periderm starts to desquamate towards the end of the second trimester and is shed once the stratum corneum of the differentiating epidermis is formed.[42,45] The immigrant cells of the epidermis, including those belonging to the LC (discussed in section 1.3.3), melanocyte and MC lineages, appear early during skin development. Sheets of melanocytes or their precursors are apparent in skin at 7 post-conception weeks (PCW), when the epidermis is only two cells thick, but melanosomes are only transferred to keratinocytes from the fifth month of gestation.[46] Merkel cells first appear in palmar skin around 8 PCW in significantly higher density compared to non-glabrous skin where they have been observed from around 11 PCW.[47]

A rudimentary basement membrane is already apparent beneath the epidermis when it is about two-cell thick, comprising all the constituents of archetypal basement membranes (type IV collagen, laminins, nidogens, and perlecan as discussed in section 1.1.1).[42] The anchoring complexes, however, are not fully developed but become structurally similar to postnatal skin complexes by the time of embryonic to foetal transition (~8-10 PCW).[42] The still delicate and flattened BMZ continues to mature with the growing epidermis during the second trimester to acquire its undulating morphology.[42]

Epidermal development is also closely linked to that of the underlying dermis which sends signals to the epidermis to dictate regional differences and patterns of appendage formation.[43] This includes the induction and formation of hair follicles which is discussed in section 1.2.2. The dermis itself begins as a cellularly dense region where deposition and organisation of the connective tissue matrix progresses slowly such that collagen bundles and elastic fibres are still immature in structure and composition even in the third trimester when dermal thickness remains reduced compared to postnatal skin.[42,48] The papillary and reticular dermis are however well-defined by this stage and the hypodermis is easily distinguished with established fat lobules.[42,48] Morphogenesis of the cutaneous endothelial and neural networks (described in section 5.1), on the other hand, occurs early in embryonic skin with a vascular pattern resembling that of adult skin already evident around the transition period from embryonic to foetal life.[49,50] A variety of immune cells seed the prenatal skin, following the different waves of haematopoiesis, and can be detected as early as 6 PCW.[51] Their composition and putative functions are discussed in section 1.3.2.

1.2.2 Development of hair follicles and related appendages

Studies of hair follicle development in human prenatal skin have primarily reported morphological descriptions with limited assays of the molecular changes involved.[42,52] Most of the current detailed knowledge about hair follicle formation derive from experiments using established cycling hair follicles from human postnatal skin or predominantly from animal studies, particularly mouse and chick models.[42,52] This information has been extrapolated to infer the processes potentially implicated during human de novo hair follicle morphogenesis but the biological factitude of these assumptions are unclear.[42,52] In this section, I have summarised what is known about human prenatal hair follicle formation and its related appendages (sebaceous and apocrine glands) and added brief insights drawn more broadly from the general appendage literature.

Human de novo hair follicle development

Hair follicle morphogenesis starts in the region of the head and face around 9-10 PCW and proceeds in a cephalocaudal direction, terminating around 20 PCW when hair fibres protrude from the last developing follicles through the skin surface.[42,53] This process is initiated by crosstalk between the mesenchymal cells in the dermis and epithelial cells of the epidermis which induces the formation of hair placodes - select areas of epidermal thickening where the hair follicles eventually develop.[42] The pattern of placode distribution is body site specific.[42] The placode stage has also been termed as 'pre-germs' in human skin, corresponding to observed areas of regularly spaced compact clusters of basal keratinocytes with an underlying aggregation of mesenchymal cells (now termed dermal condensate (Dc))[54,55] (Figure 1.4).

Following placode specification, four stages of follicular development have been described based on distinct morphological appearances: hair germ, hair peg, bulbous hair peg and lanugo follicle stages[54] (Figure 1.4). The hair germ represents the budding of basal epithelial cells into the dermis, surrounded by the initially condensed mesenchymal cells.[54] The hair germs elongate and penetrate further into the dermis at an angle relative to the epidermis, forming the hair peg[54,56] (Figure 1.4). The deep end of the elongated hair peg then flares into a bulb-like conformation with a central concavity which encases the mesenchymal cells at its base[54] (Figure 1.4). In this bulbous hair peg, the epithelial cells residing at the roof of the concavity become the matrix and the enclosed mesenchymal cells form the presumptive Dp; the mesenchymal cells still lining the outer bulbous hair peg constitute the eventual dermal sheath.[54] By 12-15 PCW, a hair fibre and the differentiated

layers of the ORS and IRS can be seen; the hair canal hollows out within the follicle and epidermis around 15 PCW, paving the way for the lanugo hair shaft to eventually emerge[54] (Figure 1.4).

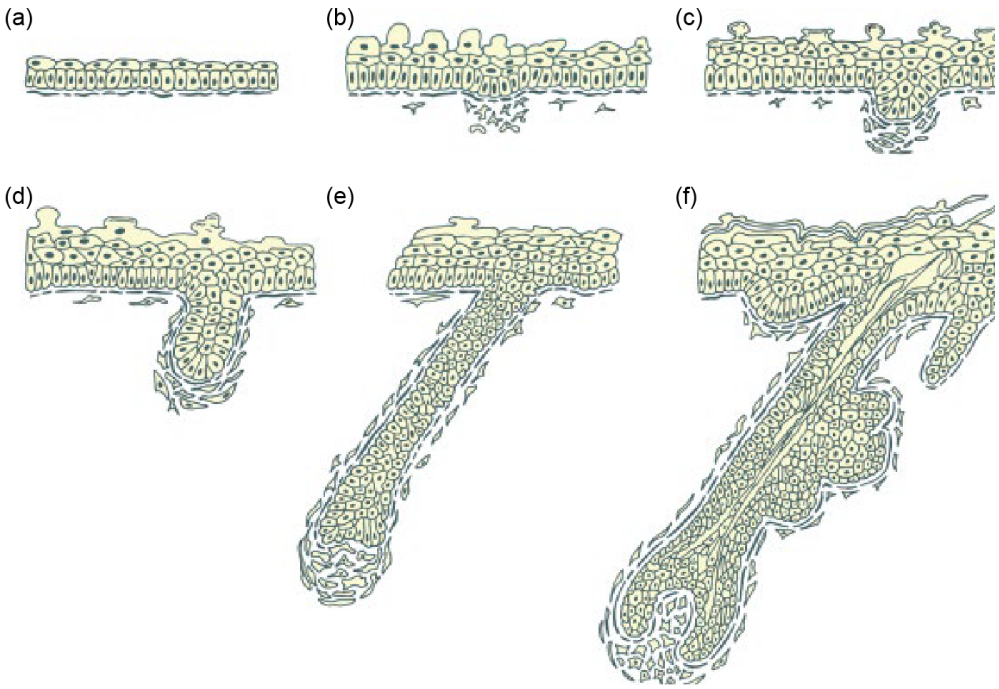

Figure 1.4. Stages of hair follicle formation.

Schematic diagram of the morphological changes during the different stages of hair follicle development. From top left: from (a) pre-placode stage to (b) placode (pre-germ) formation with underlying aggregation of Dc cells and (c) hair germ budding, followed by (d) hair peg elongation to form (e) the bulbous hair peg and eventually (f) the differentiated lanugo hair follicle. Adapted from Lee and Holbrook.[42]

The new hair follicles in prenatal skin are thus products of inductive events, involving mesenchymal-epithelial signalling, followed by molecular processes which ensure their initiation, elongation and differentiation.[56] Investigations to elucidate these interactions and molecules in human prenatal skin have largely been restricted to assessment of gene expression patterns and changes in selected morphogens, including growth factors, receptors and cell adhesion molecules, guided by a priori findings in other types of follicles (for example, rodent and sheep) and appendages (for example, teeth and feathers).[56] These studies provided some insights into the differences between the interfollicular and follicular epithelium, mesenchyme and basement membrane. For instance, the ORS expresses similar keratins to the basal layer of the epidermis with which it is continuous but the type of keratin expressed varies across the length of the hair

follicle.[56] Some morphogens (for example, nerve growth factor receptor and neural cell adhesion molecule) initially widely distributed in the upper dermis become restricted to the dermal condensate and potentially promote their cellular adhesion properties.[56] However, whether these changes actively induce hair follicle formation or result from the initial induction could not be determined.[56] The interactions that initiate and sustain human hair follicle morphogenesis have also not been conclusively identified.[56]

Formation of hair-follicle related appendages

In the bulbous hair peg, separate bulges of epithelial cells start to outgrow at defined locations along the follicle between 15 and 17 PCW.[42] The most superior protuberance appears on the posterior aspect as the primordium of the sebaceous gland.[54,55] The cells in the centre of the differentiating gland subsequently accumulate lipid droplets and begin to produce sebum which is secreted to the prenatal skin surface as part of the vernix caseosa.[54,57] The second bulge, forming simultaneously to and just under the sebaceous gland, constitutes the true bulge of the mature hair follicle which harbours the follicular epithelial stem cells and is the attachment point of the arrector pili muscle.[54,55] A third bulge develops superior and opposite to the sebaceous gland in specific body locations, including axillae, areolae, scalp and anogenital areas, as the anlage of the apocrine gland.[42,55]

Insights from animal models

Research using animal systems has considerably expanded our understanding of hair follicle morphogenesis. Classic studies starting in the 1950's, which recombined mismatched epidermis and dermis from different origins (for example, derived from two different body sites, age groups, or species) and allowed them to grow in culture or as grafts, identified that these two compartments played distinct roles during hair follicle development and that their cross-compartmental communication was key to its induction.[24,56]

Since then, significant advances have been made in unravelling the signalling pathways and regulatory programmes orchestrating de novo follicular formation especially in mice, which is arguably the most studied model to explore hair follicle biology.[52] The critical activation of pathways, including Wnt/β-catenin and NF-κB (signalling through the ligand ectodysplasin A (Eda) and its receptor (Edar)), and the sequential involvement of growth factors or their inhibitors (bone morphogenetic protein (BMP) 2 and 4, noggin, transforming growth factor β (TGF-β),

fibroblast growth factor (FGF) 20 and platelet-derived growth factor (PDGF) A) have been demonstrated[52,58] (detailed discussion in section 3.3.4). In tandem, the intermediate differentiation states that the epithelial and mesenchymal cells transit through to form the components of the mature hair follicle have been increasingly characterised.[52,58–61] Consequently, the classification of the stages of hair follicle morphogenesis in mice has been expanded (from 4 described above in human skin to 11 stages in mice), starting from the as yet unspecified epithelium and upper dermis through the pre-placode stage to complete engulfment of the Dp and formation of the sebaceous gland.[58,62] It is not established, however, to what extent hair follicle morphogenesis in prenatal human skin parallels what is seen in mice.

In summary, the remarkably detailed reports of the precise structural and ultrastructural changes displayed by the human prenatal skin across gestation, supplemented by immunohistochemical analyses, tissue culture experiments and clinical observations, have provided substantial insights into the morphological aspects of cutaneous and appendage morphogenesis.[42] Molecular information has been surmised from findings in mouse skin. These are routinely analogised to the human context on the basis of proven commonalities in the basic mechanisms of skin development between the two species as well as comparable phenotypes resulting from defined genetic mutations.[52,56] However, differences do exist between mouse and human skin, for instance in the duration of gestation, skin thickness and layering (additional panniculus carnosus in mice), hair follicle types and cycling, response to androgens, and immune composition.[52,63–65] Conceivably, these divergences may challenge the assumption of unchecked equivalence between the two species. An unbiased cellular and molecular profiling of all the differentiating cells in human prenatal skin across gestation could help address these uncertainties by establishing a comprehensive atlas of cutaneous morphogenesis, allowing differentiation trajectory inference, facilitating cross-species comparisons, and resolving some of the unanswered questions in skin and hair development in humans.

1.3 Role of immune cells in skin

1.3.1 Immune cells in healthy skin

Postanal human skin is populated by a plethora of immune cells which are essential for tissue homeostasis, defence and repair.[66] Under healthy steady state, both innate and adaptive immune cells reside in the skin and occupy functionally-related anatomical niches.[67] Some of these resident immunocytes can migrate to the lymph nodes to present antigens to induce an immune response or promote self-tolerance.[66] In the following subsections, an overview of the skin-resident myeloid and lymphoid cells is provided but additional leukocytes from the circulation can also infiltrate the skin following a cutaneous insult, such as injury or infection, and cooperate with the local cells to bolster immune barrier functions.[66]

Myeloid lineage cells

The myeloid populations normally present in the skin include LCs, dendritic cells (DCs), macrophages, mast cells and eosinophils. Langerhans cells are intra-epidermal antigen-presenting cells, which act as sentinels and extend their dendrites through the epidermis to sample the upper skin layers.[68] They can phagocytose, process and present antigens and determine whether to maintain a tolerogenic environment, by promoting regulatory T cell (Treg) activity, or elicit a defensive response by triggering innate immune mechanisms and activating adaptive T cells.[68,69]

Within the dermis, DCs are the professional antigen-presenting cells.[70] Unlike LCs, which are long-lived following differentiation from precursors prenatally seeded from yolk sac and foetal liver and are self-renewing in steady-state skin, DCs derive from bone-marrow progenitors and are frequently replenished.[71] Several subsets of DCs have been described in healthy skin, including conventional DCs (cDC1, cDC2) and monocyte-derived DCs (moDCs), based on distinct marker expression and functional specialisation.[70,71] cDC1 are highly effective at presenting exogenous antigens for cross-priming of $CD8^+$ cytotoxic T cells and induce $CD4^+$ T helper (Th)-1 differentiation while cDC2 drive Th2 and Th17 polarisation.[70,71] Arising from bloodstream monocytes that enter the skin where they acquire major histocompatibility complex (MHC) class II (MHCII) expression, moDCs phenotypically resemble cDC2 and rapidly expand following inflammatory stimuli through increased recruitment from the systemic circulation.[70,72] Additional DC subsets which are mainly found in blood and lymphoid tissues under homeostatic conditions

and increase in the skin during inflammation include the interferon (IFN)-α producing plasmacytoid DCs (pDCs) and $AXL^{+}SIGLEC6^{+}$ DCs (ASDCs) which possess a transcriptomic and phenotypic profile intermediate between pDCs and cDCs.[70,72]

Macrophages, located deeper in the dermis and hypodermis compared to DCs, are the most abundant resident immune cells in adult human skin.[71,73] Under steady state, both macrophages derived prenatally (capable of self-maintenance) and those differentiated postnatally from circulating monocytes are present in the skin.[67] Their core functions involve tissue surveillance, clearance of cellular debris and foreign bodies, mounting efficient cell-mediated immune responses, and modulating cutaneous tissue repair.[74,75] In mouse skin, it is increasingly recognised that macrophages also occupy distinct subtissular niches around blood vessels, neurons and hair follicles with corresponding functional implications.[71,76,77] Different approaches to classify macrophages have been adopted, from the dichotomous M1-M2 segregation, based on activation status and pro- or anti- inflammatory influences,[78] to the spectrum model where M1 and M2 represent extreme states, and more recently the transcriptionally-defined macrophage cell states.[75] The latter categorisation may better reflect tissue imprinting and subtissue niche-related functional specialisation. However, the correlation between macrophage state and niche-specificity, the (non)uniformity of this association across tissues and the potential plasticity among different macrophage states require further clarification.[75]

Mast cells, the prime effector cells in allergic diseases, arise from pluripotent stem cells in the bone marrow, circulate as progenitors before homing to the skin and other tissues where they physiologically mature under the effect of locally secreted factors.[79] They are characterised by their cytoplasm rich in secretory granules which contain a variety of pre-formed mediators including histamine, serotonin and the proteases tryptase and chymase.[79] The granule contents are released upon mast cell degranulation which can be triggered by cross-linking of their immunoglobulin (Ig) E receptors (IgE-mediated, resulting in immediate hypersensitivity reaction) or via non-IgE-related mechanisms.[1] Eosinophils are a subtype of granulocytic leukocytes which are resident in the skin under physiological condition.[66,80] Their cytoplasmic granules contain several cytotoxic proteins and lipid bodies, allowing them to function in immune defence against invading pathogens, typically parasitic infections, as well as participate in skin hypersensitivity reactions where they produce overlapping lipid bodies with mast cells including leukotrienes and prostaglandins.[66,80]

Homeostatic tasks, regulating Th and Treg activity and tissue repair have been described in organs such as gut and lungs but remain to be evaluated in skin.[66,80]

Lymphoid lineage cells

The normal cutaneous immune repertoire comprises lymphoid cells belonging to both the adaptive and innate systems.[67,73] T cells, including $CD4^+$ and $CD8^+$ subsets, establish residency in the skin as long-lived tissue-resident memory T cells and are the most abundant lymphocytes. At an estimated 1 million per square centimetre, they are twice as frequent in the skin compared to the circulation.[81,82] The majority are conventional αβ T cells, which undergo intrathymic maturation and selection before exiting the thymus and trafficking to peripheral tissues.[83] These T cells recognise antigens through MHC class restriction and are poised to protect against reinfection by activating antigen-specific responses.[84] A portion of $CD4^+$ tissue-resident T cells in the skin (~20%) represent Tregs, which act to limit inflammation and prevent tissue damage by self-reactive T cells.[85] Tregs may have additional roles in skin homeostasis as they have been observed to preferentially localise around hair follicles and, in murine skin, likely promote hair follicle cycling.[85]

Unconventional T cells are also present in the skin and include γδ T cells and mucosal-associated invariant T (MAIT) cells.[67,73] γδ T cells (with γ and δ T cell receptor chains instead of α and β) develop along alternate pathways in the thymus compared to classic αβ T cell maturation and selection.[86] Bridging adaptive and innate roles, they can recognise a broader array of antigens usually without requirement for MHC and co-stimulatory molecules and thus respond more rapidly even in the absence of previous antigen exposure.[81,86] Unlike αβ T cells, they are also capable of antigen presentation and contribute to skin surveillance and immunoregulation.[86] Similar to γδ T cells, MAIT cells also display innate-like properties with rapid-responder functions and production of cytotoxic mediators that directly neutralise target cells.[87] They are characterised by their specific recognition of bacterial-derived riboflavin metabolites (from vitamin B biosynthesis) and locate to the basement membrane and lower epidermis where they can interact with the skin microbiome.[87]

Apart from T cells, the skin also harbours different groups of innate lymphoid cells (ILCs) which are largely maintained and expanded locally and are activated in an MHC-independent manner by mediators (for example, cytokines and alarmins) released from epithelial, stromal or myeloid cells.[88] They have been described as the innate counterparts of adaptive T cells based on shared

transcription factors and cytokine expression profiles. As such, three groups of ILCs are recognised.[89] Group 1 ILCs consist of natural killer (NK) cells and ILC1s, express T-bet transcription factor and are involved in type 1 immune responses against intracellular pathogens through production of cytotoxic molecules (granzymes, perforins) and IFN-γ; NK cells are more cytotoxic while ILC1s generate more IFN-γ and are therefore considered the innate equivalents of $CD8^+$ cytotoxic T cells and effector Th1 cells respectively.[88,89] Similarly, ILC2s correspond to Th2 cells: they are developmentally dependent on GATA-3 and produce type 2 interleukins (IL), such as IL-4 and IL-13 which are implicated in host protection against extracellular parasites, tissue repair and allergic inflammation.[88,89] Group 3 ILCs require nuclear receptor gamma (RORγt) as transcription factor and comprise lymphoid tissue inducer (LTi) cells and ILC3s. While LTi cells are linked to histogenesis of lymphoid tissue, ILC3s induce type 3 immunity against extracellular microorganisms through production of IL-17 and IL-22 in common with Th17 cells.[88,89] However, transcriptomic-based studies suggest that there exists greater heterogeneity of ILCs within these three broad groupings, which is likely indicative of their plasticity.[88]

Unlike T cells, B-lineage cells are scarce in healthy adult skin and until relatively recently were not thought to feature in the normal cutaneous immune system.[90,91] B cells exist in different developmental states across body sites. In the bone marrow, where their development originates postnatally, B lymphocytes differentiate from haematopoietic stem cells, through several intermediate states including pre pro-B, pro-B, and pre-B cells, into immature B cells.[92] These immature B cells emigrate from the bone marrow and circulate to secondary lymphoid tissues such as spleen and lymph nodes where they undergo further maturation into memory B cells and plasma cells (terminally differentiated B lymphocytes).[92,93] In the skin, antibody-secreting plasma cells have been detected in the dermis under steady state but the presence of other mature B cell states remains contentious and, if present, likely represents transient populations trafficking intra-dermally between the blood and lymphatic systems.[66,94,95] Dermal plasma cells primarily secrete IgM, an immunoglobulin isotype implicated in pathogen neutralisation, clearance of apoptotic debris, and tissue repair, thus contributing to skin homeostasis and immune barrier functions.[91,94]

1.3.2 Immune cells in prenatal skin

The immune landscape of human prenatal skin develops in parallel to its structural morphogenesis. The full repertoire of the major immune cell lineages that populate healthy postnatal skin (section 1.3.1) also appears in the developing skin.[51] However, key differences exist in the numbers, subtypes and proportions of cutaneous immunocytes before and after birth.[51] The total counts of immune cells is much lower in prenatal skin which also contains several progenitor states that are absent in adult skin.[96–98] Additionally, a few cell types are uniquely detected either prenatally or postnatally. For instance, B cells and B cell progenitors have been reported in embryonic and foetal skin but are physiologically not resident in adult skin which conversely harbours mature plasma cells.[99–101]

The relative proportions of the various immune cell subsets, both at broad lineage and at individual celltype levels, also differ between prenatal and established postnatal skin although these ratios evolve across gestation.[51,98] The changes in cellular composition reflects the principal organs contributing to haematopoiesis at different timepoints during development of the blood and immune systems.[99,101,102] The yolk sac is the earliest known producer of immune cells in humans - a feature of haematopoiesis origination occurring extraembryonically that is conserved across several species including mammals and birds.[103] It is the site of the initial primitive wave of haematopoiesis, starting at Carnegie stage (CS) 6 (~2.5 PCW). Haematopoietic progenitors, megakaryocytes and macrophages have been isolated from the human yolk sac by CS11 (~4 PCW).[102] Subsequently, definitive haematopoiesis occurs intraembryonically in the aorto-gonad-mesonephros (AGM) at CS14 (~5 PCW) and generates long-term multi-potent haematopoietic stem and progenitor cells (HSPCs), with equivalent cells also detected in the yolk sac at CS16 (~6 PCW).[102,104] Progenitors from the yolk sac and AGM seed the embryonic liver (from around CS12) which becomes the dominant haematopoietic organ until the mid-second trimester.[99,105] HSPCs developing in the liver acquire engraftment capability for the bone marrow which eventually takes over as the primary haematopoietic centre from 20 PCW.[99,105] Lymphoid expansion, especially of the adaptive subset, typically accompanies bone marrow (~11-12 PCW) and thymus functional development (~12 PCW).[106] Innate immune cells, therefore, predominate in the first trimester embryo.[101] In addition, early haematopoietic progenitors arising in the yolk sac prior to AGM formation are biased towards the myeloid lineage[102] so that, alongside the macrophages mentioned earlier, the yolk sac also contains monocytes and DCs by 4-5 PCW and mast cells by 8 PCW.[102]

Immune cells from the different sites of haematopoiesis (yolk sac, AGM, liver and bone marrow) disseminate to peripheral tissues including the skin.[99] As a result, macrophages, mast cells, DCs, NK cells and ILCs, have been observed in prenatal skin by 8 PCW.[51,101] Langerhans cells are detectable as early as 6 PCW but their origin in human skin is unclear and they may dually emerge from yolk sac and foetal liver precursors as in mice.[51,70] T cells increase in the second trimester and until recently was thought to only comprise αβ subsets but a recent single-cell study of the developing human immune system demonstrated the existence of unconventional T cells, with expression of γ and δ receptor chains, in prenatal skin.[51,101] Although only a fraction of the adult T cell numbers are present prenatally (4 - 7%), the proportion of Tregs is already comparable to postnatal skin.[51,96] The developing skin immune profile thus dynamically alters as gestation progresses, morphing into a network that closely resembles that of adult skin in the final trimester.[51,98]

The precise roles of such a complex and near-complete immune repertoire in the presumed sterile in utero environment of the prenatal skin is unclear.[51] This could merely represent an initially passive process of immune cell diffusion throughout the embryo, where the skin provides a niche for their maturation, shapes and imprints their phenotypes through local microenvironmental factors, and retains some of the developing immunocytes based on cutaneously expressed homing molecules. The specific production of growth factors (for example, TGF-β1 and BMP7) which are essential for the differentiation and survival of epidermally-retained LCs by keratinocytes, the identification of lymphopoiesis of B cells with no long-term cutaneous persistence, and the high frequency of progenitor and replicating cells in prenatal skin endorse it as a fostering environment that nurtures future skin-resident immune cells and supports the wider blood and immune development.[51,101] However, emerging evidence from animal studies suggests that the occupancy of developing organs by immune cells may also be a symbiotic mutually-beneficial establishment which contributes to tissue morphogenesis.[77,107,108] Whether immune cells play similar developmental roles in human prenatal skin remains to be determined.

1.4 Genomic technologies to study skin development

The requirement for a comprehensive cellular and molecular assessment of prenatal skin to answer unresolved questions in human skin and hair developmental biology, including the potential roles of immune cells in cutaneous morphogenesis, was discussed in sections 1.2.2 and 1.3.2. A major challenge in embryonic and foetal studies, however, is the scarcity of material available for testing which is constrained by the frequency of donation and tissue volume per sample especially in very early or late gestation.[109] Techniques that extract maximal information from the minimum amount of tissue possible are thus indispensable. Single-cell RNA sequencing (scRNA-seq), originally developed to address similar needs, is a sensitive technique capable of profiling limited starting biological material (in this case ribonucleic acid (RNA)) at high resolution.[110,111] It additionally overcomes the limitations of transcriptomic methods based on a priori knowledge (for example, hybridisation-based microarrays) and those measuring population-averaged gene expression, such as bulk RNA sequencing, by providing whole transcriptome information at single-cell level.[110,111]

However, scRNA-seq critically loses the spatial context in which cells exist and function because of the dissociation required during tissue processing .[112] Spatially resolved transcriptomics, in contrast, can measure gene expression while preserving spatial information.[113] The technologies that spatially profile the whole transcriptome at single cell resolution, though, have only recently become more widely accessible.[113,114]

In the following sections, I briefly overview some existing single-cell and spatial approaches and their applications, describe the key steps in generating these types of data from tissue samples, and discuss how scRNA-seq data can be used to computationally deconvolve spot-resolution spatial data to model the spatial distribution of single cells.

1.4.1 Single-cell RNA sequencing

Since its inception, high throughput scRNA-seq has been deployed to dissect cellular heterogeneity and provide novel insights across diverse aspects of human development, health and disease.[115] New cell states, biological pathways and pathological mechanisms have been unravelled in the fields of developmental and stem cell biology,[99,101,116] oncogenesis and tumour metastasis,[117–119] immune diseases and therapies,[100,120] and infections and autoimmunity.[121,122] Its potential is being leveraged by the Human Cell Atlas (HCA) initiative, a global consortium which aims to create reference maps of all cells in the body (~37 trillion) across human lifespan to expand the understanding of health and ill-health and transform disease diagnosis, monitoring and treatment.[123]

Although several scRNA-seq protocols are currently in use, there are generic steps common across all the approaches (Figure 1.5).[111] First, single cells are captured: dissociation is carried out if the starting material is solid tissue and in some protocols, fluorescent-activated cell sorting (FACS) for single-cell isolation may be required.[124] Then, the single cells are lysed to release RNA molecules and select reverse transcription (RT) of messenger RNA (mRNA) transcripts is undertaken to produce complementary deoxyribonucleic acid (cDNA).[111] The minute amounts of cDNA are amplified, using polymerase chain reaction (PCR) or in vitro transcription, prior to library preparation for sequencing.[111]

The different scRNA-seq protocols vary in how mRNA is transcribed and amplified, in coverage of cDNA, and in throughput, cost and operator input for a given number of targeted cells.[124] For instance, switching mechanism at 5′ end of RNA template sequencing (SMART-seq)[125] and its improved version, SMART-seq2,[126] are designed for full-length cDNA coverage but can be expensive and time-consuming for large numbers of cells. Conversely, massively parallel RNA single-cell sequencing (MARS-seq),[127] does not capture the full length of the mRNA transcript, is focused on 3’ counting only, with addition of a unique molecular identifier (UMI), but can efficiently and cost-effectively quantify gene expression in thousands of cells simultaneously.[124]

To further facilitate the scRNA-seq process, some of these protocols have been adapted into microdroplet- or microwell-based platforms that fully or partly automate steps including cell isolation and lysis, RT and cDNA amplification.[112,124] The Chromium system from 10x Genomics is an example of such a platform which uses microfluidic technology (8-channel chip) to encapsulate single dissociated cells each with a gel bead, comprising unique barcoded oligonucleotides and RT reagents, in individual droplets (the reaction partitions) to form gel beads in oil-based emulsion (GEMs).[128,129] Cell lysis, mRNA binding, barcoding, and RT occur within each functional GEM, enabling rapid (~20 minutes) processing of around 10,000 cells per channel. This fast turn-around makes this method particularly suitable when attempting to isolate as many cells as possible from scarce tissues with rare cell types.[128]

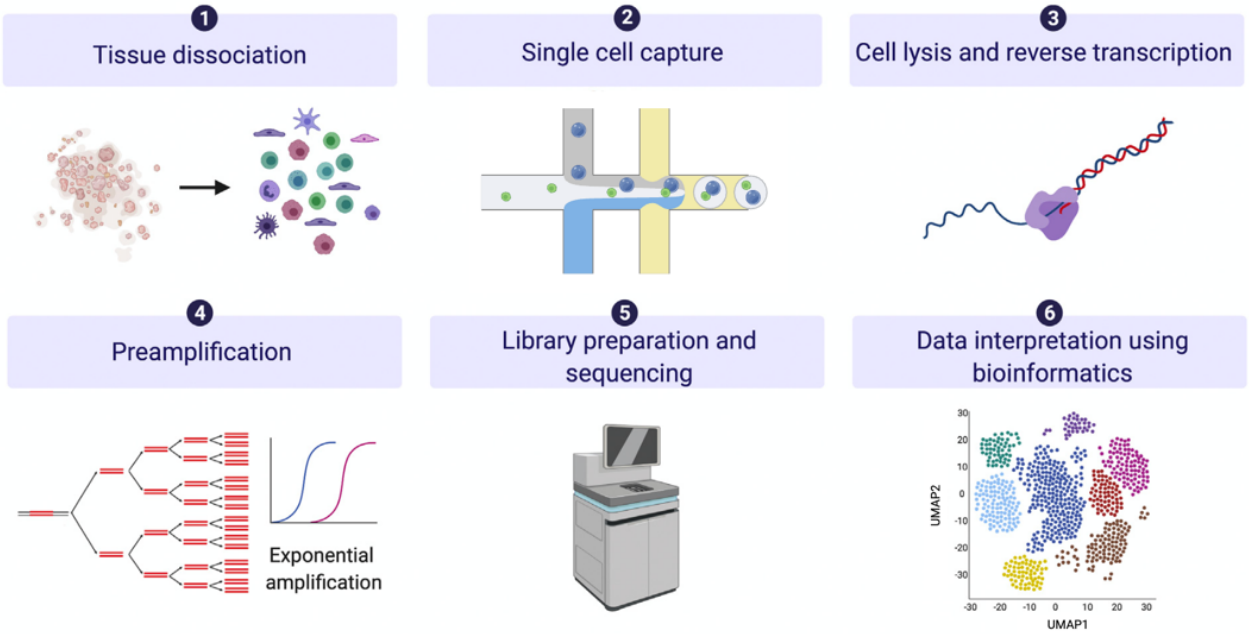

Figure 1.5. Single-cell RNA sequencing experimental workflow.

Schematic diagram showing the key steps in scRNA-seq experiments including tissue dissociation to enable capture of single cells, followed by cell lysis to release mRNA for reverse transcription into cDNA which is then amplified prior to sequencing to generate data for analysis. Adapted from Dubois et al.[115]

1.4.2 Spatial transcriptomics

The spatial positioning of cells within the tissue context holds essential information about their intercellular interactions, regulatory mechanisms and distinct functions.[113] However, this spatial dimension is negated in scRNA-seq as highlighted above. Additionally, tissue dissociation in scRNA-seq pipeline can also cause cell death and induce artificial stress gene signature.[113] Analysing the transcriptome in intact, undissociated tissue therefore presents numerous advantages. Multiple approaches exist for spatially resolved transcriptomics which continue to be optimised to improve resolution and efficiency of capture and can be broadly classified into two categories: imaging-based and sequencing-based.[130]

In imaging-based methods, the spatial arrangement of RNA molecules is visualised and captured in situ using microscopy.[113,114,130] This is achieved either through in situ hybridisation (ISH) of RNA molecules to sequence-specific probes that are fluorescently labelled,[113,114] for example in sequential fluorescence ISH[131] (seqFISH) and multiplexed error-robust fluorescence ISH[132] (MERFISH), or by in situ sequencing (ISS) where probe-hybridised deoxyribonucleic acid (DNA) or cDNA (from reverse transcribed RNA transcripts) are amplified and sequenced in the tissue and fluorophore signals from the probes are registered,[113,114] for instance in fluorescent in situ sequencing[133] (FISSEQ). These techniques have high resolution, with capability for subcellular RNA localisation and can potentially assess the whole transcriptome.[113,114] However, they are time-consuming to undertake, requiring prolonged imaging time, which may limit the number of genes measured in ISH or tissue area captured in ISS.[114] They also generally require experienced operators and complex instruments, restricting their widespread application.[114]

In sequencing-based methods, RNA is extracted from tissue with preserved spatial information before being sequenced ex situ, leveraging technological advances in library preparation and next-generation sequencing.[113,114] Two main approaches are used to retain the original positional information including microdissection of defined tissue areas, such as in laser capture and light-assisted microdissection (for example, Light-Seq[134]), or binding of RNA transcripts to spatially barcoded probes or primers in microarrays (for example, Spatial Transcriptomics[135] (ST) and Slide-seq[136,137]).[113] Protocols based on microdissection generally require a restricted tissue region of interest to be selected from which the transcriptome is then measured.[114] Conversely, in array-based methods, the dimensions of the capture areas determine the tissue size that can be profiled, for instance 6.5 x 6.5 mm in Visium, the commercialised version of ST,[135] and up to 13 × 13 cm in

spatial enhanced resolution omics-sequencing[138] (Stereo-seq). Overall, sequencing-based techniques allow whole transcriptome assessment of larger tissue sections compared to imaging-based approaches but usually with reduced sensitivity (accurate transcript detection) and at lower resolutions, although protocol advances now approach subcellular resolution (~ 1 µm).[113,114,138]

The high-throughput potential of array-based approaches, coupled with increased accessibility through commercialisation, has led to their application in diverse fields. Namely, Visium, the commercially available version of ST from 10x Genomics,[135,139] has been used to examine tissue-wide patterning of gene expression and organisation of cellular niches in reproductive biology,[140] developing systems,[101,141] inflammatory and infective conditions,[142,143] and tumour microenvironments.[144] In this method, thin fresh-frozen tissue sections are placed in capture areas (6.5 x 6.5 mm), circumscribed by a fiducial frame, on the Visium slide where they undergo fixation, staining, imaging, and permeabilisation to release mRNA (Figures 1.6 and 1.7).[139] The mRNA from the tissue binds to positionally barcoded oligonucleotides present in the capture areas. These oligonucleotides are clustered in circular spots (4992 spots per capture area), each measuring 55 µm in diameter with a centre-to-centre inter-spot distance of 100 µm.[139] The spatially barcoded mRNA are then processed through standardised steps of RT, second strand synthesis, cDNA amplification to form sequencing-ready libraries.[139] The gene expression data with positional information is then overlaid back on the pre-imaged tissue sections, providing their spatially profiled transcriptome.[139]

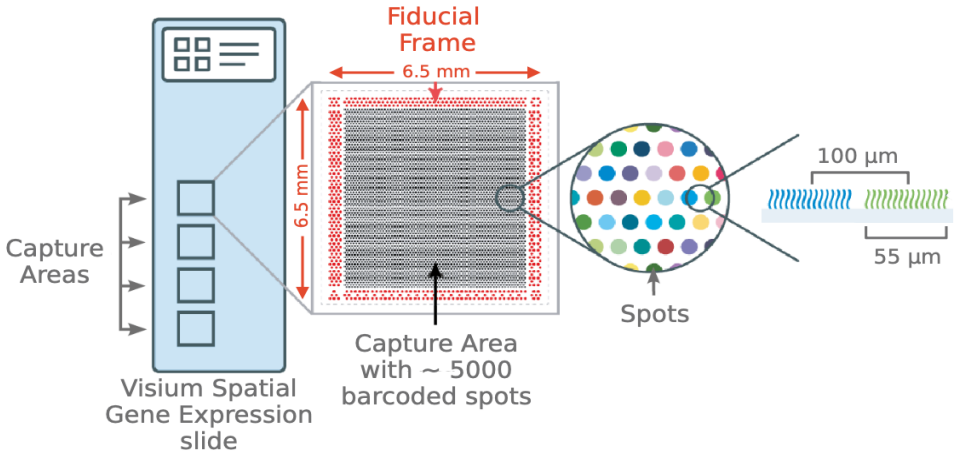

Figure 1.6. Visium spatial gene expression slide.

Schematic diagram showing the layout of the Visium gene expression slide, fiducial frame and barcoded spots. Adapted from 10x Genomics user guide.[145]

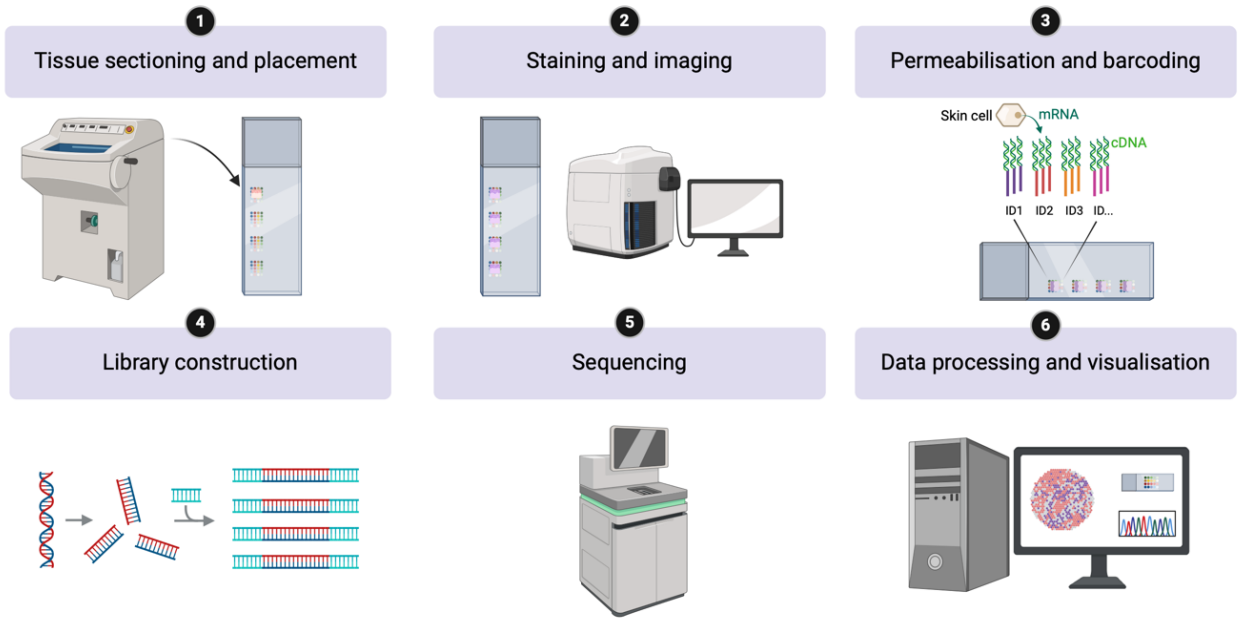

Figure 1.7. Visium spatial transcriptomic experimental workflow.

Schematic diagram showing the key steps in Visium experiments including obtaining tissue sections which are placed on Visium slide capture areas for staining, imaging and permeabilisation to generate spatially barcoded mRNA from which cDNA libraries are produced for sequencing prior to data analysis and visualisation. Created with BioRender.com.

1.4.3 Concept of tissue microenvironments

The resolution of Visium is spot-level, as opposed to cellular or subcellular, with approximately 7 to 10 cells present per 55 μm spot depending on tissue type.[130] However, single cell resolution can be modelled from Visium spatial transcriptomic data through deconvolution. This process uses computational tools and typically a reference scRNA-seq dataset to identify and quantify the relative contribution per cell state in each spot.[113] This enables the original tissue location and spatial distribution of the dissociated cells from scRNA-seq to be inferred.[113] This in silico reconstruction has been considered an alternate approach to achieve spatially resolved transcriptomics.[113,146]

In addition to decomposing spots into their cellular constituents, deconvolution methods, such as non-negative matrix factorisation (NMF), can also predict significant co-location of cell states in tissue microenvironments.[147] Computed in an unsupervised manner, these microenvironments represent distinct groupings of cell states that have a high predicted probability of occurring in the same spatial location based on their abundance profiles across a tissue section.[147] Notably, they offer detailed insights about tissue niches that cannot be distinguished on conventional histopathology. For instance, utilising this approach to deconvolute Visium spatial transcriptomic data from prenatal lymphoid and non-lymphoid tissues newly uncovered a supportive role for macrophages, unconventional T cells and ILCs in B-cell lymphopoiesis distributed across developing organs including thymus, spleen, gut and liver.[101] Human prenatal skin has not been similarly investigated.

1.4.4 Application of transcriptomic technologies to investigate skin morphogenesis

The advent of commercial scRNA-seq and spatial platforms for whole transcriptome profiling has boosted the in-depth exploration of an array of developmental tissues, driven by the Human Developmental Cell Atlas (HDCA) initiative.[109] Accordingly, a limited number of studies have recently profiled the prenatal human skin using scRNA-seq but focused primarily on its immune compartment. Using six prenatal skin samples from 10-17 PCW, Xu et al.[98] described the shift in composition of immune cell subsets, including myeloid and lymphoid precursors, mast cells, monocytes, dendritic cells, macrophages, ILCs, NK cells, B and T cells, during skin development from the first to the second trimester. This was accompanied by dynamic changes in transcriptional profiles of these cell states as gestation progressed. Early-stage macrophages, NK cells and ILCs were in a more proliferative and metabolically active state compared to later gestation. Maturation of these cells occurred in situ with immune-effector gene programmes upregulated in later gestation, indicating functional evolution. Interestingly, temporal differences in macrophage expression of genes implicated in ECM formation and cell adhesion were also noted. A potential role of macrophages in skin morphogenesis was suggested but this was not further investigated.

A further scRNA-seq study analysed prenatal skin from 17 to 22 PCW with an emphasis on cutaneous T cells and only included a small fraction of non-immune cells to interrogate immune-non-immune cellular interactions.[148] They uncovered a distinct T cell population that co-expressed αβ and γδ T cell receptors and that localised to the dermis. These double-positive (DP) αβγδ T cells were unique to developing skin, gradually decreased during gestation and were absent in newborn skin. Inferred ligand-receptor interactions demonstrated crosstalk with other immune cells, such as myeloid and NK cells, to contribute to immune homeostasis and responses in prenatal skin. Based on the limited non-immune cells profiled, a potential role of DP αβγδ T cells in skin formation was suggested through interactions with fibroblasts and endothelial cells. No further characterisation of non-immune skin cells was carried out.

A few developmental cross-tissue atlases have also been published that include prenatal skin data. Early embryonic skin (CS11 - CS23, ~ 4-8 PCW) was profiled as part of a multi-tissue study into the origins and development of human macrophages.[149] This showed that, unlike brain-resident microglia which were fully specified and overlapped with adult microglia, tissue-resident macrophages in prenatal skin did not yet resemble postnatal skin macrophages.[149] Prenatal skin data from 7 to 16 PCW was also included in a nine-tissue atlas which charted the development of the human immune system distributed across primary haematopoietic (yolk sac, liver, bone marrow), lymphoid (thymus, spleen, lymph nodes) and non-lymphoid (skin, kidney, gut) tissues across gestation.[101] Prenatal skin was identified as a potential site of haematopoiesis alongside the developing kidney, being seeded by lineage-committed B cell and myeloid progenitors during development. In keeping with findings from Xu et al.,[98] transcriptional heterogeneity was observed in prenatal skin macrophages across gestation. Whilst macrophage expression of antigen-presentation MHCII genes were enriched from the second trimester, early skin macrophages, as well as mast cells, displayed a gene signature implicating their potential involvement in tissue morphogenesis and angiogenesis.[101]

These studies profiled prenatal skin from 4 to 22 PCW at single cell resolution. However, there has been an overwhelming focus on analysing its immune constituents to better understand the origin, specification and evolution of immune cells at tissue and multi-organ level. A corresponding unbiased and systematic characterisation of the non-immune cells in human prenatal skin is still lacking. In addition, although several studies have suggested a potential contribution of immune cells to early skin morphogenesis,[98,148] a comprehensive assessment of how this occurs, and the cellular interactions implicated, has not been undertaken. Spatial contextualisation of scRNA-seq data to map cellular distribution and microanatomical organisation in prenatal skin has also not been addressed.

1.5 Skin organoids to model skin and hair follicle development

While the gold standard in the study of skin may be to utilise in vivo human tissues, their limitations, in terms of availability and amenability to manipulation and lineage tracing, have rendered it necessary to substitute alternatives, such as animal integument and lab-grown skin equivalents. Skin equivalents (used here to indicate cell-generated organs without including artificial skin substitutes) are three-dimensional reconstructions of skin or skin components that mimic one, two or all cutaneous layers and/or its appendages.[150,151] Compared to two-dimensional cell culture systems, they are morphologically and physiologically more similar to in vivo skin and provide a closer representation of its complex structure and cellular responses.[150,151] Accordingly, skin equivalents have increasingly been used for drug and cosmetic testing, disease modelling and investigating skin morphogenesis, ageing and regeneration.[150] Although widespread translation to clinical therapeutics remains limited, they have been applied to improve healing in wounds and, in isolated cases, to treat genetic skin conditions.[150,152]

Several types of skin equivalents have been developed including single component equivalents (either epidermis or dermis), layered (two or three layers) co-culture models with and without scaffolds, equivalents with follicle-like structures and organoids.[150,151] Organoids are sphere-shaped inverted equivalents derived from embryoid bodies (spheroids from pluripotent stem cells (PSCs)).[150,151] Skin organoids, appearing as cyst-like structures with an inner epidermis and outer dermis, that bear hair follicles were first generated from mouse PSCs[153] and subsequently from human PSCs (hPSCs)[154] (section 1.5.1). Although they are still technically limited, with inter-batch variability, dependence on states of PSCs and growth factors, and are labour-intensive and costly to produce, they represent one the closest equivalents to native skin, making them highly suitable as a research tool.[151]

1.5.1 The hair-bearing skin organoid model

A hair-bearing skin organoid model, derived from human embryonic stem (ES) cells and induced pluripotent stem (iPS) cells, was successfully developed by collaborators in the Koehler lab.[154] These hPSCs were cultured with carefully timed addition of growth factors to induce precursor cells that differentiated into epithelial and mesenchymal skin components (Figure 1.8). BMP4 and an inhibitor of TGF-β were added to promote induction of surface ectoderm (non-neural); this was followed by co-treatment with a BMP inhibitor and basic FGF to induce CNC-like cells which can give rise to mesenchymal cells.[154,155] This produced cysts with a central cavity lined by epithelial cells and externally surrounded by CNC cells. These early organoids were then incubated and allowed to mature over a total period of 120 days, during which differentiation into different cell lineages occurred.[154,155] The mature organoids were composed of two poles: head and tail ends (Figure 1.8). The head end contained the skin-relevant components with stratified epidermis, juxtaposing dermal structures and protruding hair follicle-like extensions.[154] The tail region consisted of off-target products, mainly hyaline cartilage.[154]

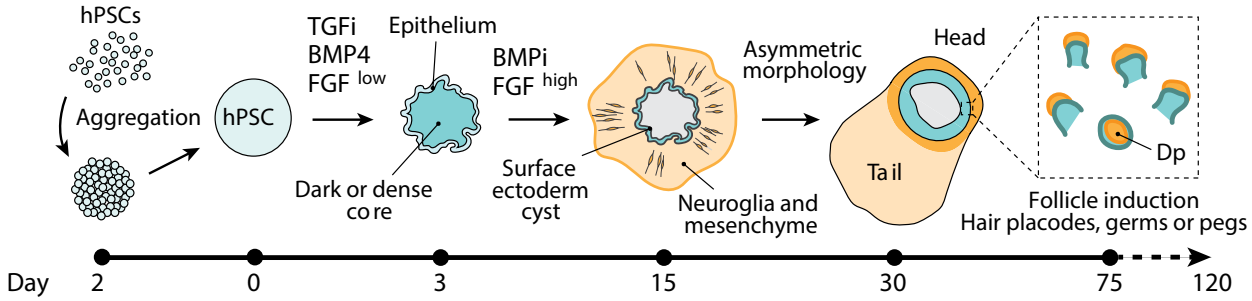

Figure 1.8. Differentiation protocol of the hair-bearing skin organoid model.

Schematic overview of the different steps during differentiation of the hair-bearing skin organoid model from hPSCs, with timed addition of growth factors and inhibitors. BMP4: bone morphogenetic protein 4; BMPi: bone morphogenetic protein inhibitor; FGF: fibroblast growth factor; hPSCs: human pluripotent stem cells; Dp: dermal papilla; TGFi: Transforming growth factor β inhibitor. Adapted from Lee et al.[154]

1.5.2 Skin organoid recapitulation of in vivo skin

The skin organoid model described above (section 1.5.1) was compared to and shown to morphologically resemble human foetal skin (from forehead at 18 weeks).[154] The epidermis was multi-layered (basal and intermediate/suprabasal) and covered by periderm. Fibroblasts were present within the dermal component, with a network of nerve-like bundles comprising neurons and Schwann cells. At regular intervals, the hair follicle-like structures developed from hair germ-like buds (appearing ~ day 70) and radiated out of the organoids.[154] These hair follicles had a defined Dp, matrix, and non-medullated hair shaft resembling vellus or lanugo hair and an associated sebaceous gland.[154] Adipose cells around the hair follicles mimicked subcutaneous fat.[154] Most of the hair follicles were pigmented and melanocytes were detected in the epidermis and hair matrix of the organoids. Merkel cells were also present in the outer layers of the hair follicles and appeared to be targeted by neurons in a formation reminiscent of the mechanosensory receptors seen in vivo.[154] Overall, this skin organoid model demonstrated near complete self-assembly of complex skin in vitro with preservation of structural and patterning elements that resembled second trimester prenatal skin.[154] However, an assessment at molecular level of how the skin organoids recapitulated human skin differentiation across gestation was not performed. Such a comparison would provide an in-depth evaluation of the similarities and differences between skin organoids and in vivo skin to determine their utility and limitations as skin equivalents and to identify optimisation approaches to improve the skin organoid model.

1.6 Research hypothesis

The existing literature on human prenatal skin and emerging suggestions that the immune cells which seed it from early gestation express gene profiles that dynamically change during development led me to hypothesise that:

Immune cells co-localise with non-immune cells in tissue microenvironments to contribute to prenatal skin morphogenesis.

1.7 Study aims

The aims of this study were to:

1. Comprehensively profile the immune and non-immune cellular composition of human prenatal skin across gestation to gain insights into skin and hair follicle morphogenesis.
2. Investigate whether immune and non-immune cells co-localise in tissue microenvironments in prenatal skin.
3. Determine the contribution of immune cells to prenatal skin formation.
4. Evaluate faithfulness of the hair-bearing skin organoid model to in vivo prenatal skin and its utility to functionally assess the role of immune cells in skin morphogenesis.

Chapter 2 . Materials and methods

2.1 Prenatal skin tissue acquisition and ethical approval

Human embryonic and foetal skin specimens were acquired from (i) the Human Developmental Biology Resource (HDBR),[156] with ethical approval from the Newcastle & North Tyneside 1 Research Ethics Committee (REC) (REC reference number: 23/NE/0135; previous REC reference numbers: 18/NE/0290 and 08/H0906/21+5) (Appendix A1), and from (ii) Cambridge University Hospitals NHS Foundation Trust under permission from the Cambridge Central REC (REC reference number: 96/085) (Appendix A2). All tissues were collected following elective medical or surgical termination of pregnancies with informed written consent. Demographic information for the prenatal skin specimens included in this study[157] is provided in Appendices B1and B2.

2.2 Single-cell transcriptomic data generation from prenatal skin

2.2.1 Tissue digestion

Prenatal skin specimens were transported in pre-cooled HypoThermosol® FRS Preservation Solution (Sigma-Aldrich) and processed either immediately upon receipt or, if received out of hours, stored overnight at 4°C and processed the following morning. The skin sample was removed from the transporting solution, washed with phosphate buffered saline (PBS) (Sigma-Aldrich), placed onto a sterile tissue culture dish, and cautiously sliced into small pieces (~ 1mm x 1mm) with a scalpel. For enzymatic digestion, it was incubated with 10% heat-inactivated foetal bovine serum (FBS; Gibco) and type IV collagenase (Worthington) in Roswell Park Memorial Institute (RPMI; Sigma-Aldrich) medium (final concentration of 1.6 mg/ml) at 37°C for 30 minutes with agitation every 10 minutes. The mixture containing digested skin was passed through a 100 µm cell strainer (Falcon) to check for undigested tissue. To any undigested tissue remaining in the strainer, 500µl of 0.25% trypsin (Sigma-Aldrich) was added and maintained at room temperature for 5 minutes. The addition of trypsin was carried out for two samples - F220 and F221.

The solution with dissociated cells was centrifuged (500*g* at 4°C for 5 minutes) to collect cells into a pellet. To remove red blood cell (RBC) excess which can overcrowd subsequent steps, the cell pellet was treated with RBC lysis buffer (eBioscience) at working concentration (1x) at room temperature for 5 minutes. The reaction was stopped by diluting with flow buffer solution, made

from PBS (Sigma-Aldrich) containing 5% volume per volume (v/v) FBS and 2 mM ethylenediaminetetraacetic acid (EDTA), followed by further centrifugation (500*g* at 4°C for 5 minutes) to obtain the final pellet for antibody staining.

2.2.2 Fluorescence-activated cell sorting

To enrich for immune cells, staining was performed with anti-CD45 antibody for all specimen samples (5µL CD45 PE, clone HI30, BD Biosciences (F220, F221) or 3 µL CD45 BUV395, clone HI30, BD Biosciences (other sorted samples)), except one (F217) as the cell sorter was not available on the day of tissue digestion. Non-immune populations with low cell abundance (for example, keratinocytes and endothelial cells) were enriched in a subset of samples by additional staining to isolate them from the abundant $CD34^+$ cells. Anti-CD34 antibody (4 µL CD34 APC/Cy7, clone 581, Biolegend) was used for samples from F220 and F221 and an antibody mixture, comprising anti-CD34 (4 µL CD34 APC/Cy7, clone 581, Biolegend) and anti-CD14 (3 µL CD14 PE-CF594, clone MφP9, BD Biosciences) antibodies, was used for samples from F69 and F71. Antibody-stained cells were passed through a 35 µm cell strainer (Falcon) and immediately before sorting, 4′,6-diamidino-2-phenylindole (DAPI; Sigma-Aldrich) was added to a final concentration of 3 µM.

Cells were sorted by a BD FACSAria Fusion Flow Cytometer, with gating to exclude dead cells, debris, and doublets. For samples treated with anti-CD45 antibody only, live single $CD45^+$ ($DAPI^-$ $CD45^+$) and $CD45^-$ ($DAPI^-CD45^-$) cells were isolated and collected in separate chilled round-bottom polystyrene tubes pre-coated with FBS and containing 500 µl of sterile PBS. Gating was contiguous to preclude cell loss. For F220 and F221, treated with additional anti-CD34 antibody, $CD34^+$ ($DAPI^-CD45^-CD34^+$) and $CD34^-$ ($DAPI^-CD45^-CD34^-$) fractions were collected from their respective gates, alongside live single $CD45^+$ cells. For F69 and F71, which were further stained with anti-CD34 and anti-CD14 antibodies, all cells from the $CD45^-$ fraction that were not within the $CD34^+CD14^-$ gate were collected, in addition to other live $CD45^-$ and $CD45^+$ cells, into separate pre-prepared tubes as above. The FACS-sorted cell proportions for each prenatal skin specimen are provided in Appendix C.

2.2.3 Droplet-based scRNA-seq

GEM generation, barcoding and reverse transcription

Cell suspensions isolated by FACS were immediately processed for droplet-based scRNA-seq using a Chromium Controller from 10x Genomics to generate GEMs, each encapsulating a single cell with a single gel bead and RT primers and enzymes in a microfluidic droplet (section 1.4.1). Cells in each sorted suspension were manually counted, and the required volume was loaded as per manufacturer's guidance[158,159] to achieve a targeted count of 10,000 cells per channel. The dilutions used aim for the majority (~90 – 99%) of GEMs produced to have no cell content in order to optimise single cell capture in the remaining GEMs.[158] Each sorted cell suspension was loaded into a separate channel of the Chromium chip (10x Genomics) as far as possible, unless the starting cell count was too low, in which case suspensions belonging to the same specimen (for example, the sorted $CD45^+$ and $CD45^-$ fractions) were pooled. If adequate cell numbers remained from a sorted cell suspension, additional channels were loaded as replicates. This increased capture of rare cell states and mitigated potential technical issues (for example, channel clogging). A list of loaded channels and corresponding sample information is provided in Appendix D.

Protocols, standard kits and reagents from 10x Genomics were used for either the five-prime Chromium single cell V(D)J kit[158] or three-prime Chromium single cell 3' reagent kit (v2).[159] Briefly, for each cell suspension, the calculated volume was added to a master mix of RT reagents, containing RT enzyme and poly(dT) RT primers (10x Genomics) in the 5' assay or template switch oligo (TSO) (10x Genomics) in the 3' assay. The mixture was dispensed into the Chromium chip alongside gel beads (10x Genomics) and partitioning oil (10x Genomics). The filled chip was covered with a gasket and run in the Chromium Controller for GEM generation (~20 minutes). Generated GEMs were aspirated from each channel, placed in a tube strip on ice ready for RT. Each tube in the tube strip corresponded to a loaded channel, that is a distinct cell fraction from the original prenatal skin specimen; where 'sample' is used in the rest of this section (2.2.3), it refers to an individual tube and loaded channel.

The gel beads had attached oligonucleotides, composed of an Illumina sequencing primer (read 1 (R1)), a 10x barcode, a UMI, and a TSO in the 5' assay[158]; in the 3' assay, the poly(dT) sequence was attached to the gel bead oligonucleotides with the barcode and UMI while the TSO was added with RT reagents[159] (Figure 2.1). The different oligonucleotide arrangements enable capture of

either the 5’ or 3’ end of the cell mRNA transcripts. Inside individual GEMs, the gel bead dissolved and the single cell was lysed releasing oligonucleotides and mRNA content respectively. The poly(A) tails of the mRNA molecules were bound by the poly(dT) primers and corresponding full-length cDNA was generated by reverse transcriptase enzyme which also added untemplated C nucleotides, enabling hybridisation by the TSO and extension of the cDNA with a common 5' sequence used in downstream amplification steps (Figure 2.1). For RT, the GEMs were incubated on a thermal cycler (Eppendorf Mastercycler Pro (Thermo Fisher Scientific)) at 53°C for 45 minutes followed by 85°C for 5 minutes.[158,159]

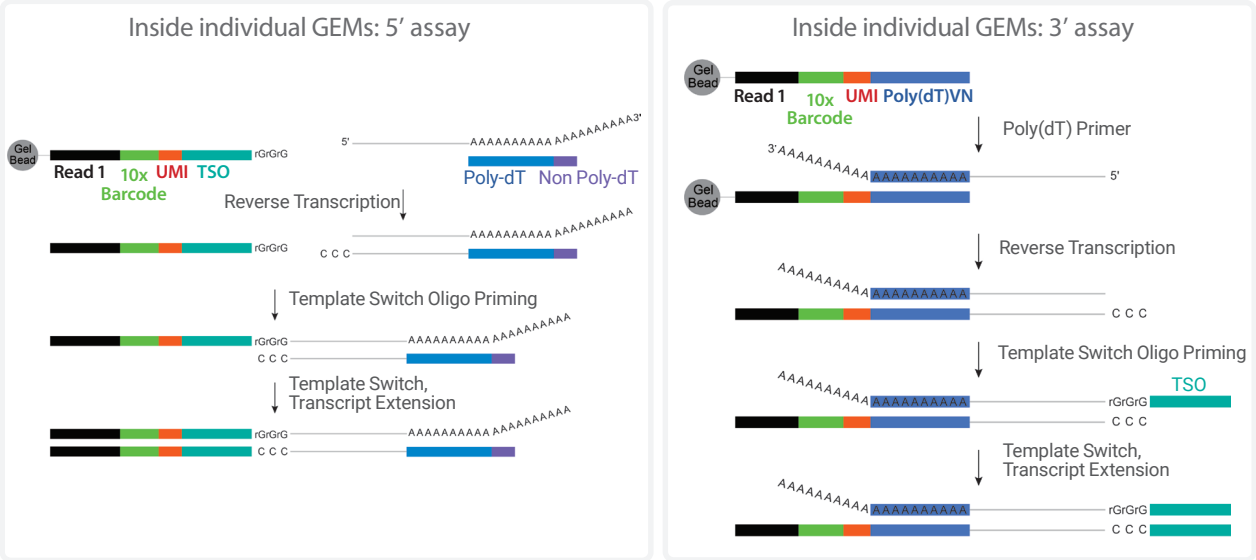

Figure 2.1. Barcoding and generation of full-length cDNA.

Schematic diagrams showing the composition of gel bead-conjugated oligonucleotides and stepwise reactions with mRNA molecules inside GEMs for the 5’ (left) and 3’ (right) assays. Adapted from 10x Genomics user guides.[158,159]

GEM cleanup and cDNA amplification

The GEMs were then cleaned to remove excess RT reagents and partitioning oil. A proprietary recovery agent (10x Genomics) was added to each GEM suspension resulting in the formation of a biphasic mixture with a clear aqueous phase containing cDNA atop a recovery agent/partitioning oil phase (pink coloured). The latter was aspirated and discarded. cDNA from the aqueous solution was bound using a cleaning mix containing magnetic beads (Dynabeads MyOne SILANE (10x Genomics)) with a magnetic separator, purified with ethanol washes and released from the

magnetic beads with an elution solution (10x Genomics). The barcoded cDNA was then amplified by adding an amplification mix containing cDNA primers and incubating on the thermal cycler with parameters preset as per manufacturer's instructions.[158,159]

cDNA cleanup and quantification

The amplified cDNA from each sample was then cleaned by adding SPRIselect reagent (Beckman Coulter) and placing on a magnetic separator until the solution cleared. Following removal of the supernatant, the magnetised pellet was washed with ethanol, air dried and eluted with Buffer EB (Qiagen). The cleaned cDNA was run on an Agilent 2100 Bioanalyzer (Agilent) as per protocol to determine the cDNA yield for each sample. The sample volume containing 50 ng of cDNA was calculated and adjusted with nuclease-free water to carry forward 20 µl for gene expression library construction.

Gene expression library construction

To prepare Illumina sequencing-ready gene expression libraries, the cleaned amplified full-length cDNA from each sample was enzymatically fragmented to produce optimally sized amplicons, followed by end-repair and A-tailing (addition of single adenine nucleotide for sequencing adaptor ligation) (Figure 2.2). Fragmentation enzyme and buffer (10x Genomics) were added to each sample which were then incubated on a Eppendorf Mastercycler Pro thermal cycler (Thermo Fisher Scientific) at 32°C for 5 minutes followed by 65°C for 30 minutes.[158,159] SPRIselect reagent (Beckman Coulter) was sequentially added at 0.6x and 0.8x (double sided size selection), followed by magnetic separation and ethanol washes as previously described. The selected cDNA was eluted with Buffer EB (Qiagen).

Illumina read 2 (R2) primer sequences were then ligated by adding an adaptor ligation mix containing ligation buffer, DNA ligase and adaptor oligos (10x Genomics) to each sample and incubating on the thermal cycler at 20°C for 15 minutes.[158,159] Post-ligation cleanup was done with SPRIselect (Beckman Coulter) at 0.8x and ethanol washes and cDNA was eluted with Buffer EB (Qiagen). To enable demultiplexing of pooled samples following sequencing, unique sample indexes, i5 and i7 associated to P5 and P7 adapters respectively, were added to each sample from a Dual Index TT Set (10x Genomics) - each well in the plate is a mix of one unique i7 (index 1) and one unique i5 (index 2) sample index - followed by PCR amplification step to incorporate the index sequences (Figure 2.2). The number of amplification cycles was determined from the

manufacturer's recommendations[158,159] based on the initial amount of cDNA used for library preparation.

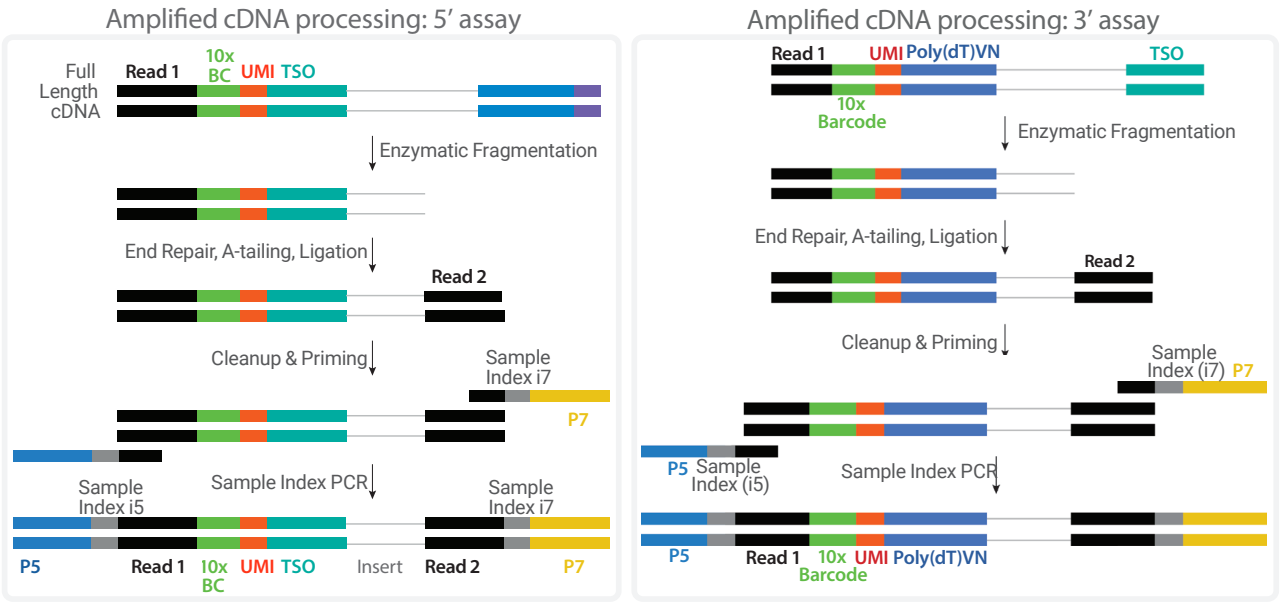

Figure 2.2. Construction of gene expression libraries for scRNA-seq.

Schematic diagrams illustrating the processes to generate sequencing libraries from amplified full-length cDNA in the 5' (left) and 3' (right) assays by enzymatic fragmentation, ligation of R2 sequences, and addition of sample indexes. Adapted from 10x Genomics user guides.[158,159]

A final round of double-sided size selection and cleanup of indexed cDNA was again performed by sequential addition of SPRIselect reagent (Beckman Coulter) at 0.6x and 0.8x, magnetic separation, ethanol washes and elution with Buffer EB (Qiagen). The constructed cDNA libraries, each corresponding to an individual channel loaded on the Chromium controller, were analysed on an Agilent 2100 Bioanalyzer (Agilent) to check the average fragment size for library quantification. The quality-controlled gene expression libraries were pooled and sequenced on Illumina NovaSeq 6000 system to achieve a minimum target depth of 50,000 reads per cell.

2.3 Visium spatial transcriptomic data generation from prenatal skin

2.3.1 Tissue cryosection and fixation

Fresh-frozen prenatal skin specimens embedded in optimal cutting temperature (OCT) compound (Tissue-Plus, Scigen) were processed for spatial transcriptomic profiling using the Visium platform from 10x Genomics[145,160] (section 1.4.2). 10 µm-thick skin sections were cut from each specimen block, following equilibration in a Leica CM1950 cryostat (chamber temperature ~ -10°C, specimen head ~ -15°C), and carefully mounted on the capture areas on Visium gene expression slides (10x Genomics). Each loaded slide, comprising four individual capture areas with prenatal skin tissue sections, was incubated on a thermocycler adaptor (10x Genomics) at 37°C for 1 minute in a DNA Engine Tetrad 2 thermal cycler (Bio-Rad) with open lid to re-equilibrate to room temperature. The slide was then immersed in pre-chilled methanol and incubated upright at -10°C for 30 minutes for tissue fixation.

2.3.2 Tissue staining and imaging

For staining, the tissue sections on the Visium slide were sequentially treated with isopropranolol (500 µl) followed by Haematoxylin (1ml, 7 minutes), Bluing buffer (1 ml, 2 minutes) and Eosin (1:10 dilution with tris-acetic acid buffer (0.45M, pH 6.0); 1 ml, 1 minute) with intervening slide rinses in Milli-Q water as per manufacturer's instructions.[160] After the final rinse, the slide was carefully dried and incubated on the thermocycler adaptor (10x Genomics) at 37°C for 5 minutes in the thermal cycler (Bio-Rad DNA Engine Tetrad 2) with open lid prior to imaging. The whole Visium slide, including fiducial frames around each capture area, was scanned at 20X magnification on a NanoZoomer S60 (Hamamatsu Photonics) using brightfield image settings.[160]

2.3.3 Array-based spatial transcriptome profiling

Tissue permeabilisation and reverse transcription

Following imaging, the Visium slide was immediately processed for tissue permeabilisation. In this step, mRNA was released from each tissue section onto its underlying capture area containing primer-covered spots (section 1.4.2). Each primer consists of an Illumina read 1 (R1) sequencing primer, a spatial barcode (identical for all primers within a given spot), a UMI, and a poly(dT) sequence (similar to the gel bead oligonucleotides in the single cell 3' assay) that anneals the poly(A) tail of mRNA molecules released from the overlying tissue to capture them in their specific spatial location.[145]

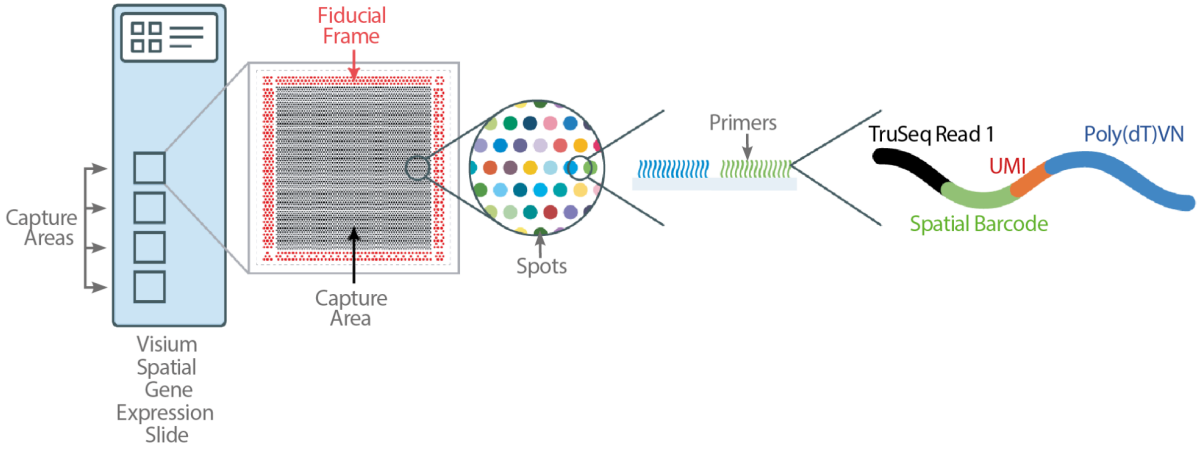

Figure 2.3. Composition of primers on Visium spatial gene expression slide.
Schematic diagram showing the layout of the Visium gene expression slide and composition of each primer attached to the capture areas. Adapted from 10x Genomics user guide.[145]

The slide was first placed in a Visium slide cassette (10x Genomics) to isolate the different capture areas from each other and form individual wells for each area with the slide and tissue sitting at the bottom of the well. This enables subsequent processing steps to be carried out on the Visium slide itself. Proprietary permeabilisation enzyme (10x Genomics) was added to each well, ensuring complete tissue coverage, and the cassette was closed with a Visium slide seal (10x Genomics). The sealed cassette was incubated on the thermocycler adaptor (10x Genomics) at 37°C for a permeabilisation time of 12 minutes (pre-optimised as per manufacturer's instructions[161]) in the thermal cycler (Bio-Rad DNA Engine Tetrad 2) with closed lid. The permeabilisation enzyme was then aspirated out and 0.1x saline-sodium citrate (SSC) buffer (Millipore Sigma) was added to each

well, with the SSC buffer facilitating hybridisation while also serving as a wash and protecting RNA integrity.

On-slide RT was then performed by adding a master mix of RT reagents, containing RT enzyme and TSO (10x Genomics), to permeabilised tissue in each well and incubating the sealed cassette on the thermocycler adaptor at 53°C for 45 minutes in the thermal cycler (Bio-Rad DNA Engine Tetrad 2). Incubation with these reagents produced single strands of spatially barcoded, full-length cDNA from the mRNA transcripts in each tissue section with an added TSO sequence.[145]

Second strand synthesis and denaturation

To produce the second strand of spatially barcoded cDNA, the RT master mix was removed after incubation and diluted potassium hydroxide (0.08M) and Buffer EB (Qiagen) were sequentially added then aspirated. A second strand mix containing proprietary second strand primers and enzyme (10x Genomics) was then added to each well and the cassette was sealed and incubated on the thermocycler adaptor at 65°C for 15 minutes in the thermal cycler (Bio-Rad DNA Engine Tetrad 2). The second strand primers bind to the TSO sequence to produce the second strand of barcoded DNA.[145]

At the end of incubation, the second strand reagents were aspirated. Each well was washed with Buffer EB (Qiagen) before addition of diluted potassium hydroxide (0.08M), maintained at room temperature for 10 minutes, for denaturation. The free barcoded cDNA from each capture area was then transferred to a corresponding individual strip tube containing tris(hydroxymethyl)aminomethane buffer (Tris; 1M, pH 7.0) (Thermo Fisher Scientific).

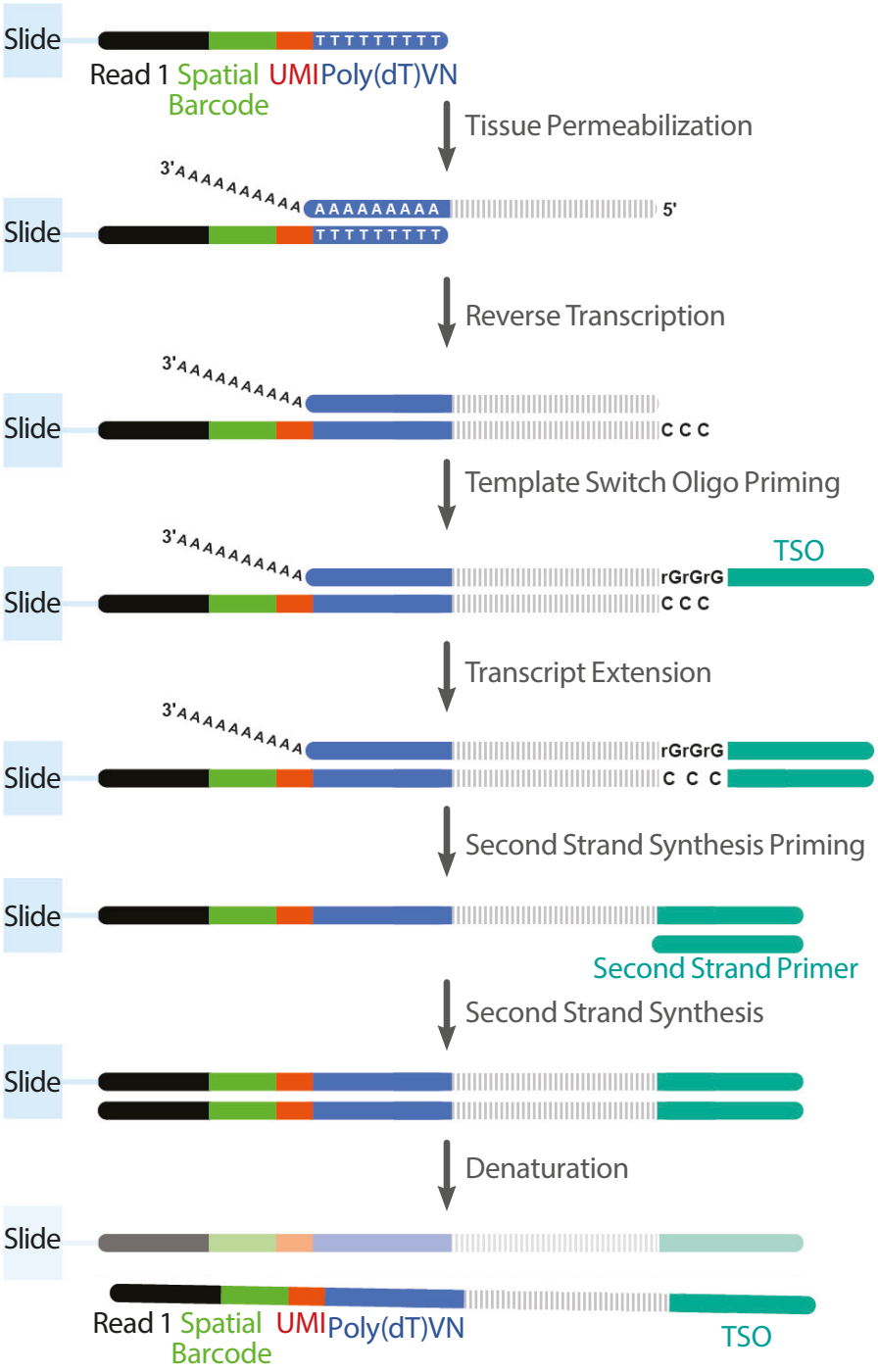

Figure 2.4. Spatial barcoding and generation of full-length cDNA.

Schematic diagram showing the stepwise reactions to convert mRNA molecules from permeabilised tissue sections into spatially barcoded cDNA. Adapted from 10x Genomics user guide.[145]

cDNA amplification and cleanup

Barcoded, full-length cDNA from each capture area was then amplified via PCR. A qPCR mix containing KAPA SYBR FAST mix (Millipore Sigma) and cDNA primers (10x Genomics) was first prepared. To determine the optimal number of amplification cycles for each sample, 9 µl of PCR mix was added to five wells (one for each of the four samples plus one negative control) of a qPCR plate with 1 µl of cDNA from each sample or 1 µl of nuclease-free water for the negative control. The sealed plate was then run on a StepOnePlus qPCR system (Thermo Fisher Scientific) as per manufacturer's protocol.[145] The resulting plots were used to find the quantification cycle (Cq) value for each sample, which was recorded as the number of cycles required to generate 25% of the peak relative fluorescence units in the exponential phase of the amplification plots, as per the manufacturer's instructions.[145]

A cDNA amplification master mix, comprising proprietary amplification mix and cDNA primers (10x Genomics), was then added to the rest of each sample. Each sample was then incubated in a thermal cycler set as per manufacturer's protocol[145] for the designated number of cycles determined above.

The amplified cDNA from each sample was then cleaned in the same manner as for suspension-based cDNA cleanup (section 2.2.3) using SPRIselect reagent (Beckman Coulter), magnetic separation, ethanol washes and elution with Buffer EB (Qiagen). The cleaned cDNA was run on an Agilent 2100 Bioanalyzer (Agilent) as per protocol[145] to determine the cDNA yield for each sample. As per manufacturer's recommendations,[145] 10 µl (25%) of the total cleaned cDNA was taken forward for gene expression library construction.

Spatial gene expression library construction

To prepare spatial gene expression libraries ready for Illumina sequencing, the cleaned amplified full-length cDNA from each sample was processed through the same steps described in section 2.2.3 for suspension-based gene expression library construction. These included enzymatic fragmentation, end-repair, A-tailing, double sided size selection, adapter ligation, post-ligation cleanup, sample index PCR (number of amplification cycles determined from the manufacturer's recommendations[145] based on amount of cDNA contained in 25% of total cleaned cDNA), post sample index PCR double sided size selection, and quality control of the constructed libraries to check the average fragment size. The quality-controlled dual-indexed spatial gene expression libraries were pooled (2.8 nM) and sequenced on NovaSeq S4 system to achieve a minimum sequencing depth of 50,000 read pairs per tissue covered spots.

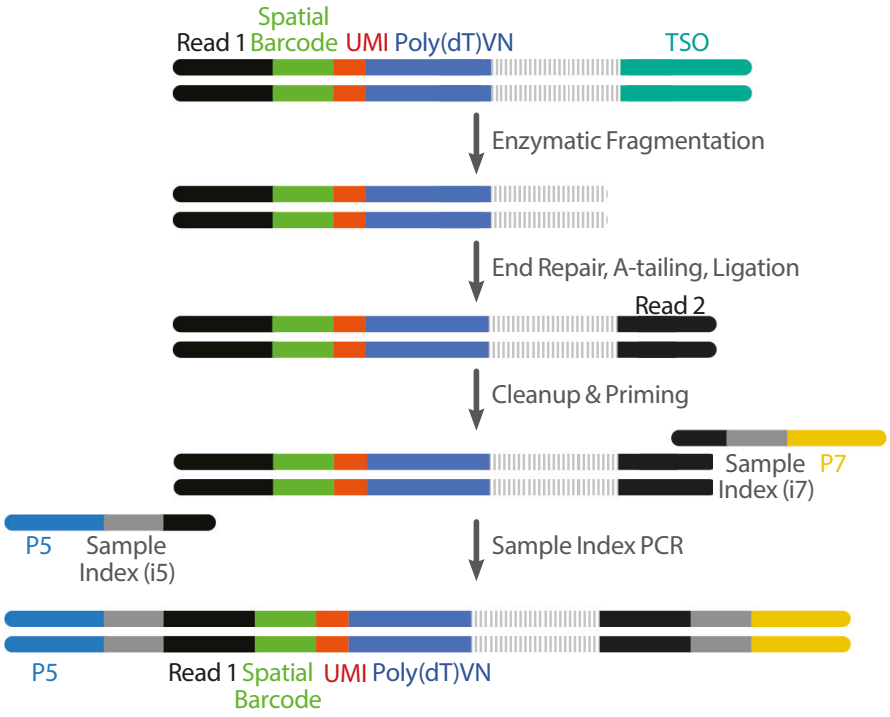

Figure 2.5. Construction of Visium gene expression libraries.

Schematic diagram illustrating the processes to generate sequencing libraries from amplified full-length cDNA by enzymatic fragmentation, ligation of R2 sequences, and addition of sample indexes. Adapted from 10x Genomics user guide.[145]

2.4 Single-cell transcriptomic data analysis

2.4.1 Pre-processing of prenatal skin scRNA-seq data for annotation

Alignment to human genome

Following sequencing, the gene expression data generated from single cell suspensions were demultiplexed, mapped using Cell Ranger software (v2.1.1 and v2.0.2) (10x Genomics) to the Ensembl 84–based human genome reference consortium 38 (GRCh38) (10x Genomics–distributed 1.2.0 version). The sequencing reads were deduplicated based on UMIs to correct for PCR amplification and obtain the UMI counts that reflect the original cellular mRNA content. Cell Ranger cell-calling algorithm, based on EmptyDrops,[162] identified cells from empty droplets, including both high RNA content and low RNA content cells. For each sequenced sample (corresponding to an individual channel on the Chromium Controller), a barcode rank plot was generated and visually inspected to ensure adequate cell calling and sample quality. An example of a typical barcode rank plot is shown in Figure 2.6, where the count of UMIs is plotted (y-axis, logarithmic scale) for each barcode (x-axis) in decreasing order of UMI counts, demonstrating the cut-off for cell calling.

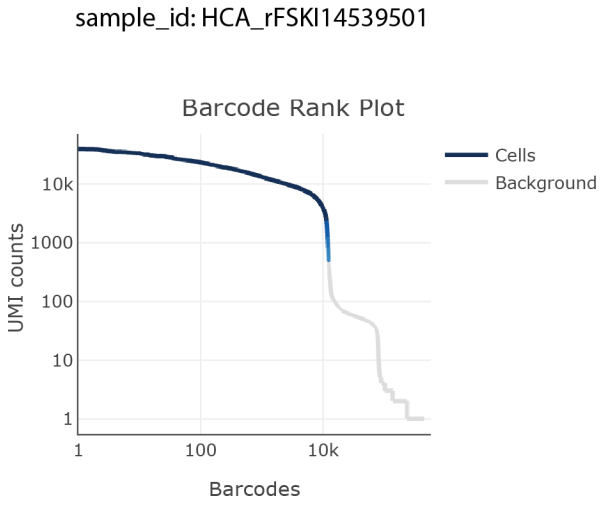

Figure 2.6. Example of barcode rank plot for prenatal skin sample.

Barcode rank plot showing all the barcodes (x-axis) detected in one prenatal skin sample ranked from highest to lowest UMI counts (y-axis); the dark blue line represents cell-associated barcodes and the grey line barcodes from empty droplets, with the sharp knee indicating adequate cell calling.

The Cell Ranger analysis pipeline also output the feature-barcode matrix files required to produce the raw counts matrix for each sample for downstream analyses. The counts matrices were generated and combined using Scanpy[163] (v1.9.3, 1.9.8). This scalable python-based toolkit, suitable for efficient handling of large scRNA-seq datasets,[163] was also used for subsequent pre-processing of prenatal skin data prior to annotation as described in the following sub-sections.

Quality control

Doublet detection

Droplet-based scRNA-seq methods are designed and optimised to ideally encapsulate a single cell in each reaction partition.[128,164] However, two or more cells may be captured within the same droplet and their combined gene expressions erroneously profiled as belonging to a single cell.[165,166] This produces artefactual doublets or multiplets which can be homotypic (from similar cell states) or heterotypic (from different cell types) in nature. These doublets, especially heterotypic ones, can interfere with downstream analyses including differential gene expression and cluster detection.[166]

Several methods to computationally detect doublets have been developed.[166–170] In a typical approach, artificial doublets are first simulated by combining the gene expression profiles of two droplets that are randomly selected.[166] Each original droplet is then compared to the artificial doublets and assigned a score based on their similarity.[166] A threshold is applied where droplets with similarity scores greater than a defined cut-off value are denoted as doublets. This method is used by Single-Cell Remover of Doublets (Scrublet)[167] which has been benchmarked as one of the top-performing python-based doublet detection algorithms.[166] Scrublet (v0.2.1) was used to flag potential doublets in the prenatal skin scRNA-seq data. It was run on each individually sequenced sample, with default parameters and automatic thresholding. An example of doublet calling in the prenatal skin data is shown in Figure 2.7. This threshold is usually permissive and additional doublets detected upon final clustering and annotations were also subsequently manually removed.

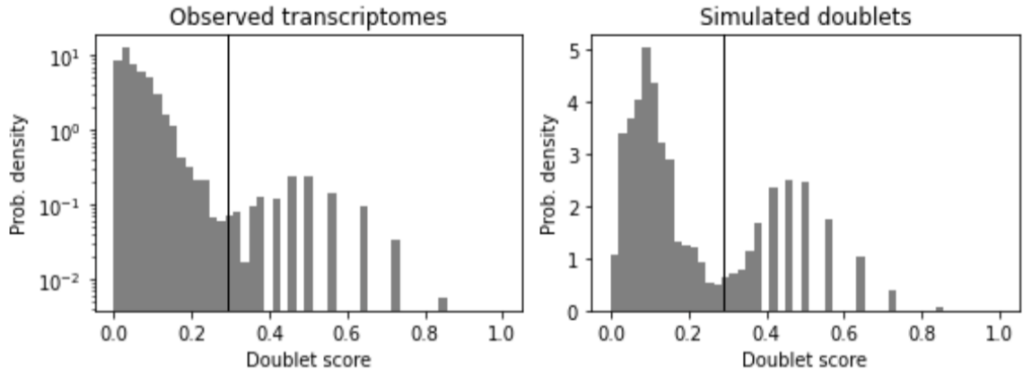

Figure 2.7. Doublet score histograms from Scrublet.

Plots of probability densities for doublet scores in the prenatal skin data (left) and in simulated doublets (right); the vertical black line is the threshold automatically set by Scrublet. The threshold is detected at the minimum in the bimodal distribution between homotypic (left mode) and heterotypic (right mode) doublets in the simulated data and the same value is applied to the observed data so that heterotypic transcriptomes (scores greater than threshold value) are labelled as doublets.

Low quality cells

Although cell sorting, washing and filtering steps are included during the generation of cell suspensions to remove dead and damaged cells, some poor-quality cells can still permeate through to the final sequenced libraries. This includes dying cells and cells with broken membranes which results in leakage of cytoplasmic mRNA and retention of disproportionately high mitochondrial mRNA.[165] Low quality cells therefore usually have lower numbers of total genes and UMI counts and a higher proportion of mitochondrial gene counts.[171,172]

To identify low quality cells, quality control metrics were computed across the whole prenatal skin dataset using the Scanpy function *scanpy.pp.calculate_qc_metrics*. These included:

- the number of genes with a positive count in a cell
- the total UMI counts per cell
- the fraction of counts mapped to mitochondrial genes per cell

To filter out low quality cells, permissive adaptive thresholds were first set for the above metrics using a score based on the median and median absolute deviation (MAD): median + (x*MAD). 5*MAD and 8*MAD were used to identify outlier cells with high fraction of mitochondrial counts and high total UMI counts respectively. Fixed cutoffs were then applied to remove cells with less than 450 genes and a mitochondrial fraction over 30% in keeping with previous studies of skin scRNA-seq data.[100]

Maternal contamination

Possible maternal contamination was identified using a previously described method[101,102] based on the Souporcell algorithm which uses genetic variants detected in scRNA-seq data to cluster and assign cells to their original donors.[173] A list of common GRCh38 variants from the Souporcell authors was used containing single-nucleotide polymorphisms (SNPs) with ≥2 % frequency from 1000 Genomes.[173] The samples from each specimen were pooled and run through the analysis pipeline twice, setting the number of genotype clusters to 1 and 2 to obtain models for no contamination and possible maternal contamination. Bayesian Information Criterion (BIC) was calculated to determine the best model, as $BIC = kn \log(m) - 2l$, where k was the set number of genotype clusters, n was the number of loci used for genotype deconvolution, m was the per-donor cell count, and l was the log likelihood obtained after running the pipeline with each number of genotype clusters (k), as implemented in Suo et al.[101] Where present, the cell cluster with the minor genotype was identified as possible maternal contaminant.

Lowly expressed genes

Raw counts matrices from scRNA-seq aligned to a human genome reference usually contain over 30,000 genes. However, many of these genes are not biologically informative or instructive of cellular heterogeneity, especially when expressed only in a few cells.[165,174] Lowly expressed genes are therefore filtered by setting a threshold for the minimum number of cells in which they are expressed. This value can be scaled based on the total number of cells in the dataset and the size of the smallest cell cluster.[165] A permissive threshold was used with genes detected in fewer than 3 cells filtered out from the combined prenatal skin data.

Data transformation

Count normalisation and log-transformation

Cells that biologically belong to the same type or state should have similar counts. However, significant differences in counts are introduced due to technical variability in cell lysis, mRNA capture, binding, RT and sequencing depth.[165] Using these 'raw' counts for gene expression assessment in downstream analyses can lead to spurious results. To address this, normalisation of counts is routinely undertaken in scRNA-seq data analysis to obtain a correct representation of the relative gene expression in each cell.[165,174] Many approaches to normalise data exist. Global-scaling is a commonly used method which adjusts per-cell gene counts by a size factor calculated based on the total counts in each cell and then multiplying by a predetermined value, usually a factor of 10 such as 10,000 or 1,000,000 (also known as counts per million normalisation).[165,175]

Single-cell RNA-seq data is also typically skewed.[165,174] Yet, many tools used for downstream analyses assume a normal distribution of data. To conform to these assumptions, a log-transformation step log (x + 1) usually follows data normalisation.[165,174] The prenatal skin scRNA-seq data was normalised using Scanpy function *scanpy.pp.normalize_total* to 1e4 counts per cell and log-transformed with *scanpy.pp.log1p*.

Batch correction and data integration

Single-cell RNA-seq data is also sensitive to batch effect.[165] This results from technical variations during sample processing where cells are treated in distinct batches, for example, collection at different times, loading on separate channels of the Chromium Controller or sequencing in different lanes. These can artifactually affect the cell transcriptome. Correcting for these unwanted batch effects is required to detect true cell identities, determine common variations across the whole dataset, and identify meaningful biological signals.[165]

A distinction is usually made in scRNA-seq data analysis when accounting for batch effects between cells in the same experiment, termed 'batch correction', as opposed to cells from different experiments, datasets or laboratories where 'data integration' is preferentially used.[165] Different tools exist to tackle each of these scenarios although some have been used interchangeably. Given that the prenatal skin dataset comprised cells derived from different experiments, with additional variations in tissue digestion, sorting and molecular barcoding, a benchmarked method for data

integration and batch correction - single-cell Variational Inference (scVI)[176] (v0.19.0) from scvi-tools[177]- was used. scVI uses deep generative modelling of scRNA-seq gene expression data and user-specified batch co-variates to correct for batch effects and has been shown to perform well for complex integration tasks while conserving biological variation.[178] In the prenatal skin scRNA-seq data, batch covariates corrected for included specimen identity and chemistry of the assay used (3' and 5').

Feature selection

Feature selection was performed to identify the most informative genes in the data that accurately reflects cell state and sampling differences. This can be done across the entire dataset or in a batch-aware manner.[179] The latter is recommended to preclude the selection of genes that are variable because of batch effects across the data and to allow detection of genes expressed by rare cell states.[179] The highly variable genes (HVGs) method from Scanpy was used for feature selection with the following parameters: *scanpy.pp.highly_variable_genes* with flavor = 'seurat', min_mean = 0.0125, max_mean = 3, min_dispersion = 0.5. The number of HVGs used in downstream analyses vary across studies but choosing a higher number of HVGs whilst balancing compute efficiency is generally advised.[165,179] Between 5000 - 15000 HVGs were used in downstream analyses of prenatal skin scRNA-seq data.

Dimensionality reduction

Dimensionality reduction is an essential step that summarises and visualises scRNA-seq gene expression data in a way that is more readily interpretable whilst retaining information about the underlying data structure.[179,180] Principal component analysis[180,181] was used to summarise the prenatal skin data first. This outputs the main ranked combination of factors responsible for the maximum variance in the data (the 'principle components').[165,179] From these principle components, a graph representation of the data was constructed using the k-nearest neighbour (KNN) approach.[165,182] In this approach, each cell is connected to its k closest neighbours to which it is most similar based on gene expression profile, so that transcriptionally similar cells are densely connected.[165,182]

The Uniform Manifold Approximation and Projection (UMAP) method was computed to visualise the data in two dimensions whereby cells occupy specific coordinates on a scatter plot based on the reduced dimensions calculated above.[183] Thus, cells with similar gene profiles have close

coordinates on the map. UMAP is recognised as one of the visualisation methods that best represents the biological manifold for data exploration and is proposed as best practice for this purpose.[163,183]

As such, for the prenatal scRNA-seq data, principal components were determined using the Scanpy function *scanpy.pp.pca.* The first 50 principal components were input to estimate the nearest-neighbour graph (*scanpy.pp.neighbors* with n_neighbors (k) = 15) prior to generating the overall UMAP (*scanpy.tl.umap*).

Cluster identification and annotation

Clustering

The reduced dimensions were then used to infer clusters which are arbitrary groupings of cells based on their similar gene expression profiles.[165] Different modalities exist to derive clusters in scRNA-seq data of which Leiden clustering is commonly used. The Leiden algorithm is a community detection method that builds on the graph representation of the data obtained using the KNN approach where transcriptionally similar cells are more densely connected.[165,182] These dense connections, or communities, are detected by the Leiden algorithm and used to partition the data into defined cell groupings (clusters).[165,182] The k number of neighbours and the scale of the partitioning (resolution) can be user-adjusted to determine the granularity of the clustering.[165]

Clustering at low resolution thus delineates broader cell-type groupings and at higher resolution, more granular cell states can be identified. Typically, coarser clusters are first generated followed by more refined clustering across the entire dataset; alternatively broad clusters can be subsetted and refined subclusters derived within each broad cell group.[165] This latter approach was used to cluster and annotate the prenatal skin cells, first at 'broad' level (resolution = 0.3) using *scanpy.tl.leiden* function in Scanpy. For each cell group identified at broad level, the corresponding cells were then subsetted and re-processed with feature selection and subclustering at high resolution to reveal its heterogenous clusters. These distinct granular cell states were then annotated at 'refined' level.

Differential gene expression

Prior to annotations, the marker genes for each cluster were identified using the *scanpy.tl.rank_genes_groups* function in Scanpy. This applies differential expression testing between two groups (the cells in one cluster against all other cells in the data) to detect differentially expressed genes (DEGs) in the tested cluster.[165] A statistical test, corrected for multiple testing, is then applied to rank the genes based on their expression difference between the two groups. The top-ranked genes constitute the marker genes.[165]

The Wilcoxon rank-sum test with Benjamini-Hochberg correction were used to compute the data-derived marker genes in the prenatal skin scRNA-seq data for broad and refined clusters which were then compared with known signature genes from the literature for annotation.[165] The top 25 genes for each cluster are provided in Appendices E and F1-F5. A further approach using the Single Cell analysis Tool Kit package[184] (v0.2.0) was also implemented. In this method, a gene filtration step was carried out after Wilcoxon-based gene ranking by comparing genes in one cluster (cluster with highest expression) directly to the next cluster (cluster with second highest expression). The maximum proportion of cells expressing the tested gene in the second cluster was set to 0.2. This enabled the identification of genes highly specific to clusters of interest, especially when comparing clusters of similar cell types.[157]

Differential abundance testing

To test for significant differences in cell abundance associated with gestational age, a python implementation of the Milo package[185] (v1.0.0) was used as previously described.[101,102] To account for differential enrichment by FACS, a correction factor was applied to each gated sample as previously carried out.[101,102] This was calculated using the total number of cells from each sample (S), the number of cells from each sorting gate (Si) and the true original proportion of cells through each gate (pi) (obtained from FACS reports) as correction factor = log(piS/Si).[101]

A new latent representation of the prenatal skin data was first obtained using the scVI default variational auto-encoder module (latent = 30) in scvi-tools[177] and treating specimen identity and assay chemistry as batches. Based on the scVI-derived latent representation, the Milo function *milopy.core.make_nhoods* was used to construct a KNN graph and determine neighbourhoods of cells. The number of cells for each cell type (broad level annotation) or cell state (refined level annotation) in each neighbourhood was counted with *milopy.core.count_nhoods* and a

neighbourhood label was assigned (*milopy.utils.annotate_nhoods*) based on majority voting, that is the cell annotation with the highest frequency (minimum of 50%) in the neighbourhood is assigned to it.

To test for differential abundance across gestational age, the Milo function *milopy.core.DA_nhoods* was applied. The prenatal skin data was grouped into four age categories (7-8 PCW, 9-10 PCW, 11-13 PCW, 15-17 PCW) and the effects of age (age categories) on cell abundance were computed while accounting for FACS sorting with the above correction factor. Significant changes in cell abundance across these age categories were assessed using log fold change (logFC) with Benjamini-Hochberg correction (outputting spatial false discovery rate (FDR)) to control for multiple testing. Cell neighbourhoods which were significantly (spatial FDR < 0.05) enriched in early (logFC < 0) or late (logFC > 0) gestation were highlighted for downstream analyses.

2.4.2 Alignment of prenatal skin, skin organoid and adult skin

Skin organoid scRNA-seq data analysis

Skin organoid scRNA-seq data (published[154] and unpublished) were obtained from collaborators in the Koehler laboratory; the skin organoids were derived from two cell lines (WTC-mEGFP-DSP-cl65 iPS and WA25 ES) and digested at four different time points (days 29, 48, 85 and 133). The organoid data was processed in a similar way to prenatal skin including alignment, quality control, data transformation, cluster identification, and annotation.

Mapping was performed using Cell Ranger software (v2.1.0 and v3.0.2) (10x Genomics) to a GRCh38 reference (10x Genomics–distributed 1.2.0 and 3.0.0 versions respectively). Low quality cells were filtered from the concatenated raw counts matrices based on fixed thresholds. Cells with less than 450 genes, UMI counts less than 1063 or more than 25559, or mitochondrial fraction over 13% were removed. Counts were normalised by global scaling and log-transformed to 1e4 as before prior to batch correction. The batch covariates corrected for included organoid cell line and the chemistry version of the single cell suspension assay used (3' v2 or v3). Highly variable genes, UMAP and marker genes were calculated for clustering and annotations at low and high resolutions. Cell annotations were checked against their original labelling in the published data to ensure they were generally consistent.

Integration of prenatal skin, skin organoid and adult skin

The processed scRNA-seq datasets from prenatal skin and skin organoid described above were then integrated with a published dataset of adult healthy skin.[100] To ensure reproducible results, two integration methods were utilised with consistent results, including scVI[176] (discussed in section 2.4.1) and Harmony.[186] Harmony is a PCA-based approach for scRNA-seq data integration which aligns cells from multiple datasets by first projecting them into a low-dimensional embedding followed by soft clustering where cells can belong to more than one cluster.[186] It iteratively balances clusters to contain cells from the different datasets and calculates linear corrections required to group transcriptionally similar cells while removing dataset-specific effects. The optimised correction that represents stable cluster membership for each cell is then applied. It performs well for datasets with low biological complexity, such as those with similar cell types, and strong (inter-dataset) batch effects (for example, different ages), while retaining biological heterogeneity similar to scVI with lower computational resource requirement.[178,187] Following integration, alignment of the datasets was determined at both broad cell type and refined cell state levels.

Broad level alignment by distance-based analysis

For broad level alignment, similarity was first assessed using distance-based transformation of gene expression profiles on Harmony-integrated data. The prenatal skin, skin organoid and adult skin datasets were pooled, downsampled and integrated using Harmony[186] (v0.0.5). Batch effects corrected for included dataset as batch and within-dataset batches as additional covariates (specimen identity for prenatal skin, donor for adult skin or cell line for skin organoid, and assay chemistry for all datasets). The principle component vectors from this integrated data was then applied to transform the gene expression matrix in the non-downsampled data using the NumPy (v1.23.4) function *linalg.lstsq* (rcond = 'warn'), obtaining an embedding for all cells in the three combined datasets (visualised as UMAP). For each broad cell type, the Euclidean distances between prenatal skin, skin organoid and adult skin cells were then calculated based on the SciPy (v1.9.3) function *spatial.distance_matrix* and plotted as a heatmap.

Broad level alignment by time-encoded cell type predictions

The above assessment, however, grouped all prenatal skin gestational ages and skin organoid culture days together. To untangle the time factor and evaluate similarity at different time points,

time-encoded logistic regression (LR) analyses were conducted as previously described[188] on scVI-integrated data. The pooled prenatal skin, skin organoid and adult skin datasets were integrated with scVI[176] (v0.19.0) using the linear module (Linearly-decoded Variational Auto-encoder) within scvi-tools[177] with the following parameters: hidden layers = 256, reconstruction-loss = negative binomial. Batch effects corrected for included dataset and assay chemistry as additional categorical covariate. The scVI batch-corrected low-dimensional representation was then used for the LR model training and prediction. The latent representation for the time-encoded labels (age_cell type) for prenatal and adult skin served as training data. The *linear_model.LogisticRegression* function from sklearn (v0.22) was utilised to build the model. The model was then applied to predict the probability of correspondence between training labels (age_cell type) and annotated time-encoded clusters (culture week_cell type) in the query skin organoid dataset. The median probabilities of training label assignment were evaluated overall (all cell types grouped together) and for individual broad cell types. The results were visualised as heatmaps.

Refined cell state comparison by co-embedding

Co-embedding of the refined cell states in prenatal skin and skin organoid datasets was determined separately for individual broad cell groups, focusing on epithelial, stromal and endothelial cell types. Each of the prenatal skin and skin organoid dataset was subsetted to the relevant cell group (all cell states belonging to each cell group were included) and the two data subsets integrated using Harmony[186] (v0.0.5) and scVI[176] (v0.19.0). Alignment of cell states was assessed by visual comparison of co-embedded UMAPs where transcriptionally similar cells occupied overlapping latent spaces.

2.4.3 Comparison of prenatal skin to tissue-specific datasets

The prenatal skin cell states were compared to published scRNA-seq data from specific tissues including adult human hair follicle[189] (chapter 3) and blood vessel organoid[190] (chapter 5). The prenatal skin and the external dataset being analysed were downsampled to have approximately the same numbers of cells per annotated cell state to mitigate class imbalance for integration and LR. Harmony[186] (v0.0.5) was used for integration. Batch effects corrected for included dataset as batch and within-dataset batches as covariates (specimen identity for prenatal skin, donor for adult hair follicle, or group (cell line_day of culture) for blood vessel organoid).

To compare cell type correspondence between prenatal skin and external datasets, LR analysis was performed using a framework similar to the CellTypist package.[191] The *linear_model.LogisticRegression* function from sklearn (v1.1.3) was utilised to build a model with the following parameters: penalty: L2, solver: saga, inverse of regularisation strength C = 0.1. The model was trained on the gene expression matrix of the training dataset and was then applied to predict the probability of correspondence between training labels and pre-existing labels for each cell in the query data. The correspondence between predicted and original labels was then summarised as Jaccard index or median probability predictions and visualised as heatmaps. For comparison to the blood vessel organoid, the prenatal skin dataset was used as training data and the blood vessel organoid data as query; for comparison to adult hair follicle dataset, the merged prenatal and organoid data (to ensure adequate keratinocyte numbers) was used as query, and the adult hair follicle dataset as training data.

2.4.4 Cross-species comparison

Comparison to embryonic mouse skin

A published scRNA-seq dataset of mouse embryonic skin[61] was accessed for comparison with human prenatal skin (chapter 3). A similar approach as described in section 2.4.2 was used. The annotated raw human and mouse skin datasets were pooled, normalised with log-transformation prior to integration with scVI[176] (v0.19.0). The default variational auto-encoder module in scvi-tools[177] was used with the following parameters: max epochs = 400, batch size = 512. Batch effects corrected for included dataset and assay chemistry as additional categorical covariate. The scVI batch-corrected latent representation was then used for the LR model training and prediction. The *linear_model.LogisticRegression* function from sklearn (v0.22) was applied to build the models with the prenatal skin latent representation as training data; a model was trained for broad cell types and one for refined cell states. The trained models were then used to predict the probability of correspondence between training labels and the pre-annotated clusters (broad cell types and refined annotations) in the query mouse skin dataset. The median probabilities of training label assignment were calculated for each model and the results were visualised as heatmaps.

Comparison to adult reindeer skin

Prenatal skin fibroblasts and macrophages were compared to the counterpart cell states in a published scRNA-seq data from reindeer skin[192] to investigate the scarless healing property of human developing skin (chapter 4). A similar approach as described in section 2.4.3 was used. The prenatal skin and reindeer skin datasets were subsetted to the relevant cell states, downsampled and integrated with Harmony[186] (v0.0.5), correcting for dataset as batch and within dataset batches as covariates (specimen identity for prenatal skin and assay chemistry for reindeer skin). The LR model was built and applied to predict the probability of correspondence between the two datasets exactly as described above (section 2.4.3). The reindeer skin fibroblast and macrophage data subsets were used as training data and the corresponding prenatal skin data subsets as query.

2.4.5 Trajectory inference analysis

To computationally infer differentiation trajectories, the CellRank package[193,194] (v1.5.2) was used. This method combined different approaches to trajectory inference - transcriptional similarity-based, RNA velocity-based, and pseudotime-based - to determine the start, intermediate and terminal cell states of a differentiation trajectory as well as the direction and probability of cell state changes.[193,194] For the similarity-based component, a KNN graph was constructed as previously discussed where cells that are more similar by gene expression profiles are closely connected. Directionality information was then added from RNA velocity analysis based on the scVelo method[195] (v0.3.0). The ratios of spliced to unspliced mRNA counts (obtained by STARsolo[196] re-alignment of sequenced scRNA-seq data) were leveraged to compute a velocity graph - a matrix of cell transition probabilities based on RNA velocity.[195] Pseudotime-inferred transition probabilities were calculated using Palantir[197] within CellRank. A weighted combination of the velocity-based and pseudotime-based components provided the directed single-cell transition probability matrix. This matrix, which can be very large and difficult to interpret, was then summarised by grouping into macrostates cells with similar gene and transition profiles.[193] The terminal (high probability of self-transition), start (low probability of incoming transition) and intermediate macrostates were automatically inferred. Finally, cell fate probabilities (likelihood to transition towards each terminal state) were estimated, cells were ordered along the pseudotime from initial to terminal states, and trajectory-specific driver genes were identified.[193]

Trajectory inference analyses were conducted for keratinocytes, fibroblasts and vascular endothelial cells. A combined embedding of prenatal skin and skin organoid was used except for endothelial cells which were too low in numbers in the skin organoid. The velocity-based and pseudotime-based matrices were weighted at 30% and 70% respectively to provide the final transition matrix. The generalized Perron cluster analysis estimator in CellRank estimated macrostates, including initial and terminal states (parameters: n_components = 25, method = 'brandts'), and the *compute_lineage_drivers* function was used to derive trajectory-specific driver genes. Partition-based graph abstraction (PAGA) graphs and UMAPs (overlaid with velocity vectors) were plotted to visualise the results.

2.4.6 Analysis of cell-cell interaction

The CellPhoneDB package[198] (v3.0.0) was used to infer putative cell-cell communication in the prenatal skin and skin organoid scRNA-seq datasets. This tool comprises a repository of ligands, receptors and their interactions which it integrates with a statistical framework to predict likely interactions between pairs of cell states, where one cell state expresses a ligand and the other cell state its corresponding receptor.[198] For each ligand or receptor gene present in the scRNA-seq data, CellPhoneDB calculates the percentage of cells expressing it and its average expression in each cell state. It then computes the ligand-receptor combinations that demonstrate significant specificity for cell state pairs (by permutation testing), outputting ligand-receptor interactions and the cell state pairs in which they are significantly enriched.[198]

Analysis of cell-cell interaction in the prenatal skin scRNA-seq data was conducted with all gestational ages or including only early (≤ 11 PCW) or late (≥ 12 PCW) gestation to account for cell states present at specific time points. The skin organoid data was analysed with all organoid ages included. The relevant dataset (prenatal skin overall, prenatal skin early, prenatal skin late, or skin organoid overall) was randomly subsampled to contain at most 200 cells per cell state and the CellPhoneDB analysis pipeline was run, using the statistical method to determine significant (p-value cut-off = 0.05) ligand-receptor interactions for pairs of cell states. Subsampling was undertaken 3 times for each dataset and the pipeline was run on each subsampled data to check for consistency of results. A summary results matrix was produced from each run, compiling: significantly enriched ligand-receptor interactions (at p-value cut-off = 0.05), the corresponding pair of cell states for which it is specific, the mean expression of the ligand-receptor combination across all cells of the cell state pairs, the actual p-values and p-values adjusted for multiple testing.

The Circlize package[199] (v0.4.15) was used to generate circos plots for downstream visualisation of selected significant (adjusted p-value < 0.05) interactions between defined pairs of cell states (for example, co-locating cell states), keeping only interactions identified across all three runs in each dataset.

To assess cell-cell communication between macrophage subsets and endothelial cells, the predicted interactions between each macrophage subset and the different types of endothelial cells (early endothelial cells, arterioles, capillary arterioles, capillaries, postcapillary venules, venules) were aggregated. This was done by averaging the mean expression values and using the minimum adjusted p-values as previously implemented.[101] A list of aggregated interactions was manually curated and plotted for visualisation using ggplot2 (v3.3.6). A similar approach was used to explore cell-cell interactions between hair follicle mesenchymal and epithelial cells in prenatal skin. For each hair follicle mesenchymal subset, the predicted interactions with early epithelial cells (≤ 11 PCW: immature basal) or late epithelial cells (≥ 12 PCW: *DPYSL2*$^+$ basal, *POSTN*$^+$ basal, placode, matrix, ORS, CL, IRS, cuticle/cortex) were aggregated. The top 10 interactions per cell type pair were visualised using a heatmap. The interactions identified from the prenatal skin dataset were also queried from the skin organoid data and plotted to highlight similarities and differences between the two tissues.

2.4.7 Gene set enrichment analysis

Gene set enrichment analysis was carried out using the python-based implementation of the Enrichr[200–202] workflow from the GSEApy package[203] (v0.10.7). Enrichr performs over-representation analysis (ORA) on a selected list of genes (input gene list) by computing enrichment against its database of annotated gene sets which are organised in different gene set libraries. These comprise, for instance, libraries of pathways (for example, Molecular Signatures Database (MSigDB) Hallmark) and ontologies (for example, Gene Ontology Biological Process (GOBP)). It thus identifies the pathways or processes that are significantly over-represented in the input gene list, providing meaningful information about the collective biological functions of these genes.[200]

Fibroblasts from prenatal and adult skin

To compare fibroblasts from prenatal skin to those in adult healthy skin (published data with original annotations[100]), the scVI-integrated data from section 2.4.2 was subsetted to the datasets

and cell group of interest. The DEGs between prenatal and adult skin fibroblasts were derived using the Wilcoxon rank-sum test with Benjamini-Hochberg correction for multiple testing with the Scanpy function *scanpy.tl.rank_genes_groups* as described in section 2.4.1. The top 1000 DEGs, ranked by scores, were used as the input list for each category of fibroblasts (prenatal or adult skin) in GSEApy[203] (v0.10.7) Enrichr module with GOBP (2021) as query library. The enriched pathways and biological processes enriched in each category were analysed and a curated set of genes was plotted to highlight identified differences between prenatal and adult skin fibroblasts.

Early and late gestation fibroblasts from prenatal skin

Gene set enrichment analysis was conducted for prenatal skin *WNT2*$^+$ fibroblasts significantly enriched in early or late gestation. The results from Milo analysis (section 2.4.1) were used to identify the index cells belonging to early neighbourhoods (logFC < 0, spatial FDR < 0.05) and late neighbourhoods (logFC > 0, spatial FDR < 0.05). The DEGs between early and late *WNT2*$^+$ fibroblasts were then derived as above using the Wilcoxon rank-sum test with Benjamini-Hochberg correction for multiple testing with the Scanpy function *scanpy.tl.rank_genes_groups*. Significantly increased genes (logFC > 1 and adjusted p-value < 0.01) in each category of *WNT2*$^+$ fibroblasts (early or late) were selected as the input lists in GSEApy[203] (v0.10.7) Enrichr module with GOBP (2023) as query library.

Prenatal skin myeloid cells

For comparison of prenatal skin myeloid cells, the DEGs between the different myeloid cell states were identified as above using the Wilcoxon rank-sum test with Benjamini-Hochberg correction for multiple testing with the Scanpy function *scanpy.tl.rank_genes_groups*. Significantly overexpressed genes (logFC > 1.5 and adjusted p-value < 0.01) in each subset of macrophages were selected as the input lists in GSEApy[203] (v0.10.7) Enrichr module with GOBP (2023) and MSigDB Hallmark (2020) as query libraries.

2.4.8 Analysis of angiogenic gene profiles

Gene module scoring

The Scanpy function *sc.tl.score_genes* was applied in analyses where gene module scores were computed. In this tool, a list of genes is provided for each gene module or gene set of interest. The average expression of the input genes is subtracted with the average expression of a reference gene set.[163] To derive the reference gene set, all genes in the dataset that passed quality control (the default gene pool) are divided into a defined number of bins by expression level and a user-specified number of genes (the control size) are randomly sampled from each bin. Genes in the input list are excluded from sampling and do not form part of the reference gene set. For each gene module scored, the reference gene set was derived by sampling 100 genes from each of 25 expression level bins.

The angiogenesis and hypoxia gene sets used for module scoring were obtained from the GOBP (2021) and MSigDB Hallmark (2020) databases respectively in Enrichr libraries[204] as pre-annotated sets. For endothelial cell modules, gene sets defining tip and stalk phenotypes and arteriole, venule, lymphatic, and capillary cell types were derived from published literature.[205–208] The list of genes for each scored module is provided in Appendices G1-G2.

Comparison of pro- and anti-angiogenic genes

The scVI-integrated data from section 2.4.2 was subsetted to the prenatal skin and skin organoid datasets. Differential gene expression analysis was carried out between prenatal skin and skin organoid cells (all cell types) with the Scanpy function *scanpy.tl.rank_genes_groups* as described in section 2.4.1, using the Wilcoxon rank-sum test with Benjamini-Hochberg correction for multiple testing. The identified DEGs for each category were filtered to retain only those encoding a secreted protein by intersecting with a publicly available list of proteins.[209] Lists of filtered DEGs that were significantly (adjusted p-value < 0.05) upregulated (logFC > 0) or downregulated (logFC < 0) in prenatal skin were generated. These lists were used separately as input for gene set enrichment analysis which was conducted as described in section 2.4.7 in GSEApy[203] (v0.10.7) Enrichr module with GOBP (2021) as query library. The resulting significantly (adjusted p-value < 0.05) over-represented GOBP gene sets (terms) were then filtered based on their relevance to vasculature and angiogenesis. The overlapping genes corresponding to these filtered terms were

compiled as angiogenesis-related genes and their expressions were plotted across prenatal and skin organoid cells.

2.4.9 Gene regulatory network analysis

Regulon analysis

The python implementation of the SCENIC package, pySCENIC[210] (v0.11.2) was used to reconstruct regulons - transcription factors and their target genes - from the scVI-integrated prenatal skin and skin organoid data (from section 2.4.2). PySCENIC uses a pre-defined list of transcription factors to predict regulatory interactions of transcription factors and target genes based on their co-expression patterns in the scRNA-seq data.[210] This outputs an adjacency matrix, where transcription factors are connected to genes in a weighted manner, from which modules (a transcription factor and its predicted target genes) are inferred. The modules are then filtered to only retain those where the transcription factor directly regulates its target genes. This is done through assessment of motif enrichment. The genome-wide rankings for all motifs (binding sequences for transcription factors in gene regulatory regions) associated with known transcription factors are pre-computed. If a binding motif associated with a transcription factor is enriched in its target genes, this indicates likely direct regulation and the module is retained. Pruning of target genes is also undertaken in this step and all target genes regulated by the same transcription factor are grouped into a single regulon. Finally, the activity of the identified regulons is quantified in each cell in the scRNA-seq data and their specificity across different cell types can be determined (regulon specificity score).

For the analysis, the ranking (hg38 refseq-r80 500bp_up_and_100bp_down_tss.mc9nr.feather) and motif annotation (motifs-v9-nr.hgnc-m0.001-o0.0.tbl) databases were downloaded from the pySCENIC github page.[210] The integrated data was randomly subsampled to contain at most 1000 cells per cell state for each tissue type (prenatal skin or skin organoid) to mitigate class imbalance and ensure computational efficiency. Ten runs of the above pipeline were performed on the subsampled data. Only regulons commonly present in at least 6 out of 10 runs were retained and the regulon specificity scores, computed for each cell state per tissue type, were averaged across the multiple runs. These average scores were used to compare regulon activity between prenatal skin and skin organoid.

The STRING database[211,212] was then queried to construct a gene interaction network based on regulons identified from pySCENIC analysis, for example for *GATA2* as transcription factor. The list of *GATA2* target genes highlighted were pruned to only keep genes that were either part of the regulons (top 5) detected in prenatal skin and/or skin organoid data, among endothelial lineage driver genes from trajectory inference analysis, known vascular endothelial growth factor (VEGF) receptors, or known to be involved in angiogenesis-related cellular processes from the GOBP (2021) database gene sets (for example, 'regulation of angiogenesis' (GO:0045765)).

Analysis of ligand-to-target gene links

The NicheNet package[213] (v.1.1.1) was used to infer links between ligands and their target genes by combining gene expression data (prenatal skin and skin organoid scRNA-seq) of interacting cells (sender and receiver cells) with existing information on signalling and gene regulatory networks. The data sources providing this information are integrated in the open-source R-based NicheNet implementation and available from the github page.[213] NicheNet first performs a ligand activity analysis and ranks ligands in the user-defined sender cell type which best predict observed changes in expression of target genes of interest in receiver cell type compared to background genes. Ligand activity scores are calculated as the Pearson correlation coefficient between a ligand's target predictions and the observed target gene expression. The top ranked ligands, based on the ligand activity scores, are then used to predict the active target genes and construct the active ligand-target links matrix. NicheNet also identifies the receptors of the top ranked ligands, filtering only for bona-fide ligand-receptor interactions documented in the literature and in existing databases.

Signalling paths can then be inferred by defining the ligand and target genes of interest. The transcription factors which best regulate the defined target genes and are closest downstream of the defined ligand are identified from the weighted ligand-signalling and gene regulatory networks integrated in NicheNet.[213] The shortest paths between the transcription factors and the defined ligand constitute the signalling paths; genes along these paths are the signalling mediators. NicheNet then prioritises these signalling mediators by cross-checking the interactions between the defined ligand, target genes, identified transcription factors and signalling mediators across its different integrated data sources.[213]

For the analysis, macrophage subsets in prenatal skin were designated as sender cell types and vascular endothelial cells as the receiver cell type. The potential ligands included all ligands in the NicheNet model that were expressed in at least 10% of cells in each macrophage subset and for which at least one receptor was expressed in endothelial cells (at least 10%). The target genes were defined as the DEGs between prenatal skin and skin organoid endothelial cells; these were identified using the *FindMarkers* function in NicheNet with the following parameters: adjusted p-value ≤ 0.05, average logFC > 0.25, expressed in $\geq 10\%$ of endothelial cells). From the calculated ligand activity scores, the top 20 ranked ligands (Appendix H) were used to predict active target genes from which the top 200 were selected to build the ligand-target links matrix. To infer signalling paths, *VEGFA* was defined as ligand and *GATA2* as target gene of interest.

2.5 Spatial transcriptomic data analysis

2.5.1 Alignment to human genome

The newly generated spatial gene expression data were mapped using Space Ranger software (v.2.0.1) (10x Genomics) to the GRCh38 reference (10x Genomics–distributed 1.2.0 version). In addition, publicly available spatial transcriptomic data from embryonic limb[141] (Appendix B2) was accessed and the skin-overlayed spots were manually selected for analysis.

2.5.2 Cell type deconvolution

To resolve the spatial transcriptomic profiles of prenatal skin sections from spot-resolution to single-cell resolution, deconvolution analysis was performed using Cell2location[147] (v0.1). Of the various approaches available for cell type deconvolution, Cell2location has been benchmarked as one of the top-performing methods.[214] It enabled the integration of the spatial and single-cell transcriptomic prenatal skin datasets. Using the prenatal skin suspension data as reference, it derived gene expression signatures to decompose each Visium spot into its individual cellular composition, and thus mapped single cell states to their predicted tissue location.[147]

A negative binomial regression model was trained to estimate the reference transcriptomic profile for cell states identified in the prenatal skin scRNA-seq data. Cell states were excluded if there were less than 20 cells present in samples of gestational ages ≤ 10 PCW as previously implemented.[101] Genes that were lowly expressed were filtered out using recommendations by the package authors with the following parameters: cell_count_cutoff = 5, cell_percentage_cutoff2 = 0.03, nonz_mean_cutoff = 1.12. For integration of the scRNA-seq data prior to model training, the sample identifier was considered as the batch covariate while the specimen identity and chemistry assay (3’ and 5’) were included as categorical covariates (Appendices B1 and D). The model was trained for 250 epochs and deemed to have reached convergence based on manual inspection.

The spot abundance and spatial distribution of cell states were then inferred in the prenatal skin spatial transcriptomic data (all slides jointly analysed) using the reference transcriptomic profiles estimated above. Cell2location required an expected cell number per spot to be input (n_cells_per_location) which was set at 30 with a regularisation strength of detection efficiency effect (detection_alpha) of 20 to account for variability in gene detection. All other parameters were set to default settings, and the model was trained for a maximum of 50,000 iterations to

prevent over-fitting. Cell2location estimated the posterior distribution of cell abundance for cell states in each spot which was summarised using 5% quantile. This represented the value of cell abundance for which the model had high confidence while accounting for estimate uncertainty and was used in further downstream analyses.[147]

2.5.3 Prediction of tissue microenvironments

Non-negative matrix factorisation was then applied to computationally predict microenvironments of co-locating cell types (section 1.4.3) as previously implemented.[101,147] The matrix (X) of estimated cell state abundance output from Cell2location had dimensions $n \times c$ where n was the total number of spots included across all Visium slides and c was all the cell states included from the prenatal skin reference data. This matrix was first normalised by dividing by the total cell abundance per spot (per-spot normalisation). The resulting normalised matrix (Xn) was then decomposed as $X\text{n} = WZ$, where W is a matrix ($n \times d$) of latent factor values for each spot and Z is a matrix ($d \times c$) of the abundance fraction for each cell state attributed to each latent factor.[101] The latent factors represent tissue microenvironments and correspond to a defined set of co-localised cell states. The R-based NMF package[215,216] was used with a pre-set number of latent factors (d) to 10 and the NMF coefficients were normalised by a per-latent factor maximum.[101] The NMF algorithm was run 100 times and a coincidence matrix was generated from which mean silhouette scores were calculated. The best run was chosen as the one with the lowest silhouette score; if more than one run had the lowest score, the one with the smaller deviance (reported by NMF) was selected.

Correlation analysis of cell state abundance was also conducted on the normalised matrix Xn. A Pearson correlation coefficient was computed for every possible pair of cell states for each Visium sample (corresponding to an individual prenatal skin tissue section). The results of the correlation analysis were plotted for selected cell pairs for visualisation. These cell pairs were chosen based on the earlier NMF results which indicated the groups of cell states that were likely to co-localise in tissue microenvironments.

2.6 Assessing vascular network in skin organoids cultured with and without macrophages

Hair-bearing skin organoids were derived from Kolf2.1S iPS cells using the method[154] described in section 1.5.1 and associated protocol.[155] This cell line was obtained from the HipSci Initiative[217,218] and tested negative for mycoplasma. Autologous macrophages were separately cultured from the same cell line using a published protocol.[219] For co-culture, macrophages were first harvested and phenotyped by flow cytometry and then added to a portion of the skin organoids.

2.6.1 Macrophage harvesting and phenotyping

Macrophage harvesting was undertaken through selective isolation by incubating with TrypLE (Gibco) at 37°C for 5 minutes in an atmosphere of 5% CO_2 - 95% air followed by centrifugation (500*g* for 6 minutes). Harvested cells were washed with cell staining buffer (Biolegend) and counted prior to antibody staining which was performed in the dark. To prevent non-specific antibody binding, Human TruStain FcX (BioLegend), an Fc receptor blocking solution, was added with incubation on ice for 10 minutes. LIVE/DEAD fixable blue dead cell stain (1:500, Thermo Fisher Scientific) was then added, with further incubation for 30 minutes on ice, to highlight viable cells. The cells were then washed twice with cell staining buffer (Biolegend) and single-stained to distinguish macrophages from other myeloid cells such as monocytes and DCs. The following mix of antibodies was added followed by incubation in the dark for 30 minutes on ice: anti-CD206 antibody (1:200, PE, clone 19.2, Thermo Fisher Scientific), anti-CD16 antibody (1:50, PE-Cyanine7, clone eBioCB16, Thermo Fisher Scientific), anti-CD14 antibody (1:100, PerCP-Cyanine5.5, clone 61D3, Thermo Fisher Scientific), anti-CD1c antibody (1:25, Pacific Blue, clone L161, BioLegend), anti-CD45 (1:300, BV480, clone HI30, BD Biosciences) and anti-human Lineage Cocktail (1:100, CD3, CD19, CD20, CD56, clones UCTH1, HIB19, 2H7, 5.1H11, BioLegend).[157] The stained cells were washed once with cell staining buffer (Biolegend) and passed through a 35 μm cell strainer (Falcon) prior to flow cytometry acquisition on a BD LSRFortessa Cell Analyzer (BD Biosciences) and analysis using FlowJo (v10.9.0).

2.6.2 Co-culturing skin organoids with macrophages

In skin organoids cultured with macrophages, co-culture was started on day 12 of skin organoid differentiation by addition of autologous iPS cell-derived macrophages at a ratio of 1:5 (1 macrophage: 5 skin organoid cells). This was done by first transferring the skin organoids to a low-

attachment Nunclon Sphera 96U-well plate (Thermo Fisher Scientific). One skin organoid was placed in each well in organoid maturation medium (OMM)[154] containing 20% matrigel matrix (Corning). Macrophages were then added to each well and the co-culture plate was briefly centrifuged (100*g* for 6 minutes) to initiate contact between the macrophages and skin organoids. On day 3 of co-culture (day 15 of skin organoid differentiation), the contents of each well (skin organoids and macrophages) were transferred from the 96U-well plate to a low-attachment Nunclon Sphera 24-well plate (Thermo Fisher Scientific) to allow space for continued growth and the matrigel matrix was diluted with 500 µL of fresh OMM. The skin organoids were fed with fresh OMM by performing half media changes every three days and a full media change once per week.

2.6.3 Whole-mount immunostaining

Cell fixation of skin organoids with and without macrophages was undertaken on day 35 of co-culture (day 47 of organoid differentiation) by transferring to a 5 ml round-bottom polystyrene tube (Falcon) with 4% paraformaldehyde (PFA) solution (Thermo Fisher Scientific) overnight. These included skin organoids with macrophages (n=5) and without macrophages (n=5) across two different batches of skin organoid differentiation. Following fixation, cells were permeabilised and blocked in a blocking solution, containing 0.3% (v/v) Triton X-100 (Thermo Fisher Scientific), 1% (v/v) bovine serum albumin (Sigma-Aldrich) dissolved in 1x PBS (Gibco), and 1% (v/v) species-specific (goat) serum (Abcam), maintained for 8 hours at room temperature on a shaker.

Antibody labelling of macrophages and skin endothelial cells was then carried out. Primary and secondary antibodies were sequentially added, with incubation at 4°C on a shaker (65 revolutions per minute (rpm)) and between-antibody cell wash, in the following order: first primary antibody anti-CD45 (1:100, clone YAML501.4, Thermo Fisher Scientific) for macrophages with 48-hour incubation, first secondary antibody (goat anti-rat IgG, Alexa Fluor Plus 647, Thermo Fisher Scientific) with overnight incubation, second primary antibody anti-CD31 (1:100, clone JC70A, Dako) for endothelial cells with 48-hour incubation, and lastly second secondary antibody (goat anti-mouse IgG1, Alexa Fluor 568, Thermo Fisher Scientific) and DAPI with overnight incubation.[157] A full list of primary and secondary antibodies and their corresponding technical information is provided in Appendix I.

2.6.4 Confocal imaging

Prior to imaging, clearing and mounting of skin organoids were performed using 50% glycerol for 30 minutes followed by 70% glycerol overnight, both at room temperature on a shaker. The following morning the organoids with or without macrophages were mounted on a transparent holder to enable imaging from two directions, using mounting medium containing 1,4-Diazabicyclo[2.2.2]octane (DABCO; Sigma-Aldrich), 90% glycerol, 5% Tris hydrochloride (Sigma-Aldrich) and 5% distilled water. Images were captured on a custom four-camera spinning disk confocal microscope - this consisted of an OpenFrame microscope frame connected to a CrestOptics X-Light V3 spinning disk confocal module with four Teledyne Photometrics Kinetix cameras mounted to it and was assembled by Cairn Research UK.[157] A consistent setting was used to image all organoids: tiled stacks 800 micron deep on an Olympus 10x air objective with numerical aperture of 0.3 and 5 µm z-step;[157] each organoid was imaged twice, one time each from two opposing directions. Bigstitcher[220] was used for tile stitching to produce the final images for analysis.

2.6.5 Analysis of skin organoid confocal images

The area covered by endothelial cells in skin organoids cultured with and without macrophages was then quantified. The FIJI distribution of the ImageJ software (v2.14.0)[221] was used to analyse the maximum intensity Z projections of $CD31^+$ staining from the confocal stacks. Using intensity thresholding for segmentation, the $CD31^+$ endothelial areas were measured (in μm^2); the endothelial areas were normalised to the whole organoid area (in μm^2) to derive the endothelial density (in percent). Each analysed stack comprised 161 or 201 slices which measured 1 µm in the Z dimension and up to 1415 µm by 1415 µm in the X and Y dimensions with a total area (in μm^2) of maximum intensity Z projections per organoid ranging from 1.86 to 14.74 million μm^2.[157]

2.7 Scratch wound assay of fibroblasts cultured with and without macrophages

Fibroblasts were isolated from skin organoids derived from Kolf2.1S iPS cells on day 76 of differentiation. The skin organoids (n=3) were washed in Dulbecco's PBS (Gibco) and incubated in a mix of dispase (Corning) and ROCK inhibitor (Stemolecule) at 37°C for 40 minutes. The epidermal and dermal layers of the skin organoids were then gently separated using forceps. The dermis was placed in collagenase (Life Technologies) at 37°C for 40 minutes for digestion. Fibroblast medium, containing advanced Dulbecco's modified eagle medium (DMEM; Gibco), 10% FBS (Gibco), 1% GlutaMAX supplement (Gibco), and Normocin (Invivogen), was then added to neutralise the collagenase and the cell suspension was passed through a 40 μm cell strained (Falcon). Cells were collected by centrifugation (180*g* for 3 minutes) and resuspended prior to seeding in fibroblast media and cultivation as primary fibroblasts. Autologous macrophages were also differentiated from Kolf2.1S iPS cells as in section 2.6.

For the scratch wound assay, the fibroblasts were seeded with and without macrophages in 48-well plates at a ratio of 5:1 (5 fibroblasts: 1 macrophage). The plates were incubated at 37°C for 24 hours. A scratch was then generated down the centre of each well using a p-1000 pipette tip. The wells were imaged using the Incucyte S3 (whole well module) every 6 hours for 72 hours. The images were analysed using the FIJI distribution of the ImageJ software (v2.14.0)[221] with *Wound_healing_size_tool_updated* plugin.[222] Scratch width closure between fibroblasts cultured with and without macrophages were compared in graphpad using two-way analysis of variance (ANOVA) with Tukey's multiple comparisons testing, across 4 independent experiments for each culture condition with 3 replicates per experiment (Appendix J).

2.8 Validating cellular co-localisations and interactions

2.8.1 Multiplex RNA fluorescence in situ hybridisation

Tissue preparation and probe hybridisation

Fresh-frozen prenatal skin specimens at the required age (8, 10 or 15 PCW) in OCT compound (Tissue-Tek, Sakura Finetek) were sectioned and processed for 4-plex single-molecule fluorescence in situ hybridisation (smFISH) using either RNAscope Multiplex Fluorescent Assay v2 (ACDBio) (manual system) or RNAscope LS Multiplex Fluorescent Assay (ACDBio) (automated system). Standard pre-treatment was performed for prenatal skin sections of 10-20 µm thickness including permeabilisation with proprietary Protease IV (ACDBio) for 30 minutes at room temperature.

RNAscope human probes (ACDBio) against the following groups of transcripts were assayed: *SLC26A7*, *SHH*, *NDP*, and *FOXP3*; *ELAVL4*, *CDH5*, *CD68*, and *P2RY12*; *ACKR3*, *CXCL12*, *PDGFD*, and *SERPINB7*. Atto-425 (ATTO-TEC) and opal dyes (Akoya Biosciences) at a dilution of 1:1000 were used in the fluorophore step to develop each channel, including Opal 520 Reagent Pack (FP1487001KT), Opal 570 Reagent Pack (FP1488001KT) and Opal 650 Reagent Pack (FP1496001KT).[157] The slides were counterstained with DAPI for nuclear staining and coverslips were mounted with ProLong Gold Antifade Mountant (Thermo Fisher Scientific) prior to imaging.

Confocal imaging

Two imaging systems were used. Slides with probes against *ACKR3*/*CXCL12*/*PDGFD*/*SERPINB7* were imaged on a custom four-camera spinning disk confocal microscope, which consisted of an OpenFrame microscope frame connected to a CrestOptics X-Light V3 spinning disk confocal module with four Teledyne Photometrics Kinetix cameras mounted to it and was assembled by Cairn Research UK.[157] A 40X CFI Plan Apochromat Lambda D objective (Nikon Instruments) was used with numerical aperture of 0.95 and 1.5µm z-step. The images were stitched using the BigStitcher Fiji plugin into a final z-projected image from individual tiles.

Slides with probes against *SLC26A7*/*SHH*/*NDP*/*FOXP3* and *ELAVL4*/*CDH5*/*CD68*/*P2RY12* were imaged on an Opera Phoenix Plus High-Content Screening System (PerkinElmer) using a 40X water-immersion objective with numerical aperture of 1.1 at resolution of 0.149 µm/pixel and 2

µm z-step. The following excitation (ex.) and emission (em.) wavelengths were used for each channel: Atto-425 (ex. 425 nm, em. 463-501 nm), Opal 520 (ex. 488 nm, em. 500-550 nm), Opal 570 (ex. 561 nm, em. 570-630 nm), Opal 650 (ex. 640 nm, em. 650-760 nm), and DAPI (ex. 375 nm, em. 435-480 nm). The confocal image stacks were stitched using proprietary Acapella software scripts (PerkinElmer) into two-dimensional maximum intensity projections and visualised using OMERO Plus (Glencoe Software).

Image analysis for *FOXP3* signal quantification

Once imaged, the slides with probes against *FOXP3* were analysed to quantify the amount of *FOXP3* signal coverage between prenatal skin regions with and without hair follicles. The QuPath image analysis software (v0.5.1)[223] was used. Two pixel classifiers were trained - one to distinguish the skin tissue from the image background and one to segment *FOXP3* signals from the background. The hair follicle regions were manually segmented from the rest of the skin image (hair follicle mask); a new segmentation mask was created for the latter by subtracting the hair follicle masks from the mask of the whole skin section (non-hair follicle mask). The *FOXP3* signal was quantified for hair follicle and non-hair follicle masks by calculating the percentage of each mask covered by segmented *FOXP3* signals.

2.8.2 Immunofluorescence assays of prenatal skin and skin organoid cryosections

Tissue preparation and immunostaining

Fresh-frozen prenatal skin and iPS cell-derived skin organoid specimens in OCT compound (Tissue-Tek, Sakura Finetek) were sectioned in a Leica CM1950 cryostat. 10 µm thick sections were cut from each specimen block onto glass slides which was then stored at -80°C until assayed.

Prior to immunostaining, the slides were thawed at room temperature, carefully dried and the tissue sections were fixed in 4% PFA in PBS (Thermo Fisher Scientific) for 10 minutes. Following fixation, the slides were washed in 1x PBS (Gibco) and cell permeabilisation and blocking was done using a blocking solution consisting of 3% species-specific (goat) serum (Abcam) prepared in 1x PBS with 0.1% Triton X-100 (Merck Millipore) maintained for 1 hour at room temperature. The relevant primary antibodies were then added in the blocking solution with overnight incubation at 4°C. The slides were then washed thrice in 1x PBS the following morning prior to incubation

with the secondary antibodies in blocking solution for 1-2 hours at room temperature. The list of primary and secondary antibodies used is provided in Appendix I.

Confocal imaging

DAPI was then added in between further slide washes in 1x PBS and coverslips applied with ProLong Gold Antifade Mountant (Thermo Fisher Scientific). The slides were allowed to dry overnight at room temperature in the dark prior to image acquisition on a Leica SP8 Lightning confocal microscope.

Chapter 3 . Prenatal skin multi-omics atlas reveals cellular crosstalk and immune cell co-location during de novo hair follicle formation

3.1 Introduction

The human skin undergoes dynamic morphological and molecular changes in utero to develop from the primary germ layers during gastrulation (ectoderm and mesoderm) into a structurally complex organ with critical functions in postnatal life.[42,43] The processes underlying this transformation, including de novo skin appendage formation, remains incompletely characterised. Studies investigating human prenatal skin morphogenesis have mainly been restricted to microscopic observations or focused on expressions of a priori determined genes and proteins.[42] This is further compounded by the scarcity of human embryonic and foetal tissues, especially from the very early or late gestation periods.[109] A comprehensive assessment of the spatio-temporal cellular and molecular shifts in prenatal skin is therefore still lacking.

Recent studies have attempted to address this by leveraging newer technologies such as scRNA-seq which can provide a global transcriptional profiling of prenatal skin and allow capture of rare cell states from small tissue volumes.[98,148] However, there was no spatial contextualisation performed within these studies to understand the cellular microenvironmental organisation that potentially contributes to prenatal skin development. In addition, these studies primarily focused on the immune landscape in the developing skin.[98,148] An in-depth evaluation of non-immune cells, including hair follicles, during human prenatal skin development has not been performed.

A lot of what is known about mammalian hair follicle formation derives from animal studies particularly from mouse models.[43,52] The greater access to in vivo and ex vivo tissues and possibility of performing fate-mapping and lineage tracing experiments in mice have yielded a detailed understanding of the different stages of hair follicle organogenesis and cytodifferentiation and the cellular signalling involved.[52,224] Apart from morphological descriptions and limited assessments of pre-defined morphogens during development (section 1.2.2), human studies have primarily focused on adult skin where established hair follicles cycle through the distinct phases of hair growth (anagen), regression (catagen) and resting (telogen).[42,54,56] To understand prenatal human hair follicle neogenesis, parallels have been drawn to embryonic mouse skin.[52,224] However, human and mouse skin differ in several respects (described in section 1.2.2) and developmental

features are not always conserved across the two species as shown in immune system and brain development.[65,225–227] This highlights the need for studies focused on human prenatal skin and hair follicle development to identify human-specific features and understand cross-species similarities and differences between human and murine skin.

This chapter describes the whole-tissue profiling of human prenatal skin using high throughput scRNA-seq to capture both immune and non-immune cells. Samples were collected from 7 to 17 PCW to capture the onset of hair follicle formation and maturation of the different skin layers. All identified cell states were annotated at broad and refined levels to provide a comprehensive view of the cellular composition of prenatal skin across gestation. Alignment to adult healthy skin and skin organoid datasets were undertaken to confirm cell identities with appraisals of the faithfulness of the skin organoid model to in vivo skin punctuated throughout the chapter. To gain insights into knowledge gaps surrounding the molecular changes and cellular crosstalk during skin and hair follicle differentiation, inferred trajectory and ligand-receptor interactions analyses were performed. Comparative analyses with mouse and human adult hair follicles were also carried out to determine distinct characteristics of human prenatal hair follicles. Finally, the single-cell atlas was then integrated with spatial transcriptomic data from early prenatal skin to map the location of the different cell states in situ and determine tissue microenvironments.

3.2 Objectives

This chapter addresses the first two overall study aims, which were to:

1. Comprehensively profile the immune and non-immune cellular composition of human prenatal skin across gestation to gain insights into skin and hair follicle morphogenesis.

2. Investigate whether immune and non-immune cells co-localise in tissue microenvironments in prenatal skin.

These were met by achieving the following chapter objectives:

1. Generate an annotated single cell suspension dataset of first and second trimester prenatal human skin.

2. Assess the differential abundance of prenatal skin cell states across gestation

3. Confirm the cell identities in prenatal skin by aligning with adult skin and skin organoid cell states.

4. Assess the genes from pseudotime trajectories and ligand-receptor interactions of hair follicle epithelial and mesenchymal cells.

5. Integrate and compare prenatal skin single cell suspension data with published scRNA-seq data from mouse skin and adult skin.

6. Produce a spatial transcriptomic dataset of early prenatal skin for deconvolution using annotated single cell suspension data.

3.3 Results

3.3.1 Annotated single cell atlas of human prenatal skin

Prenatal skin sampling

A total of 18 human prenatal skin specimens were obtained from HDBR from first and second trimester conceptuses aged between 7 and 17 PCW (Appendix B1). This included male (n=4) and female (n=14) samples collected from trunk and limb skin.

scRNA-seq data generation

Skin samples were mechanically and enzymatically digested as described in section 2.2.1 to generate single cell suspensions. Fluorescence-activated cell sorting was used to isolate all live, single immune ($CD45^+$) and non-immune ($CD45^-$) dissociated cells. Additional staining and gating strategies were used on four samples to increase capture of less abundant non-immune populations, such as keratinocytes and endothelial cells, by separating them from the abundant $CD34^+$ or $CD34^+CD14^-$ stromal cells (section 2.2.2). Figure 3.1 shows an example of the gating and sorted cell populations for one prenatal skin sample. The FACS-isolated cell proportions for each sample are provided in Appendix C. The droplet-based scRNA-seq platform from 10x Genomics was then used to generate cDNA gene expression libraries from sorted cell suspensions prior to sequencing (section 2.2.3). Based on the number of cells available, sorted cell populations were either loaded on the 10x Genomics Chromium Controller separately or pooled to ensure adequate recovery (section 2.2.3). Overall, 80 individual channels (Appendix D) were loaded for single cell encapsulation.

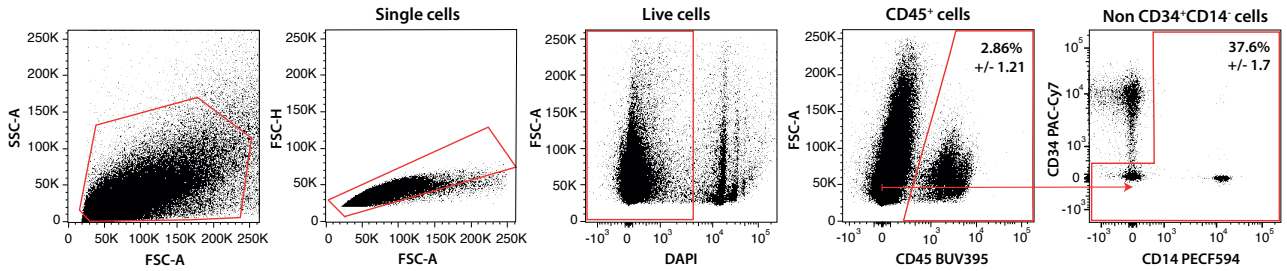

Figure 3.1. Isolation of prenatal skin cells by FACS.

Live single cells were sorted into CD45+ and CD45- fractions (n=18); the CD45- fraction (n=4), was further sorted to enrich for rarer non-immune populations not within the CD34+ or CD34+CD14- gates. Representative data (n=1) is shown as mean percentage ± standard deviation (SD).

scRNA-seq data pre-processing

Following sequencing, alignment to the human reference genome (GRCh38) and cell calling using Cell Ranger software (v2.1.1 and v2.0.2) (10x Genomics), a matrix of gene counts (the 'counts matrix') was obtained for each sequenced sample, corresponding to each channel loaded on the Chromium Controller (10x Genomics) (n=80) (section 2.4.1). The counts matrix provides the number of counts of each gene (columns) in every cell (rows) called by the Cell Ranger algorithm.[174] Using the scRNA-seq processing packages Scanpy,[163] the gene expression matrices of all sequenced samples from the 18 specimens were concatenated into a single large matrix (the 'anndata' object) and the relevant metadata was added. This data object comprised of 534,581 recovered cells by 36601 genes.

To ensure accuracy of downstream analyses and results, standard quality control steps[165,174] were carried out on the prenatal skin scRNA-seq data as outlined in section 2.4.1. This consisted of detection and removal of doublets or multiplets (mixture of two or more cells captured within a single droplet) and low quality cells. Scrublet package[167] was used as doublet detection tool and run on each sequenced sample to flag potential doublets (section 2.4.1). 7,936 cells (~1.5%) flagged as doublets were removed from the prenatal skin scRNA-seq data. This is lower than the expected rate of approximately 8% expected when targeting 10,000 cells per channel on the 10x Genomics Controller[158,159] due to the permissive thresholding used as discussed in section 2.4.1.

Quality control metrics showed similar distributions of the total UMI counts per cell and fraction of mitochondrial gene counts across all sequenced samples (Figure 3.2), indicating comparable data quality. Using thresholds defined in section 2.4.1, 63,062 low quality cells were initially removed, corresponding to ~10% of the total number of cells. The prenatal skin scRNA-seq consisted of heterogeneous cell types and thresholds were purposely set to preclude unnecessary filtering of cells. Additional poorer quality cells which were highlighted in subsequent steps, during clustering and differential gene expression analyses, were manually removed at that stage. Lowly expressed genes, expressed in less than three cells, were also filtered out (section 2.4.1).

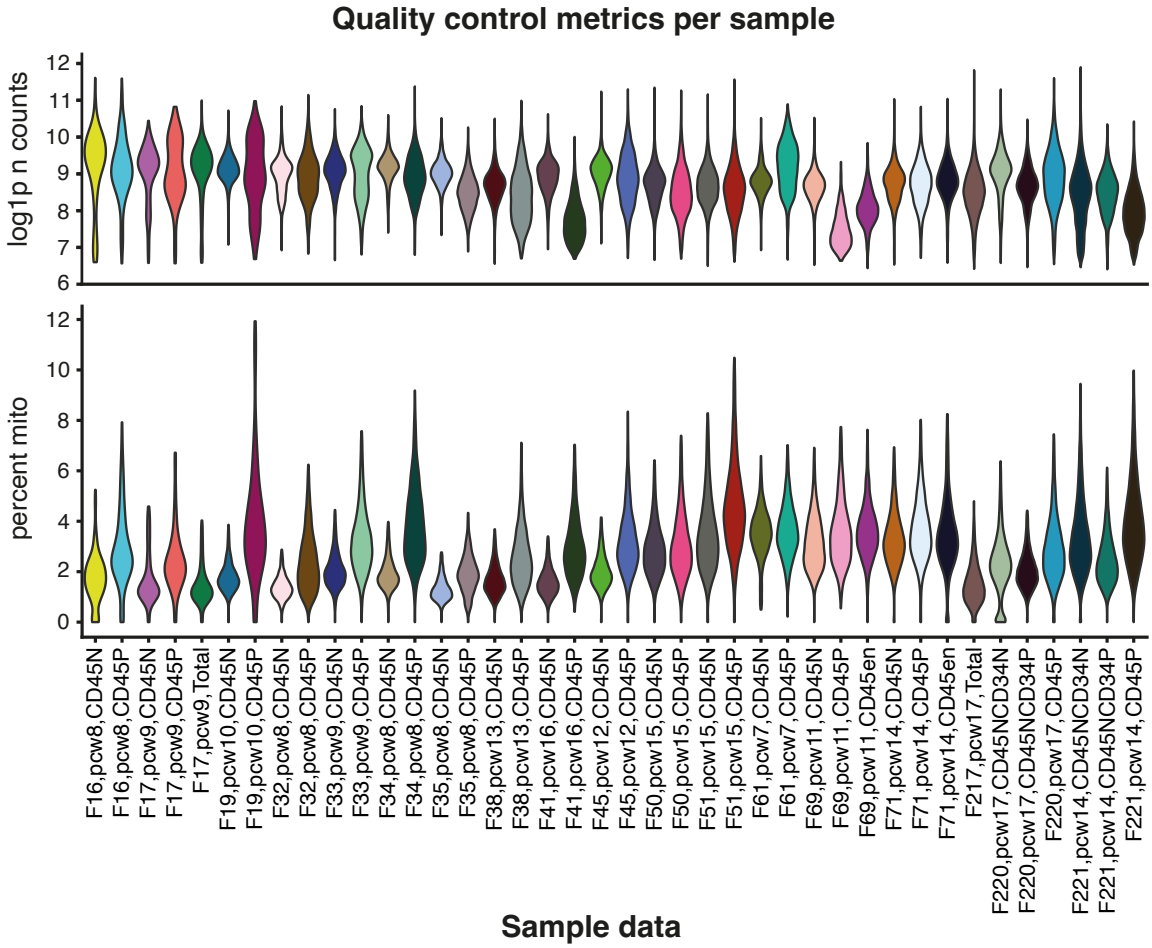

Figure 3.2. Quality control metrics.

Violin plots of the frequency distribution of cellular UMI counts (log-transformed) (top) and of the percentage of UMI counts corresponding to mitochondrial genes (bottom) in sequenced samples; for samples where multiple channels were loaded, data from the replicate channels were grouped for visualisation.

In addition, assessment for maternal contamination was carried using a previously described method[101,102] based on the Souporcell algorithm (section 2.4.1). A total of 118 cells of potential maternal origin were detected and were removed from the prenatal skin data. Overall, a total of 433,961 high quality cells were retained for downstream analysis.

Annotation of cell states in prenatal skin

The quality-controlled data was then subjected to batch correction and dimensionality reduction to generate clusters of similar cell identities for annotations (section 2.4.1). Clusters were visualised and manually annotated at two levels (section 2.4.1): (i) low resolution for broad cell type labels (Figure 3.3) and (ii) higher resolution for more granular, refined cell state annotations within each broad cell grouping.

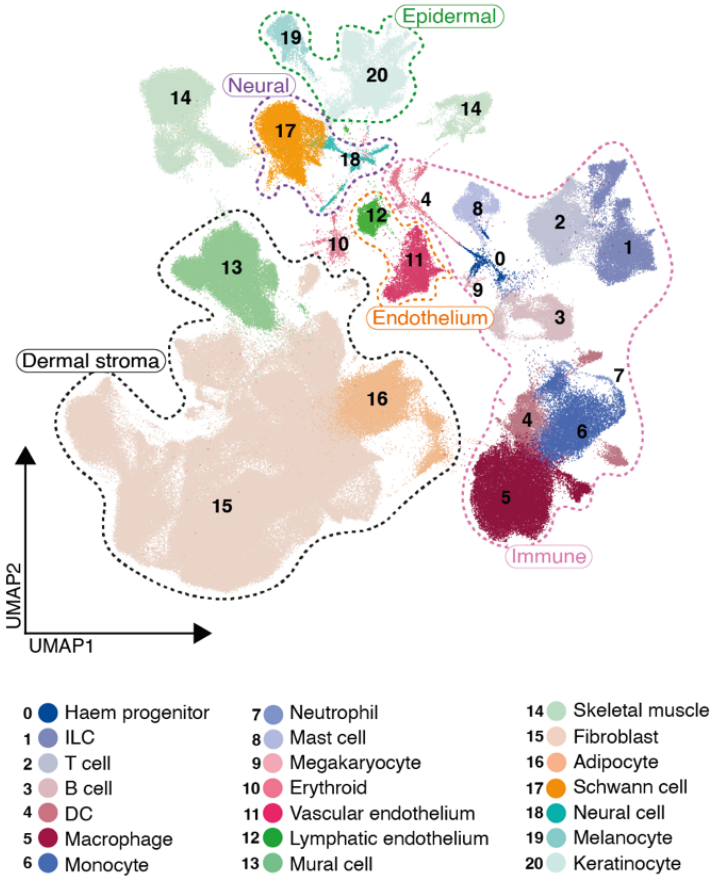

Figure 3.3. Broad cell clusters in prenatal skin.

UMAP visualisation of the prenatal skin scRNA-seq data (7-17 PCW, n=18, k=433,961); clusters are coloured and numbered by broad cell type annotations. DC: dendritic cell; Haem progenitor: hematopoietic progenitor cell, ILC: innate lymphoid cell.

Broad cell type annotations

Broad cell labels were assigned for each of the 21 broad cell clusters based on expression of established marker genes (Figure 3.4, Appendix E). Keratinocytes were denoted by expression of *TP63*, a key regulator in development of stratified epithelia,[228] its effector *PERP* which promotes cellular adhesion for epithelial integrity,[228] as well as several keratin genes (*KRT17*, *KRT5*, *KRT14*) (Appendix E). Melanocytes differentially expressed *MLANA* and *PMEL* which are active in the formation of melanosomes.[229,230] Neuronal cells upregulated genes which are predominantly enriched in neurons and are implicated in neural induction (*NNAT*)[231] and synaptic activity (*UCHL1*)[232]while pan-Schwann cell markers (*S100B* and *ERBB3*)[233] designated this particular cluster.

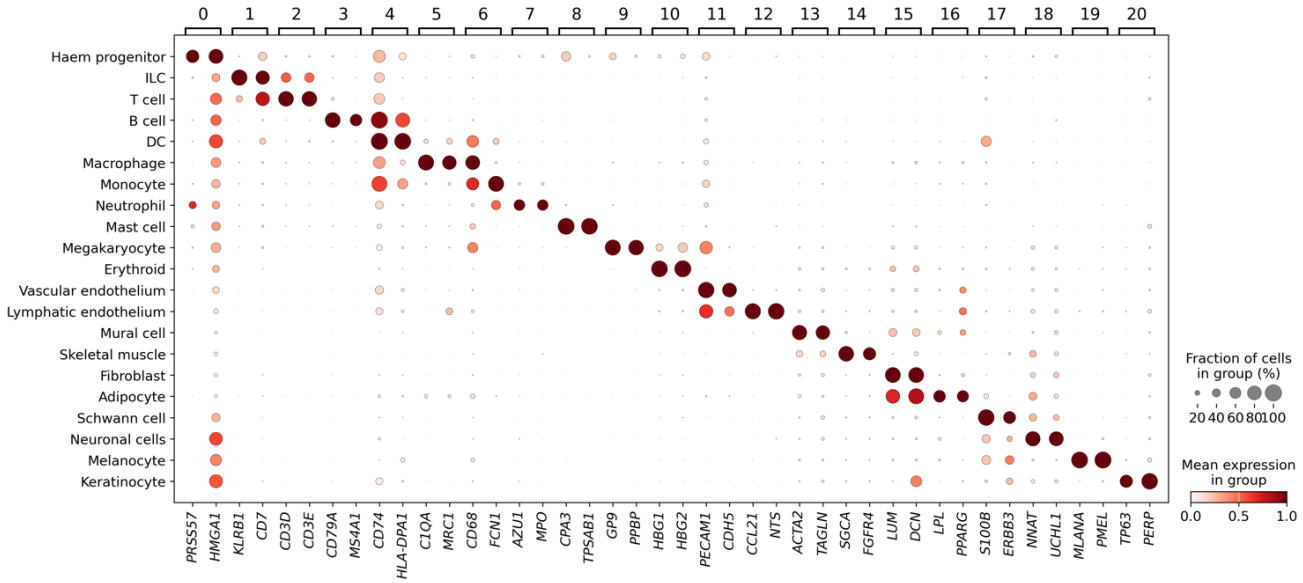

Figure 3.4. Annotation of broad cell types by differential gene expression.

Dot plot of selected genes differentially expressed by broad cell categories in prenatal skin; for a given gene, dot colour indicates normalised variance-scaled mean expression and dot size indicates the percentage of expressing cells in each category. DC: dendritic cell; Haem progenitor: hematopoietic progenitor cell, ILC: innate lymphoid cell.

Fibroblasts expressed several collagen genes (*COL1A1*, *COL1A2*, *COL3A1*) (Appendix E) alongside the proteoglycans *LUM* and *DCN*, which regulate assembly of collagen fibrils[234] (Figure 3.4). These proteoglycans were also present in adipocytes which further upregulated the adipogenesis modulator *PPARG* [235] and the enzyme *LPL* which facilitates lipid degradation and fatty acid uptake by adipocytes.[236] *SGCA*, which constitutes part of the protein complex that mechanically stabilises muscle fibres[237] and *FGFR4*, a transcriptional regulator of myogenesis and skeletal muscle differentiation,[238] were increased in the skeletal muscle cluster. Canonical markers of smooth muscle cells (*TAGLN* and *ACTA2*)[239] were conversely highly expressed in mural cells; *TAGLN* is abundant in smooth muscle cells and is involved in their differentiation[240] while *ACTA2* is commonly present in vascular smooth muscle cells and enable vascular contractility.[241] Vascular endothelial cells were characterised by expression of known markers such as *PECAM1* and *CDH5* which have key roles in vascular biology including endothelial cell-cell adhesion and control of vascular permeability.[242,243] Lymphatic endothelial cells upregulated *NTS*, previously shown to be highly expressed in dermal lymphatics and to contribute to adipose thermogenesis,[244] and the chemokine *CCL21* secreted by lymphatic cells to mediate DC migration, entry and return to lymph nodes.[244,245]

Among the blood and immune cell clusters, haematopoietic progenitors were distinguished by expression of genes which are typically enriched in HSPCs (*PRSS57* and *HMGA1*),[246,247] ILCs by their signature cluster differentiation molecules (*KLRB1* (*CD161*) and *CD7*),[248,249] T cells by lineage-defining genes encoding the invariant CD3 subunits (*CD3D*, *CD3E*),[250] and B cells by their canonical markers (*CD79A*, *MS4A1*)[251] (Figure 3.4). Dendritic cells had increased expression of *CD74* which is implicated in assembly of MHCII complexes,[252] several of which were also highly expressed in DCs (for example, *HLA-DPA1*, *HLA-DRA*, *HLA-DRB1*) (Appendix E), while macrophages upregulated marker genes commonly found in tissue-resident macrophages (*C1QA*, *MRC1*)[253,254] (Figure 3.4). The mononuclear phagocyte glycoprotein *CD68* was expressed by both macrophages and monocytes,[255] with the latter also differentially expressing the monocyte marker *FCN1* which contributes to identification and elimination of microbes by binding pathogen-associated molecular patterns[256]. *MPO* and *AZU1*, encoding major components of neutrophilic granules, delineated the neutrophil cluster[257,258] and mast cells were highlighted by their specific proteases (*CPA3*, *TPSAB1*)[259,260] (Figure 3.4). Genes associated with the platelet lineage, including the platelet surface receptor *GP9* and the platelet-derived growth factor *PPBP,*[261,262] identified

megakaryocytes while erythroid cells were annotated based on expression of foetal globin genes (*HBG1*, *HBG2*)[263] (Figure 3.4).

Refined cell state annotations

Subclustering revealed a total of 86 Leiden clusters in prenatal skin at high resolution (section 2.4.1). These were annotated by assessing the expression of distinctive DEGs in each cluster and cross-referencing with markers reported in the literature. In the following sections, I describe the cell states identified and some of the signature genes used to label them, focusing on cell identities within the major broad populations - epithelial, stromal, endothelial and immune lymphoid and myeloid. A list of the top 25 DEGs for every cell state identified in the prenatal skin is also provided in Appendices F1-F5.

Epithelial cells

The epithelial compartment comprised 12 distinct cell states. This included cells of the periderm, interfollicular epidermal (IFE) cells (immature basal, immature suprabasal, *POSTN*$^{+}$ basal, *DPYSL2*$^{+}$ basal, suprabasal IFE cells) and specialised epithelial cells of the hair follicle: placode, matrix, IRS, cuticle/cortex, CL and ORS.

The periderm differentiates from the ectoderm early in gestation to form a protective layer over the underlying nascent epidermis, interfacing with the surrounding amniotic fluid as well as preventing epithelial adhesion formation.[45,264] In line with this, the periderm cluster had the highest expression of *KRT8,* which is known to be expressed in human periderm,[265,266] and *KRT18 and KRT19* (Figure 3.5, Appendix F1) which are usually found in the simple epithelia of developing embryos.[267,268] Interestingly, expression of *KRT4*, which is commonly present in suprabasal layers of the oral mucosa,[269] was also increased (Figure 3.5). *CLIC3*, which encodes an ion channel implicated in transepithelial chloride movement and regulation of cell growth,[270,271] and *MUC16* which forms a lubricating barrier to prevent membrane adhesions,[272] were also differentially expressed (Figure 3.5, Appendix F1) in keeping with the protective functions of the periderm.[45,264]

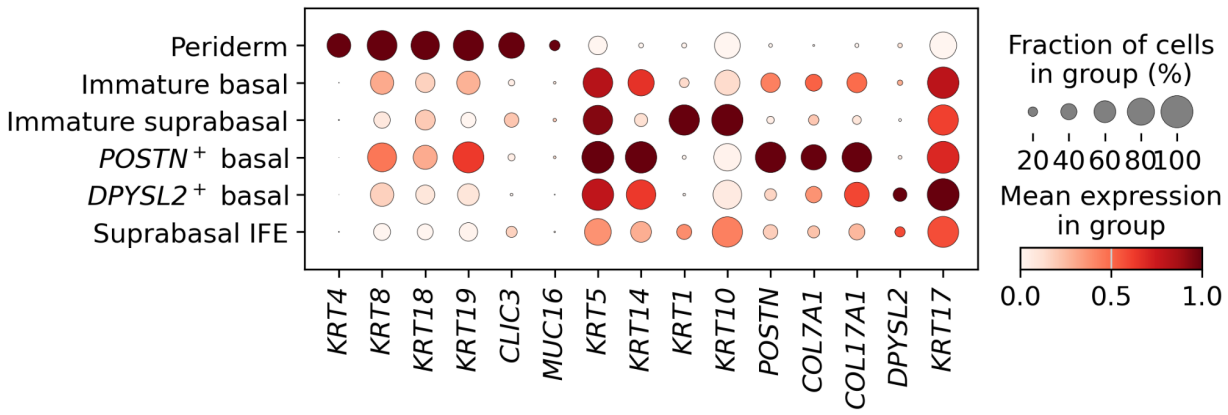

Figure 3.5. Annotation of epidermal cells by differential gene expression.

Dot plot of selected marker genes differentially expressed by epidermal cell states in prenatal skin; for a given gene, dot colour indicates normalised variance-scaled mean expression and dot size indicates the percentage of expressing cells in each category. IFE: interfollicular epidermis.

The periderm made up the majority of epithelial cells identified in first trimester prenatal skin, alongside two 'immature' cell states which proportionally decreased after 12 PCW (Figure 3.6), during the transition from embryonic to foetal skin. One of the immature cell states expressed *KRT1* and *KRT10* which characterise suprabasal cells of cornifying stratified epithelia whilst the other expressed the basal marker *KRT5*[269] (Figure 3.5). These were termed 'immature suprabasal' and 'immature basal' respectively.

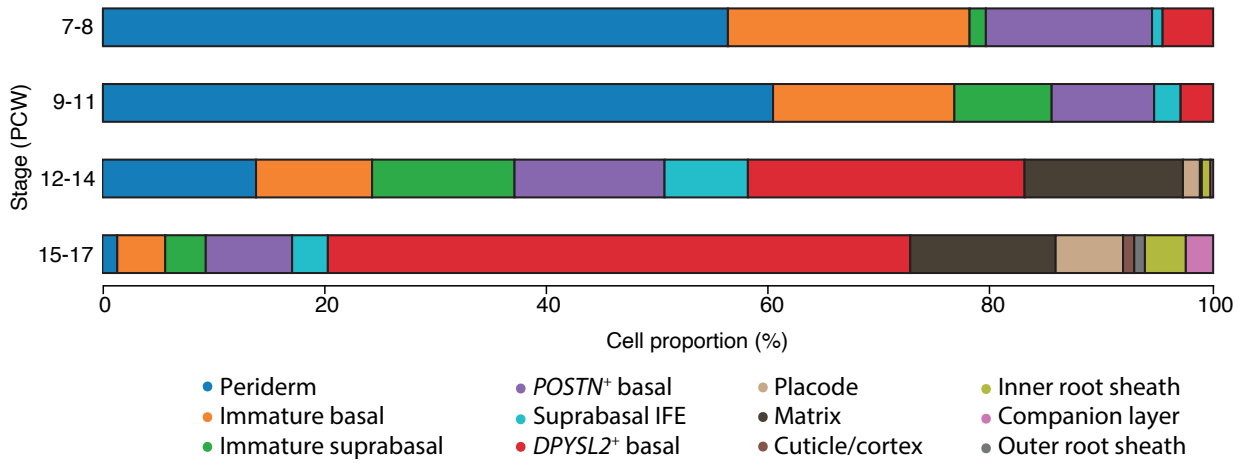

Figure 3.6. Frequency of epithelial cell states.

Bar plot of the average proportions of epithelial cell states in prenatal skin by developmental stage; gestational ages (PCW) are grouped into four stages and bar colours represent the different cell states. IFE: interfollicular epidermis.

Based on the expression pattern of the above keratins, two further basal (*POSTN*$^{+}$, *DPYSL2*$^{+}$) and one suprabasal (suprabasal IFE) populations that were present throughout the first and second trimesters were annotated (Figures 3.5 and 3.6). *POSTN*$^{+}$ basal cells additionally expressed the primary basal keratin *KRT14,*[267,268] *COL7A1* and *COL17* which mediate attachment of basal keratinocytes to underlying basement membrane,[273] and *POSTN* which promotes epithelial cell adhesion and migration[274] (Figures 3.5). A similar gene profile has been described in a small population of basal stem cells in newborn skin.[275] Accordingly, *POSTN*$^{+}$ basal cells were consistently found throughout gestation in relatively low proportion. Conversely, *DPYSL2*$^{+}$ basal cells significantly expanded after 12 PCW. This cluster differentially expressed the secondary basal keratin *KRT15* as well as *KRT17* which is involved in wound healing and skin appendage development,[276] suggesting this population may play a role in subsequent hair follicle formation (Figures 3.5).

Hair follicle epithelial cells were observed from 14 PCW, including cells from the placode and differentiated inner and outer layers (section 1.1.2). These were annotated using their DEGs and literature-derived markers, including genes from mouse hair follicles which have been better profiled at transcriptional level compared to human skin. Placode cells were characterised by upregulation of *SHH*, *WNT10B* and the WNT inhibitory factor *WIF1*, and matrix cells by expression of the transcriptional regulators *MSX2* and *LHX2*, mirroring markers of murine hair placode and matrix[58,277] (Figure 3.7). The IRS and cuticle/cortex both expressed *KRT25* and *KRT28*, with differential expressions of *KRT71* and *KRT35/KRT85* further distinguishing between the IRS and cuticle/cortex respectively as previously reported[268,278] (Figure 3.7). Keratins 6 and 17 are known to be expressed in the CL and ORS[27,268,279] and were used to identify these clusters with additional expressions of *KRT79* and *APOE* also defining ORS cells as described in the outer layers of murine hair follicles[60] (Figure 3.7, Appendix F1).

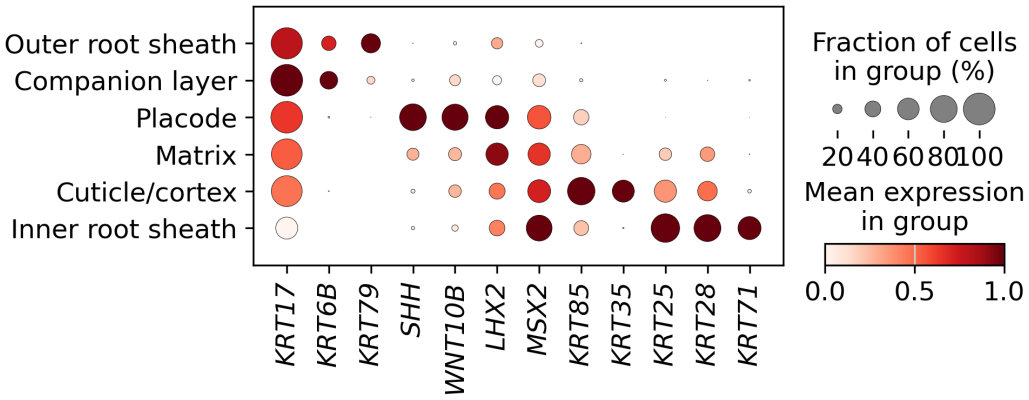

Figure 3.7. Annotation of hair follicle epithelial cells by differential gene expression. Dot plot of selected marker genes differentially expressed by hair follicle epithelial cell states in prenatal skin; for a given gene, dot colour indicates normalised variance-scaled mean expression and dot size indicates the percentage of expressing cells in each category.

Stromal cells

Prenatal skin stromal cells comprised fibroblasts, adipocytes, mural, muscle and neural cells (Figures 3.8 and 3.9). The fibroblast population consisted of dermal fibroblasts, myofibroblasts and the hair follicle mesenchymal cells. Four distinct subsets of dermal fibroblasts were identified and labelled based on their expression of distinctive DEGs: *FRZB*, *HOXC5*, *WNT2* and *PEAR1* (Figure 3.10). Compared to *WNT2*$^{+}$ and *PEAR1*$^{+}$ fibroblasts that increased as gestation progressed, *FRZB*$^{+}$ and *HOXC5*$^{+}$ fibroblasts were abundant mainly before 11 PCW and were therefore denoted as 'early' fibroblasts (Figure 3.9). *FRZB*$^{+}$ early fibroblasts were primarily found in one sample from the earliest gestation stage (7 PCW, CS18) and likely represent an age-specific effect in prenatal skin as *FRZB*-expressing fibroblasts have been described in other developing organs such as yolk sac, spleen, and gut.[101] Myofibroblasts clustered with other fibroblast subsets (Figure 3.8) and upregulated genes implicated in induction of actin polymerisation (*NRK*)[280] and myofibroblast differentiation, such as *ACTA1* and *IGF2*[281,282] (Figure 3.10, Appendix F2).

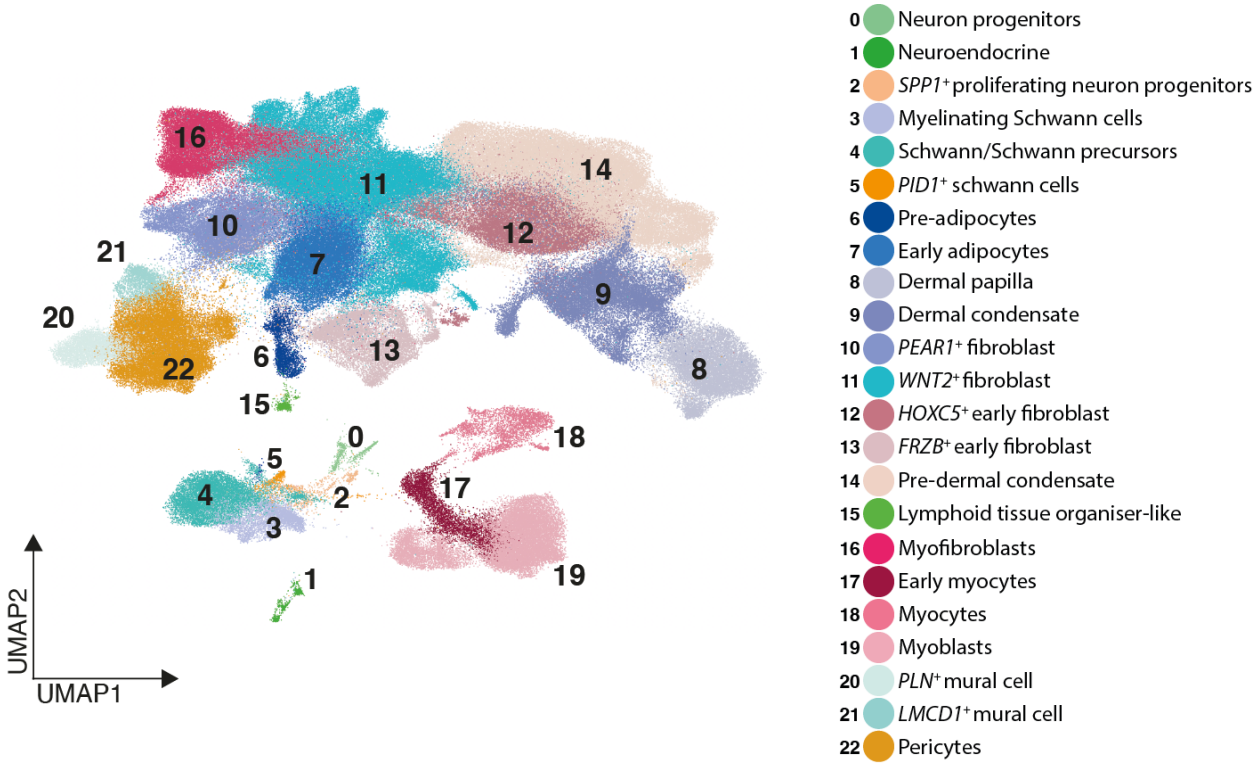

Figure 3.8. Stromal cell states in prenatal skin.

UMAP visualisation of the stromal cell clusters in prenatal skin scRNA-seq data; clusters are coloured and numbered by refined cell state annotations.

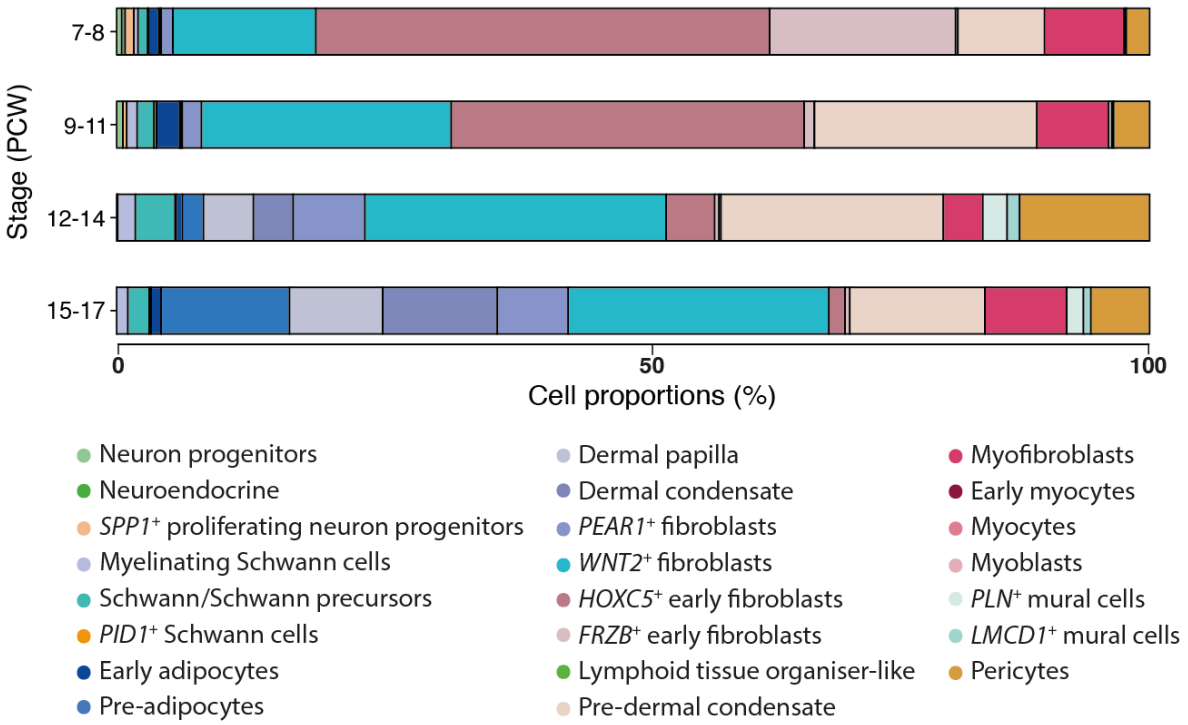

Figure 3.9. Frequency of stromal cell states.

Bar plot of the average proportions of stromal cell states in prenatal skin by developmental stage; gestational ages (PCW) are grouped into four stages and bar colours represent the different cell states.

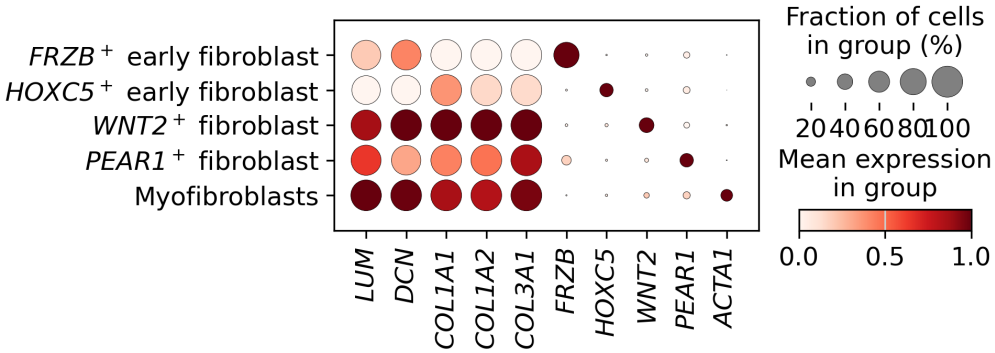

Figure 3.10. Annotation of fibroblasts by differential gene expression.

Dot plot of selected marker genes differentially expressed by fibroblast and myofibroblast cell states in prenatal skin; for a given gene, dot colour indicates normalised variance-scaled mean expression and dot size indicates the percentage of expressing cells in each category.

Three distinct clusters representing the mesenchymal cells of the developing hair follicle were also captured. These cells downregulated fibroblast cluster markers (*WNT2*, *HOXC5*, *PEAR1*) and myofibroblast marker (*ACTA1*), and upregulated Dc genes (*SOX2, FOXD1*). Hair follicle mesenchymal cell states typically include the Dc and Dp[28] (section 1.1.2). The pre-dermal condensate (pre-Dc) is a transitional fibroblast state, only recently described in mouse skin, which aggregates to form the Dc that abuts the epithelial hair placode during embryonic murine hair follicle formation and becomes eventually encapsulated as the Dp at the base of the hair follicle during downgrowth.[59] Using orthologous markers from mouse skin,[59] *PDGFRA*$^{+}$*FOXD1*$^{+}$*SOX2*^{low} cells were annotated as pre-Dc in prenatal skin, followed by Dc and Dp respectively with increasing levels of *FOXD1* and *SOX2* expression (Figure 3.11). Typical expression of *RSPO3* was also noted in the prenatal skin Dp (Appendix F2). Notably, the pre-Dc has not previously been reported in human skin and this represents the first characterisation of the precursors of the Dc during human hair follicle neogenesis.

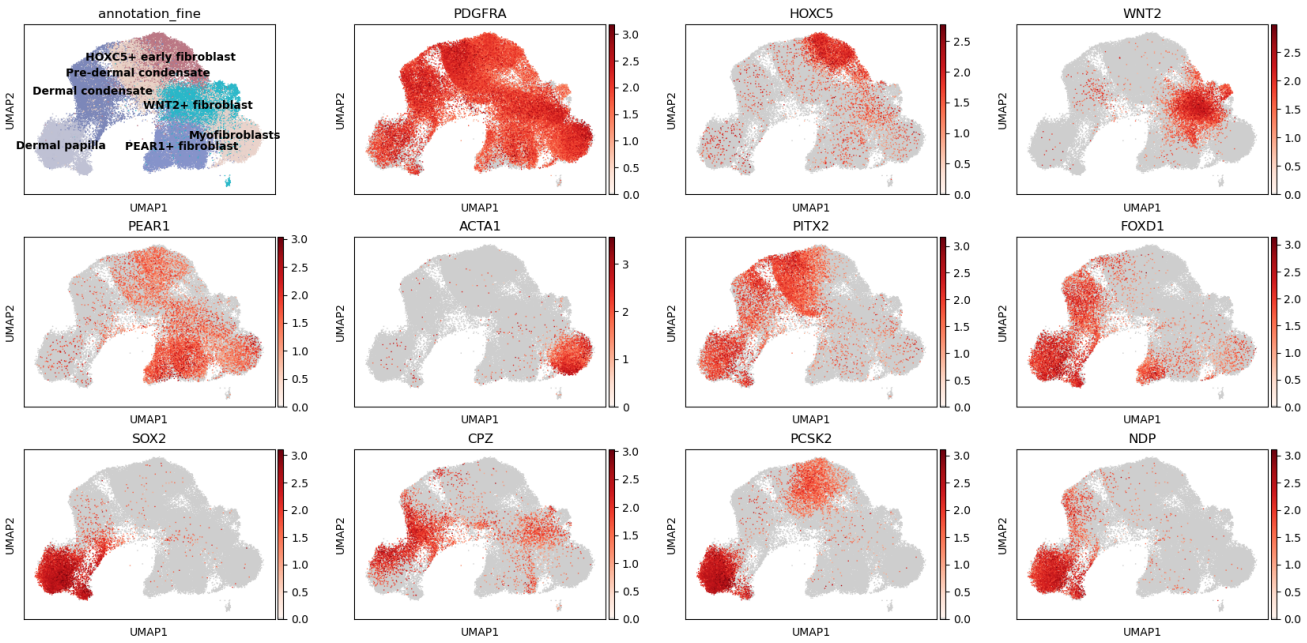

Figure 3.11. Annotation of hair follicle mesenchymal cells.

UMAP visualisation of hair follicle mesenchymal cells and dermal fibroblasts in prenatal skin, coloured by expression (log-transformed) of fibroblast DEGs and orthologous markers from mouse skin.

Two subsets of adipocytic cells, pre-adipocytes and early adipocytes, were defined per published markers for adipocyte progenitors, pre-adipocytes, early and mature adipocytes.[283–286] Both populations expressed to varying degrees genes which are upregulated in adipocyte progenitors (*CD34*, *PDGFRA*, *PDGFRB*) and in committed pre-adipocytes and early adipogenesis (*PPARG*, *ATXN1*, *TBX15*, *ZNF423*, *CEBPA*).[285,286] They also expressed *FABP4*, usually found in mature adipocytes, but lacked other mature adipocyte-specific genes such as *ADIPOQ* and *SAA1* and the stem cell marker *CD24*.[285,286] Pre-adipocytes were annotated based on higher expression of adipocyte progenitors/pre-adipocytes markers and lower expression of early adipogenesis genes compared to early adipocytes.

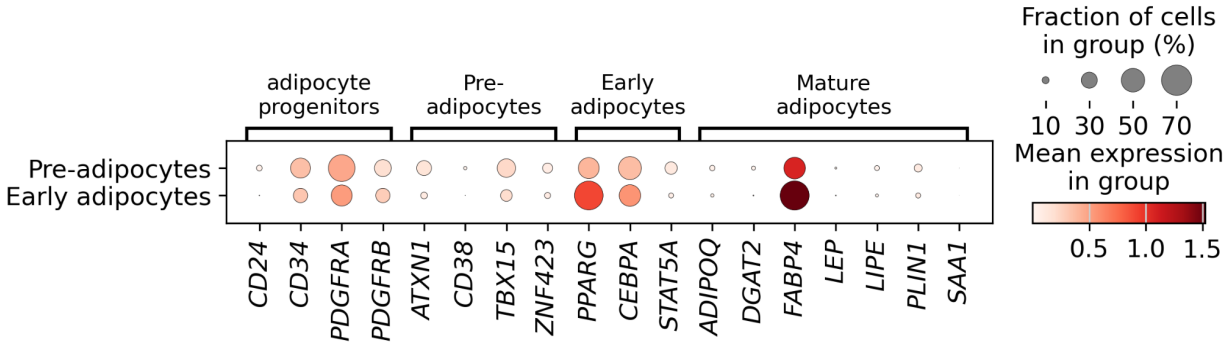

Figure 3.12. Annotation of adipocytic cells.

Dot plot of marker gene expression by adipocytic cell states in prenatal skin; for a given gene, dot colour indicates normalised mean expression and dot size indicates the percentage of expressing cells in each category.

Mural cells, which cover the abluminal side of blood vessels, can be divided broadly into pericytes and vascular smooth muscle cells.[239] These cells universally expressed transgelin (*TAGLN*) and alpha smooth muscle actin (*ACTA2*) (Figure 3.4), with lower levels of the latter present in pericytes (Figure 3.13) as previously reported.[239] Pericytes were also characterised by expression of genes encoding adenosine triphosphate-regulated potassium channel (*KCNJ8* and *ABCC9*) with known functions in pericyte physiology[287,288] (Figure 3.13). Two further subsets of mural cells were identified and named based on their differential expression of reported vascular smooth muscle cell genes: *LMCD1* and *PLN* [289,290] (Figure 3.13).

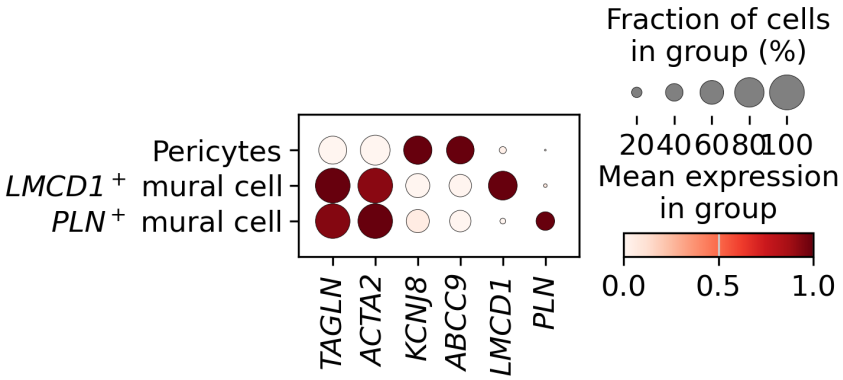

Figure 3.13. Annotation of mural cells by differential gene expression.

Dot plot of selected marker genes differentially expressed by mural cell states in prenatal skin; for a given gene, dot colour indicates normalised variance-scaled mean expression and dot size indicates the percentage of expressing cells in each category.

Within the skeletal muscle cluster, cell states at different stages of differentiation were observed with constitutive expression of *SGCA* (Figure 3.4, Appendix E). Myoblasts, representing the earliest progenitor state, also upregulated *MYF5* and *PAX7* which are involved in muscle stem cell fate commitment and proliferation[291,292] (Figure 3.14). The transcriptional activator *MYOD1*, regulating muscle cell differentiation,[293] was increased in early myocytes (Figure 3.14). Finally, markers of differentiated muscle cells were expressed by myocytes, including *ACTA1*, *MYLPF* and *MYL1* which function in skeletal muscle maintenance and contraction[294,295] (Figure 3.14). Notably, several of these genes differentially regulated across gestation are associated with musculoskeletal diseases such as limb-girdle muscular dystrophy and congenital myopathies.[294,296]

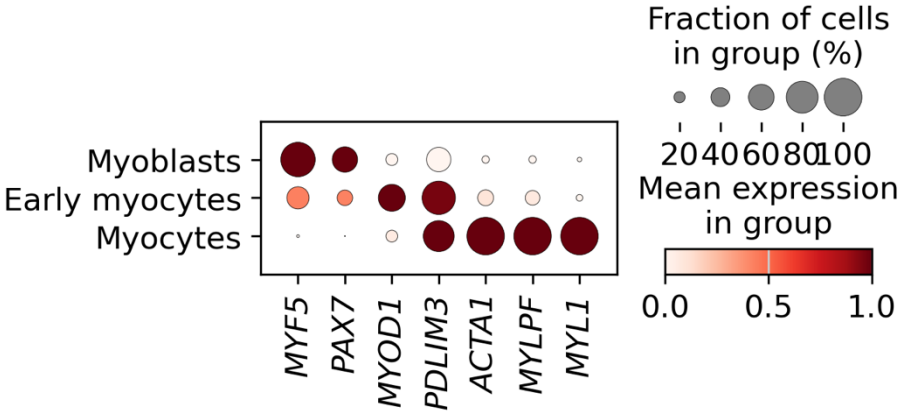

Figure 3.14. Annotation of skeletal muscle cells by differential gene expression.
Dot plot of selected marker genes differentially expressed by skeletal muscle cell states in prenatal skin; for a given gene, dot colour indicates normalised variance-scaled mean expression and dot size indicates the percentage of expressing cells in each category.

Neuronal and Schwann cells were broadly classified based on marker gene expression as described earlier (Figure 3.4). *ELAVL4* specifically promotes differentiation of neuronal progenitor cells which suggested that the neuronal cluster consisted mainly of neuron progenitors during development[297] (Figure 3.15). These cells also expressed *TUBB2* and *TUBB3* which guide axon formation during neurogenesis[298] (Figure 3.15). One of the neuron progenitor clusters differentially upregulated markers of cell cycling and proliferation (for example, *MCM7* and *PAX3*)[299,300] as well as *SPP1*, which has a role in modulation of neuroinflammation,[301] and was therefore labelled as *SPP1*$^{+}$ proliferating neuron progenitors (Figure 3.15). A distinct cluster, expressing genes of the neuroendocrine signalling pathway, including *PCSK1N* and *NELL2*,[302,303] was also identified and termed 'neuroendocrine' cells (Figure 3.15). Among the Schwann cell subclusters, myelinating Schwann cells had the highest expression of myelin proteins *MPZ* and *PLP1* (Figure 3.15). Genes involved in early embryonic development (*OLFML3*)[304] and Schwann cell migration (*NRP1*)[305] were upregulated by Schwann precursors (Figure 3.15). *PID1*$^{+}$ Schwann population was specified by additional distinct gene profiles including *PID1*, implicated in neural processes and neurodegeneration,[306] and *KCNN2* which encodes a voltage-gated potassium channel which facilitates nervous system signal conduction[307] (Figure 3.15).

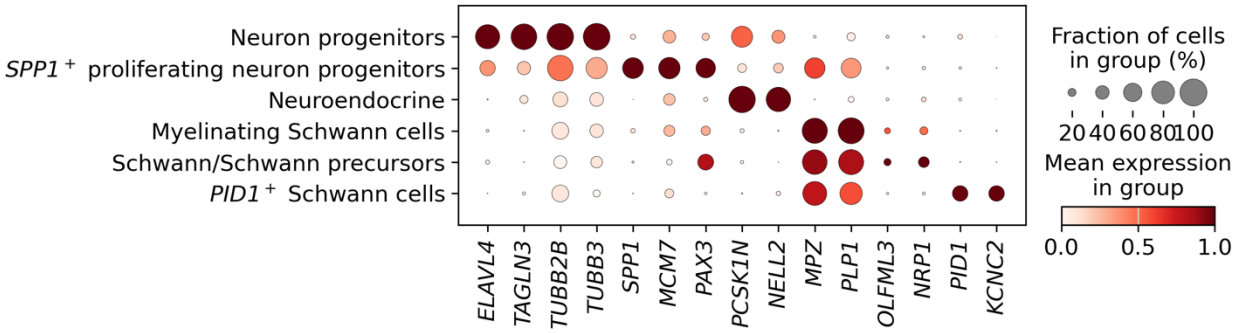

Figure 3.15. Annotation of neural cells by differential gene expression.

Dot plot of selected marker genes differentially expressed by neuronal and Schwann cell states in prenatal skin; for a given gene, dot colour indicates normalised variance-scaled mean expression and dot size indicates the percentage of expressing cells in each category.

Endothelial cells

Both arteriolar and venular cell types were captured within the vascular endothelial cluster. Among the arteriolar cell types, arterioles differentially expressed *GJA4* and *NOTCH4* that indicate arterial fate commitment and differentiation[207,308] (Figure 3.16, Appendix F3). Known markers of capillary arterioles (*RGCC*)[207] and capillaries (*CD36*)[206] were noted in both capillary arterioles and capillaries clusters in prenatal skin (Figure 3.16). Capillary arterioles, however, additionally upregulated genes that characterise tip cells (*APLNR*, *ESM1*) and promote angiogenesis (*VWA1*) (Figure 3.16), suggesting that these cells may be actively involved in sprouting of new blood vessels.[309]

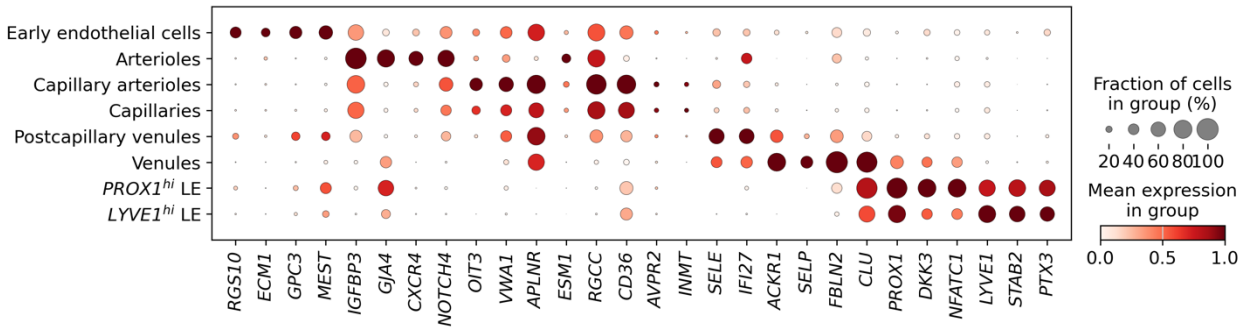

Figure 3.16. Annotation of endothelial cells by differential gene expression.

Dot plot of selected marker genes differentially expressed by vascular and lymphatic endothelial cell states in prenatal skin; for a given gene, dot colour indicates normalised variance-scaled mean expression and dot size indicates the percentage of expressing cells in each category. LE: lymphatic endothelium.

Venular cell types were also annotated using published signature genes for post-capillary venules and venules, including *SELE*, a cell adhesion molecule found in post-capillary venules that allows interaction with neutrophils,[207] and *FBLN2* which is typically increased in the elastic wall of larger venular cells[205] (Figure 3.16). In addition, a separate vascular endothelial cluster which was proportionally increased in early gestation was identified, with high expression of genes involved in cell proliferation and early vascular development (*GPC3*, *ECM1*),[310,311] and was labelled as early endothelial cells (Figures 3.16 and 3.17).

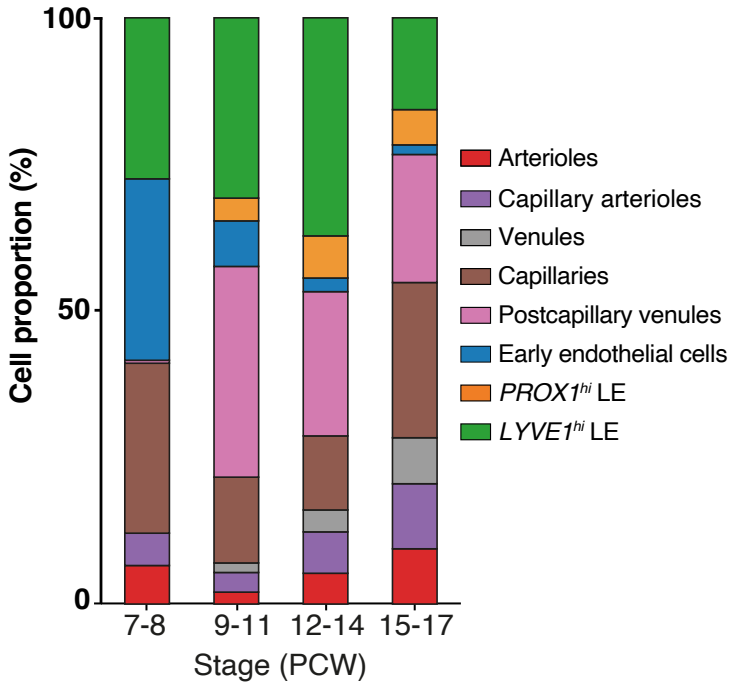

Figure 3.17. Frequency of endothelial cell states.

Bar plot of the average proportions of endothelial cell states in prenatal skin by developmental stage; gestational ages (PCW) are grouped into four stages and bar colours represent the different cell states.

Two subsets of cells from the lymphatic endothelium (LE), expressing *PROX1* and *LYVE1* to different degrees were also observed: *PROX1^{hi}* LE and *LYVE1^{hi}* LE (Figure 3.16). The transcription factor PROX1 is a specific marker for LE cells in prenatal and adult human tissues[312] and has been shown to drive lymphatic induction, differentiation and growth during lymphangiogenesis in mice.[313,314] The hyaluronan receptor LYVE1, present on the luminal surface of lymphatic vessels, is usually upregulated following fate determination by PROX1.[315,316] *PROX1^{hi}* LE, which also differentially expressed a transcriptional regulator of lymphatic patterning (*NFATC1*),[317] and *LYVE1^{hi}* LE, with higher expression of the additional hyaluronan receptor *STAB2* (Figure 3.16), may therefore respectively represent early and late populations of lymphatic endothelial cells in prenatal skin.

Myeloid cells

Myeloid cells captured in prenatal skin comprised DCs, monocytes, neutrophils and macrophages (Figure 3.18). Subclusters of DCs were annotated based on established marker genes for DC subsets. Conventional DC1 cluster was characterised by expression of *CLEC9A*, encoding a C-type lectin receptor, and the transcription factor *IRF8* while DC2 cells expressed *CLEC10A* and the antigen-presenting molecule *CD1C*[70,318] (Figure 3.19, Appendix F4). Inflammatory DC, which have been reported to lack unique surface markers and share signature genes with DC2,[70] differentially expressed genes linked to DC maturation, activation and survival (*LAMP3*, *BIRC3*)[319,320] (Figure 3.19). Plasmacytoid DCs were annotated based on upregulation of genes associated with type I interferons induction (*IRF7, IRF8*) and the master regulator of pDC development *TCF4*[70,321] (Figure 3.19). As previously reported, the ASDC cluster shared several genes with pDCs but also uniquely expressed receptor tyrosine kinase *AXL* and cellular adhesion molecule *SIGLEC6*[321] (Figure 3.19). LCs were identified by the specific expression of the Langerin (*CD207*), which induces formation of Birbeck granules,[322] and *CD1A* which functions in presentation of lipid antigens[323] (Figure 3.19).

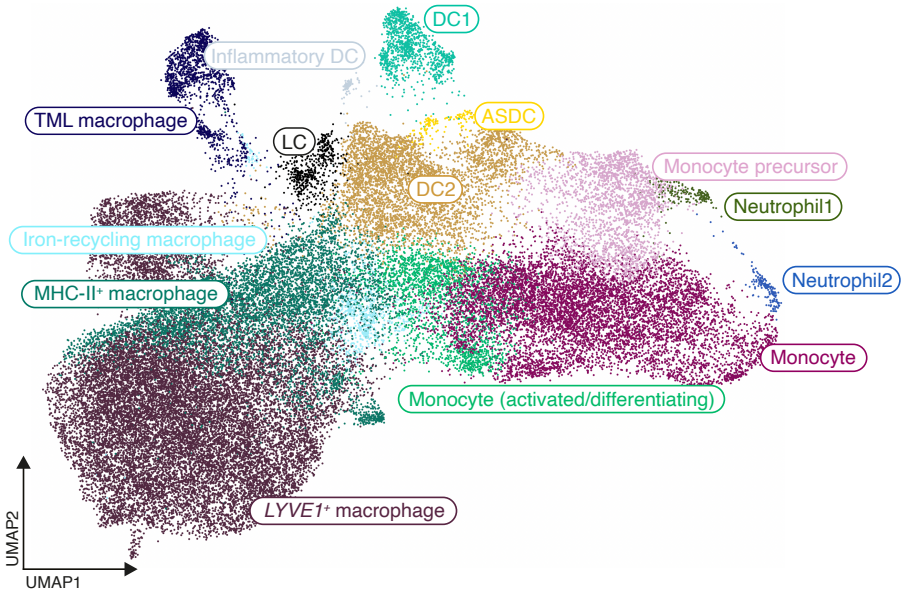

Figure 3.18. Myeloid cell clusters in prenatal skin.

UMAP visualisation of the prenatal skin myeloid cells; clusters are coloured and numbered by refined cell state annotations. ASDC: AXL^{+}SIGLEC6^{+} dendritic cell; DC: dendritic cell; LC: Langerhans cell; TML macrophage: *TREM2*$^{+}$ microglia-like macrophage.

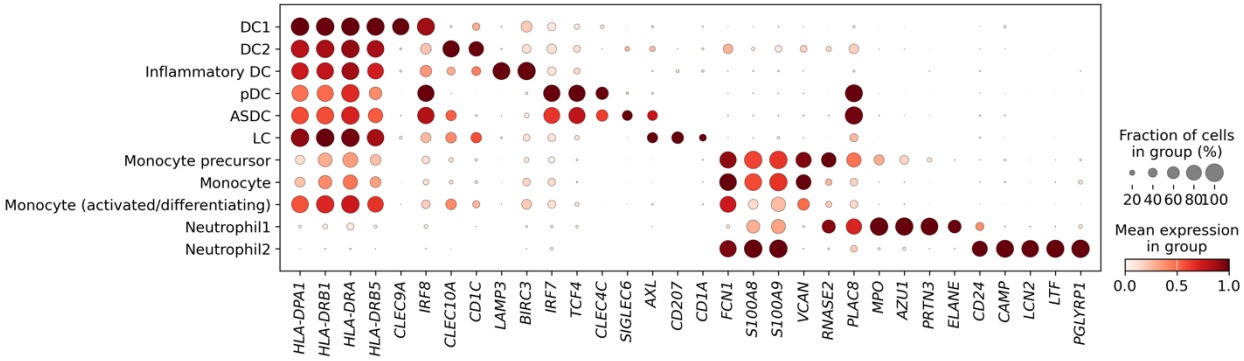

Figure 3.19. Annotation of myeloid cells by differential gene expression.

Dot plot of selected marker genes differentially expressed by myeloid cell states (excluding macrophages) in prenatal skin; for a given gene, dot colour indicates normalised variance-scaled mean expression and dot size indicates the percentage of expressing cells in each category. ASDC: AXL^{+}SIGLEC6^{+} dendritic cell; DC: dendritic cell; LC: Langerhans cell; pDC: plasmacytoid dendritic cell.

Three monocyte subclusters were delineated, all displaying increased expression of typical monocyte markers including *FCN1*[256] (Figures 3.4 and 3.19) as well as *VCAN* and S100 genes (*S100A8*, *S100A9*) which promote monocyte migration[324] (Figure 3.19, Appendix F4). The activated/differentiating subcluster additionally upregulated expression of several MHCII genes (for example, *HLA-DRB1*, *HLA-DPA1*, *HLA-DRB5*) (Figure 3.19, Appendix F4) which, in monocytes, apart from antigen presentation, have also been associated with lysosome-mediated degradation.[325] The precursor subcluster differentially expressed *RNASE2*, encoding an alarmin usually elevated in circulating monocytes prior to tissue infiltration,[326] and *PLAC8* which is implicated in monocyte survival and proliferation[327] (Figure 3.19). Supporting the precursor state of these monocytes, *RNASE2* and *PLAC8* were also increased in neutrophils 1 which co-expressed neutrophil progenitor markers (Figure 3.19). Neutrophils 1 upregulated myeloperoxidase (*MPO*) which is stored in azurophilic granules whose primary components are encoded by neutrophil elastase (*ELANE*), azurocidin (*AZU1*), and proteinase 3 (*PRTN3*).[257,258] Transcription of the latter three genes are restricted to promyelocytes during granulopoiesis,[257] indicating that neutrophils 1 are in an earlier stage of differentiation compared to neutrophils 2. Accordingly, neutrophils 2 differentially expressed the mature granulocyte marker *CD24*, alongside more specific granule genes (*LTF*, *CAMP*, *LCN2, PGLYRP1*)[328,329] (Figure 3.19).

The macrophage clusters were annotated using marker genes from a recently published scRNA-seq cross-tissue study of the developing blood and immune system[101] which included part of the skin data presented in this project (Figure 3.20). *LYVE1*$^+$ macrophages constituted the largest cluster and highly expressed the hyaluronan receptor *LYVE1*, the coagulation factor *F13A1*, which regulate macrophage differentiation and phenotype acquisition,[330] and the adhesion molecule osteopontin (*SPP1*) which has been reported to foster macrophage chemotaxis and migration[331] (Figure 3.20). *LYVE1*-expressing macrophages have been observed to localise perivascularly in various murine tissues and to support blood vessel integrity and modulate collagen degradation by vascular smooth muscle cells.[332,333] Iron-recycling macrophages differentially expressed the iron transporter ferroportin (*SLC40A1*)[334] and *APOE* which promotes anti-inflammatory activity in macrophages[335] (Figure 3.20). MHCII$^+$ macrophages shared a gene expression profile with *LYVE1*$^+$ and iron-recycling macrophages but further upregulated MHCII genes (for example, *HLA-DRA*, *HLA-DRB1*) compared to *LYVE1*$^+$ macrophages and lacked the specific markers for iron-recycling macrophages such as *APOE* (Figure 3.20). *TREM2*$^+$ microglia-like (TML) macrophages expressed several microglia markers in addition to Triggering receptor expressed on myeloid cells 2

(*TREM2*), including the purinergic receptor *P2RY12*, the fractaline receptor *CX3CR1*, and the genes encoding transmembrane protein 119 (*TMEM119*) and the glycoprotein Olfactomedin-like 3 (*OLML3*)[336,337] (Figure 3.20). These microglia-associated transcripts have also been identified in embryonic brain microglia and microglia-like macrophages in other developing organs, such as yolk sac and gonads.[102,149,338]

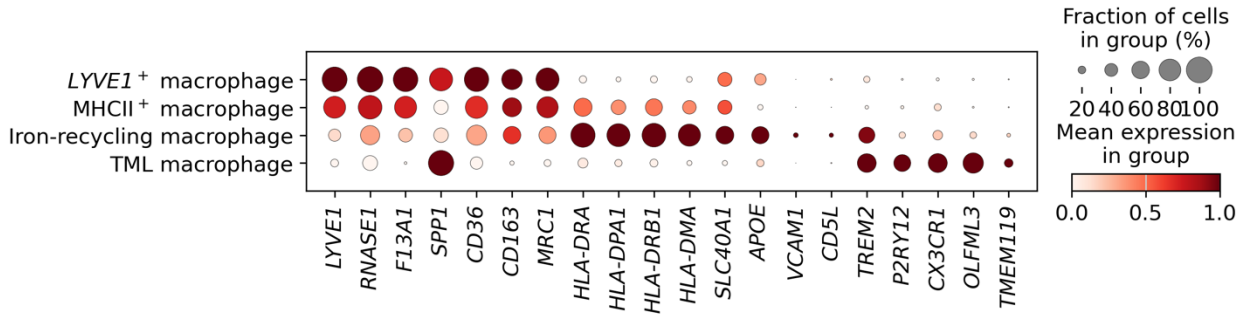

Figure 3.20. Annotation of macrophages.

Dot plot of marker gene expression by macrophage cell states in prenatal skin; for a given gene, dot colour indicates normalised mean expression and dot size indicates the percentage of expressing cells in each category.

Lymphoid cells

A diverse array of lymphoid cells was detected in prenatal skin, including common lymphoid progenitors, conventional and unconventional T cell subsets, ILCs, and B cells at different stages of maturation. Lymphoid progenitors were characterised by upregulation of *SPINK2*, a marker for HSPCs,[246,339] and *MEF2C* which commits cell fate in multipotent progenitors towards the lymphoid lineage by antagonising pro-myeloid differentiation[340] (also involved in early B-cell development[341]) (Figure 3.21). Conventional T cells were annotated based on expression of genes encoding lineage-defining CD3 chains (*CD3D*, *CD3E*, *CD3G*) (Appendix F5) in conjunction with markers for CD4 (*CD4*, *CD40LG*) and CD8 (*CD8A*, *CD8B*) T cells (Figure 3.21); both subsets also expressed high levels of naive T cell markers such as *SELL*, *TCF7* and *CCR7*.[342] Tregs differentially expressed the transcriptional factor *FOXP3*, which is crucial for the development of Tregs, and receptors involved in modulation of immune tolerance (*CTLA4*, *IL2RA*)[342,343] (Figure 3.21).

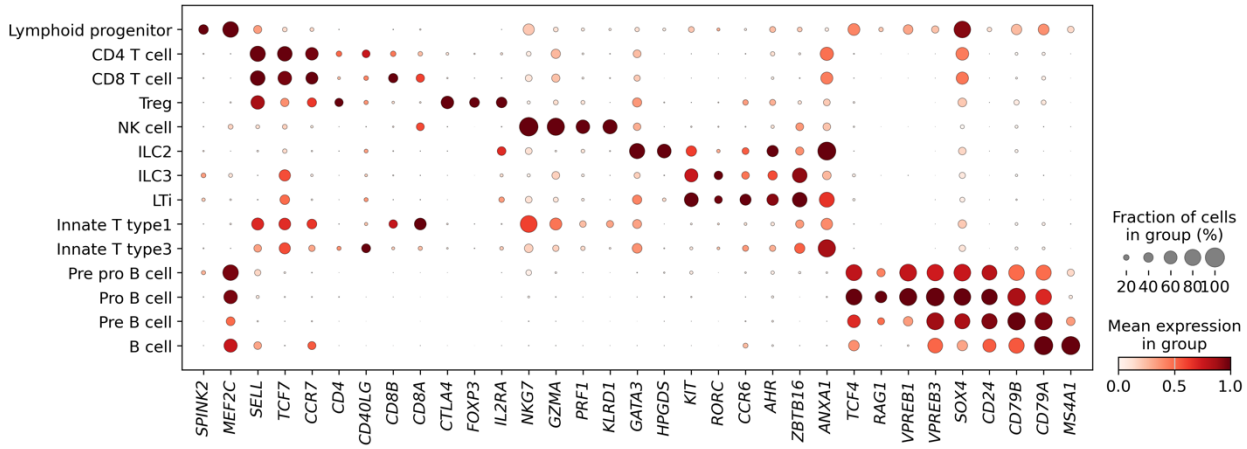

Figure 3.21. Annotation of lymphoid cells by differential gene expression.

Dot plot of selected marker genes differentially expressed by lymphoid cell states in prenatal skin; for a given gene, dot colour indicates normalised variance-scaled mean expression and dot size indicates the percentage of expressing cells in each category. ILC: innate lymphoid cell; LTi: lymphoid tissue inducer; NK cell: natural killer cell; Treg: regulatory T cell.

Among the ILCs, NK cells were denoted by the increased expression of molecules involved in meditating and regulating their cytotoxic functions including granule proteins (*NKG7*), killer cell lectin-like receptors (*KLRD1*), granzymes (*GZMA*), and perforin (*PRF1*), all of which are recognised NK cell signature genes[344] (Figure 3.21). Group 2 and 3 ILCs were identified based on transcription factors required for their differentiation: *GATA3* for ILC2, *RORC* for ILC3 and LTi, with *AHR* also elevated in LTi.[88,345] ILC2 cells additionally upregulated *HPGDS*, which functions in lipid and prostanoid metabolism and constitutes part of the core ILC2 transcriptome as previously published,[346] whereas ILC3 and LTi cells typically expressed the chemokine receptor *CCR6*, which is involved in skin homeostasis and mucosal immunity[345,347,348] (Figure 3.21). The transcriptional regulator *ZBTB16* was increased in all innate cells, including innate T type 1 and type 3 cells as previously reported for these unconventional T cells,[101] and was particularly high in those with a type 3 immune profile (ILC3, LTi and Innate T type 3 cells)[249] (Figure 3.21). Innate T type 1 and type 3 cells were further distinguished by co-expression of CD3 genes (Appendix F5) alongside *ZBTB16*, with the phospholipase inhibitor (*ANXA1*) higher in Innate T type 3 as previously shown in this T cell subset[101] (Figure 3.21).

The four B cell subsets expressed known B lineage markers to different degrees in keeping with their individual stage of differentiation.[92] *TCF4*, usually silenced following commitment to the B cell lineage after the pro-B cell stage,[349] was highly expressed in pre pro- and pro-B cells (Figure 3.21). Pro-B cells also differentially expressed *RAG1* which catalyses the recombination of immunoglobulin genes during B cell development[350] (Figure 3.21). Genes encoding the surrogate light chains (*VPREB1*, *VPREB3*), which form part of the pre-B cell receptor complex that marks transition into pre-B stage,[251,351] were increased in pro- and pre-B cells (Figure 3.21). These latter two stages also expressed *SOX4* and *CD24* which are involved in control of early B cell development and in regulation of pro- and pre-B cell survival.[352,353] *CD79A* and *CD79B*, forming key components of the mature B cell receptor and essential for its functional signalling, were upregulated in pre-B and B cells,[251] with B cells also differentially expressing the canonical marker *MS4A1*, which is typically absent in the earliest B-cell precursors and is implicated in B cell activation and proliferation[251,354] (Figure 3.21).

3.3.2 Differential abundance of cell states across gestation

Evaluation of the proportional changes of the various cell populations across gestation, as shown in Figures 3.6, 3.9 and 3.17, suggested that some cell states may be enriched at different timepoints during development. To assess for significant shifts in composition between early and late gestation, a recently developed computational package for single-cell data, called Milo,[185] was used. This performs differential abundance testing on neighbourhoods of cells across time, modelling gestational age (in PCW) as a continuous variable (section 2.4.1). This was first applied using the broad prenatal skin annotations to identify the overall pattern of how the different cell types and lineages temporally appear in the developing skin (Figure 3.21).

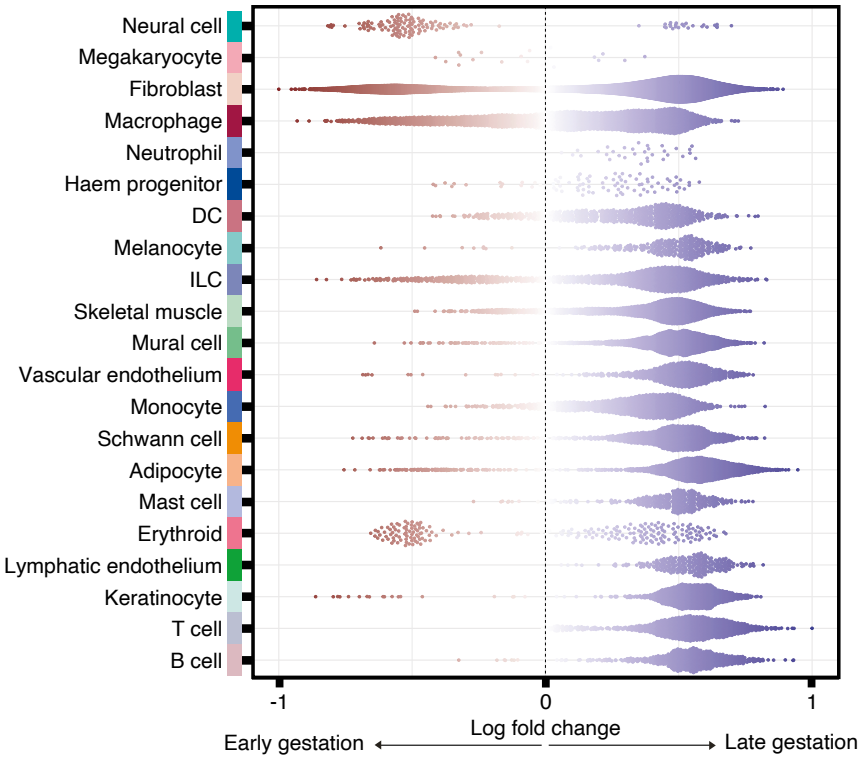

Figure 3.22. Differential abundance of broad cell types across gestation.
Beeswarm plot showing the distribution of the fold change (log-transformed) in abundance across gestation time in Milo-derived neighbourhoods of broad cell categories in prenatal skin. Red and blue colours represent neighbourhoods in early and late gestation respectively; the colour intensity indicates degree of significance in differential abundance. DC: dendritic cell; Haem progenitor: hematopoietic progenitor cell, ILC: innate lymphoid cell.

This showed that some lineages, such as neural and erythroid cells were notably enriched in early gestation (Figure 3.22). Neural cells in prenatal skin arise from the trunk neural crest which disperses around the time of the neural tube closure.[355,356] Erythroid cells, key for oxygen delivery in the developing embryo, are produced through the different waves of erythropoiesis first from the yolk sac and subsequently by the liver and bone marrow.[357,358] The relative abundance of these cell groups in early gestation is in keeping with their derivation from early developmental structures. Enrichment of additional cell types was observed as gestation progressed and the skin architecture matured, including keratinocytes, adipocytes, endothelial, mural, and muscle cells. Of the immune populations, cells conferring innate immunity, such as macrophages and ILCs, were observed from early gestation whilst B and T cells only emerged later once the thymus, bone marrow and spleen formed from around 11 PCW. Other bone-marrow derived haematopoietic cells, including granulocytes and DCs were accordingly also primarily present in later gestation. Some cell types, such as macrophages, ILCs and fibroblasts displayed marked within-population differential abundance across time, as indicated by enrichment of different cell neighbourhoods in early or late gestation (Figure 3.22). This suggested underlying transcriptional differences within these populations, potentially resulting from temporal changes in the cellular composition of their respective sub-populations.

To further investigate this, the refined cell annotations were then used for Milo analysis (Figure 3.23). This showed the varying enrichment of each cell state and confirmed that some specific sub-populations were differentially present across gestation. For instance, *FRZB*$^{+}$ and *HOXC5*$^{+}$ early fibroblasts were enriched in early gestation compared to *WNT2*$^{+}$ and *PEAR1*$^{+}$ fibroblasts. Conversely, the Dc and Dp of the hair follicle mesenchyme became abundant later, once the hair follicle began to form. The hair follicle epithelial cells followed the same pattern being exclusively present in late gestation alongside differentiated suprabasal epidermal cells, while the periderm was enriched early during development (Figure 3.23).

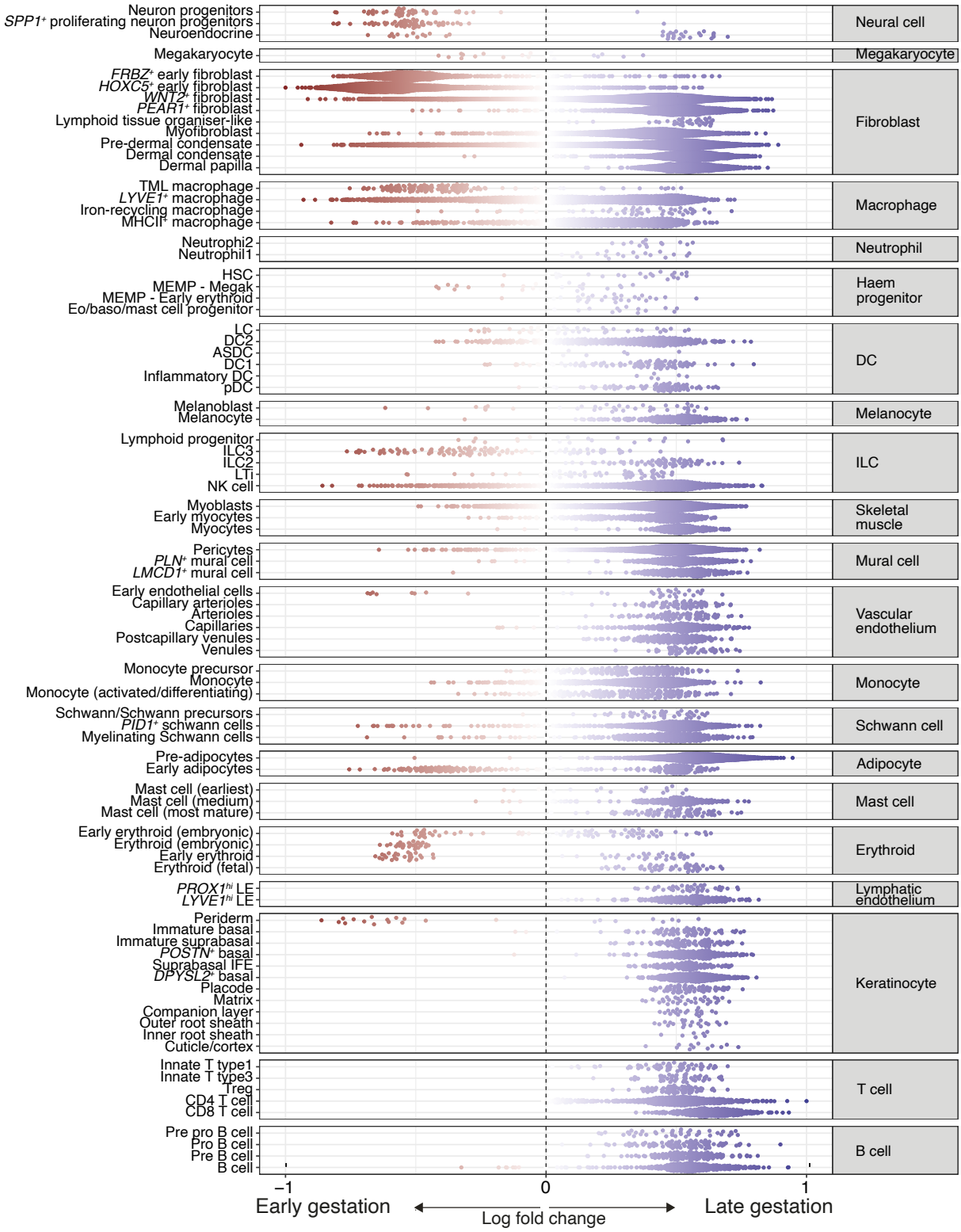

Figure 3.23. Differential abundance of refined cell states across gestation.

Beeswarm plot showing the distribution of the fold change (log-transformed) in abundance across gestation time in Milo-derived neighbourhoods of refined cell states in prenatal skin.

Red and blue colours represent neighbourhoods in early and late gestation respectively; the colour intensity indicates degree of significance in differential abundance. ASDC: $AXL^{+}SIGLEC6^{+}$ dendritic cell; DC: dendritic cell; HSC: hematopoietic stem cell; ILC: innate lymphoid cell; LC: Langerhans cell; LTi: lymphoid tissue inducer; MEMP: megakaryocyte-erythroid-mast cell progenitor; NK cell: Natural killer cell; LE: lymphatic endothelium; pDC: plasmacytoid dendritic cell; Treg: regulatory T cell; TML macrophage: *TREM2*$^{+}$ microglia-like macrophage.

Differences in abundance were also seen for subsets of macrophages and ILCs whereby TML macrophages and ILC3 were mainly found in early gestation while iron-recycling macrophages and ILC2 were enriched in later gestation. Notably, in addition to particular subpopulations being differentially enriched between early and late gestation, differential abundance was also observed within cell states, including *LYVE1*$^{+}$ macrophages and *WNT2*$^{+}$ fibroblasts as seen in Figure 3.23. This suggested potential transcriptional differences within these cell states, possibly resulting from dual waves of production or progressive functional maturation as prenatal skin developed. This is explored further in chapter 4 for *WNT2*$^{+}$ fibroblasts.

3.3.3 Alignment of prenatal skin with skin organoid and adult skin

Having established the cell states present in the prenatal skin dataset, the next step was to assess their alignment to cell populations in the skin organoid model (described in section 1.5.1, also referred to as the skin organoid for short) and adult skin. This not only allowed confirmation of cell identities identified in prenatal skin but also enabled comparative analyses of skin from prenatal, adult and organoid tissues to begin evaluating the faithfulness of the skin organoid to in vivo skin. A morphological comparison of the skin organoid with prenatal skin was carried out in the original publication from Lee et al.,[154] demonstrating resemblance to second trimester developing human skin (section 1.5.2). However, prenatal skin from only one gestational age (18 weeks) was used and assessment of the molecular recapitulation of human skin differentiation across gestation by the skin organoid has not been performed.

To achieve this, scRNA-seq data from prenatal skin, adult skin[100] and skin organoid[154] were integrated and similarity was assessed for broad cell clusters using distance-based transformation of gene expression profiles (section 2.4.2). The adult skin data was generated from healthy interfollicular epidermis and dermis (top 200µm) of surplus trunk skin collected from mammoplasty surgery.[100] The skin organoid dataset included single-cell data from human ES/iPS cell-derived organoids at 29, 48, 85 and 133 days (approximated to 4, 7, 12 and 19 weeks) of culture to capture the different stages of differentiation including formation of hair follicles.[154]

Overall, prenatal skin cells were closely aligned to corresponding cell categories in the adult and/or skin organoid data. This was evident from the integrated UMAP where matching cell groups from the three datasets occupied similar coordinates (Figure 3.24) and was also observed when distance within the integrated latent space was visualised as heatmap (Figure 3.25).

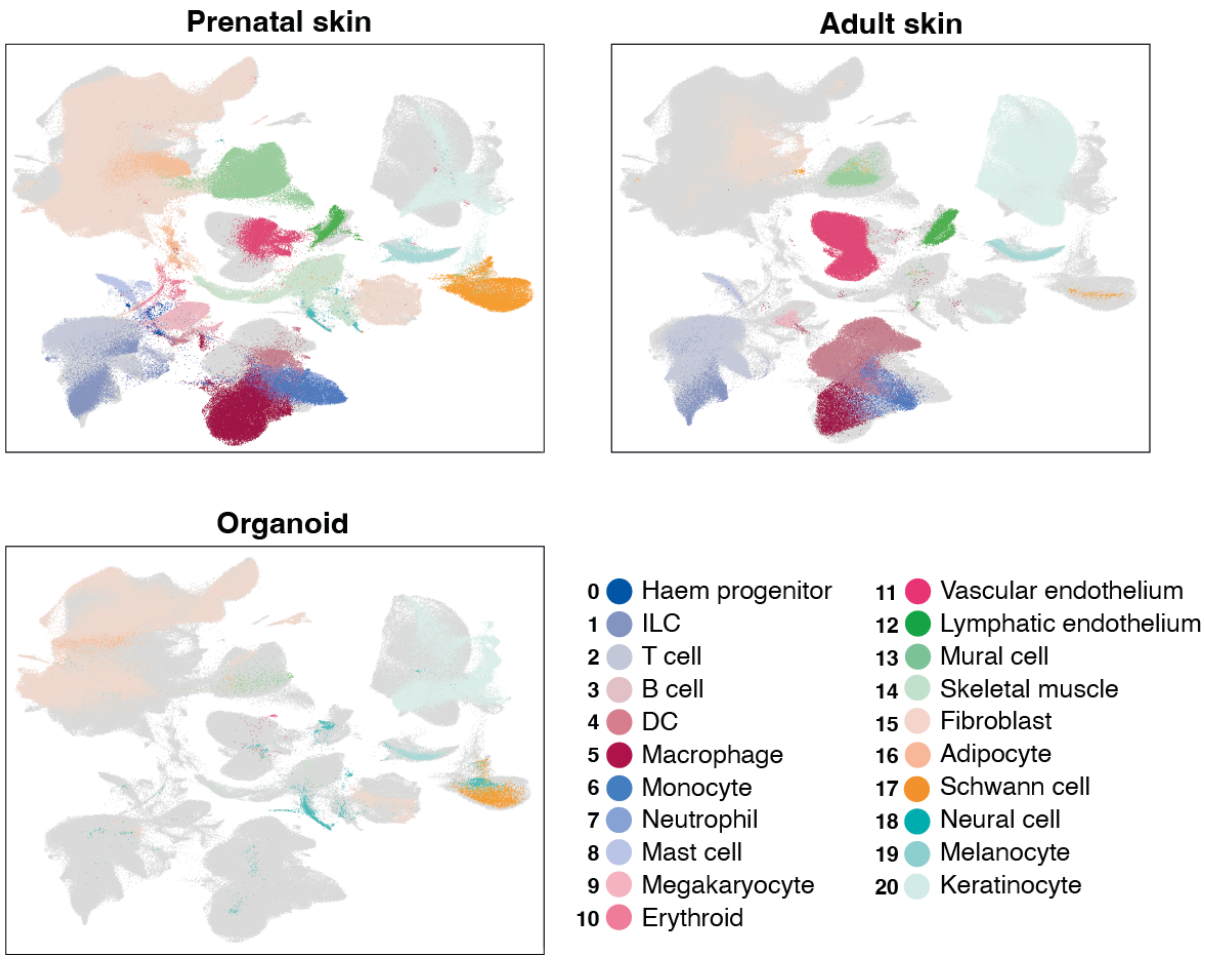

Figure 3.24. Broad cell types in integrated prenatal skin, adult skin and skin organoid data. UMAP visualisation of the prenatal skin (top left), adult skin (top right) and skin organoid (bottom left) clusters in the integrated scRNA-seq data; clusters are coloured by broad cell type annotations. DC: dendritic cell; Haem progenitor: hematopoietic progenitor cell, ILC: innate lymphoid cell.

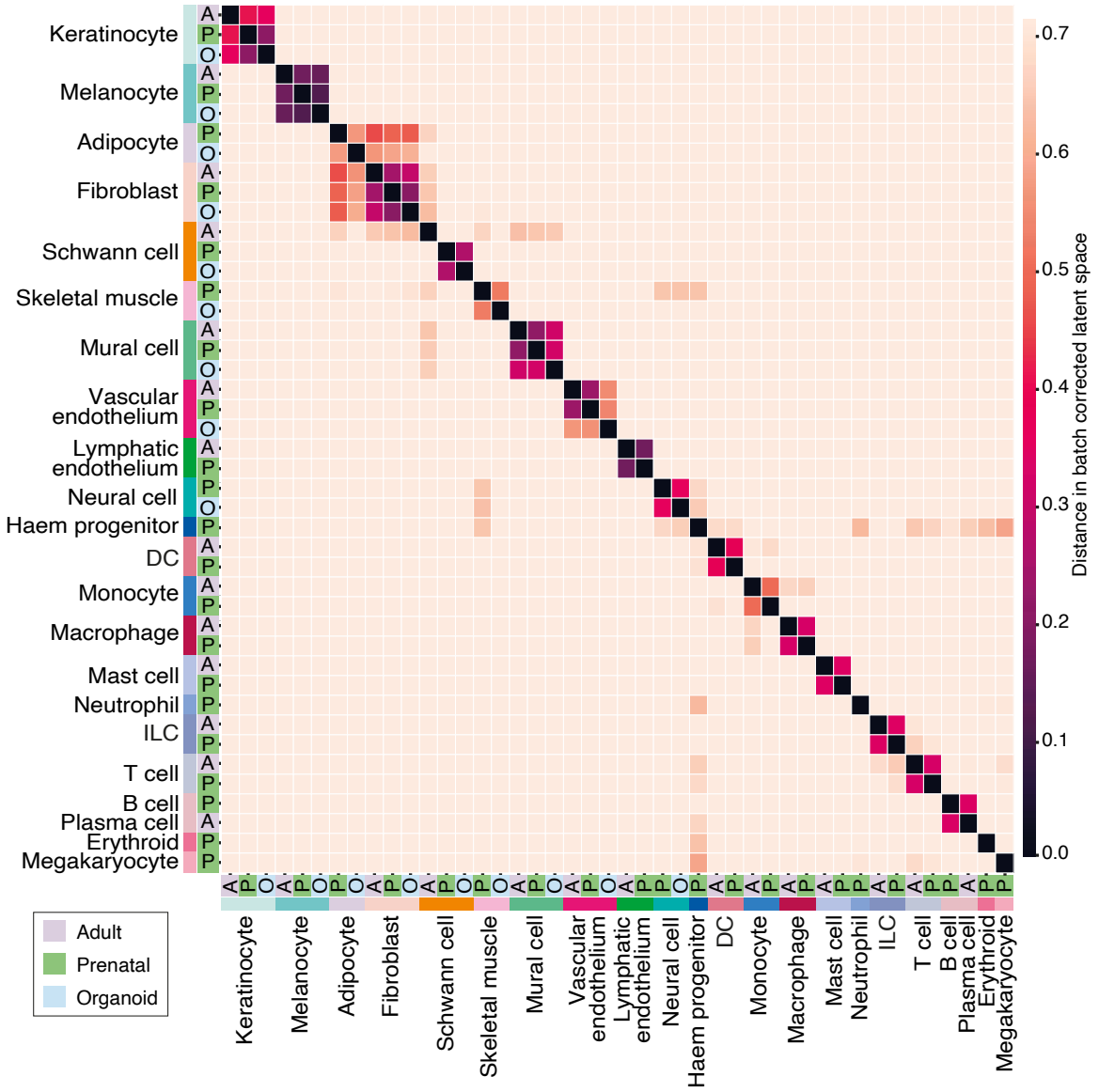

Figure 3.25. Alignment of broad cell types.

Heatmap showing the level of alignment between prenatal skin, adult skin and skin organoid for broad cell types; colour scale indicates distance in batch corrected latent space in the integrated scRNA-seq data from the three tissues. DC: dendritic cell; Haem progenitor: hematopoietic progenitor cell, ILC: innate lymphoid cell.

The heatmap further revealed a degree of alignment of prenatal and organoid adipocytes to fibroblasts (Figure 3.25). Adipocytes likely differentiate from mesenchymal progenitor cells which also give rise to skin fibroblasts,[359] suggesting that their overlap in this analysis may reflect incomplete differentiation of captured adipocytic cells as also noted in section 3.3.1. Schwann cells from adult skin also exhibited transcriptional similarity to fibroblasts (Figure 3.25). This potentially indicated the inclusion of a subtype of Schwann cells co-expressing typical Schwann cell markers and fibroblast markers - lumican (*LUM*) and decorin (*DCN*) - which have previously been described in adult skin.[360] Interestingly, apart from differentiated haematopoietic cells, haematopoietic progenitors from prenatal skin also aligned with other cell types which included progenitor states such as neural cells (with neuron progenitors) and skeletal muscle (with myoblasts), implying that progenitor-specific gene expression profiles may be shared among these early cell states.

Some cell states, such as erythroid, megakaryocytes, neutrophils and B cells were uniquely captured in the prenatal skin data, limiting similarity assessment to adult skin counterparts. Hair follicle cells were also not represented in adult skin due to areas sampled as described above. Notably, the skin organoid model appeared to recapitulate the different components of prenatal skin hair follicle, IFE, dermal fibroblasts, neural and Schwann cells, but lacked blood and immune cells and had significantly reduced endothelial cells. This is shown in Figure 3.26 with cells regrouped under broader labels of dermal stroma, endothelium, epidermal, erythroid, immune, neural and skeletal to highlight the differences between prenatal skin and skin organoid.

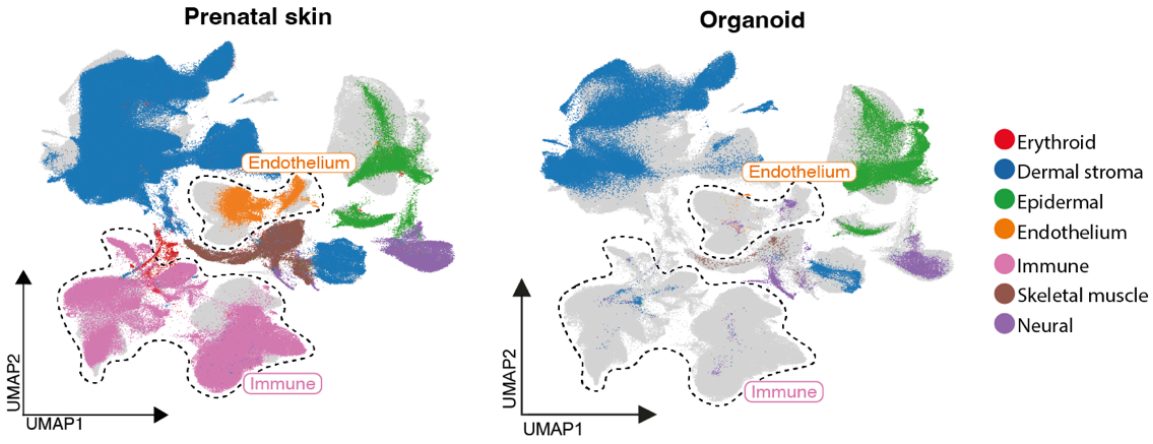

Figure 3.26. Broad cell groups in integrated prenatal, adult and skin organoid data. UMAP visualisation of the prenatal skin (left) and skin organoid (right) regrouped clusters in the integrated scRNA-seq data; clusters are coloured by broad cell group labels.

The above analysis provided a global assessment of transcriptional similarity across all prenatal skin gestational ages and weeks of organoid culture. To investigate whether this was consistent at different timepoints, time-encoded logistic regression analyses were performed on the integrated prenatal skin, skin organoid and adult skin data (section 2.4.2). This showed that the skin organoid generally matched prenatal skin more closely than adult skin as indicated by the overall higher prediction probabilities to prenatal stages across culture duration (Figure 3.27). However, differences were noted among the different cell categories (endothelial cells excluded because of low counts in the skin organoid), suggesting variations in the tempo of differentiation across skin cell lineages. Mesoderm-derived fibroblasts and mural cells in the skin organoid had a low probability of correspondence to adult cell states even after 19 weeks of culture. In contrast, ectoderm-derived keratinocytes and melanocytes displayed accelerated differentiation, aligning to adult skin as early as 4 weeks of organoid culture, although a similar pattern was not seen for Schwann cells. This likely resulted from the skin organoid culture conditions which were optimised to promote epithelial differentiation to produce hair follicles.

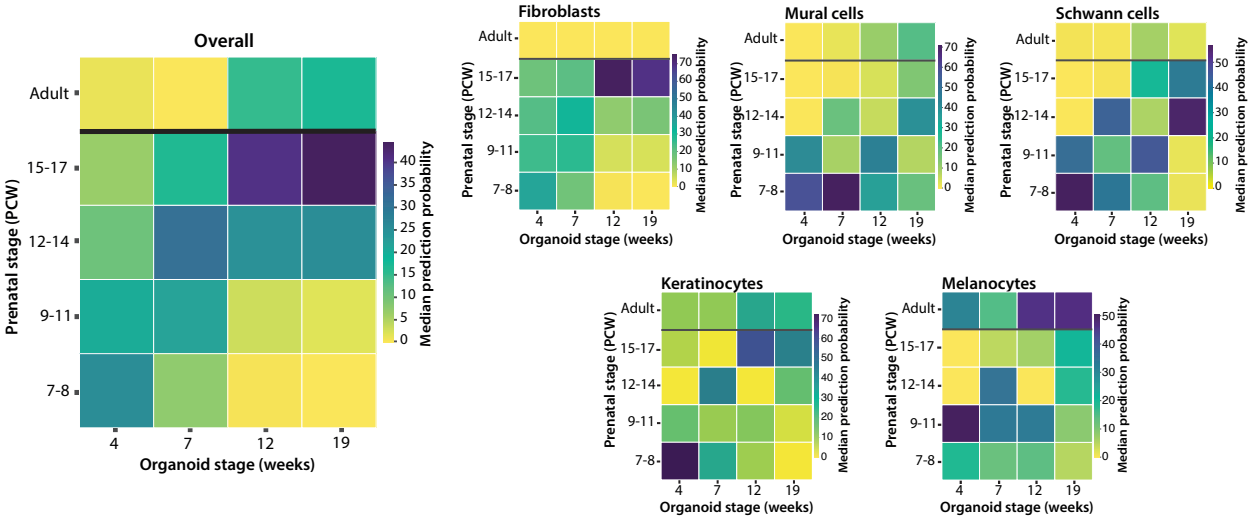

Figure 3.27. Alignment of broad cell types across gestation.

Heatmap showing degree of correspondence between skin organoid and prenatal/adult skin overall and for broad cell types across gestation; colour scale indicates median prediction probabilities for skin organoid culture stages (x-axis) from a logistic regression model trained on combined time-encoded prenatal/adult skin data (y-axis).

Given that prenatal skin and skin organoid cell types demonstrated close alignment at broad level, integration of these two datasets was next assessed for refined cell states and was performed individually for epithelial, stromal and endothelial cells (section 2.4.2). This demonstrated that matching cell states from prenatal skin and skin organoid grouped together during co-embedding, representing their transcriptional similarity (Figures 3.28 and 3.29 for epithelial and stromal cell states). The results of the endothelial cell integration are shown and discussed in chapter 5.

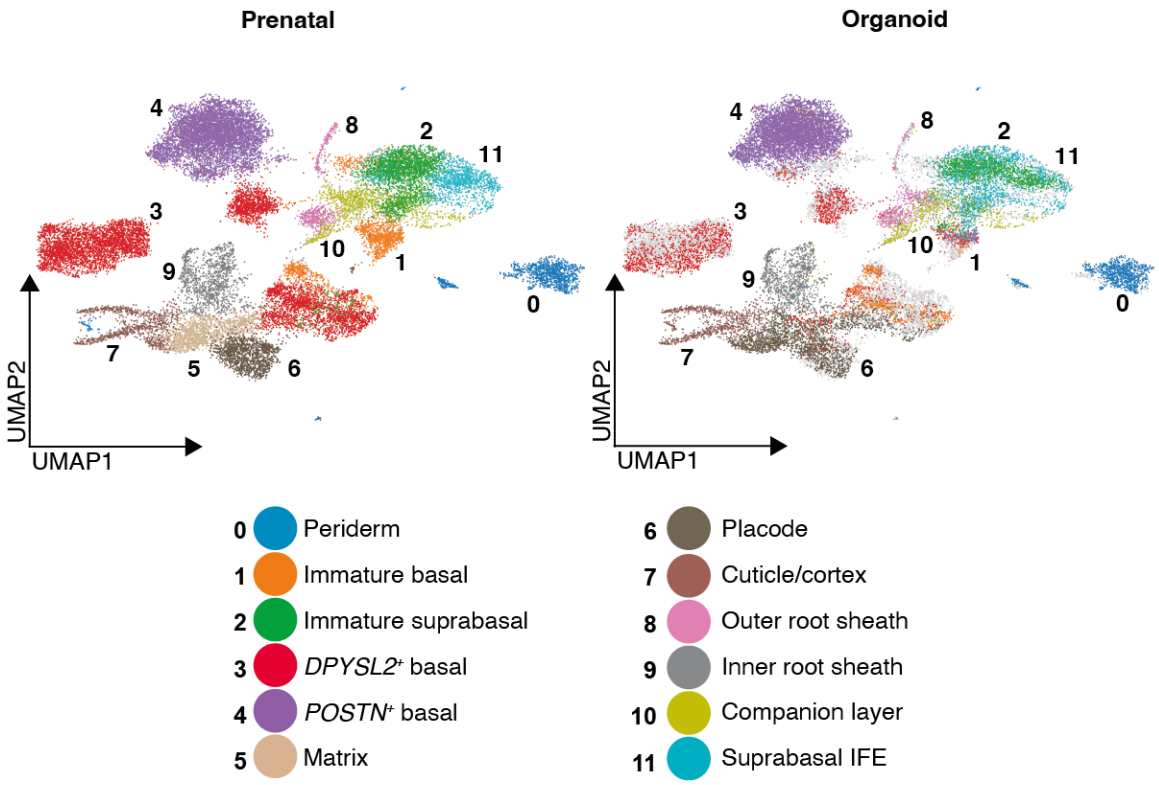

Figure 3.28. Refined epithelial cell states in integrated prenatal skin and skin organoid data. UMAP visualisation of co-embedded prenatal skin (left) and skin organoid (right) epithelial clusters in the integrated scRNA-seq data; clusters are coloured by refined cell state annotations. IFE: interfollicular epidermis.

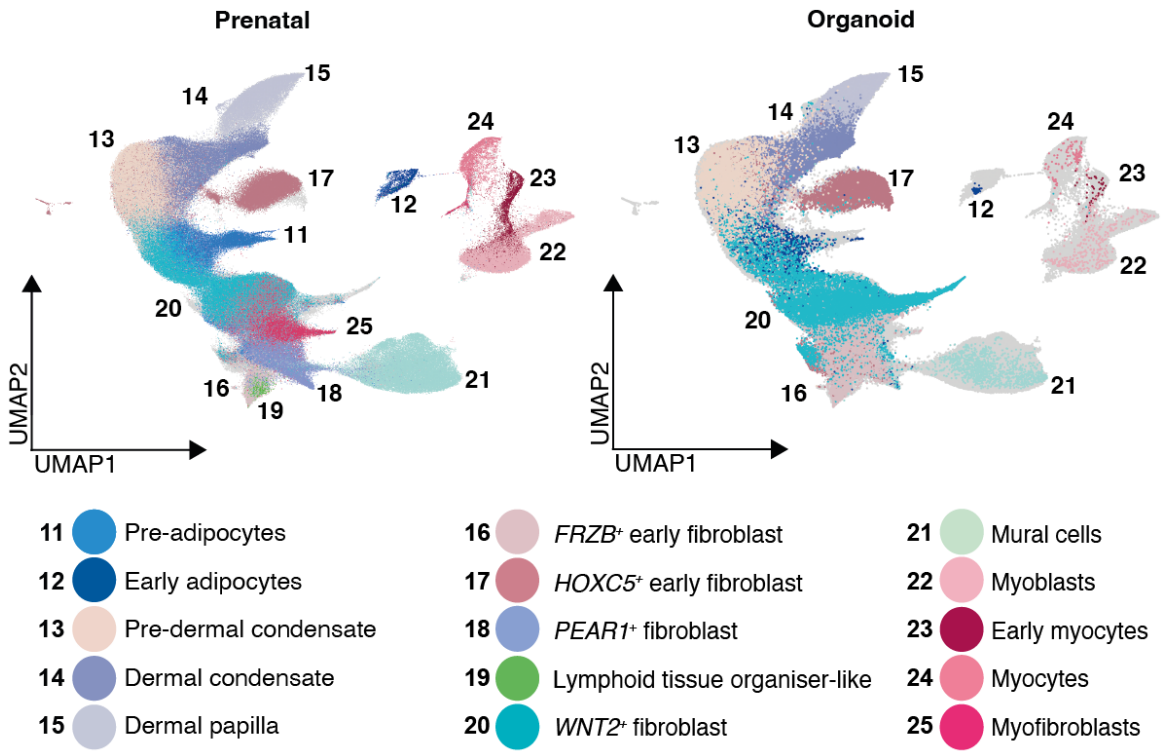

Figure 3.29. Refined stromal cell states in integrated prenatal skin and skin organoid data. UMAP visualisation of co-embedded prenatal skin (left) and skin organoid (right) stromal clusters in the integrated scRNA-seq data; clusters are coloured by refined cell state annotations.

3.3.4 Hair follicle formation

The detailed annotation of the refined cell states in prenatal skin (section 3.3.1) and comparison with the hair-bearing skin organoid model (section 3.3.3) indicated that several cell types from the developing hair follicle were captured from both epithelial (placode, matrix, cuticle/cortex, CL, IRS and ORS) and mesenchymal (pre-Dc, Dc and Dp) compartments. In this section, I describe the analyses conducted to ensure reliable identification of hair follicle cells, including microscopic examinations and comparison to a published human hair follicle dataset, prior to investigating the cellular and molecular mechanisms underpinning human hair follicle morphogenesis.

Confirmation of captured cell states

Histological examination

Images of haematoxylin and eosin (H&E)-stained skin sections at different gestational ages were obtained covering around the same time span and same site as the samples in the scRNA-seq dataset (Figure 3.30). At 6 PCW, prenatal skin comprised a 2-layer epithelium overlying a cellularly dense, homogeneous dermal stroma. Stratification of the epidermis was then observed between 8 and 14 PCW. Hair follicle structures became apparent around 14-15 PCW consistent with findings from the scRNA-seq data analysis (section 3.3.1). These were seen as condensates of mesenchymal cells abutting the epidermis as well as budding of the hair germ and early invagination of the hair peg, captured in transverse and longitudinal sections (Figure 3.30). By 17 PCW, downgrowing elongated hair follicles were present underneath the multi-layered interfollicular epidermis (Figure 3.30).

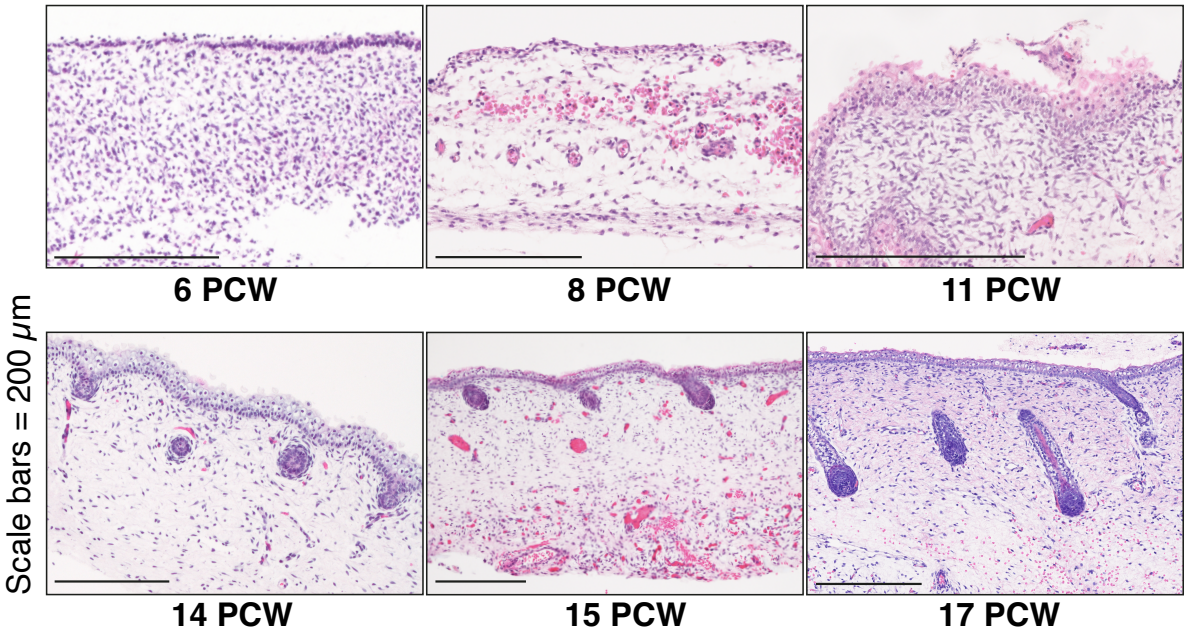

Figure 3.30. Histological changes in prenatal skin during gestation.

Light microscopy images of H&E-stained prenatal skin sections demonstrating different stages of skin and hair follicle development. Representative image shown for each gestational age from n=13 independent biological samples (6 PCW: n=1, 3 replicates; 8 PCW: n=3; 11 PCW: n=2; 14 PCW: n=1, 2 replicates; 15 PCW: n=4; 17 PCW: n=2). Scale bars, 200 μm.

Multiplex in situ hybridisation

To confirm the morphological features seen on histology analysis, multiplex smFISH was performed with RNAscope. Probes against specific genes identified from prenatal skin scRNA-seq data were used, providing further validation of cellular annotations. Markers for ORS (*SLC26A7*), matrix (*SHH*) and Dp (*NDP*) were chosen to outline hair follicle structures in situ as seen in Figure 3.31.

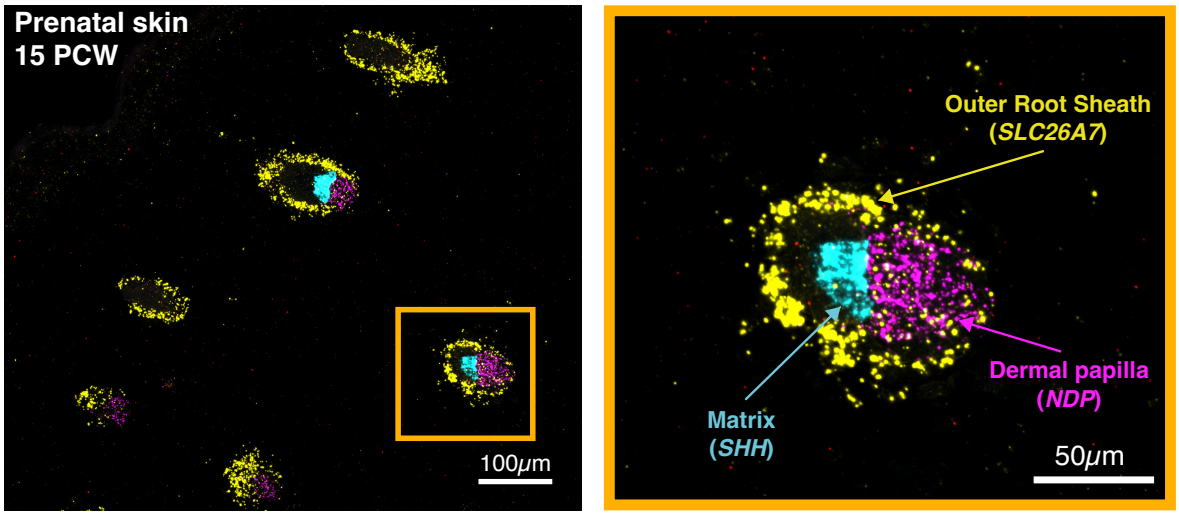

Figure 3.31. RNAscope FISH of prenatal skin hair follicles.

Large-area (left) and magnified (right) RNAscope images showing the ORS (*SLC26A7*, yellow), matrix (*SHH,* cyan), dermal papilla (*NDP*, magenta) of prenatal skin hair follicles. Representative image (15 PCW) shown from n=5 independent biological samples. Scale bars, 100µm (left) or 50µm (right).

Comparison with human adult hair follicles

In section 3.3.3 where prenatal skin was compared to the skin organoid and adult skin, transcriptional similarity of cells from prenatal skin and skin organoid hair follicles was demonstrated. However, the adult skin data included in the analysis did not include hair follicles due to the sampling strategy as previously discussed. An additional scRNA-seq dataset of human hair follicles[189] was therefore sourced for further comparison. This dataset primarily comprised data generated from anagen hair follicles, obtained from follicle-enriched adult scalp skin collected during hair transplant surgery, with limited amounts of surrounding interfollicular epidermis and dermis.[189] As epithelial cells constituted the majority of cells in this dataset, comparative analysis with prenatal skin and skin organoid data, using integration and logistic regression steps, was therefore restricted to the epithelial compartment (section 2.4.3).

Overall, prenatal skin/skin organoid cell states transcriptionally aligned with their adult counterparts (Figures 3.32 and 3.33). The CL cells were underrepresented in adult hair follicles,[189] precluding assessment of their alignment to prenatal skin/skin organoid CL. The placode, being a prenatal-specific feature only present during hair follicle neogenesis, had accordingly no equivalent cell state in the adult data (Figures 3.32 and 3.33).

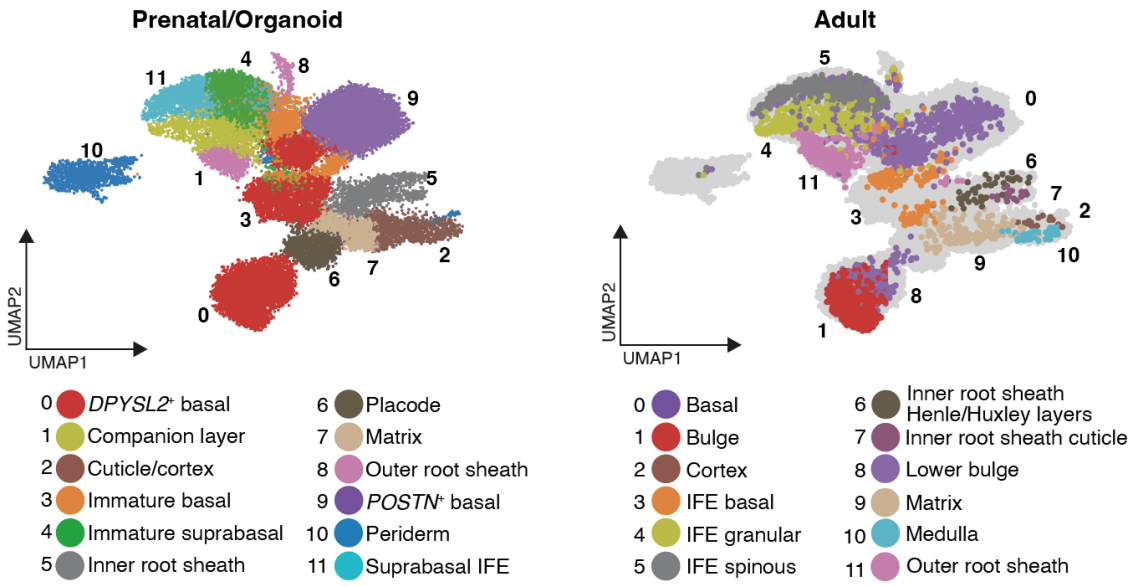

Figure 3.32. Epithelial cell states in integrated prenatal/organoid and adult hair follicle data. UMAP visualisation of co-embedded prenatal skin/skin organoid (left) and adult hair follicle (right) epithelial clusters in the integrated scRNA-seq data; clusters are coloured and numbered by epithelial cell state annotations. IFE: interfollicular epidermis.

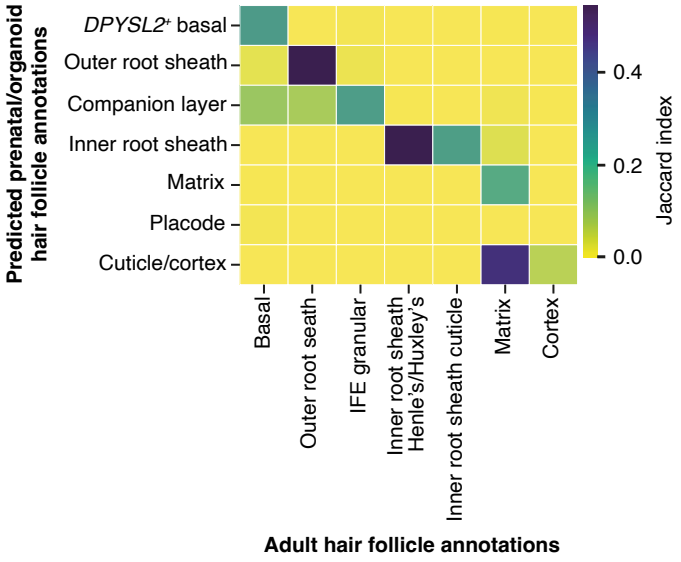

Figure 3.33. Alignment of adult hair follicles to prenatal skin/skin organoid. Heatmap showing degree of correspondence between prenatal skin/skin organoid and adult hair follicle epithelial cells; colour scale indicates the Jaccard index for combined prenatal skin/skin organoid cell states (y-axis) from a logistic regression model trained on adult hair follicle data (x-axis).

The prenatal skin/skin organoid cuticle/cortex (components of the hair shaft) aligned to the adult cortex as expected - the adult data only included cells from the hair shaft cortex and not the hair cuticle which differs from the IRS cuticle (as described in section 1.1.2) (Figure 3.33). Interestingly, these cells from prenatal skin/skin organoid also matched to adult matrix cells (Figure 3.33). Matrix progenitors in postnatal skin are known to differentiate into the inner layers of the hair follicle, including the cuticle and cortex.[28,361] The concurrent alignment to adult hair follicle matrix suggested that prenatal skin/skin organoid cuticle/cortex may be in an earlier stage of differentiation compared to adult cuticle and cortex or that there may be inherent differences between prenatal skin/skin organoid and adult matrix cells. To evaluate this, the prenatal and adult hair matrix clusters were compared (Figure 3.34).

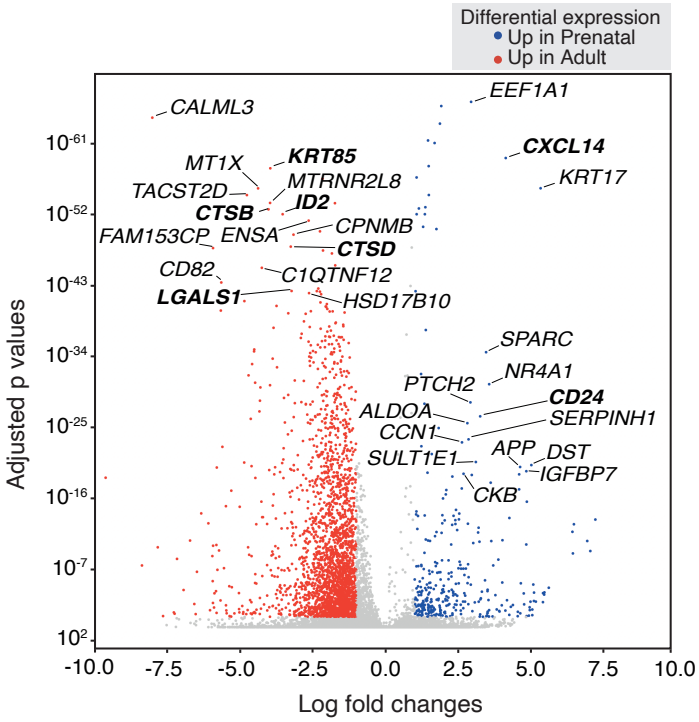

Figure 3.34. Comparison of prenatal and adult hair follicle matrix.

Volcano plot showing selected genes differentially expressed between prenatal and adult matrix cells. Blue and red colours indicate genes significantly upregulated in prenatal skin and adult skin respectively; statistical significance assessed using Wilcoxon rank-sum test and adjusted with Benjamini-Hochberg correction.

Matrix cells from adult skin expressed genes associated with regulation of cell differentiation (*ID2*, *LGALS1*)[362,363], control of keratinocyte proliferation (*CTSB*, *CTSD*)[364,365] and upregulated *KRT85* which functions in anchoring of different hair follicle cell types to maintain tissue integrity.[366] This indicated that prenatal matrix cells are in a higher state of proliferation and differentiation with reduced cellular attachments which are essential for full invagination and formation of the mature hair follicle. The prenatal matrix cluster also had increased expression of genes encoding CXCL14, a chemokine previously reported to recruit Tregs,[367] and CD24, a signalling molecule involved in control of autoimmunity,[368] implying that Treg accumulation and immune protection are potentially involved during early matrix differentiation. Tregs have been shown to localise around the hair follicle in postnatal skin and in prenatal skin in late second trimester (~21 PCW).[85,369] Validation using RNAscope (*FOXP3*$^{+}$) and immunofluorescence (FOXP3^{+}) assays confirmed the increased presence of Tregs within and around hair follicles compared to interfollicular areas in prenatal skin from as early as 15 PCW (Figures 3.35, 3.36 and 3.37).

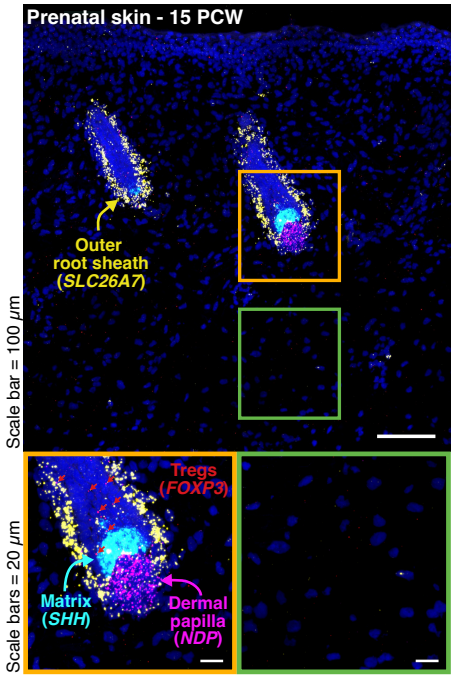

Figure 3.35. RNAscope FISH of perifollicular Tregs.

Large-area (top) and magnified perifollicular (bottom left) and interfollicular (bottom right) prenatal skin RNAscope images showing the ORS (*SLC26A7,* yellow), matrix (*SHH,* cyan), dermal papilla (*NDP*, magenta) with Tregs (*FOXP3*, red) around hair follicles. Representative image (15 PCW) shown from n=5 independent biological samples. Scale bars, 100µm (top) or 20µm (bottom). Tregs: Regulatory T cells.

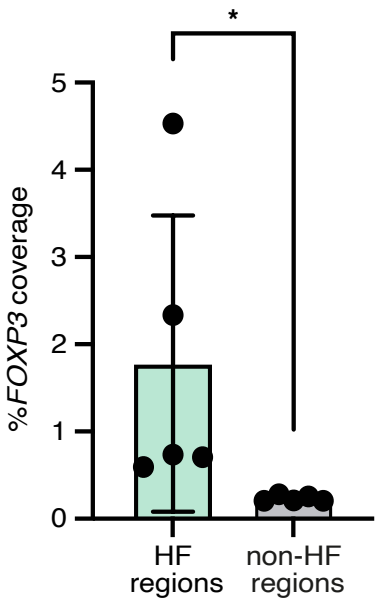

Figure 3.36. Quantification of perifollicular Tregs.

Percentage of *FOXP3* coverage in perifollicular (green) and interfollicular regions (grey) in prenatal skin. Data from n=5 independent biological samples shown as mean ± SD; *p = 0.0131 from unpaired t-test. HF: hair follicle.

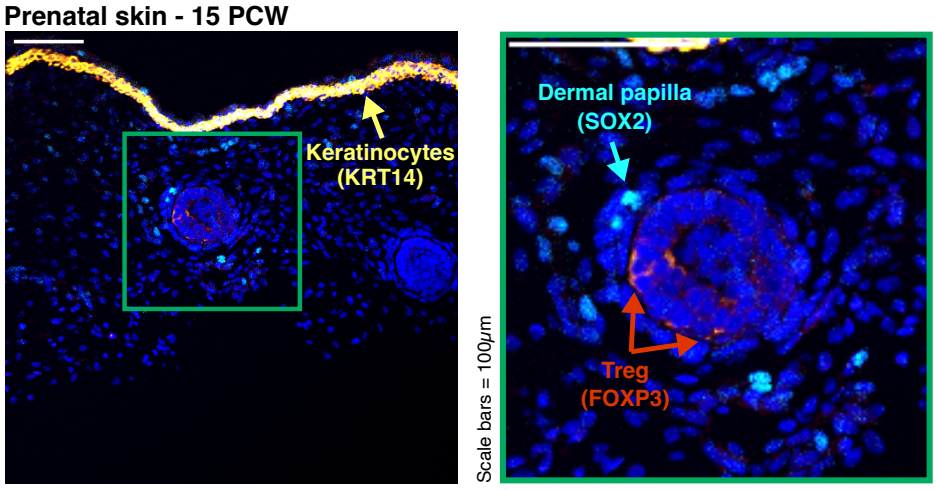

Figure 3.37. Immunofluorescence assay of perifollicular Tregs.

Large-area (left) and magnified perifollicular (right) images of prenatal skin immunostained for Tregs (FOXP3, red), dermal papilla (SOX2, cyan), and basal epidermal keratinocytes (KRT14, yellow). Representative image (15 PCW) shown from n=3 independent biological samples with 2 replicates. Scale bars, 100µm. Tregs: Regulatory T cells.

Overall, these analyses confirmed the hair follicle cell states identified in the prenatal skin scRNA-seq data, demonstrating capture of the onset and differentiation of new hair follicles within the included gestational ages. Additionally, inherent transcriptional differences in matching cell states between prenatal and adult skin were revealed, highlighting developmental-specific features and their biological implications during hair follicle formation.

Inferred differentiation trajectories

The inclusion of cell states present during hair follicle induction, organogenesis and differentiation in the prenatal skin scRNA-seq data was next leveraged to gain insight into the molecular changes during human hair follicle morphogenesis. Inferred trajectory and pseudotime analysis, using CellRank[193,194] with scVelo[195] (section 2.4.5), was carried out to assess the gene expression dynamics during differentiation of the epithelial and mesenchymal hair follicle cell states. CellRank inferred start, intermediate and terminal cell states and ordered them along a pseudotime based on combined gene expression and RNA velocity data (section 2.4.5). Correspondence between prenatal skin and skin organoid cell states was demonstrated in section 3.3.3. Analysis of integrated prenatal skin and skin organoid data, providing increased cell numbers, produced a smoother transition of cell states for trajectory inference and is presented in the PAGA and UMAP plots below. The genes differentially expressed across pseudotime were calculated solely from prenatal skin and are similar to those identified from inferred trajectories that utilised in vivo prenatal skin data only.[370]

Epithelial cell states

Inferred trajectory and pseudotime analysis of epithelial cells predicted the differentiation of *POSTN*$^{+}$ basal cells into two distinct trajectories (Figure 3.38). The first consisted of *DPYSL2*$^{+}$ basal cells, ORS and CL and was labelled ‘ORS/CL trajectory’; the second, designated as ‘IRS trajectory’, included the placode, matrix, cuticle/cortex and IRS.

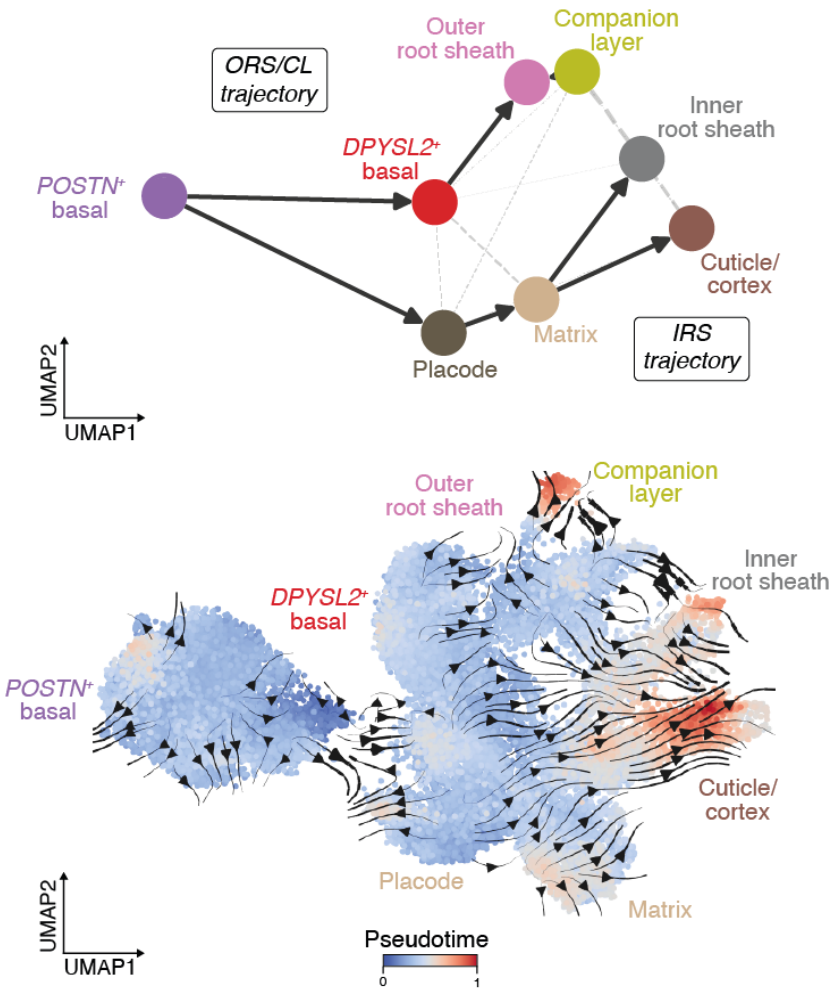

Figure 3.38. Inferred differentiation trajectory of hair follicle epithelial cells. Differentiation along 'ORS/CL' and 'IRS' trajectories of combined prenatal skin and skin organoid epithelial cells. Inferred trajectories shown by PAGA plot (top) with weighted connectivities between nodes (coloured by cell states) and UMAP (bottom) overlaid with velocity-based directionality and coloured by pseudotime. CL: companion layer; IRS: inner root sheath; ORS: outer root sheath.

This analysis highlighted several genes upregulated during ORS (*BARX2* and *SOX9*) and IRS (*SHH* and *WNT10B*) differentiation (Figure 3.39) that have previously been reported in murine skin.[58,60,371] *BARX2* is expressed in the outer layers during hair growth in mice whilst *SOX9* has been shown to direct ORS differentiation and formation of hair stem cell niche.[60,371] *SHH* and *WNT10B* are increased in precursor cells that eventually form the hair matrix.[58,60] In addition to these known genes, *SPON2* and *AGR2* were newly identified as being upregulated along the ORS/CL trajectory by *DPYSL2*$^{+}$ basal cells (Figure 3.39). *SPON2* encodes an integrin ligand which mediates cellular adhesion.[372,373] *AGR2* is involved in the assembly of cysteine-rich receptors enriched in hair follicles and loss of *AGR2* has been shown to promote cell migration.[374,375] The downregulation of *SPON2* and *AGR2* along the IRS trajectory suggested that decreased cellular adhesion and increased migration potential may characterise matrix specification and invagination during development, in line with the earlier findings from prenatal and adult matrix comparison.

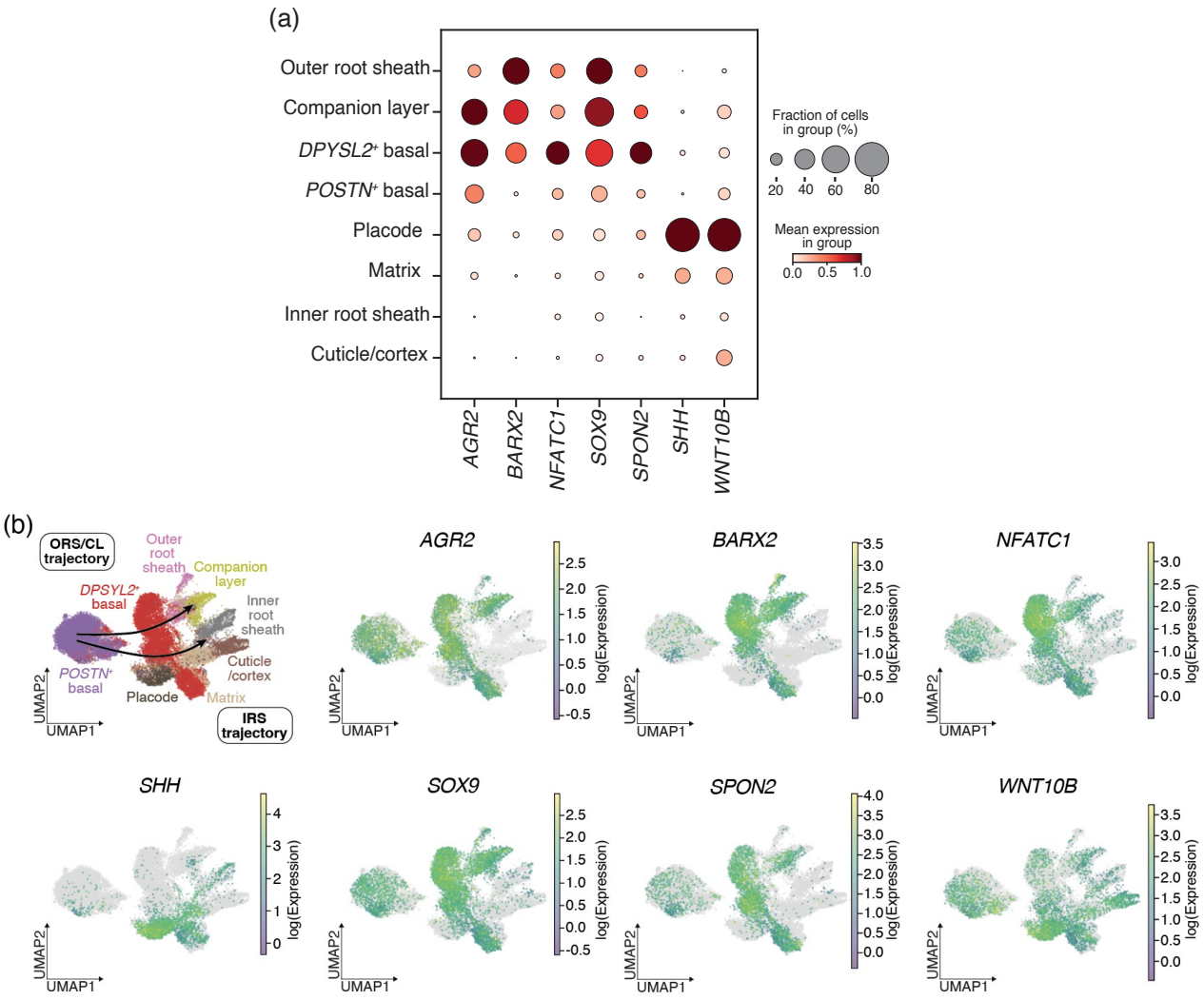

Figure 3.39. Gene expression of differentiating hair follicle epithelial cells.

(a) Dot plot of genes differentially expressed by epithelial cell states along the 'ORS/CL' and 'IRS' trajectories in prenatal skin; for a given gene, dot colour indicates normalised variance-scaled mean expression and dot size indicates the percentage of expressing cells in each category. (b) UMAP visualisation of the inferred differentiation trajectory of prenatal skin hair follicle epithelial cells along the 'ORS/CL' and 'IRS' trajectories, coloured by gene expression (log-transformed).

Of note, differentiation of the CL was inferred along the same trajectory as the ORS. Although differing opinions about the origin of the CL have been proposed since its first identification, the current consensus based on lineage tracing studies is that it constitutes one of the inner layers of the hair follicle, differentiating from early matrix progenitors adjacent to the Dp[376,377] (see section 3.4.3 for discussion). Its observation along the same trajectory as the ORS (Figure 3.38) was therefore surprising. However, a fate-mapping study in mice has shown that the CL develops prior to the fully formed matrix.[377] In addition, a recent scRNA-seq study of mouse hair follicle development further identified greater transcriptional similarity of the CL to ORS cells compared to inner layer structures,[60] in line with findings here in the human prenatal skin.

The genes differentially expressed along the ORS/CL and IRS trajectory pseudotimes were next assessed and highlighted several genes known to cause genetic hair disorders, with features of reduced hair growth (hypotrichosis) or abnormally-shaped hair. These genes are marked on the heatmaps below (Figures 3.40 and 3.41), with a list of associated genetic hair diseases and clinical features provided in Table 1. The distinct expression of these genes suggested that these genetic hair diseases likely begin during initial hair follicle development in utero.

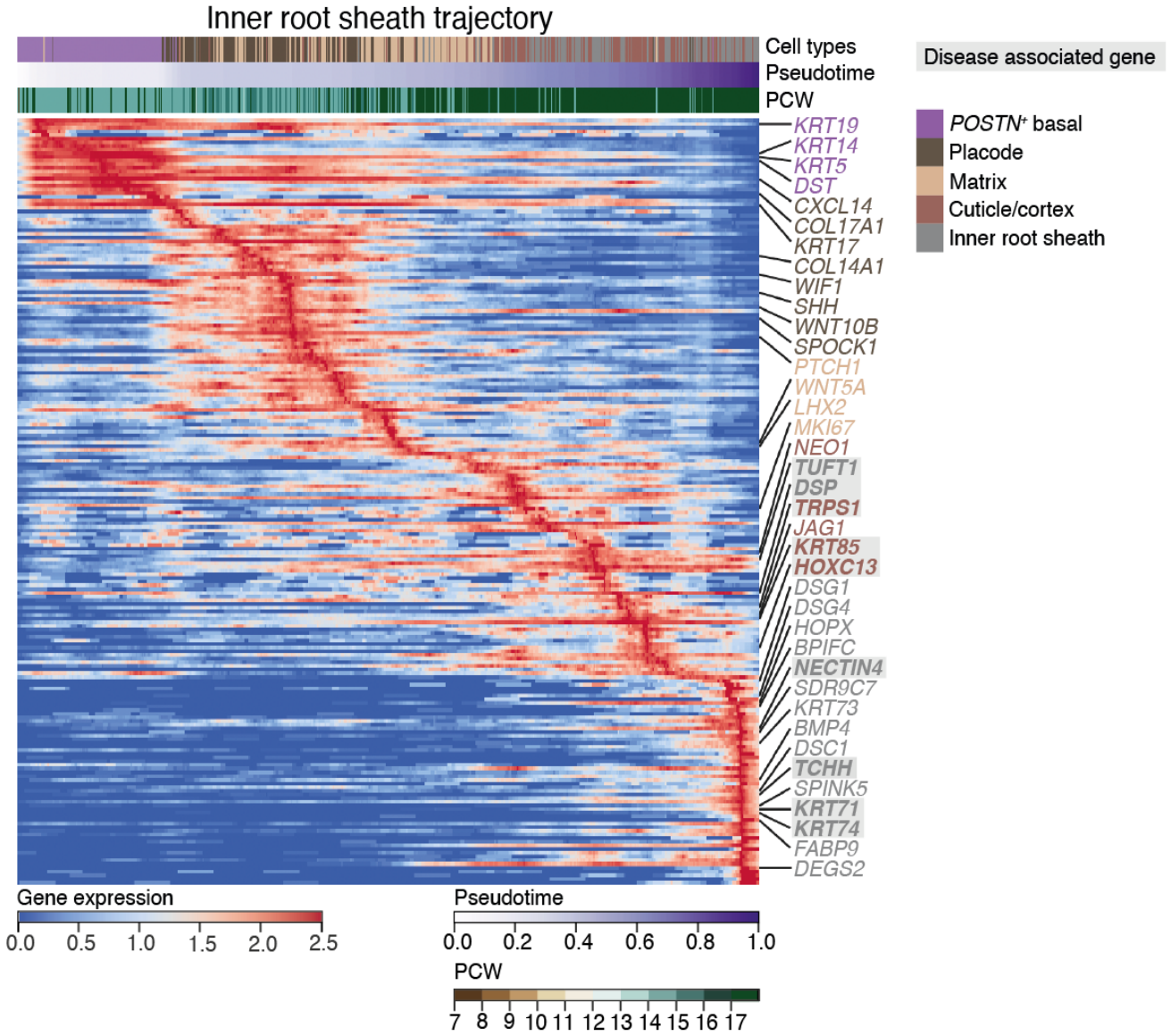

Figure 3.40. Driver genes along the IRS trajectory.

Heat map of genes (y-axis) differentially expressed across pseudotime (x-axis) along the IRS trajectory; corresponding hair follicle cell states and gestational ages (PCW) are indicated alongside pseudotime and blue-red colour scale represents normalised gene expression. Genes associated with genetic hair disorders are highlighted in grey.

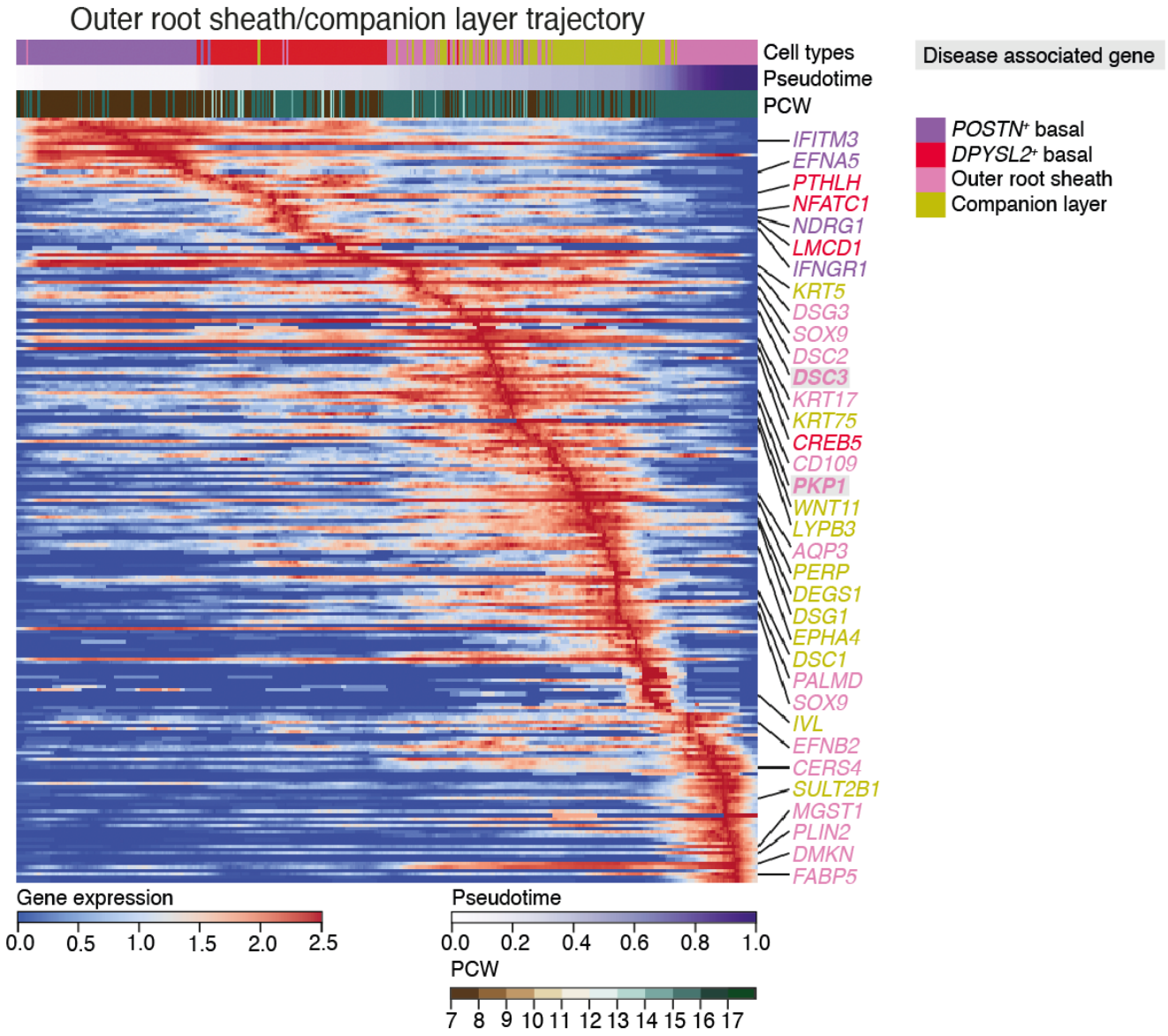

Figure 3.41. Driver genes along the ORS/CL trajectory.

Heat map of genes (y-axis) differentially expressed across pseudotime (x-axis) along the ORS/CL trajectory; corresponding hair follicle cell states and gestational ages (PCW) are indicated alongside pseudotime and blue-red colour scale represents normalised gene expression. Genes associated with genetic hair disorders are highlighted in grey.

Gene	Disease	Hair-related clinical features
PKP1	Ectodermal dysplasia / skin fragility syndrome[378]	Short and sparse hair
NECTIN4	Ectodermal dysplasia / syndactyly syndrome[379]	Sparse and fragile hair, pili torti
HOXC13	Pure hair and nail ectodermal dysplasia[380]	Sparse hair to complete hair loss
KRT85	Pure hair and nail ectodermal dysplasia[366]	Sparse hair to complete hair loss
TRPS1	Trichorhinophalangeal syndrome[381]	Sparse and slow-growing hair
DSC3	Hypotrichosis and recurrent skin vesicles	Sparse and fragile hair
KRT71	Hypotrichosis and woolly hair syndrome[382]	Tightly curled, short and sparse hair
KRT74	Woolly hair syndrome[383]	Tightly curled, short hair
DSP	Woolly hair / skin fragility syndrome[384]	Tightly curled, short and sparse hair
TUFT1	Woolly hair / skin fragility syndrome[385]	Tightly curled, short hair
TCHH	Uncombable hair syndrome[386]	Dry and spangly hair, pili trianguli et canaliculi

Table 1: Genetic hair diseases associated with genes identified along the IRS and ORS/CL trajectories with corresponding hair-related clinical features.

At this stage, the expressions of the identified disease-causing genes were also checked in the skin organoid scRNA-seq data compared to prenatal skin as part of evaluating its faithfulness to in vivo skin. Similar expression patterns were observed in prenatal skin and skin organoid for most genes (Figure 3.42), supporting the value of the skin organoid as a model to study genetic hair diseases.

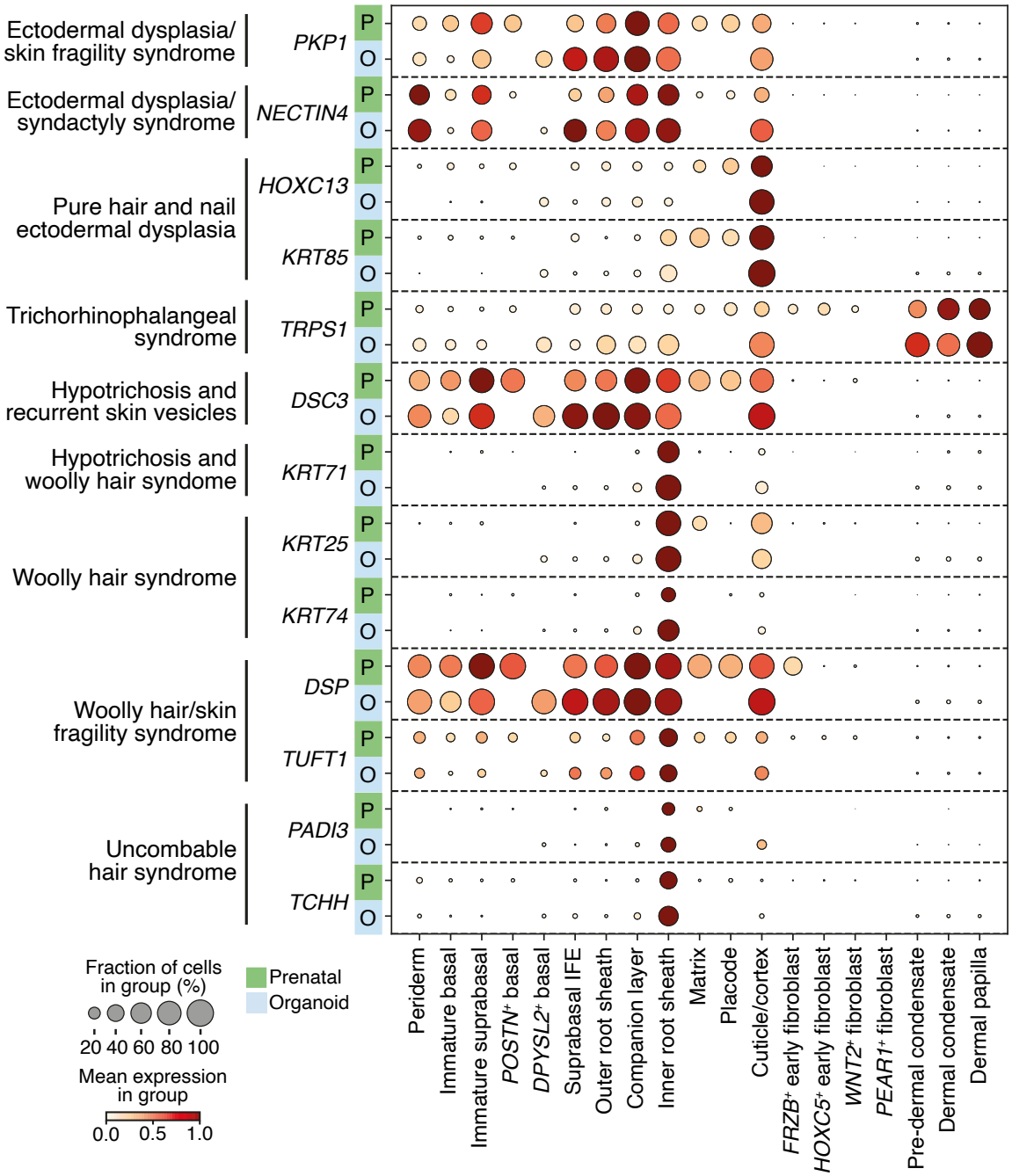

Figure 3.42. Disease-causing genes in the skin organoid model.

Dot plot of genes implicated in genetic hair diseases in prenatal skin and skin organoid scRNA-seq data; for a given gene, dot colour indicates normalised variance-scaled mean expression and dot size indicates the percentage of expressing cells in each cell state in the individual dataset. IFE: interfollicular epidermis.

Mesenchymal cell states

The hair follicle mesenchymal cell states identified in the prenatal skin data (pre-Dc, Dc and Dp) were presented in section 3.3.1, including the first description of the human pre-Dc. To further explore the origin and gene programs underlying differentiation of the hair mesenchyme, inferred trajectory and pseudotime analysis of the different fibroblast subsets (combined prenatal skin and skin organoid) was carried out. *FRZB*$^{+}$ early fibroblasts were not included as they were mainly found in one sample from the earliest gestation stage (section 3.3.1). This analysis predicted that *HOXC5*$^{+}$ fibroblasts served as a common progenitor differentiating along two trajectories (Figure 3.43). The first produced the specialised fibroblasts of the hair follicle (pre-Dc, Dc and Dp) and was labelled 'hair fibroblast trajectory'; the second gave rise to *WNT2*$^{+}$ fibroblasts, *PEAR1*$^{+}$ fibroblasts and myofibroblasts and was termed 'dermal fibroblast trajectory' (Figure 3.43).

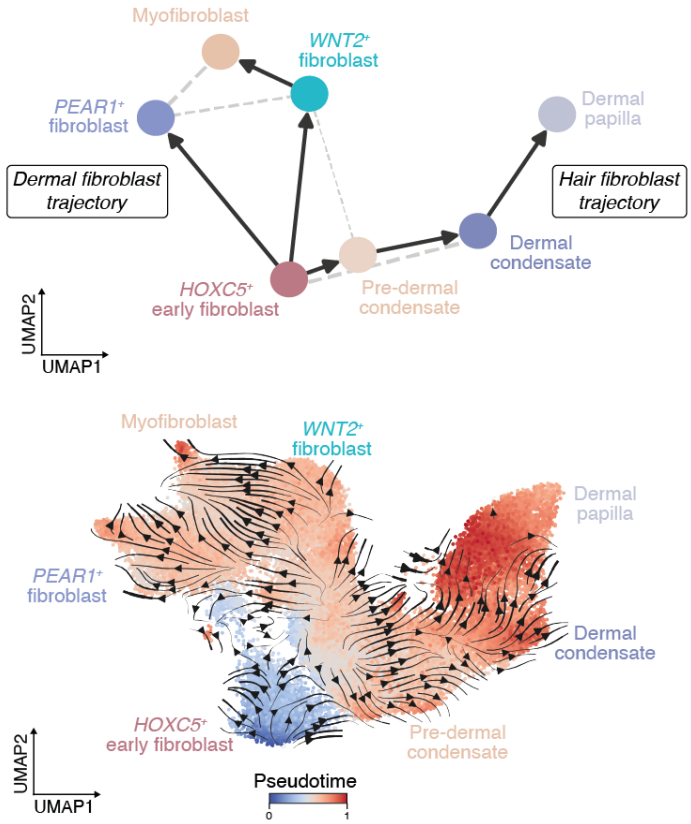

Figure 3.43. Inferred differentiation trajectory of hair follicle mesenchymal cells. Differentiation along 'Hair fibroblast' and 'Dermal fibroblast' trajectories of combined prenatal skin and skin organoid mesenchymal cells. Inferred trajectories shown by PAGA plot (top) with weighted connectivities between nodes (coloured by cell states) and UMAP (bottom) overlaid with velocity-based directionality and coloured by pseudotime.

The genes differentially expressed along the prenatal skin 'hair fibroblast' pseudotime (Figure 3.44) revealed the mechanisms activated during mesenchymal differentiation to form the Dp. Several genes which regulate cell adhesion (*ADAMTS1*), maintain cell-cell contact (*CLDN11*) and direct migration (*CXCL12*) were expressed as the pre-Dc was specified from *HOXC5*$^{+}$ early fibroblasts.[387–389] This suggested that a process of collective cellular migration occurs as the pre-Dc moved towards the epidermis.[387,389] Formation of the Dc, by aggregation of the pre-Dc underneath the epithelial placode, was then characterised by upregulation of genes involved in collagen fibril formation and cell adhesion (*COL6A3, MFAP4, PTK7*).[390,391] Establishment of the Dp was accompanied by expression of genes such as *RSPO3* and *WNT5A* that co-ordinate the differentiation and proliferation of epithelial cells in the overlying hair matrix.[392,393] This analysis provided insights into the processes involved during differentiation of the hair follicle mesenchyme in human prenatal skin and is summarised in Figure 3.45.

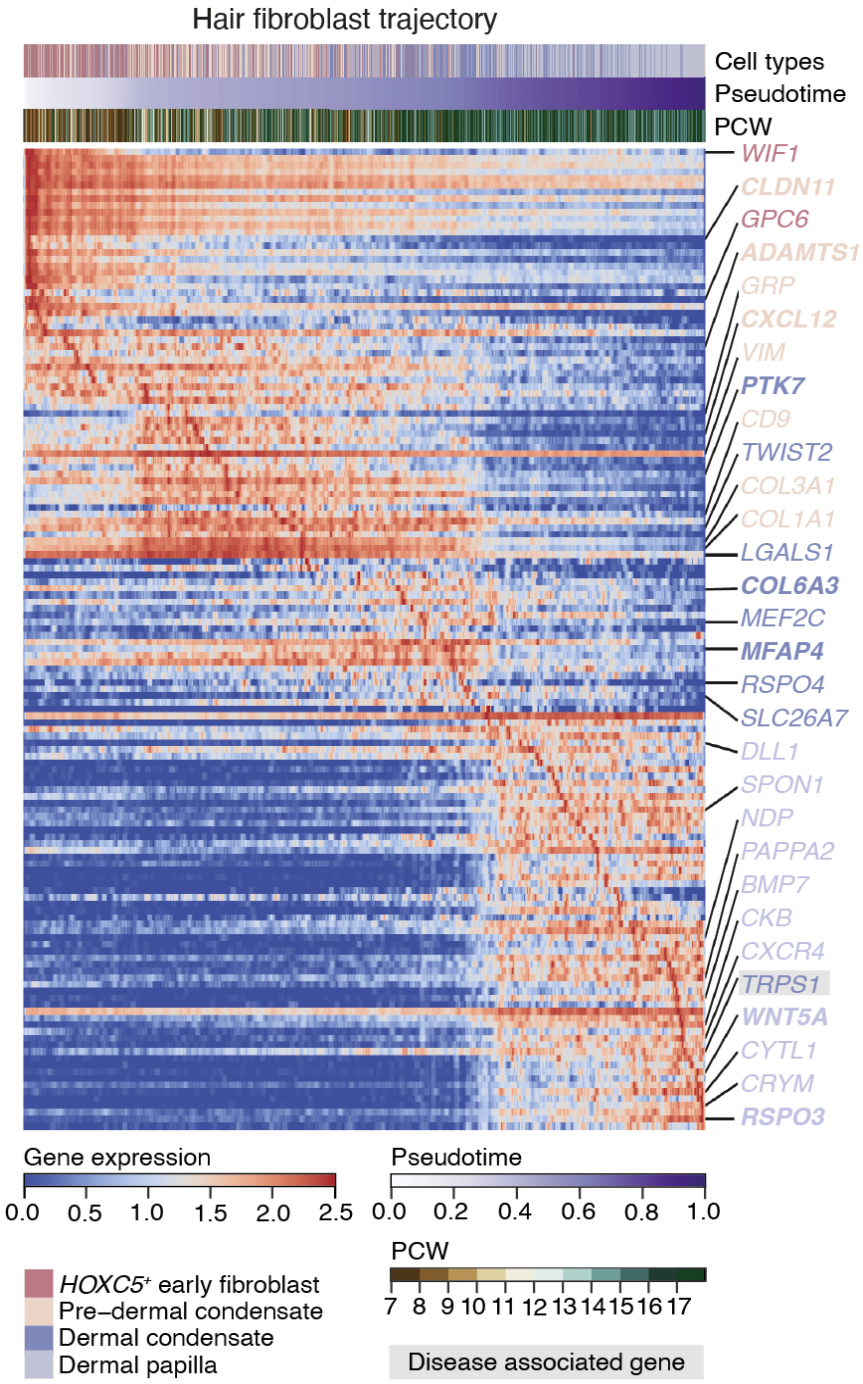

Figure 3.44. Driver genes along the hair fibroblast trajectory.

Heat map of genes (y-axis) differentially expressed across pseudotime (x-axis) along the hair fibroblast trajectory; corresponding hair follicle cell states and gestational ages (PCW) are indicated alongside pseudotime and blue-red colour scale represents normalised gene expression.

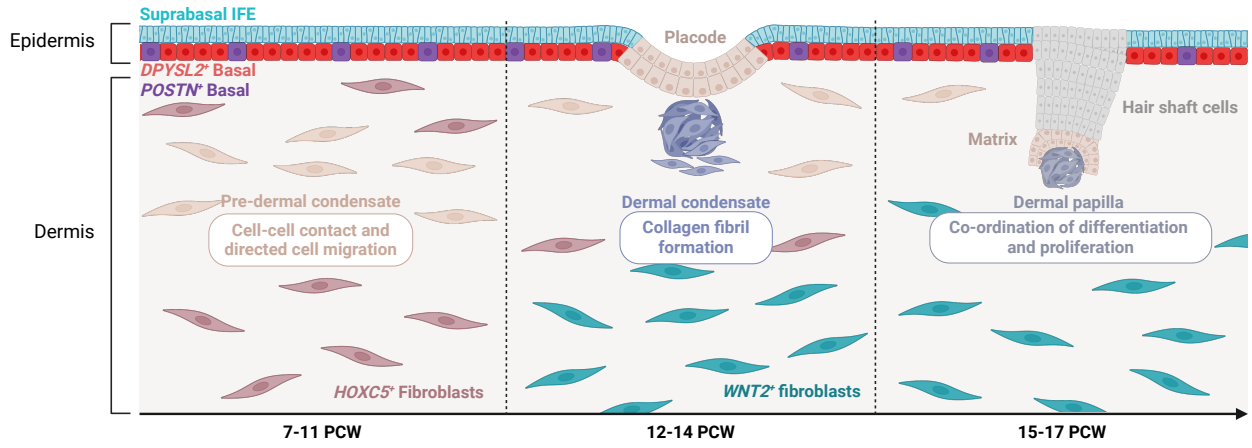

Figure 3.45. Development of hair follicle mesenchyme.

Schematic representation illustrating the cellular processes during specification of the hair follicle mesenchyme in prenatal skin. Adapted from Gopee et al.[157]

Mesenchymal-epithelial cellular crosstalk orchestrating hair follicle development

Having mapped the differentiation of the epithelial and mesenchymal components of the hair follicle individually, the cross-compartment cellular communication which are critical for hair follicle morphogenesis[24,52] was next examined. CellPhoneDB[198] was used to predict the significant ligand-receptor interactions between pairs of cell states in prenatal skin (section 2.4.6). The various epithelial and mesenchymal cell subsets were differentially present across gestation, with some cell states only identified in specific age groups as previously described (sections 3.3.1 and 3.3.2). This was factored into the analysis with cells states abundant in early (≤ 11PCW) or late (≥ 12 PCW) gestation interrogated separately (section 2.4.6).

Assessment of the predicted cell-cell interactions showed that the prevailing mesenchymal-epithelial signal dynamically changed during hair follicle formation (Figure 3.46). The ligand *CXCL12*, on *HOXC5*$^{+}$ early fibroblasts and pre-Dc, was predominantly predicted to interact with the receptor *ACKR3* on early epithelial basal cells before 11 PCW. Consistent with this, the expression of *CXCL12* by hair follicle mesenchymal cells was downregulated after 12 PCW (Figure 3.47).

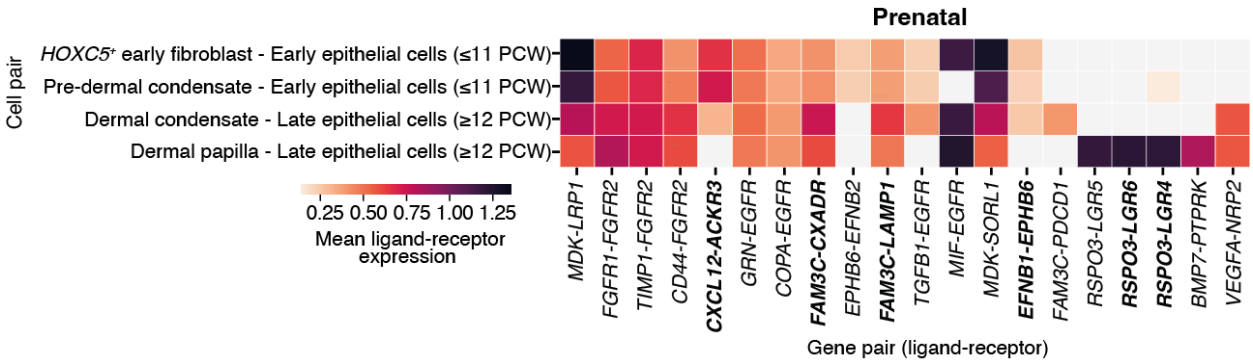

Figure 3.46. Hair follicle mesenchymal-epithelial cellular interactions.

Heat map of predicted ligand-receptor interactions between hair follicle mesenchymal cells and early epithelial (Immature basal) or late epithelial (DPYSL2+ basal, POSTN+ basal, placode, matrix, ORS, CL, IRS, cuticle/cortex) cells in prenatal skin; colour scale indicates the mean expression values for ligand-receptors pairs. The top 10 significant interactions per cell pair are shown; significance determined by permutation testing (adjusted p-value < 0.05) in CellphoneDB.

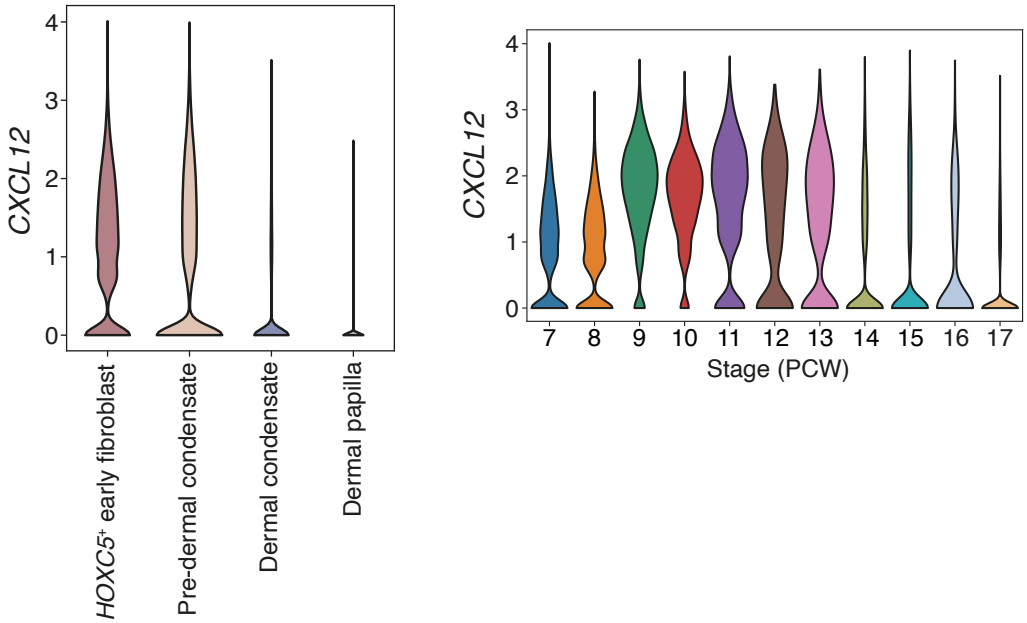

Figure 3.47. Expression of *CXCL12* by hair follicle mesenchymal cells.

Violin plot of *CXCL12* expression (violin width proportional to counts) in prenatal skin hair follicle mesenchymal cells by cell state (left) and by gestational age (PCW) (right).

Differential expression of *CXCL12* was noted earlier along the 'hair fibroblast' trajectory during specification of the migratory pre-Dc (Figure 3.44). Its expression in pre-Dc cells (*PDGFD*$^{+}$) and co-localisation with *ACKR3* on early epithelial cells (*SERPINB7*$^{+}$) was validated by RNAScope analysis (Figure 3.48). This indicated that *CXCL12-ACKR3* interaction may play a role in mediating the migration of the pre-Dc towards the epidermis during hair follicle formation.[388,394]

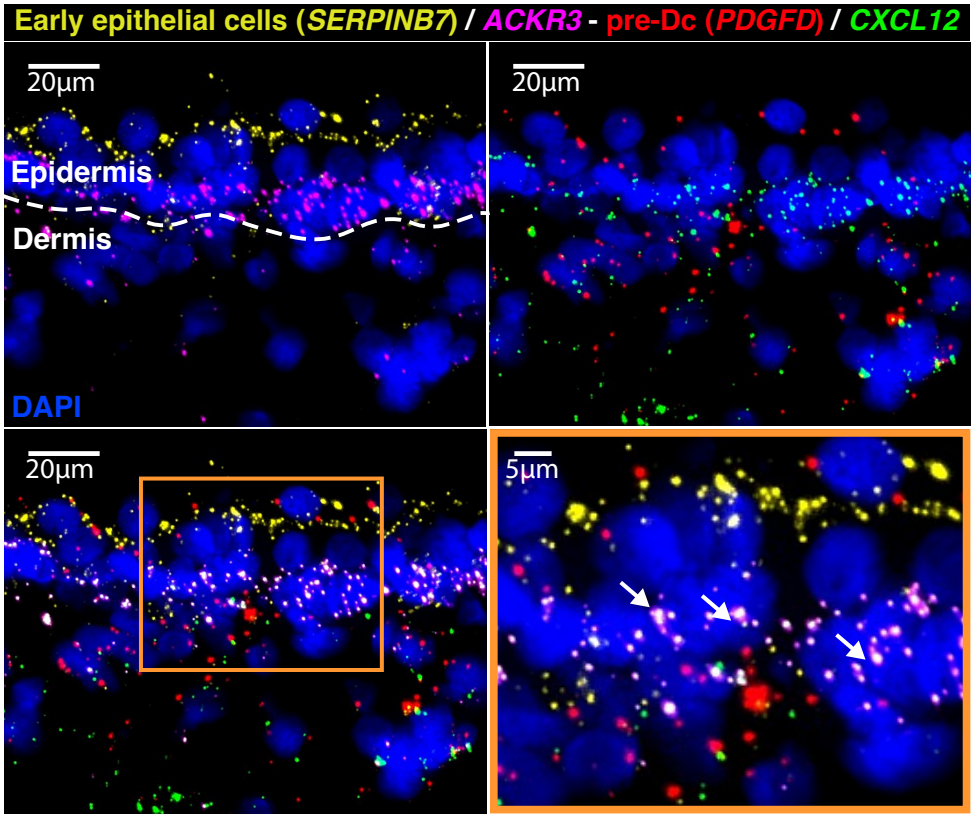

Figure 3.48. RNAscope FISH of mesenchymal-epithelial cellular interactions. RNAscope images showing *ACKR3* (magenta) and *CXCL12* (green) expression in early epithelium (*SERPINB7*$^{+}$; yellow) and pre-Dc (*PDGFD*$^{+}$; red) respectively and co-expression at the dermo-epidermal junction (white arrows) in prenatal skin with DAPI (blue) for nuclear staining. Representative image (10 PCW) shown from n=1 independent biological sample with 4 replicates. Scale bars, 20µm.

The highest mean expression for *FAM3C*, interacting with *LAMP1*/*CXADR* on late epithelial cells (Figure 3.46), was predicted for the Dc which aggregates underneath the placode (Figure 3.45). *FAM3C* is a signalling molecule known to promote cellular migration and invasion,[395,396] suggesting that these interactions may be involved in instructing placode cells to begin invading the dermis. Similarly, ephrin-bs (*EFNB1* and *EPHB6*), which support epithelial cell migration,[397] were predicted to enable cell-cell communication between the Dc and placode (Figure 3.46), suggesting their potential role in Dc-mediated dermal invagination of the hair placode.

The upregulation of *RSPO3* during differentiation of the Dp was already noted along the 'hair fibroblast' pseudotime (Figure 3.44). *RSPO3* specifically from the Dp was predicted to interact with R-spondin receptors *LGR4/6* in hair follicle epithelial cells (Figure 3.46) and these interactions have been shown to contribute to proliferation of adjacent matrix cells which subsequently give rise to the differentiated inner layers of the hair follicle.[392] Overall, this analysis of predicted ligand-receptor interactions provided novel insights into the distinct mesenchymal-eptithelial crosstalk that orchestrate the different stages of human prenatal hair follicle formation and the processes they support are summarised in Figure 3.49 alongside the mechanisms involved during differentiation of the hair follicle mesenchyme.

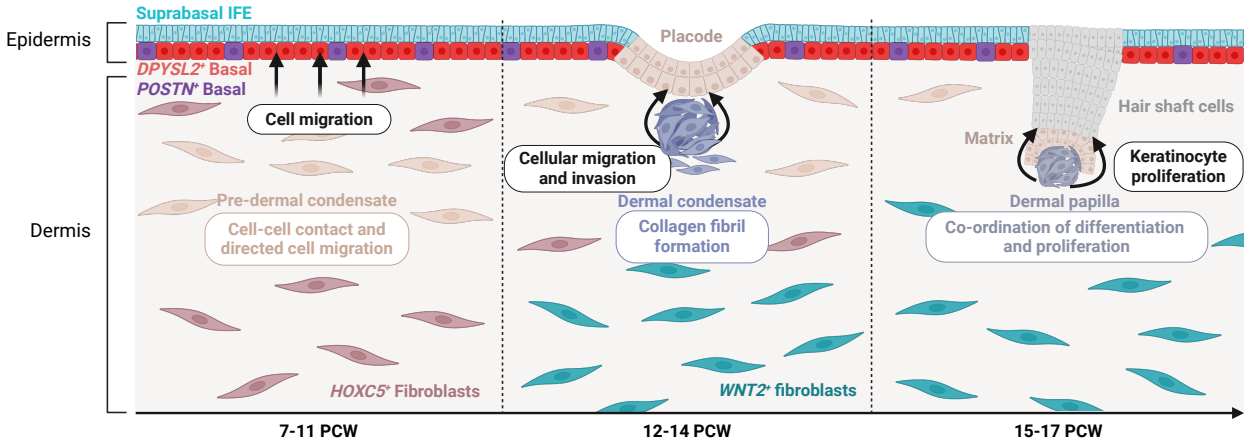

Figure 3.49. Mesenchymal-epithelial crosstalk.

Schematic representation illustrating the crosstalk between the mesenchymal and epithelial compartments alongside cellular processes during the different stages of hair follicle formation in prenatal skin. Taken from Gopee et al.[157]

The ligand-receptor pairs identified in prenatal skin were also evaluated in the skin organoid data. The majority of these interactions were notably conserved between the mesenchymal and epithelial cells of the skin organoid at the relevant stages during hair follicle formation (Figure 3.50). This corroborated the findings from the prenatal skin analysis, providing orthogonal validation, and further highlighted the faithful recapitulation of in vivo skin by the skin organoid model and its utility to study hair follicle development.

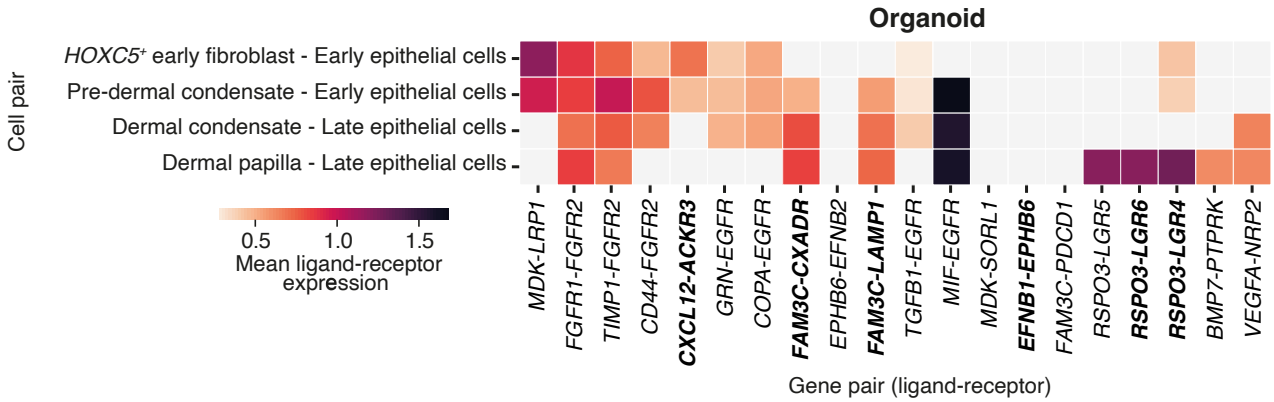

Figure 3.50. Conservation of mesenchymal-epithelial interactions in skin organoids. Heat map of predicted ligand-receptor interactions between hair follicle mesenchymal cells and early epithelial (Immature basal) or late epithelial (*DPYSL2*$^+$ basal, *POSTN*$^+$ basal, placode, matrix, ORS, IRS, cuticle/cortex) cells in skin organoid data; colour scale indicates the mean expression values for ligand-receptors pairs. The same top 10 significant interactions per cell pair identified in prenatal skin are shown; significance determined by permutation testing (adjusted p-value < 0.05) in CellPhoneDB.

Comparison between human and mouse hair follicle development

The above analyses hinted at several parallels between human and mouse hair follicle development including the presence of the transitional pre-Dc stage during hair mesenchymal differentiation,[59] upregulation of overlapping genes during ORS (e.g. *SOX9*) and IRS (e.g. *WNT10B*) specification,[58] and involvement of a few similar cell-cell interactions such as *RSPO3* from the Dp with R-spondin receptors.[392] A focused comparison was, therefore, additionally conducted to assess for further similarities and identify potential differences between human and mice hair follicle morphogenesis.

First, the expression of key signalling genes involved in murine hair follicle formation was tested in the prenatal skin hair follicle epithelial and mesenchymal cells. The Wnt/β-catenin pathway is crucially important for hair follicle induction.[52,58] In mice, this involves signalling through the epidermally-expressed β-catenin binding transcription factor *Lef1*, whose elimination results in absent hair follicles, as well as *Wnt10b* and *Edar* which are expressed in the placode and its precursors and are required for placode formation.[52,58] Wnt signalling is further controlled by an isoform of the p63 protein, which plays a vital role in cell fate commitment in the epidermis.[58] Following placode initiation, fibroblast growth factor 20 (*Fgf20*) from the placode and its precursor states induces fate-specification of the pre-Dc in the underlying dermis and its subsequent aggregation to form the Dc.[58,59] The Dc then provides inhibitory signalling via *Bmp4* to inhibit hair follicle formation in surrounding interfollicular epidermis whilst also supporting placode maturation through the BMP inhibitor Noggin (*Nog*).[58] Eventually, hair follicle downgrowth into the dermis ensues via Pdgfa and Tgf-β signalling in the epidermal and dermal compartments respectively.[58] Assessment of the expression profiles of the corresponding orthologous genes showed that similar pathways were activated in human prenatal skin during hair follicle development (Figure 3.51).

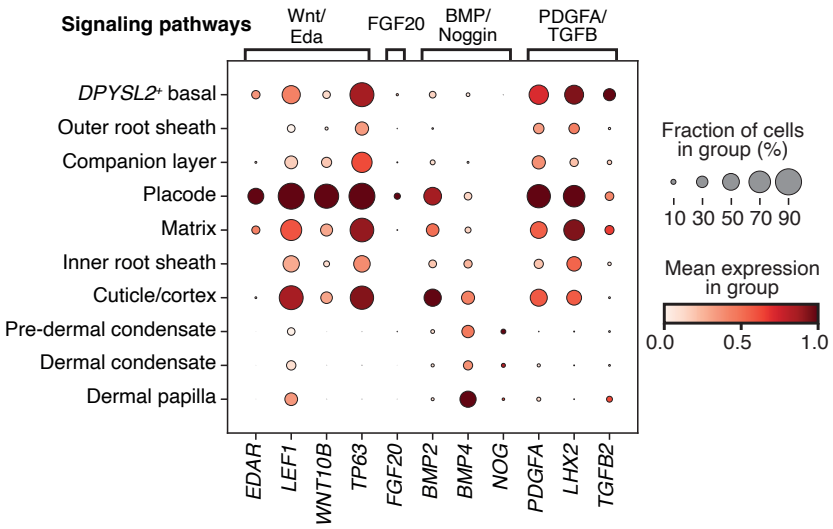

Figure 3.51. Expression of known genes involved in hair follicle signalling.

Dot plot of expression of genes reported in mouse hair follicle formation[58] by epithelial and mesenchymal cell states in prenatal skin; for a given gene, dot colour indicates normalised variance-scaled mean expression and dot size indicates the percentage of expressing cells in each category.

Cross-species data integration and analysis were then performed using a scRNA-seq (10x platform) dataset of mouse embryonic skin.[61] This consisted of several cutaneous cell lineages from different stages of mouse embryogenesis (E12.5, E13.5 and E14.5): keratinocyte, melanocyte, Schwann cell, vascular (vessel BECs) and lymphatic (vessel LECs) endothelium, mural cells, muscle (early, mid and late), immune cells (macrophage, mast cell, DC) and fibroblast (Fib).[61] The fibroblasts comprised different subsets, including progenitor fibroblasts (Fib Origin) which formed into muscle-supportive fibroblasts (Fib Muscle), fascia-forming fibroblasts (Fib Inter), and fibroblasts of the lower and upper dermis (Fib Lower and Fib Upper).[61] The upper dermal fibroblasts (Fib upper) further differentiated into the pre-Dc (Fib EarlyDC) and Dc (Fib LateDC) of the hair follicle.[61] This dataset did not include the Dp, which develops after E14.5. Another dataset which captured the Dp from E16.5 was added but integrated poorly with the rest of the mouse skin data, contributing only a small number of cells (< 100 cells), and was thus excluded from further analyses.

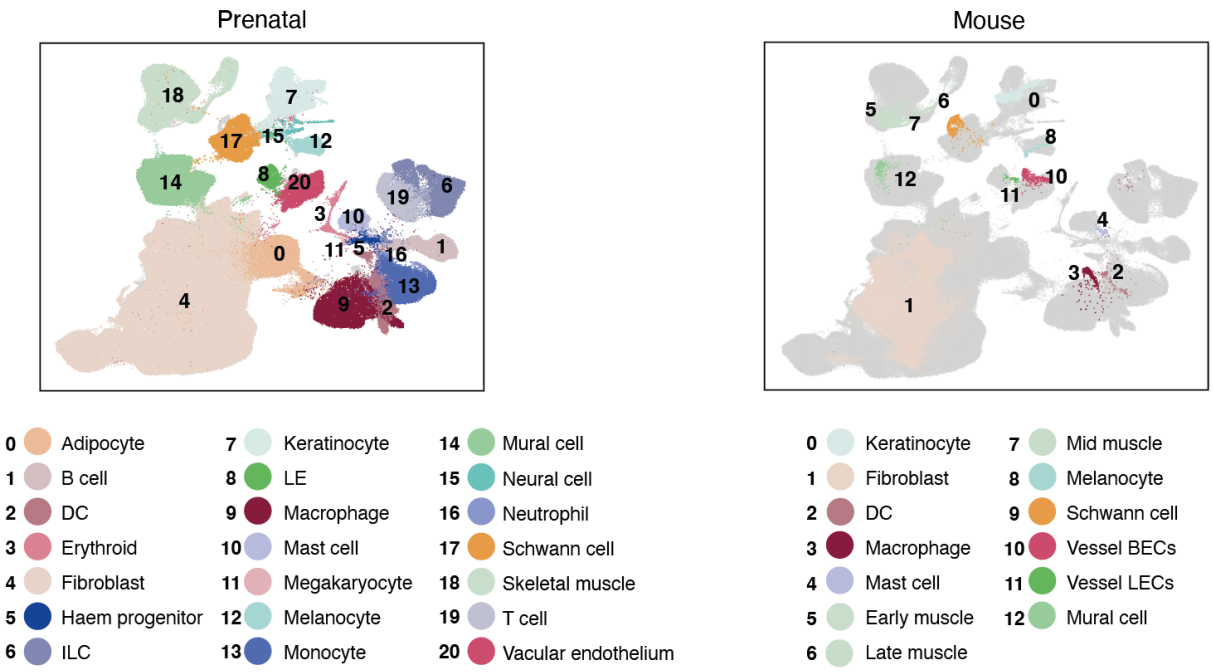

Figure 3.52. Cross-species comparison with mouse skin.

UMAP visualisation of co-embedded cell clusters from human prenatal skin (left) and mouse embryonic skin (right) in integrated scRNA-seq data; clusters are coloured by broad cell type annotations. DC: dendritic cell; ILC: innate lymphoid cell; LE: lymphatic endothelium; Vessel BECs: vessel blood endothelial cells; Vessel LECs: vessel lymphatic endothelial cells.

Comparison of the human prenatal skin and mouse embryonic skin data, using scVI integration and LR (section 2.4.4), demonstrated high correspondence across the broad lineages (Figures 3.52 and 3.53). However, assessment of within-lineage sub-populations showed less clear-cut distinctions as shown for the fibroblast subsets (Figure 3.54). For instance, the human Dc aligned to both the murine Dc as well as its precursor state pre-Dc. (Figure 3.54). Likewise, the human pre-Dc corresponded to the early stage fibroblasts (Fib Origin and Fib Upper) which differentiate into the pre-Dc (Figure 3.54).

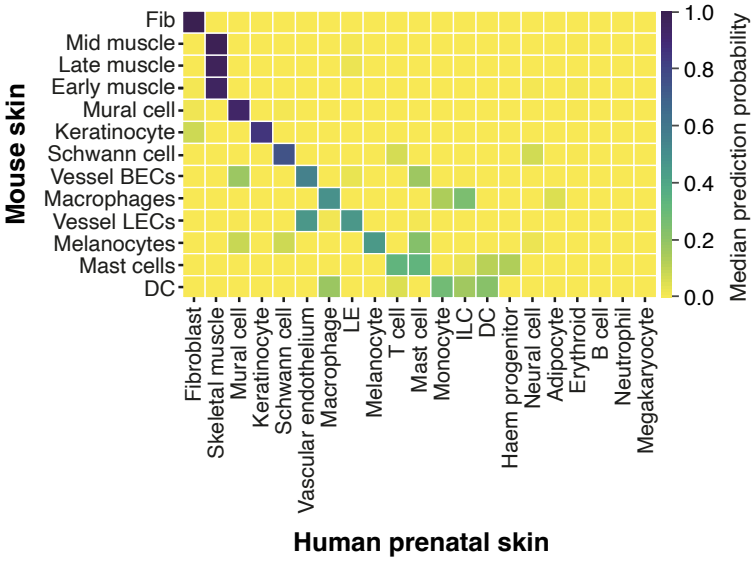

Figure 3.53. Comparison of broad cell types between human and mouse skin. Heatmap showing degree of correspondence between human prenatal and mouse embryonic skin for broad cell types; colour scale indicates median prediction probabilities for mouse broad cell labels (y-axis) from a logistic regression model trained on human prenatal skin data (x-axis).

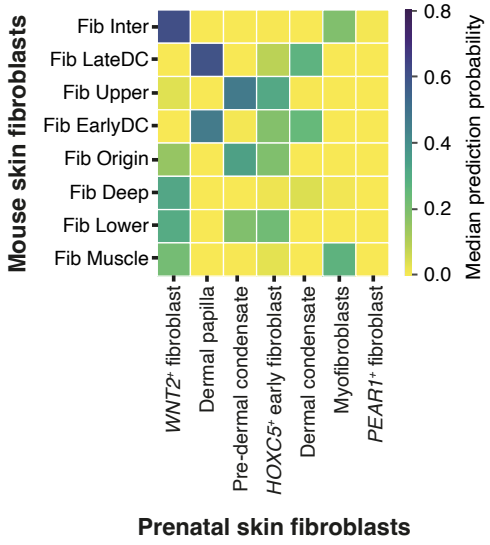

Figure 3.54. Comparison of fibroblast cell states between human and mouse skin. Heatmap showing degree of correspondence between human prenatal and mouse embryonic skin for refined cell states (only fibroblast populations shown from all cell states); colour scale indicates median prediction probabilities for mouse fibroblast labels (y-axis) from a logistic regression model trained on human prenatal skin data (x-axis). Fib: fibroblast.

These results could be explained by the recognised limitations of cross-species comparative analyses using gene expression-based methods to accurately distinguish closely related cell states,[398] especially hair follicle sub-populations with highly shared gene expression profiles. Alternatively, this could be due to potential transcriptional differences between human and mouse skin whereby mouse hair follicle mesenchymal cells are in a more differentiated state compared to the corresponding cell types in human skin.[157] Additionally, no murine counterpart was identified for some human fibroblast populations such as *PEAR1*$^{+}$ fibroblasts (abundant in later gestation prenatal skin) which may result from the limited gestation periods sampled in mice or species-specific fibroblast differentiation.[157]

To further probe the mis-match noted between human and mouse pre-Dc and Dc, differential gene expression and pathway enrichment analyses were conducted on the scVI-combined dataset. This revealed differences in the expression profiles of key genes involved in hair follicle formation. The Wnt inhibitors *DKK1* and *CAV1*, that were expressed in early mouse fibroblasts (Fib upper) but downregulated as they acquired Dc-fate,[61] were still significantly expressed by the human Dc (Figure 3.55). Similarly, expression of *DKK2*, which is permanently downregulated by mouse progenitor fibroblasts as they transition into hair-committed mesenchymal cells,[61] was still retained in the human pre-Dc (Figure 3.55). Additionally, several genes implicated in hair mesenchymal-epithelial signalling (*ALX4, CD109, FGF7/10*)[399–402] were differentially expressed between human and mouse pre-Dc and Dc (Figure 3.55).

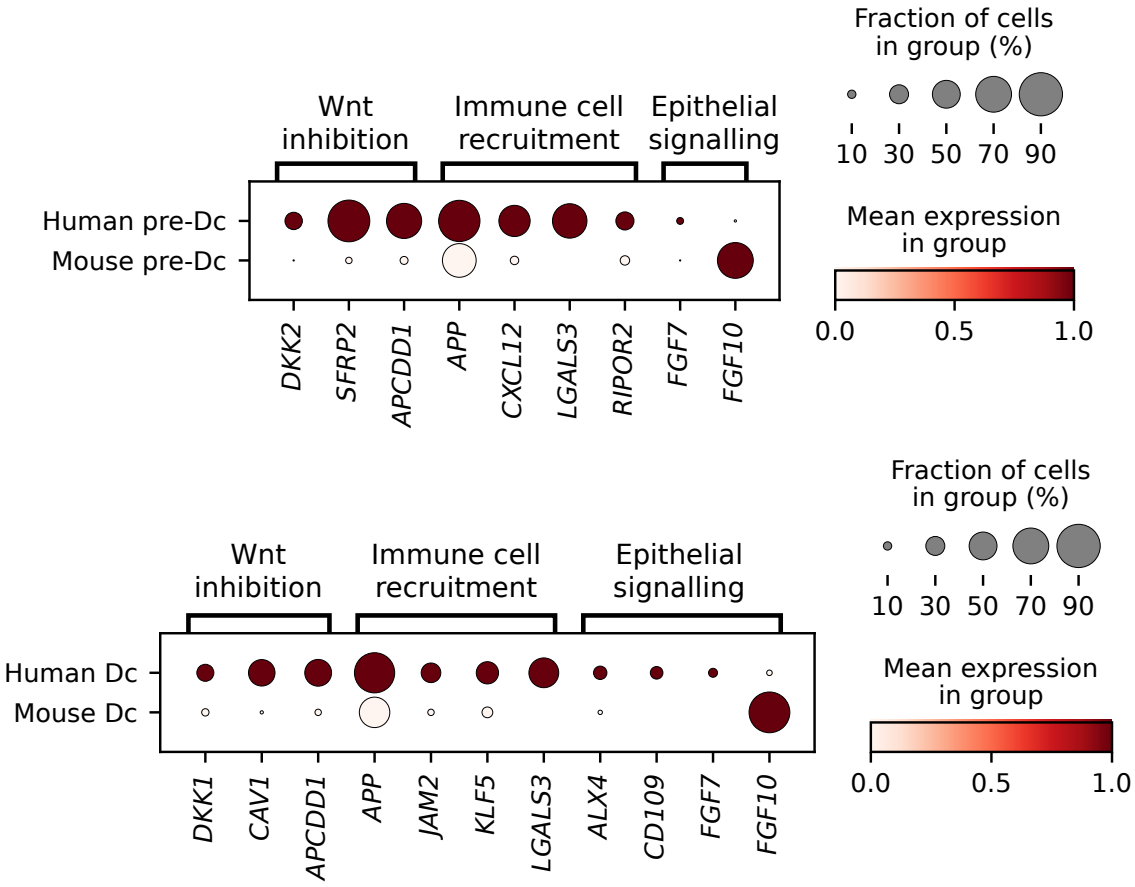

Figure 3.55. Comparison of hair follicle mesenchymal cells between human and mouse. Dot plot of genes differentially expressed by human and murine pre-Dc cells (top) and Dc cells (bottom) during hair follicle development; for a given gene, dot colour indicates normalised variance-scaled mean expression and dot size indicates the percentage of expressing cells in each category.

Interestingly, pathways related to immune recruitment were also identified as significantly enriched in human prenatal skin only. Hair follicles are known to chemotactically attract immune cells, such as macrophages and T cells, which influence stem cell quiescence and proliferation and hair follicle regeneration.[403] Human pre-Dc and Dc upregulated genes involved in lymphocyte and macrophage chemotaxis (*JAM2*, *KLF5*, *LGALS3*)[404–406] compared to mouse pre-Dc and Dc (Figure 3.55), with a notable absence of T cells in mouse embryonic skin up to E14.5.[61] This suggested that immune cell recruitment and their contribution to hair follicle formation may begin earlier in humans compared to mice.

Overall, these analyses indicated that although several signalling pathways contributing to hair follicle induction and development were conserved between human and mouse, heterogeneity in the gene expression profiles of corresponding cell states were readily identifiable. This implied potential differences may exist in the tempo of hair mesenchyme differentiation and the timings of immune cell contribution between human and mouse prenatal skin development.

3.3.5 Spatial transcriptomic atlas of early human prenatal skin

The single cell atlas provided a detailed census of the cellular constitution of human prenatal skin across gestation. However, the dissociative nature of scRNA-seq data generation critically loses the spatial context within which these cells operate (section 1.4). Understanding cellular microanatomical organisation can uncover the roles played by these various immune and non-immune fractions during development by illuminating the neighbouring cells with which they potentially interact.[113,147] In this section, I describe how the scRNA-seq data generated above was used to decompose spatial transcriptomic data from prenatal skin to spatially re-situate the identified cell states in situ and infer the tissue microenvironments to which they localise.

Prenatal skin sampling

Spatial transcriptomic data was newly generated from four skin sections using the 10x Visium platform (section 2.3), including two replicates from each of two tissue specimens at 10 PCW (Appendix B2). This was combined with a published spatial transcriptomic dataset of human embryonic limb[141] (from which only skin-related information was retrieved) to give a total of 11 Visium samples (6-10 PCW) (Appendix B2). These included male (n=7) and female (n=4) samples collected from face, trunk and limb skin. Samples from early gestational ages were used given the objective to investigate if immune cells co-localise with non-immune cells to contribute to skin morphogenesis and the previous indication that this may occur prior to uptake of immune functions in the second trimester.[101]

Spatial transcriptomic data analysis

Alignment of Visium sequenced data using Space Ranger software (10x Genomics) (section 2.5.1) provided the transcriptome profile for each skin section in the form of a 'counts matrix' (Visium spot (rows) by genes (columns)) mapped to its corresponding H&E image. The matrices from the different skin sections were concatenated and relevant metadata added to produce the final spatial dataset for further analysis.

To resolve the location of cell states identified in the prenatal skin scRNA-seq data within the spatially profiled skin sections, Cell2location[147] analysis was performed (section 2.5.2). This estimated the abundance of the early-gestation resident cell states in each tissue spot to create a map of their spatial distribution.[147] The results revealed distinct compartmentalisation of fibroblast subsets in prenatal skin (Figure 3.56) which were not obvious on H&E images (Figure 3.30), with *HOXC5*$^{+}$ early fibroblasts restricted to the upper dermal region and *WNT2*$^{+}$ fibroblasts present throughout and increasing in relative abundance further into the dermis.

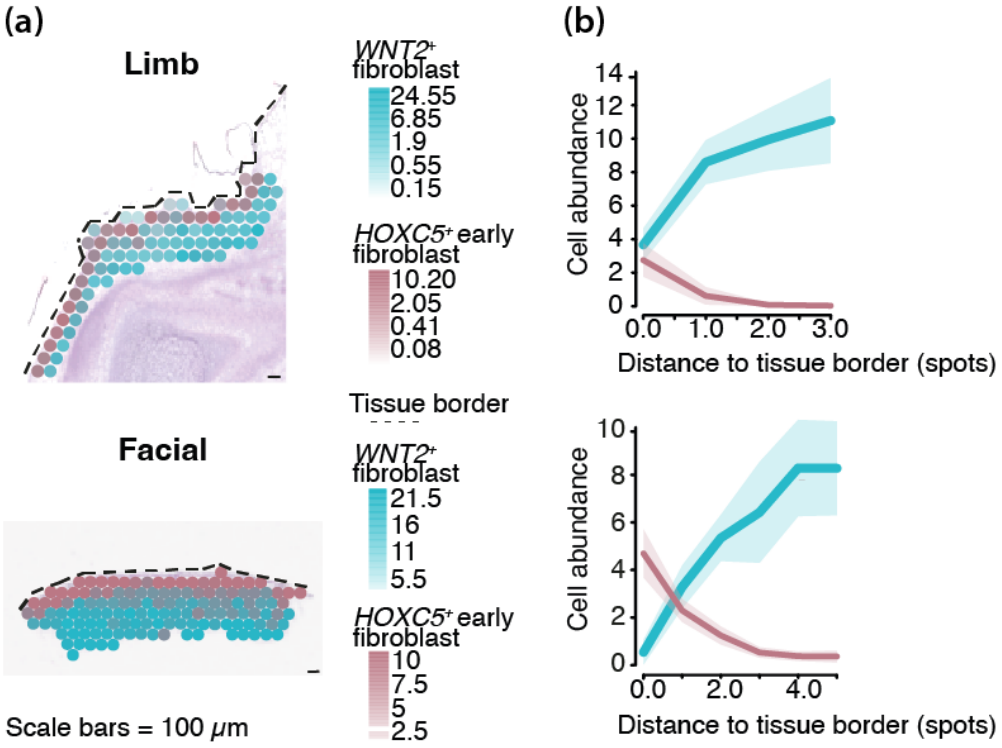

Figure 3.56. Spatial distribution and abundance of *WNT2*$^{+}$ fibroblasts and *HOXC5*$^{+}$ early fibroblasts from skin surface.

(a) Mapping of the estimated cell abundances (colour gradients) of *WNT2*$^{+}$ fibroblasts (cyan) and *HOXC5*$^{+}$ early fibroblasts (red) overlaid on Visium histology images of limb (top) and facial (bottom) prenatal skin. Dashed lines represent tissue borders. Representative images from n=5 independent biological samples with 2-3 replicates. Scale bars, 100 µm. (b) Curve plots showing the mean per-spot normalised abundance (y-axis) of *WNT2*$^{+}$ fibroblasts (cyan) and *HOXC5*$^{+}$ early fibroblasts (red) along the axial distance (x-axis) to skin surface (tissue border); data shown as mean (line) ± 2 SD confidence intervals (CI) (shaded area).

Identification of tissue microenvironments

The abundance map from Cell2location was then used to determine which cell states were likely to co-locate in tissue microenvironments in prenatal skin. This was done by applying NMF to predict tissue microenvironments (section 2.5.3). The output of the NMF analysis provided the estimated contribution of each cell state to every predicted microenvironment (1 to 10) (Figure 3.57). Although cell states were assigned a primary microenvironment in which their highest fraction was present, smaller contributions to additional microenvironments were also apparent (Figure 3.57). Correlation analyses were carried out to confirm co-location in these additional microenvironments by calculating the Pearson coefficients between the normalised abundances of pairs of cell states in each sample (section 2.5.3). From these two approaches, co-location was designated by a high proportion of two or more cell states within the same microenvironment and/or positive correlation coefficients between cell state pairs.

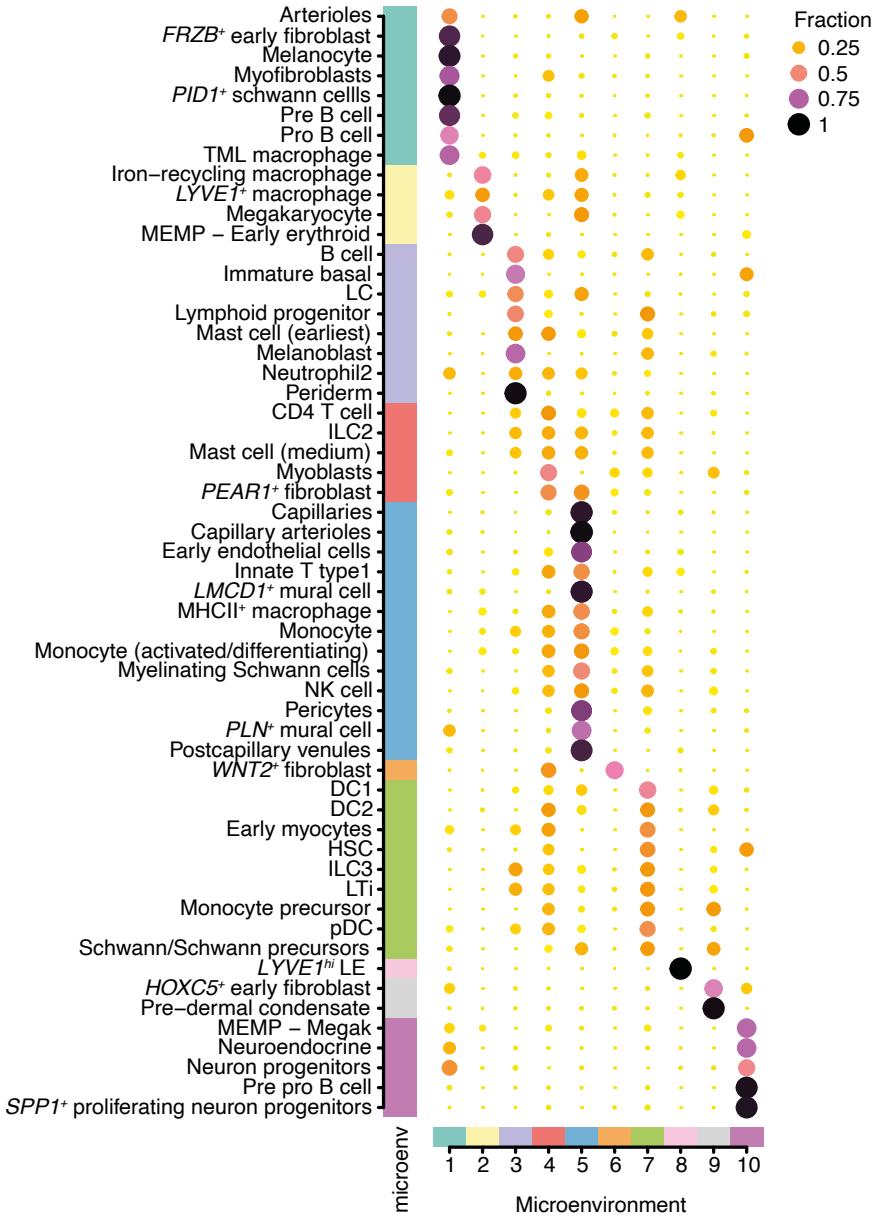

Figure 3.57. Spatial microenvironments in prenatal skin.

Dot plot showing estimated fractions of cell states across predicted tissue microenvironments (NMF-based factors) in prenatal skin (normalised by cell state); the colour bar indicates assignment of cell states to microenvironments. DC: dendritic cell; HSC: hematopoietic stem cell; ILC: innate lymphoid cell; LC: Langerhans cell; LTi: lymphoid tissue inducer; MEMP: megakaryocyte-erythroid-mast cell progenitor; NK cell: Natural killer cell; LE: lymphatic endothelium; pDC: plasmacytoid dendritic cell, TML macrophage: *TREM2*$^{+}$ microglia-like macrophage.

Distinct groupings of cell states, each including specific types of immune cells, were predicted to co-localise in tissue microenvironments in prenatal skin (Figure 3.57). For instance, macrophage subsets co-located with endothelial and neural cells in microenvironments 1 and 5 (Figure 3.57) which were termed ‘early neurovascular’ and ‘late neurovascular’ microenvironments respectively - early and late designations were based on the differential abundance of certain cell states such as TML macrophages enriched in early gestation and MHCII^{+} macrophages in late gestation (Figure 3.23). This was further supported by correlation analyses of the different endothelial and macrophage subsets (Figure 3.58).

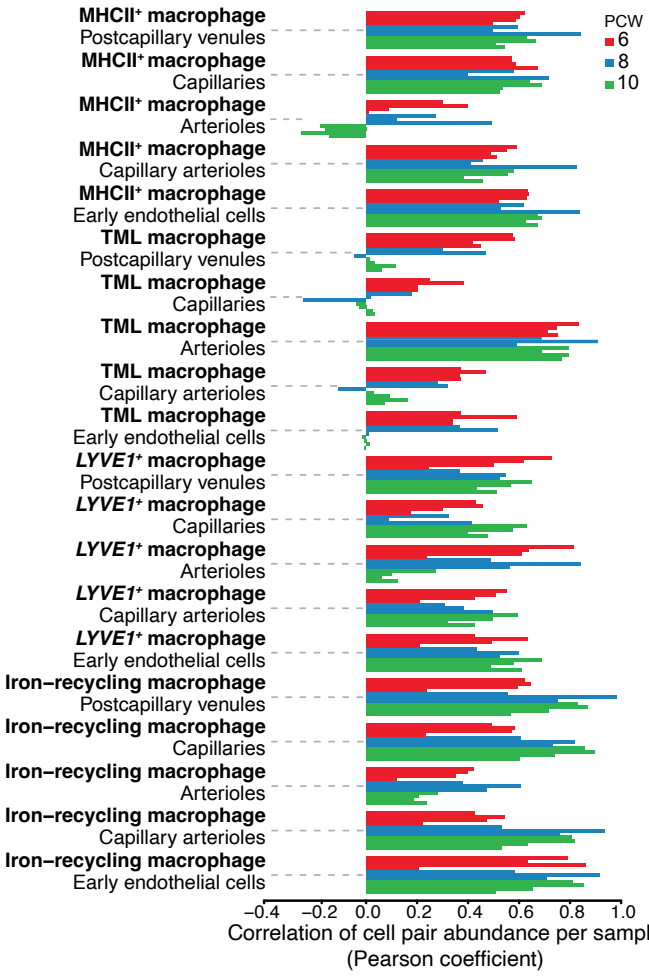

Figure 3.58. Co-location of macrophages and endothelial cells by correlation analysis. Bar plot showing Pearson correlation coefficients between pairs of cell state abundances (normalised per spot) for macrophage and endothelial cell populations in prenatal skin. Pearson correlation coefficients were calculated across all skin-covered spots of Visium samples; each sample is shown by an individual bar. TML macrophage: *TREM2*$^{+}$ microglia-like macrophage.

Early epithelial cells co-located with lymphoid subsets (microenvironment 3) whilst fibroblast populations contributed to several microenvironments where macrophages were also predicted to localise (1, 4, and 5) (Figure 3.57), suggesting potential interactions between these immune and non-immune cells during skin morphogenesis. The pre-Dc formed a distinct microenvironment (microenvironment 9) with *HOXC5*$^{+}$ early fibroblasts (Figure 3.57), as expected from their common location in the upper dermis of early gestation skin. Interestingly, this microenvironment also had small contributions from immune cells such as DCs, monocyte precursors and ILCs, which co-located with the pre-Dc based on positive coefficients from correlation testing (Figure 3.59). Recruitment of immune cells, including lymphocytes, during hair follicle development in prenatal skin was also identified in earlier analyses (section 3.34). The cell-cell communication between pre-Dc and co-locating ILC3/LTi cells were therefore assessed. This revealed ligand-receptor interactions between pre-Dc and ILC3/LTi cells that are involved in modulation of cellular adhesion and migration (*CXCL12-CXCR4/DPP4*),[394,407] suggesting that these ILCs may play a role in supporting the migration of the pre-Dc during hair follicle formation (Figure 3.60).

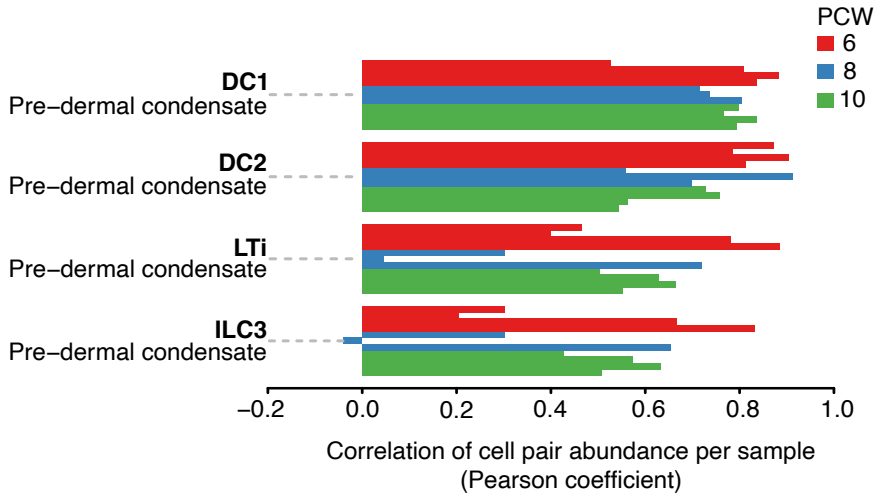

Figure 3.59. Co-location of pre-Dc and immune cells by correlation analysis.

Bar plot showing Pearson correlation coefficients between pairs of cell state abundances (normalised per spot) for pre-Dc and immune cells (DC1, DC2, LTi and ILC3) in prenatal skin. Pearson correlation coefficients were calculated across all skin-covered spots of Visium samples; each sample is shown by an individual bar. DC: dendritic cell; ILC: innate lymphoid cell; LTi: lymphoid tissue inducer.

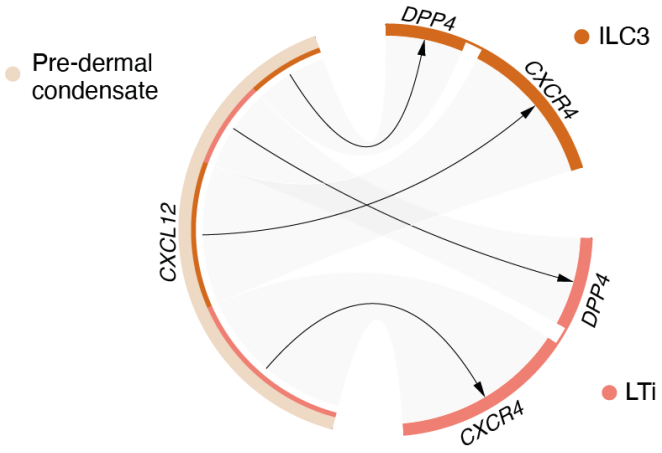

Figure 3.60. Cell-cell interactions between pre-Dc and immune cells.

Circos plot showing selected significant interactions predicted between pre-Dc and ILC3 or LTi cells in prenatal skin. Arrows indicate directionality (ligand to receptor) and connection widths (shaded areas) are proportional to the mean expression values of ligand-receptors pairs; significance determined by permutation testing (adjusted p-value < 0.05) in CellPhoneDB.

Overall, these findings lend support to the hypothesis that immune cells co-localise with non-immune cells in tissue microenvironments in prenatal skin. The functional implications are further explored in Chapters 4 and 5.

3.4 Section discussion

The human prenatal skin, and the cellular and molecular changes it undergoes during development, holds invaluable clues to improve our understanding of cutaneous and trichological disorders, identify disease-coopted programmes for therapeutic targeting and enhance in vitro modelling. Yet, this complex organ has been limitedly profiled, hindered by availability of tissue and techniques that enable unbiased examination at scale. The greater accessibility to commercial scRNA-seq and spatial platforms for whole transcriptome profiling has propelled the in-depth exploration of developmental tissues, driven by the HDCA initiative.[109] Investigations of the prenatal skin, however, have focused primarily on its immune compartment at the expense of its diversity of non-immune cells.[98,148] A thorough understanding of prenatal skin development requires joint assessment of both immune and non-immune cells as well as the spatial context in which they operate. In this section, I summarise the generation of a comprehensive multi-omics atlas of human prenatal skin to address the constraints of previous studies and the novel insights unravelled from its analysis. The limitations and areas for future research are also discussed.

3.4.1 Multi-omics profiling of human prenatal skin

In this chapter, I described the systematic charting of human prenatal skin cellular composition between 7-17 PCW, identifying 86 granular cell states, grouped into 21 broad cell groups, and their differential abundance across gestation. Loss of spatial information resulting from the dissociative nature of scRNA-seq data generation was overcome by generating spatial transcriptomic profiles of prenatal skin and using computational methods to locate resident cells identified from scRNA-seq experiments in situ. This multi-omics human prenatal skin atlas, the first of its kind, presents a valuable resource for the skin and developmental scientific communities and has been made freely accessible at: https://developmental.cellatlas.io/fetal-skin.

Although careful consideration was given to ensure capture of all cell states, including adjustment of FACS gating strategies (sections 2.2.2 and 3.3.1), the absence of some skin cell types were noted and investigated. Sebaceous and sweat gland cells were not captured. As these cells mature after 16-18 PCW[29,408] and are expected to be few in number, several samples from later gestation stages would be needed to reliably detect them. Similarly, dermal sheath cells which contain the self-renewing mesenchymal cells that maintain the Dp in postnatal hair follicles[409] were not distinguished. These were, however, present in a previous single cell analysis of human foetal scalp from 16 and 17 PCW.[410] Scalp hair follicles develop earlier compared to trunk skin (cephalo-caudal development),[42,53] suggesting that older samples would be required to isolate them from trunk skin. The scarcity of late gestation samples coupled with the unavailability of foetal samples over 20 PCW from HDBR in the UK[109] may however preclude this. Integration with additional published scRNA-seq datasets of prenatal skin, from different anatomical sites and later gestational ages from other research groups, could potentially address this issue if non-immune cells are routinely included and would provide an even more comprehensive assessment of prenatal skin across space and time.

3.4.2 Evaluating the faithfulness of the skin organoid model to in vivo skin

The skin organoid model recapitulated in vivo skin to a degree. Epidermal, dermal stromal, neural and melanocytic cells were present with organoid epithelial and stromal cell states demonstrating high transcriptional alignment to prenatal skin counterparts. This similarity was further evident from inferred trajectory analysis, which showed the same differentiation paths for skin organoid and prenatal skin, and comparable gene expression profiles between the two tissues such as for disease-causing genes. However, notable differences were also observed: immune cells were absent in the skin organoid and endothelial cells were markedly reduced. It is reasonable to suppose that information garnered from analysis of skin development could be harnessed to engineer the skin organoid model towards improved representation of in vivo skin. The feasibility of this is further assessed in Chapter 5.

Of note, the comparative analyses undertaken between skin organoid and in vivo skin are based on assessment of cellular end-states. The dynamic changes occurring, such as in transcription factor regulation, to reach these terminal cell states were not compared. The specific biological pathways and processes activated in in vitro models can differ from in vivo tissues despite differentiation into cell states that are transcriptionally similar.[411] Recognising these divergent points between the two systems is critical to understand limitations and optimisation of organoid models.[411] New computational frameworks that enable the precise alignment of differentiation trajectories of two conditions, such as in vitro versus in vivo systems, and identification of mismatches are being developed.[411] These could be applied to further query the skin organoid against prenatal skin at transcriptional factor level and fine-tune culture conditions accordingly.

3.4.3 Insights into hair follicle development

The prenatal skin atlas allowed for unprecedented insights into human de novo hair follicle formation, for which molecular information has up to now largely been inferred from mouse models.[224] Prenatal-specific cell states were isolated including the hair placode and pre-Dc, the latter representing the first identification of this transitional fibroblast state in humans. The progenitor states (*POSTN*$^{+}$ basal cells and *HOXC5*$^{+}$ early fibroblasts) that give rise to the differentiated hair follicle structures such as IRS, ORS and Dp were revealed, alongside the cellular processes and mesenchymal-epithelial interactions that underpin directed migration and aggregation of the pre-Dc underneath the epithelial placode, loss of cellular adhesion accompanying matrix invagination, and Dp-guided proliferation and differentiation of adjacent matrix progenitors (section 3.3.4). Crucially, immune cells appeared to be involved in early hair follicle development. Tregs accumulated from 15 PCW, potentially recruited by matrix-expressed chemoattractants, and ILC3 and LTi cells were implicated in pre-Dc migration, supporting the potential moonlighting functions of immune cells in skin and hair follicle morphogenesis. The specific roles played by these immune cells in hair follicle formation would need to be confirmed in future experiments.

Intriguingly, the CL was observed to be transcriptionally similar to and differentiate along the same trajectory as the ORS, despite the current prevailing view that it is part of the inner layers of the hair follicle and develop from matrix progenitors.[376,377] The compartmental association of the CL, if any, has historically been debated. For some, it belongs to the outer layer of the hair follicle with the ORS,[412,413] for others to the inner group as the outermost covering of the Henle layer of the IRS,[414,415] and for others still to neither the outer nor inner compartments but rather constitutes a discrete hair follicle structure.[27,416] A clonal analysis study by Sequeira and Nicolas[376] in adult mice eventually demonstrated that the CL shares an origin and growth kinetics with other inner layers, deriving from cells adjacent to IRS progenitors in the hair matrix. The CL was thus established as the seventh member of the hair follicle internal compartment, alongside the hair shaft and IRS layers.[376] However, evidence in the past years suggests this may not be the complete picture. A fate-mapping study traced CL development to earlier than hair matrix specification and showed that ablation of signalling (BMP and Shh) which disrupted IRS differentiation did not impact CL formation, which was confirmed in both embryonic and adult mice follicles.[377] The CL was distinguished as separate from the IRS and inner hair follicle layers and proposed to arise from early matrix progenitors.[377] More recently, a single cell study of embryonic mice hair follicles further reported increased transcriptional similarity between CL cells and ORS cells,[60] in line with results described in section 3.3.4. Although additional validation experiments are required, these findings suggest that the CL may be developmentally closer to the outer layer ORS and form independent of the hair matrix.[60]

Although several parallels were noted between human and mouse prenatal hair follicle development, including the signalling pathways coordinating hair follicle initiation and downgrowth as well as overlapping genes during ORS and IRS differentiation, cross-species differences in mesenchymal cell states were also revealed (section 3.3.4). Consistently, both the murine pre-Dc and Dc were in a more advanced stage of differentiation compared to corresponding cell states in prenatal skin. This could be due to organismal differences in the length of gestation and tempo of differentiation. The longer gestation in humans allows for slower-paced cellular differentiation and more progressed organ maturation in utero compared to the shorter gestational periods in mice requiring more rapid differentiation to form functional tissues at birth.[417–419] Additionally, immune chemotactic genes were differentially upregulated by Dc and pre-Dc between species, suggesting potential disparities in the involvement of immune cells during human and murine hair follicle formation. However, the restricted gestational ages sampled in mouse

embryonic skin (E12.5-E14.5), resulting in absence of cell states such as Dp, together with the intrinsic fallibilities of existing computational tools for cross-species analysis[398] limit the interpretation of these findings. Further analyses with murine samples from later gestation and more sophisticated methods for stringent cross-species alignment and comparison are required as they become available.

3.4.4 Immune and non-immune cells co-locate in prenatal skin microenvironments

Finally, the multi-omics atlas also exposed the intricate cellular micro-anatomical organisation of prenatal skin, uncovering tissue microenvironments where specific immune and non-immune cells were predicted to co-locate (section 3.3.5). Whether these microenvironments constitute actual functional units where immune cells support prenatal development is explored in subsequent chapters 4 and 5. Based on suggestions from prior studies that immune cells may exercise in these non-canonical roles in early gestation before adopting their immune functions,[101] spatial transcriptomic data was primarily generated from first trimester prenatal skin. The spatial transcriptomic repertoire of prenatal skin may need to be broadened in future works to assess whether co-location of immune and non-immune cells continues throughout later trimesters and whether morphogenic roles of immune cells, if any, evolve as gestation progresses.

Chapter 4 . Early dermal fibroblasts and macrophages contribute to scarless healing potential of prenatal skin

4.1 Introduction

The comprehensive single-cell and spatial profiling of prenatal skin began to untangle the intimate relationship between immune and non-immune populations during human development. Several subsets of resident immunocytes were predicted to co-locate with cells that form the structural components of the developing skin, including epidermis, dermis and blood vessels, in tissue microenvironments (section 3.3.5). In particular, macrophages shared microenvironments with early prenatal skin fibroblasts (section 3.3.5), suggesting they may influence these dermal stromal cells during skin morphogenesis. Macrophages are known to interact with fibroblasts to mediate repair, regeneration and fibrosis after injury in various tissues, adopting a spectrum of states from pro-inflammatory and pro-fibrotic to anti-inflammatory and pro-regenerative.[420] As such, they have been shown to play key roles in postnatal skin wound healing in mice and humans.[420–422] However, their specific contributions during development have not been fully explored, particularly whether they may contribute to the scarless healing potential of early prenatal skin for which fibroblasts are one of the major effector cells.[423]

In mammalian skin, the ability to heal without scarring is a feature unique to the early to mid stages of in utero development.[424,425] First studied in animal models,[426,427] this remarkable regenerative capacity was also subsequently observed in the skin of human foetuses undergoing surgery through hysterotomy.[424,428] This followed initial reports that human intrauterine wounds appeared to heal differently from postnatal skin injuries, with little inflammatory response and no granulation tissue formation.[425] The potential for scarless healing is retained until around 24 weeks of gestation in small wounds in human prenatal skin after which transition to postnatal-type repair (with fibrotic scarring) is seen.[43,429,430]

To date, the complete mechanisms enabling scarless repair remain unresolved although several interplaying factors have been proposed. Differences in ECM composition, growth factors, cytokine profiles and immune cell infiltration are all thought to promote scar-free regeneration in prenatal skin compared to adult skin.[43,431,432] Prenatal skin comprises mainly of type III collagen instead of type I collagen typically present in adult skin, has increased levels of glycosaminoglycans and cell adhesion proteins facilitating fibroblast and keratinocyte migration, and has a high proportion of matrix metalloproteinases (MMPs) to tissue-derived inhibitors of proteinases (TIMPs) favouring tissue remodelling over collagen accumulation.[43,431] The growth factors differentially present in the developing skin, such as TGF-β, FGF and epidermal growth factor, are also thought to promote skin regeneration over scarring.[43,431] Finally, prenatal skin is characterised by an attenuated immune profile compared to postnatal skin, marked by both reduced numbers of immune cells (including macrophages) and less cytokines that drive inflammation (for example, IL-6 and IL-8).[43,97] Aside from quantitative differences, prenatal macrophages have also been suggested to be qualitatively distinct and in a less differentiated state compared to postnatal skin.[43] In line with this, during the conduct of this research, another study was published demonstrating that macrophages typified by an 'immature' phenotype contributed to the scarless healing ability of reindeer antlers' velvet.[192] Whether prenatal skin macrophages behave similarly whilst interacting with local fibroblasts to confer scarless healing capacity has not been explored in human embryonic skin.

In this chapter, I leveraged the single-cell atlas of developing skin and the integrated dataset including adult skin to assess specific features of prenatal dermal fibroblasts and macrophages that may contribute to scarless healing. Based on their predicted co-location, the cell-cell interactions between fibroblasts and macrophages were further evaluated. Comparative analyses with the reindeer skin data were then performed to determine if prenatal skin potentially mirrors features of antler velvet which also heals scarlessly. Finally, in vitro studies were undertaken to verify whether fibroblasts behave differently in the presence of macrophages in culture.

4.2 Objectives

After thoroughly profiling prenatal skin cellular composition and identifying that immune and non-immune cells co-localise in tissue microenvironments in the previous chapter, this chapter starts to address the next overall study aim which was to 'Determine the contribution of immune cells to prenatal skin formation'. Specifically, the potential roles in fibroblast maintenance and scarless healing are examined. The following chapter objectives were set to achieve this:

1. Determine whether prenatal skin dermal fibroblasts transcriptionally change from early to late gestation.

2. Assess prenatal-specific features of dermal fibroblasts compared to healthy adult skin.

3. Analyse the biological processes enriched in prenatal skin macrophages and their ligand-receptor interactions with co-locating fibroblasts.

4. Investigate whether human prenatal skin fibroblasts and macrophages align to corresponding cell types in reindeer antler or back skin.

5. Validate whether macrophages co-locate with and functionally support fibroblasts through immunofluorescence and in vitro culture assays.

4.3 Results

4.3.1 Comparison of early- and late-gestation prenatal skin dermal fibroblasts

Significant temporal shifts in the composition of prenatal skin dermal fibroblasts were demonstrated earlier through analyses of proportional changes (section 3.3.1) and differential abundance (section 3.3.2) of cell states across gestation. *FRZB*$^{+}$ early fibroblasts and *HOXC5*$^{+}$ early fibroblasts (inferred as the common progenitor state to dermal and hair follicle fibroblasts (Figure 3.43, section 3.3.4)), were enriched in early gestation and declined after 11 PCW (Figures 3.9 and 3.23). *WNT2*$^{+}$ fibroblasts, on the other hand, were present throughout gestation and constituted the largest stromal subpopulation after 12 PCW (Figure 3.9). Within this fibroblast subset, differential abundance of cell neighbourhoods was additionally noted between early and late gestation by Milo analysis (Figure 3.23), suggesting that *WNT2*$^{+}$ fibroblasts transcriptionally changed during development. To further assess this transcriptomic heterogeneity, cell neighbourhoods of *WNT2*$^{+}$ fibroblasts significantly enriched in early versus late gestation were compared using differential gene expression and gene set enrichment analyses (section 2.4.7). This revealed that the expressions of function-defining genes involved in ECM and collagen deposition were increased in late *WNT2*$^{+}$ fibroblasts, including various procollagen encoding genes (for example, *COL3A1*, *COL1A1* and *COL1A2*) and associated metalloproteinases (for example, *ADAMTS5* and *MMP2*) (Figures 4.1 and 4.2, Appendices K1-K2). In contrast, early *WNT2*$^{+}$ fibroblasts upregulated genes related to cell growth and differentiation such as those encoding growth factors (*IGF1*), Wnt modulators (*SFRP1*, *SFRP4*) and transcriptional regulators (*SOX11*) (Figures 4.1 and 4.2, Appendices K1-K2).

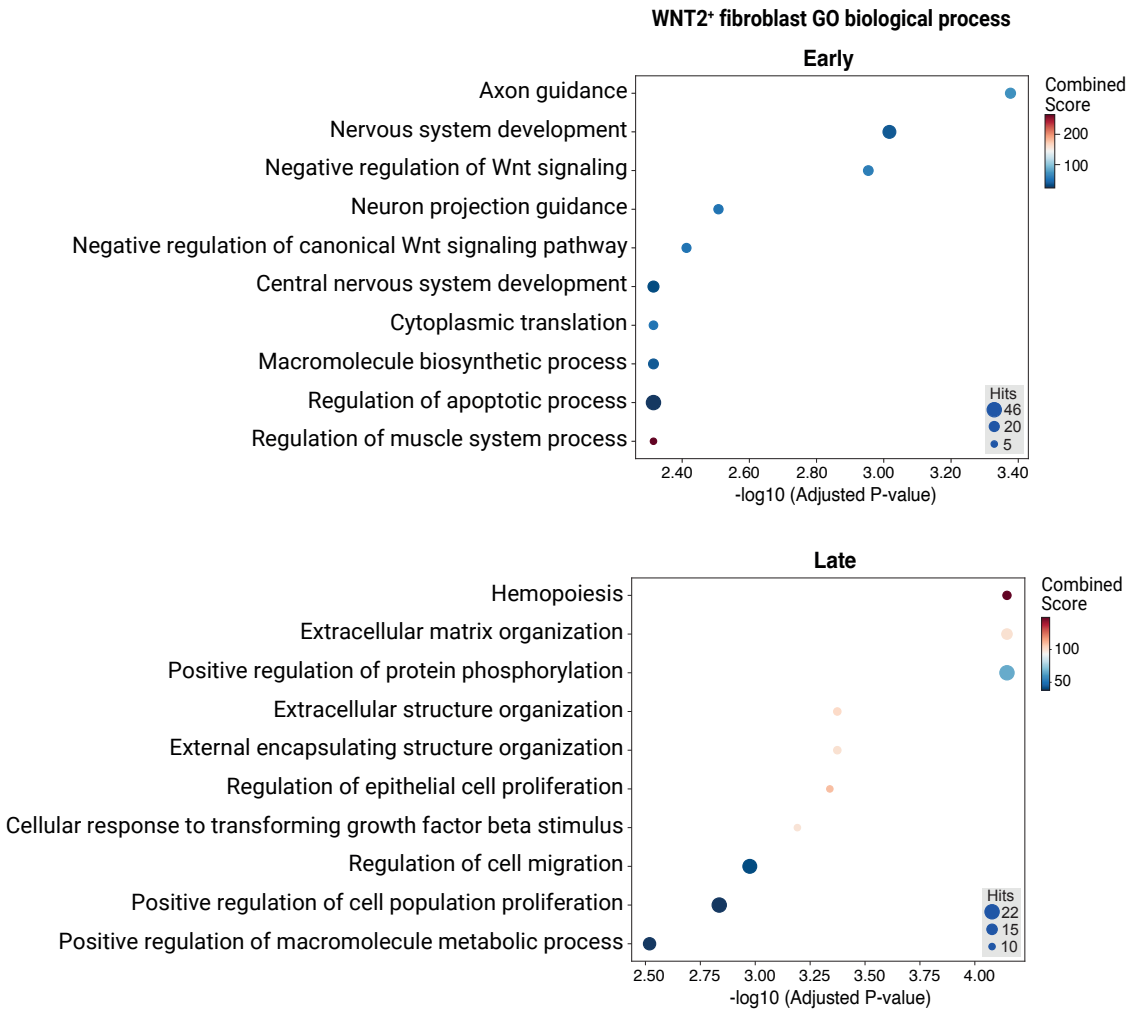

Figure 4.1. Gene set enrichment in early and late *WNT2*$^+$ fibroblasts.

Dot plots showing results of ORA for genes differentially expressed by *WNT2*$^+$ fibroblasts in early (top) and late (bottom) gestation (defined by Milo neighbourhoods). The top 10 enriched gene sets from GOBP 2023 (y-axis) and the degree of significance, calculated as the negative $\log_{10}$ of the adjusted p-value (from Fisher's exact test, Benjamini-Hochberg corrected for multiple testing) (x-axis), are shown in each plot; the colour scale indicates the combined score computed by Enrichr and the dot size is proportional to the number of genes associated with the gene set.

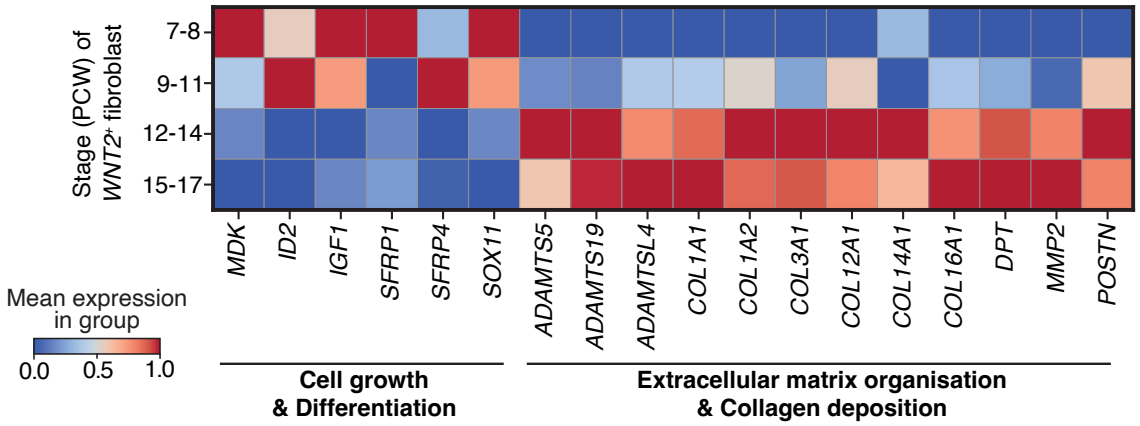

Figure 4.2. Comparison of early and late *WNT2*$^+$ fibroblasts.

Matrix plot of selected genes (from ORA) differentially expressed by *WNT2*$^+$ fibroblasts at different gestational stages (grouped PCW) in prenatal skin; for a given gene, colour scale indicates normalised variance-scaled mean expression.

These results indicated that dynamic changes occurred in both the resident subtypes and gene expression profiles of prenatal skin fibroblasts as gestation progressed. The enrichment of progenitor-like fibroblasts and downregulation of genes related to collagen deposition and ECM formation in early gestation could promote regeneration over scarring in prenatal skin. However, expression of these genes increased from the beginning of the second trimester when prenatal skin has still been clinically reported to heal without scars. This suggested that these transcriptional changes may be apparent much earlier than their phenotypic translation, potentially starting in a small proportion of fibroblasts, and that other factors may be at play to enable scarless repair.

4.3.2 Comparison of prenatal and adult skin dermal fibroblasts

To investigate additional elements contributing to its regenerative potential, prenatal skin was next compared to healthy adult skin - used as a model of scar-prone skin in the absence of prenatal skin from gestational ages over 24 PCW. The same adult skin scRNA-seq dataset integrated earlier with prenatal skin data was used and comprised three fibroblast populations annotated as F1, F2 and F3 as in the original publication.[100] Genes differentially expressed between prenatal and adult skin fibroblasts globally were identified prior to gene set enrichment analysis (section 2.4.7). Relative to prenatal skin fibroblasts, adult fibroblast subsets universally upregulated genes involved in 'pro-inflammatory and immune activation' pathways (Figure 4.3). These included genes encoding inflammatory interleukins (*IL6*, *IL32*), cytokine receptors (*IL1R1*, *IL15RA*), interferon-induced molecules (*IFITM1*), antigen-presenting complexes (*HLA-A*, *HLA-B*), complement-pathway components of innate immunity (*C1R*, *C1S*, *CD55*), and mediators of inflammatory response (*CD44*, *PTGES*, *SQSTM1*, *CDKN1A*). Conversely, prenatal skin fibroblasts expressed higher levels of genes implicated in immune suppression (*CD200*)[433] and regulation of inflammation (*RAMP2*, *PLD3*, *TMSB4X*, *MDK*)[434–436], with the growth factor midkine (*MDK*) also involved in tissue regeneration[435] (Figure 4.3).

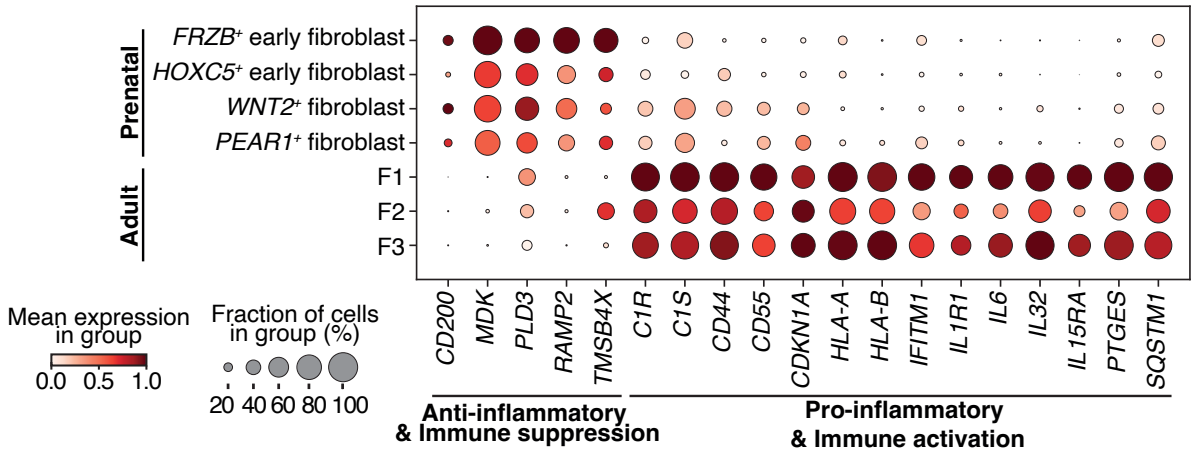

Figure 4.3. Comparison of prenatal and adult skin fibroblasts.

Dot plot of selected genes (from ORA) differentially expressed by dermal fibroblasts in integrated prenatal skin and adult skin scRNA-seq data; for a given gene, dot colour indicates normalised variance-scaled mean expression and dot size indicates the percentage of expressing cells in each category.

When assessed across all prenatal skin dermal fibroblasts by gestational age, expression of the adult 'pro-inflammatory and immune activation' gene profile was generally upregulated in later age groups (Figure 4.4). This expression profile was also higher in *WNT2*$^{+}$ and *PEAR1*$^{+}$ fibroblasts (abundant in later gestation) compared to *FRZB*$^{+}$ and *HOXC5*$^{+}$ fibroblasts (enriched in earlier gestation) (Figures 3.9 and 4.3), suggesting acquisition of an inflammatory phenotype with progressing gestation. Accordingly, genes previously reported in fibroblasts with a pro-inflammatory phenotype (*APOE*, *IGFBP7*, *ITM2A*)[437,438] were also increased during differentiation from *HOXC5*$^{+}$ early fibroblasts to *PEAR1*$^{+}$ fibroblasts as observed along the prenatal skin 'dermal fibroblast' pseudotime (Figure 4.5).

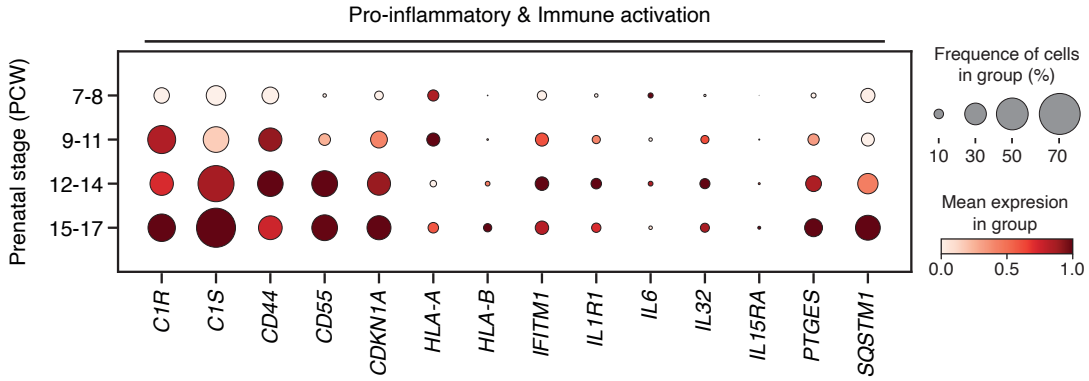

Figure 4.4. Expression of adult gene profile in prenatal skin fibroblasts.

Dot plot of pro-inflammatory and immune activation genes in prenatal skin dermal fibroblasts at different gestational stages (grouped PCW); for a given gene, dot colour indicates normalised variance-scaled mean expression and dot size indicates the percentage of expressing cells in each category.

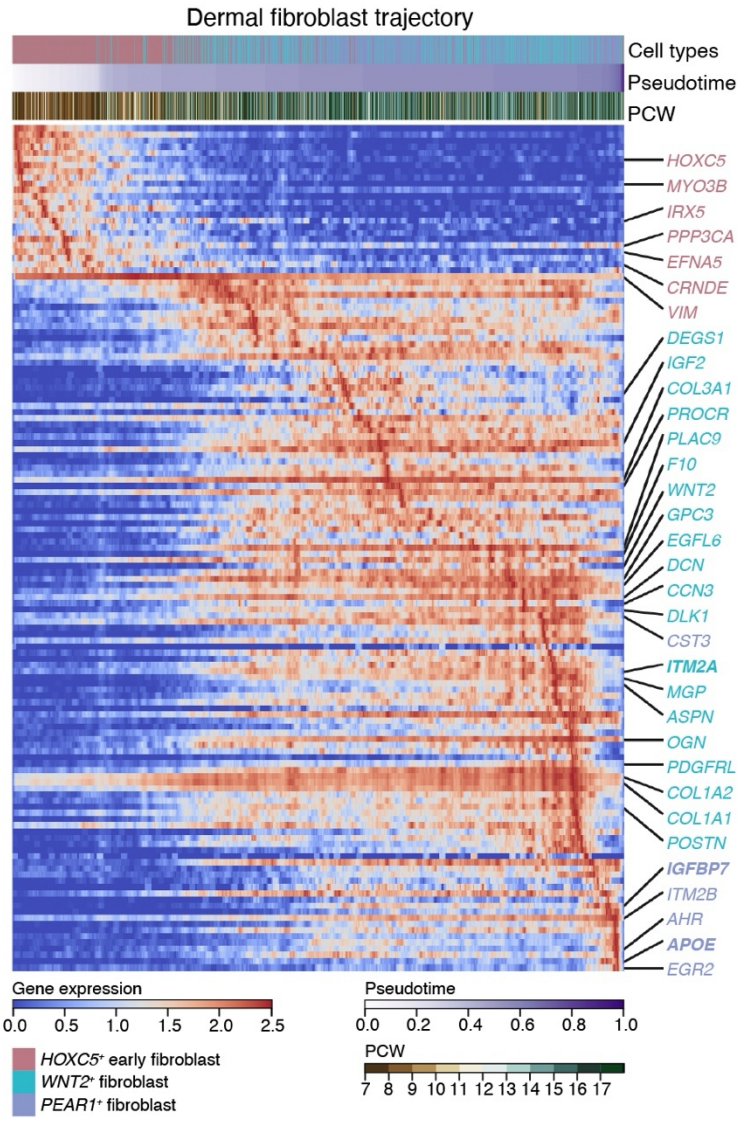

Figure 4.5. Driver genes along the dermal fibroblast trajectory.

Heat map of genes (y-axis) differentially expressed across pseudotime (x-axis) along the dermal fibroblast trajectory; corresponding fibroblast cell states and gestational ages (PCW) are indicated alongside pseudotime and blue-red colour scale represents normalised gene expression.

Of note, several pro-inflammatory (*IL1R1*, *IL32*, *CDKN1A*) and ECM component (*COL1A1*, *COL3A1*, *POSTN*) genes, which were upregulated by prenatal fibroblasts in later gestation (Figures 4.2, 4.3 and 4.4), have also been associated with pathologic fibroblasts from fibrosing cutaneous disorders such as systemic sclerosis and keloids.[439,440] This further supported that the intrinsic changes occurring in prenatal skin dermal fibroblasts during development contribute to the transition from pro-regenerative to pro-fibrotic tendency observed with advancing gestation.

4.3.3 Macrophages and prenatal skin dermal fibroblast growth and scarless repair

Having assessed the inherent features of prenatal skin fibroblasts that potentially contribute to scarless healing, the functional implication of their predicted co-location with early macrophages was next explored. The co-localisation of fibroblasts with macrophages in early prenatal skin was first confirmed in situ followed by gene set enrichment and cell-cell communication analyses to deduce the contributive role of macrophages.

Co-location of macrophage subsets with dermal fibroblasts in early prenatal skin

Macrophages were predicted to co-locate with dermal fibroblasts populations in tissue microenvironments based on NMF analysis (Figure 3.57, section 3.3.5). Namely, *FRZB*$^+$, *PEAR1*$^+$ and *WNT2*$^+$ fibroblasts shared microenvironments (1, 4 and 5) with macrophages (Figure 3.57). As *FRZB*$^+$ early fibroblasts were observed primarily in one sample from the earliest gestational age and *PEAR1*$^+$ fibroblasts were mainly enriched after 12 PCW (Figure 3.9, section 3.3.1), the investigations in this section focused on *WNT2*$^+$ fibroblasts. Outputs from correlation analysis of cell state abundances (section 2.5.3) were assessed and supported the co-localisation of *WNT2*$^+$ fibroblasts with different macrophages subsets (Figure 4.6).

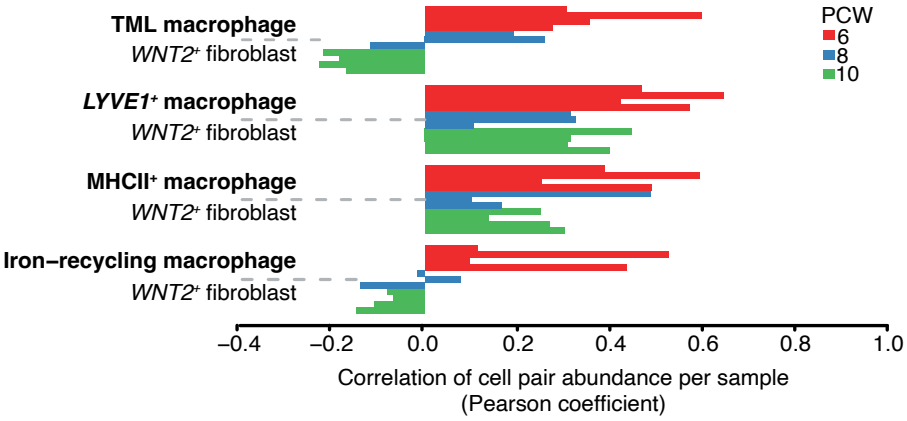

Figure 4.6. Co-location of *WNT2*$^+$ fibroblasts and macrophages by correlation analysis. Bar plot showing Pearson correlation coefficients between pairs of cell state abundances (normalised per spot) for *WNT2*$^+$ fibroblasts and macrophages subsets in prenatal skin. Pearson correlation coefficients were calculated across all skin-covered spots of Visium samples; each sample is shown by an individual bar. TML macrophage: *TREM2*$^+$ microglia-like macrophage.

To validate these computationally predicted co-locations, immunofluorescence and RNAscope smFISH assays were carried out. Early gestation prenatal skin samples were used, in line with the hypothesis-driven sampling undertaken for spatial transcriptomic data generation (discussed in section 3.3.5). To increase the likelihood of detecting potentially sparsely distributed macrophages on tissue sections, staining for *LYVE1*$^+$ and TML macrophages was preferentially performed given that these macrophage subsets were abundant in early gestation compared to MHCII$^+$ and iron-recycling macrophages which were enriched in later gestation (Figure 3.23). Immunofluorescence examinations showed *LYVE1*$^+$ (CD45$^+$LYVE1$^+$) and TML (P2RY12$^+$) macrophages in close proximity to fibroblasts (VIM$^+$) in early prenatal skin (Figures 4.7 and 4.8). To confirm the subtype of fibroblast, additional in situ hybridisation was done on a consecutive skin section using an RNAscope probe (*SFRP4*$^+$) specific for *WNT2*$^+$ fibroblasts and the images were overlaid as shown in Figure 4.8.

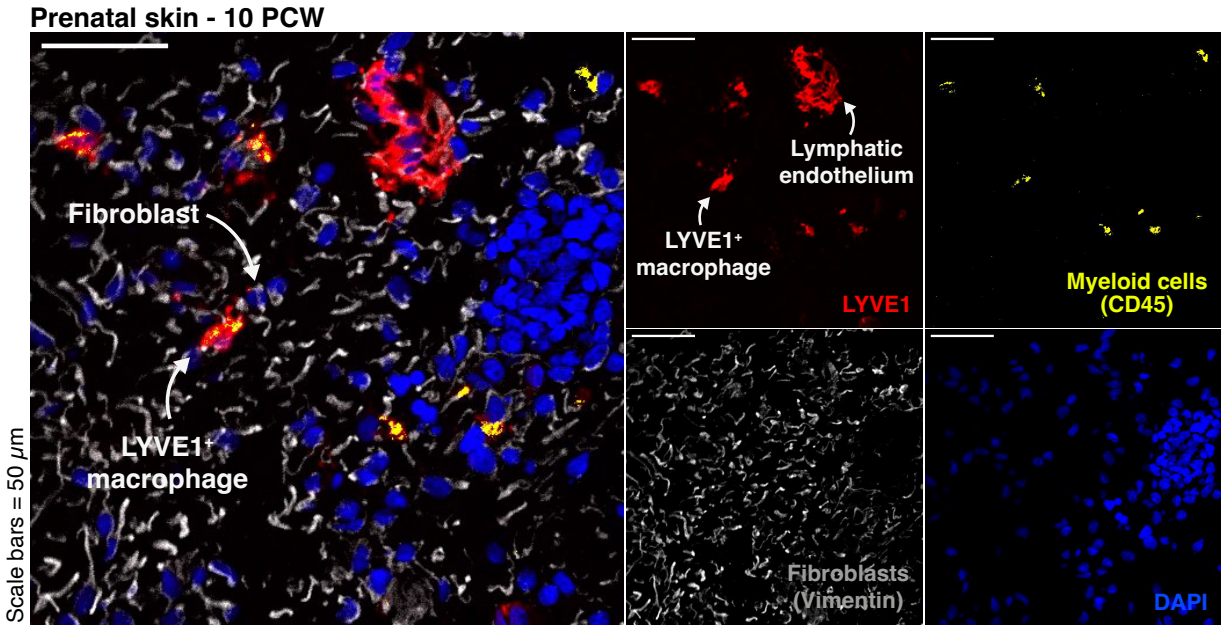

Figure 4.7. Immunofluorescence assay of *LYVE1*$^+$ macrophage and fibroblast co-location. Images of immunostained prenatal skin showing *LYVE1*$^+$ macrophages (LYVE1, red; CD45, yellow) in close proximity to dermal fibroblasts (VIM, grey) with DAPI (blue) nuclear staining. Representative image (10 PCW) shown from n=1 independent biological sample with 2 replicates. Scale bars, 50 μm.

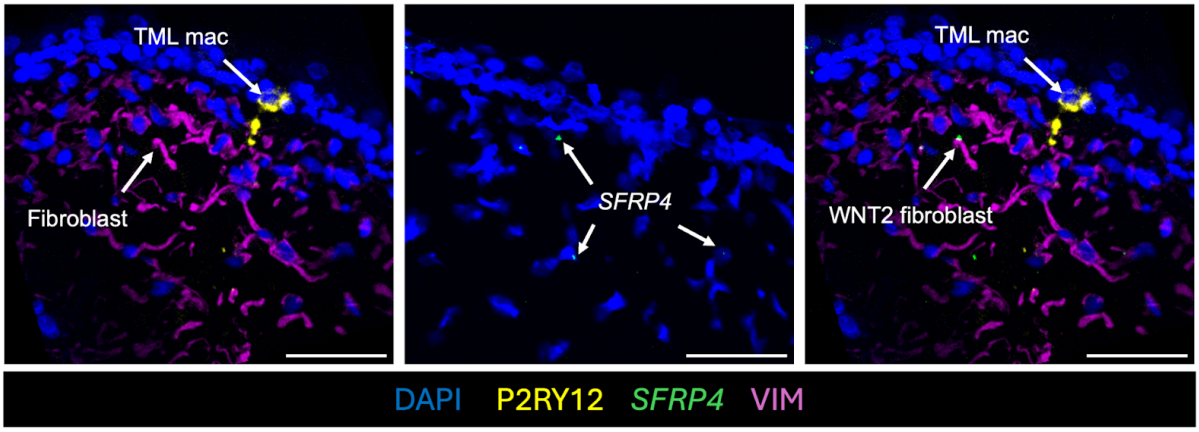

Figure 4.8. TML macrophage and fibroblast co-location.

Immunofluorescence assay (left), RNAscope FISH (centre), and merged images (right) showing TML macrophages (P2RY12, yellow) in close proximity to *WNT2*$^{+}$ fibroblasts (VIM, magenta; *SFRP4*, green) with DAPI (blue) nuclear staining. Representative images (consecutive 10 PCW sections) shown from n=1 independent biological sample with 2 replicates. Scale bars, 50 µm.

These findings validated the co-location of *WNT2*$^{+}$ fibroblasts with *LYVE1*$^{+}$ and TML macrophages in early prenatal skin. This was further reflected in the in silico mapping of the abundance of these cell states across prenatal skin sections (Figure 4.9). As shown in Figure 4.9(b), parallel distributions were observed for *WNT2*$^{+}$ fibroblasts and *LYVE1*$^{+}$ macrophages, as well as for *WNT2*$^{+}$ fibroblasts and TML macrophages, along the epidermal-dermal axis, implying enrichment of these cell pairs in the same areas in prenatal skin.

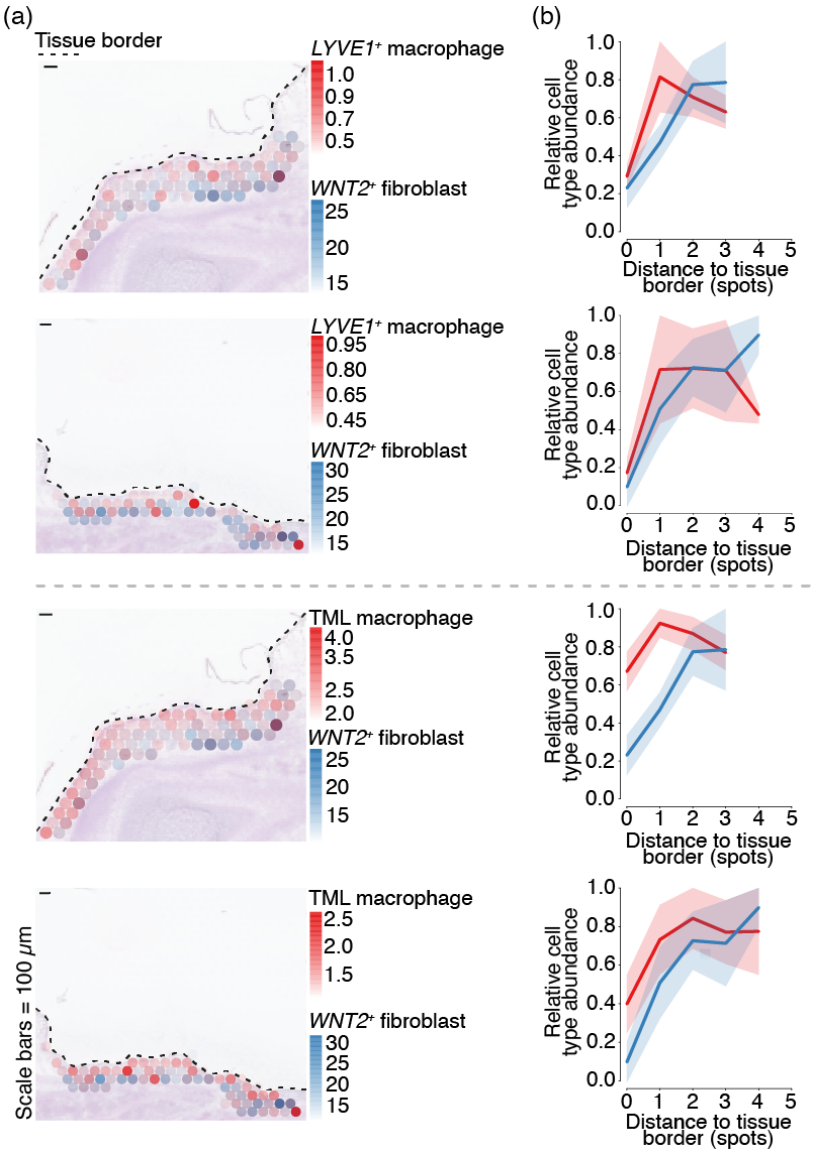

Figure 4.9. Spatial distribution and abundance of *WNT2*$^+$ fibroblasts and macrophages from skin surface.

(a) Mapping of the estimated cell abundances (colour gradients) of *WNT2*$^+$ fibroblasts (blue) and *LYVE1*$^+$ macrophages (top, red) or TML macrophages (bottom, red) overlaid on Visium histology images of prenatal skin. Dashed lines represent tissue borders. Representative images from n=5 independent biological samples with 2-3 replicates. Scale bars, 100 µm. (b) Curve plots showing the mean per-spot normalised abundance (y-axis) of *WNT2*$^+$ fibroblasts (cyan) and *LYVE1*$^+$ macrophages (top, red) or TML macrophages (bottom, red) along the axial distance (x-axis) to skin surface (tissue border); data shown as mean (line) ± 2 SD CI (shaded area).

Gene set enrichment analysis of macrophage subsets

To infer the biological processes and pathways enriched in the different macrophage subsets, differential gene expression and over-representation analyses were conducted (section 2.4.7). This revealed that TML macrophages were involved in several immunomodulatory processes including regulation of inflammatory response and of cytokine and chemokine production (Appendix L). Accordingly, TML macrophage differentially expressed genes encoding immune-inhibitory receptors (*LILRB4*, *SIGLEC10*, *CX3CR1*)[441–443] and modulators of interleukin production such as IL-6 (*SYT11*, *GHRL*)[444–446] (Figure 4.10). These results suggested that the yolk-sac derived TML macrophages, enriched in early gestation, may directly contribute to the diminished inflammatory and immunosuppressive environment that is conducive to scarless repair in prenatal skin.[43,97]

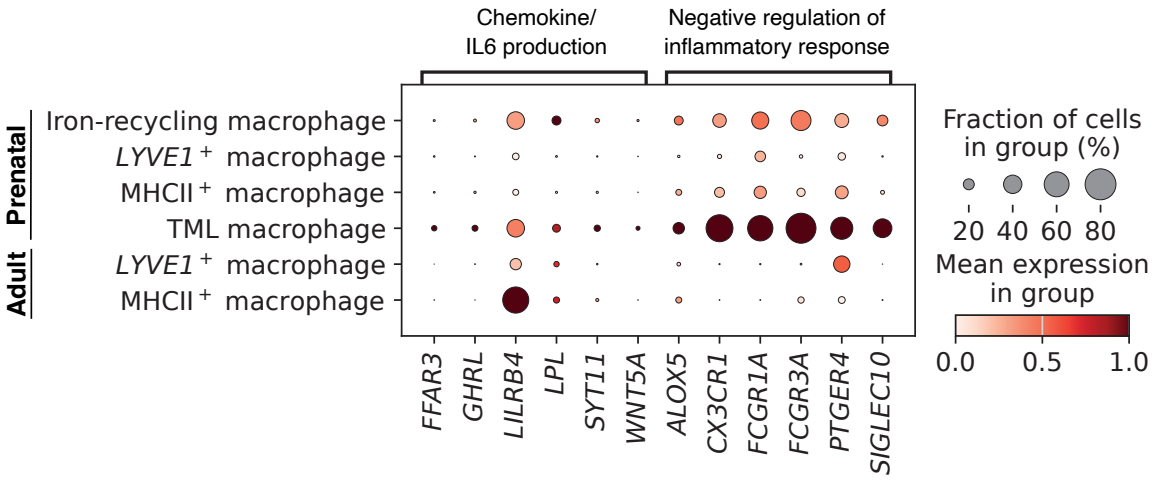

Figure 4.10. Immune-inhibitory gene modules enriched in TML macrophages.

Dot plot of selected genes (from ORA) differentially expressed by TML macrophages compared to other prenatal and adult skin macrophages; for a given gene, dot colour indicates normalised variance-scaled mean expression and dot size indicates the percentage of expressing cells in each category.

In addition, reduction in inflammation and IL-6, which is paracrinally secreted by macrophages and autocrinally produced by fibroblasts under macrophage stimulation,[447,448] has been shown to promote regeneration in mouse skin transplants and foetal wounds.[449,450] Blocking of IL-6 receptors by the monoclonal antibody tocilizumab in explant dermal fibroblasts from systemic sclerosis patients also led to a decrease in fibrogenic molecules, such as collagen alpha 1 and connective tissue growth factor.[451] In prenatal skin, *WNT2*$^{+}$ fibroblasts were observed to have downregulated

IL6 expression compared to adult fibroblasts (Figure 4.3). This connoted that perhaps interactions between *WNT2*$^+$ fibroblasts and TML macrophages may induce the anti-inflammatory profile observed in early prenatal skin dermal fibroblasts.

Cell-cell interactions between early prenatal skin fibroblasts and macrophages

The predicted ligand-receptor interactions between *WNT2*$^+$ fibroblasts and co-locating macrophages (*LYVE1*$^+$ and TML) were therefore evaluated in early prenatal skin (section 2.4.6). This identified that *GAS6*, expressed by TML macrophages, interacted with *AXL* on *WNT2*$^+$ fibroblasts (Figure 4.11). Binding of human growth inhibitor specific 6 (GAS6) to Tyro3-Axl-Mer (TAM) receptors has been reported to induce immunosuppression, dampening of inflammation, and tissue regeneration in liver, lung and joint synovium.[452–454] This supported the potential contribution of macrophage-fibroblast crosstalk to the attenuated inflammation and regenerative healing seen in early prenatal skin.

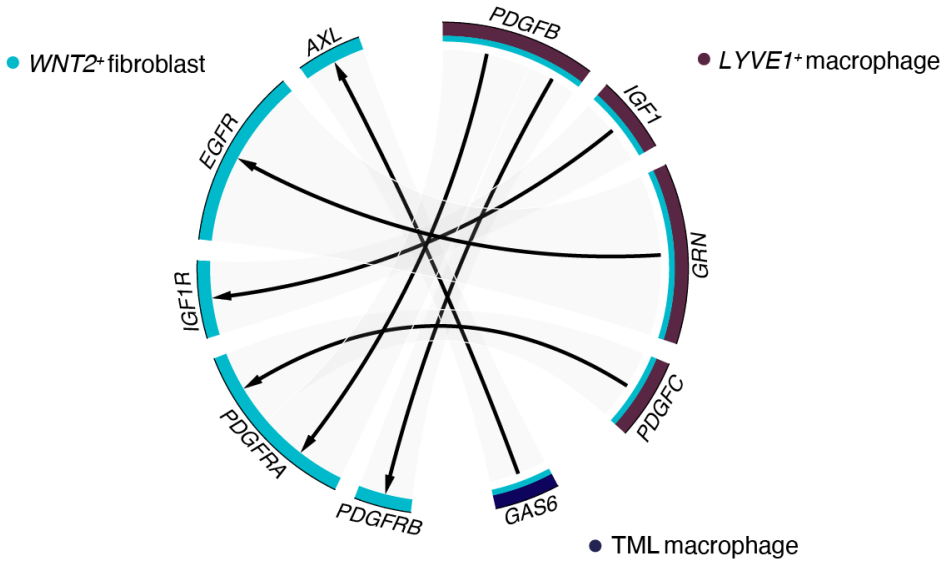

Figure 4.11. Cell-cell interactions between *WNT2*$^+$ fibroblasts and macrophages.
Circos plot showing selected significant interactions predicted between *WNT2*$^+$ fibroblasts and *LYVE1*$^+$ or TML macrophages in prenatal skin. Arrows indicate directionality (ligand to receptor) and connection widths (shaded areas) are proportional to the mean expression values of ligand-receptors pairs; significance determined by permutation testing (adjusted p-value < 0.05) in CellPhoneDB.

Additionally, *LYVE1*$^{+}$ macrophages also expressed PDGFs (*PDGFB*, *PDGFC*) which were predicted to interact with receptors (*PDGFRA, PDGFRB*) on *WNT2*$^{+}$ fibroblasts (Figure 4.11). Platelet-derived growth factors produced by macrophages are known to maintain fibroblast homeostasis in multiple tissues such as heart, spleen and peritoneum.[447] The identification of similar signalling between macrophages and fibroblasts, alongside other growth factor interactions, such as *IGF1-IGF1R* and *GRN-EGFR*, indicated that *LYVE1*$^{+}$ macrophages further support the growth and maintenance of dermal fibroblasts in prenatal skin.

Collectively, the above findings confirmed that macrophages co-located with dermal fibroblasts in early prenatal skin and suggested that these innate immune cells may play a role in fibroblast development during skin morphogenesis through growth-promoting cellular interactions. Furthermore, by modulating the immune milieu and resident fibroblasts towards an immune-suppressed anti-inflammatory state, early macrophages potentially confer to prenatal skin its unique regenerative competency and scarless healing property.

4.3.4 Comparison between human prenatal and reindeer skin

To verify whether the profile of early prenatal skin fibroblasts and macrophages indeed conduce to regenerative repair, comparisons were made to an in vivo model of scarless healing in postnatal skin, the velvet (skin) of reindeer antlers. Reindeer antlers represent one of the very few cases where adult mammalian integument can regenerate and heal without scarring in contrast to the scar-forming skin from other anatomical locations, such as the back, in the same species.[192] A recent single-cell study from Sinha et al.[192] demonstrated that this resulted from differences in fibroblasts and macrophages present in antlers compared to back skin during wound healing. Antler velvet fibroblasts were enriched in pro-regenerative genes and interacted with 'early macrophages' (in a more immature state) leading to tissue regeneration.[192] Conversely, back skin fibroblasts were inflammatory-primed and secreted immunostimulatory factors that engaged mature macrophages to predispose to scar formation.[192]

Fibroblasts and macrophages from prenatal skin scRNA-seq data were compared to their counterparts in the single-cell reindeer dataset using LR analysis (section 2.4.4). Prenatal skin fibroblasts in early gestation had a higher probability of matching to pro-regenerative reindeer fibroblasts (Figure 4.12). This was reversed in later gestation stages where the probability of correspondence to pro-fibrotic reindeer fibroblasts was higher (Figure 4.12). Consistent with this observation, several genes expressed by pro-regenerative reindeer fibroblasts (*CRABP1*, *MDK*, *PTN*, *TPM1*)[192] were downregulated in later gestation prenatal skin whilst pro-fibrotic genes (*PTGDS*, *SCARA5*, *COCH*) were generally lowly expressed throughout (Figure 4.13).

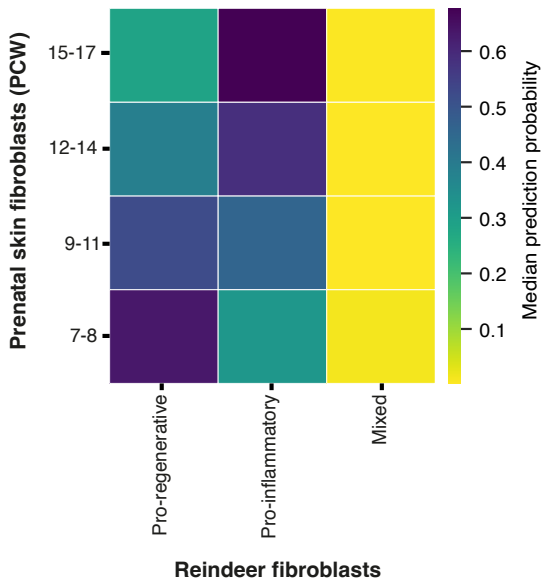

Figure 4.12. Alignment of prenatal skin and reindeer skin fibroblasts.

Heatmap showing degree of correspondence between fibroblasts from prenatal skin and reindeer skin; colour scale indicates median prediction probabilities for prenatal skin fibroblasts at different gestational stages (grouped PCW) (y-axis) from a logistic regression model trained on reindeer fibroblast data (x-axis).

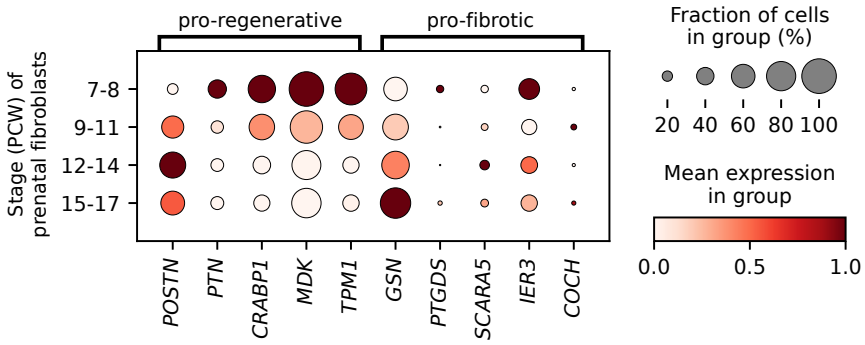

Figure 4.13. Expression of pro-regenerative and pro-fibrotic genes in prenatal skin.

Dot plot of expression of pro-regenerative and pro-fibrotic genes reported in reindeer skin[192] by prenatal skin fibroblasts across gestational stages (grouped PCW); for a given gene, dot colour indicates normalised variance-scaled mean expression and dot size indicates the percentage of expressing cells in each category.

Crucially, comparison of the macrophage populations showed that prenatal skin macrophages aligned to 'early macrophages' (clusters 1, 3 and 5), enriched in reindeer velvet and contributing to scarless healing,[192] but not to reindeer back skin macrophages (clusters 0, 2 and 4) (Figure 4.14). These results corroborated the earlier findings that the distinct profiles of early human prenatal skin fibroblasts and of the local macrophages with which they interact favour tissue regeneration over scar formation and further suggested that the mechanisms of scarless healing may be conserved across species.[192]

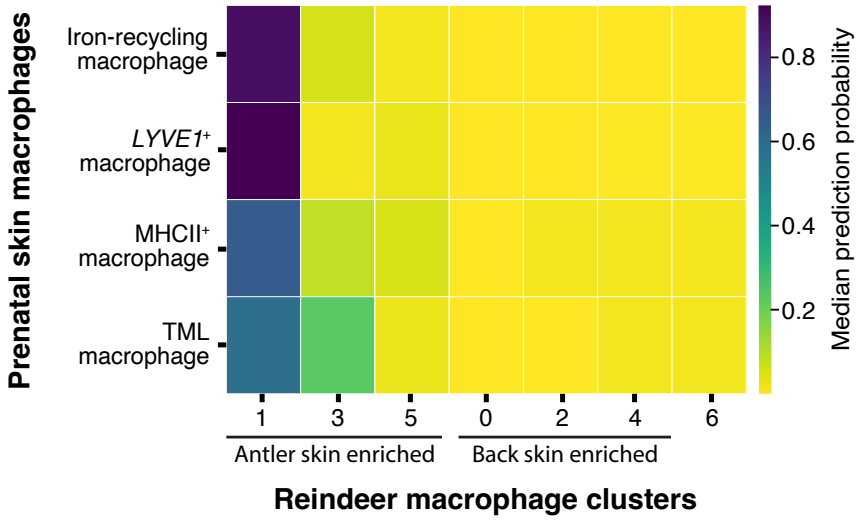

Figure 4.14. Alignment of prenatal skin and reindeer skin macrophages.

Heatmap showing degree of correspondence between macrophage clusters from prenatal skin and reindeer skin; colour scale indicates median prediction probabilities for prenatal skin macrophages (y-axis) from a logistic regression model trained on reindeer macrophage data (x-axis).

4.3.5 Scratch wound healing assay

Finally, to determine whether macrophages definitely influence fibroblast behaviour to enhance wound healing, an in vitro scratch assay of fibroblasts cultured with or without iPS cell-derived macrophages was performed (section 2.7). Organoid fibroblasts, which were shown to recapitulate prenatal skin in earlier comparative analyses (section 3.3.3), were used to ensure availability and consistency across replicated experiments. Co-culture with macrophages improved scratch wound closure (Figure 4.15), thereby implying a role for macrophages in supporting fibroblasts during wound healing.

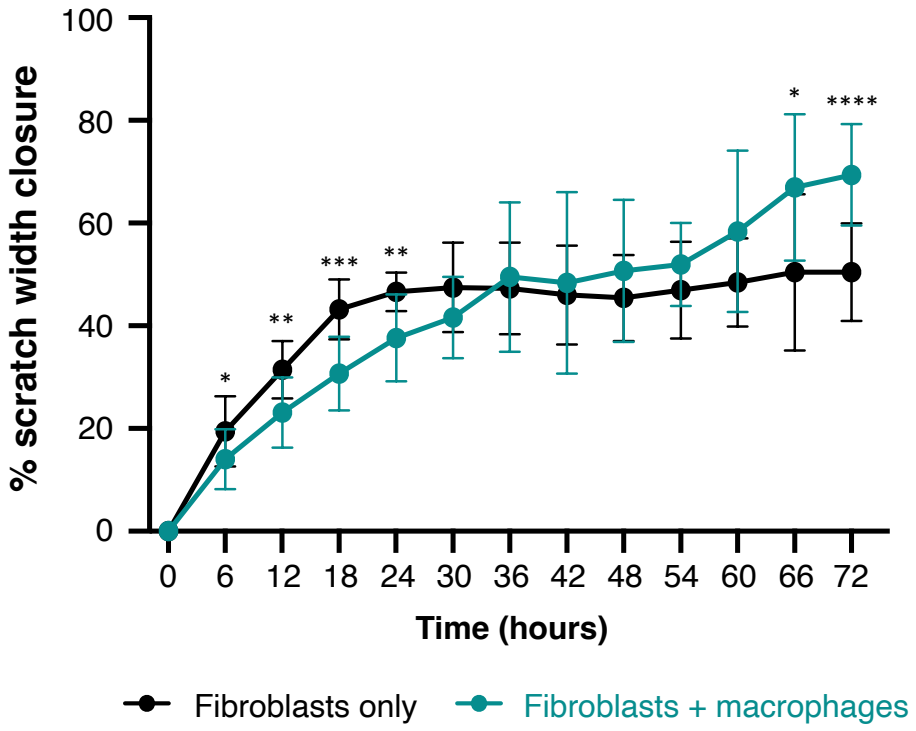

Figure 4.15. Scratch wound healing assay with and without macrophages.
Line graph showing the percentage scratch wound closure (quantified as wound width relative to original size, y-axis) over time (x-axis) for fibroblasts cultured with macrophages (green) or in isolation (black). Data from 3 independent samples conducted in n=8 independent experiments (n=4 with macrophages, n=4 without macrophages, 3 replicates each) shown as mean percentage ± SD; *p < 0.05, **p < 0.005, ***p < 0.0005, ****p < 0.0001 from two-way ANOVA with Tukey's multiple comparisons test.

4.4 Section discussion

Unlocking the mechanisms to skin regeneration and scar-free repair represents a formidable challenge that has been the subject of intense research for over half a century. Being almost exclusive to gestation (approximately up to mid stages) in mammalian skin, this fascinating phenomenon has been studied in embryonic animal models and limitedly in human foetal skin. Although it is still largely elusive to therapeutic translation, significant advances have been made in dissecting the multitude of cellular and molecular determinants of scarless healing.[43] Components of the ECM, profiles of growth factors and cytokines, infiltrates of immune cells, and responses to mechanical forces that differ between prenatal and postnatal skin have been proposed as potential contributors.[431,432] However, the precise contribution of each element as well as the interplay of intrinsic cellular versus extrinsic microenvironmental factors remain to be elucidated. In this section, I discuss the results of the investigations instigated by the predicted co-location of macrophages with fibroblasts - the main effector cell type in wound healing - from the multi-omics prenatal skin atlas, providing new insights into the roles of these immune cells in skin morphogenesis and scarless healing.

4.4.1 Changes in prenatal skin fibroblasts across gestation

Comparative analyses across gestation and with adult skin, revealed key temporal changes in prenatal skin dermal fibroblasts populations and expression profiles (sections 4.3.1 and 4.3.2). In early gestation, the inferred common progenitor *HOXC5*$^{+}$ early fibroblasts were enriched and genes promoting cell growth, differentiation and immune suppression were upregulated. Conversely, genes involved in collagen deposition, ECM formation, immune activation and inflammatory priming were upregulated by dermal fibroblasts in later gestation. These compositional and transcriptional shifts suggest that factors inherent to developing fibroblasts may be responsible, at least in part, for the scarless healing potential of prenatal skin. Accordingly, pivotal experiments have shown that foetal fibroblasts were able to heal wounds scarlessly in human prenatal skin transplanted subcutaneously onto athymic adult mice.[423,455] Scarless healing occurred independent of the intrauterine environment and irrespective of perfusion by postnatal serum and immune cells.[423,455] However, whether local cutaneous microenvironmental factors conferred prenatal fibroblasts with this capacity for regeneration was not assessed.

Additionally, analysis of the prenatal skin atlas revealed that upregulation of pro-scarring genes begins much earlier (around 12 PCW) than when the inflection from regenerative to reparative repair has been observed (towards the end of the second trimester).[43,429,430] Transcriptomic scarring competence, therefore, is acquired by prenatal skin fibroblasts well before its phenotypic clinical manifestation. The implication then is that, for some period during gestation, skin fibroblasts balance between regenerative and fibrotic capabilities, tipped towards the former likely by extrinsic factors, until this is permanently overcome in the final trimester and in postanal life. Indeed, this is supported by the observation that external determinants such as wound size can modulate the transition point between scarring and scarless healing, with larger wounds precipitating scar formation earlier in foetal skin.[430] An in-depth assessment of the molecular changes that eventually offset prenatal skin fibroblasts towards scarring during normal human development is still required in future studies. This may provide insightful clues about whether and how the scales could be shifted back into regenerative competency to achieve the ultimate goal of controlling scar formation and restoring normal skin architecture during physiological and pathological healing.

4.4.2 The immune and inflammatory milieu of prenatal skin

The prenatal skin environment that permits scarless healing is characterised by attenuated immune and inflammatory responses.[43,425,432] Previous studies have shown that foetal skin, healthy or wounded, has significantly reduced numbers of immune cells and pro-inflammatory mediators compared to adult skin.[43,97,425,431,450,456] These studies have also suggested that the phenotype of resident leukocytes, such as macrophages, may favour tissue regeneration over fibrosis.[43,97] Analysis of the assembled multi-omics atlas confirmed a relative absence of inflammation in human prenatal skin compared to postnatal skin. The findings further uncovered the co-location of macrophages with fibroblasts in early human prenatal skin and revealed the enrichment of gene programmes and cell-cell interactions which implicated macrophages as crucial regulators of inflammation and promoters of regenerative repair (sections 4.3.3, 4.3.4, 4.3.5). This contrasts with their dual roles in postnatal skin where macrophages contribute to the initial inflammatory phase and subsequent anti-inflammatory scar-forming stage of wound healing.[420,431,457]

Specifically, the yolk-sac derived TML macrophages appeared to play a key part in prenatal skin regenerative capability. These macrophages declined in late gestation and have up to now not been described in postnatal skin, strengthening their potential contribution to prenatal-specific scarless healing. Interestingly, a corresponding microglia-like macrophage population has recently been

reported to migrate alongside neural crest cells which also give rise to the fibroblasts of the head and neck regions.[39,41,458] Wounds from these areas, such as facial excisions, repair more effectively.[459] It could be hypothesised that some microglia-like macrophages persist in the skin of the head and neck or that the cutaneous environment in these anatomical locations enable macrophages to re-engage developmental programmes to support enhanced healing. A deeper characterisation of macrophages from the head and neck compared to trunk and limb from adult human skin in healthy state, physiological and pathological wound healing, and scarring should be assessed in future studies.

The findings from the reindeer skin study somewhat supported that site-dependent differences in immune cells, notably macrophages, may instruct healing without (antlers) or with (back) scarring.[192] These distinct macrophage profiles were themselves determined by differential priming of local fibroblasts in antler and back skin towards pro-regeneration or pro-fibrosis respectively, analogous to mesenchymal stem cells shifting mouse bone marrow macrophages from a pro-inflammatory to a tissue regenerative phenotype.[460] This suggests the possibility of bi-directional modulation between fibroblasts and macrophages where fibroblasts, with inherent transcriptional differences across space (antlers or back) and time (prenatal or postnatal), govern the numbers and types of macrophages present in or recruited to the skin. In turn, these immune cells influence not only the skin and wound milieu but also the healing patterns the dermal fibroblasts subsequently effect. Analysis of the prenatal skin atlas identified the cell-cell communication potentially mediating the interactions from macrophages to fibroblasts. Exploration of the instructive cues originating from fibroblasts to macrophages, together with mechanistic investigations of these signalling pathways, should also be undertaken in future works to fully delineate the reciprocal immune-non-immune crosstalk underpinning scarless healing for therapeutic exploitation.

4.4.3 Additional factors influencing scarless healing potential

The results described in this chapter, together with findings from previous animal studies, compellingly indicate that features which are constitutional to fibroblasts and macrophages and the reciprocal interactions between these two cell groups are instrumental to prenatal scarless healing. Yet, it should be acknowledged that other additional factors such as mechanical tension and microbiota which may also affect the predisposition to scarring were not assessed in this study. Mechanotransduction signalling has been shown to impact wound healing.[461] Increasing mechanical load induces hypertrophic scar formation whereas off-loading wound tension or

blocking mechanotransduction signals promote skin regeneration to prevent scarring.[462,463] The influence of skin commensals on wound repair is more complex.[464] These microorganisms typically promote reparative closure in acute wounds and reduction or alteration in the skin microbiome can delay healing.[464] In their absence, though, germ-free mice have been shown to heal quickly and scarlessly.[465]

In developing skin, however, the physiological transition from pro-regenerative to pro-fibrotic repair manifestly occurs whilst still in utero without exposure to extrauterine mechanical stress or microbiome, suggesting that these factors may secondarily modulate scarring by affecting the skin-intrinsic effectors identified above, that is fibroblasts and macrophages. Nevertheless, further studies of these secondary modifiable variables, including in human skin or organoid models, can help decipher the complex molecular machinery that generates scars and consequently identify the critical cues that could redirect postnatal skin fibroblasts towards a regenerative path.

Chapter 5 . Macrophages support neurogenesis and angiogenesis in prenatal skin

5.1 Introduction

The organisation of prenatal skin as an intricate composition of microanatomical niches where immune cells co-localise with non-immune cells to perform specific functions started to emerge from the analysis of the multi-omics atlas. Macrophages co-located with dermal fibroblasts and were found to support the growth of these stromal cells and potentially contribute to their ability to heal prenatal skin scarlessly (section 4.3.3). Macrophages were also predicted to co-locate with vascular endothelial and neural cells in neurovascular microenvironments (Figure 3.57 section 3.3.5), which suggested that macrophages may also be implicated in skin blood vessel and peripheral nerve development during gestation.

Prenatal development of human cutaneous vasculature is relatively under-reported. During embryogenesis, the vascular system is formed by two distinct mechanisms, namely vasculogenesis and angiogenesis (Figure 5.1).[39,466] Vasculogenesis involves the de novo differentiation of mesoderm precursor cells into angioblasts (endothelial cell progenitors) which then fuse to generate the primitive vessels of the early vascular plexus.[467,468] Angiogenesis, on the other hand, entails the formation of new blood vessels from pre-existing ones and occurs through distinct processes termed sprouting angiogenesis - growth by proliferative extension of endothelial cells towards an angiogenic stimulus, led by the 'tip' cell and followed by 'stalk' cells in the new sprout - and intussusception - transluminal splitting and division of an existing vessel into two separate components (Figure 5.1).[466,468,469] More broadly, angiogenesis is also used to encompass not only the growth but also the remodelling of an expanding vascular network.[469] Embryologically, it is thought that genesis of the major vessels, such as the dorsal aorta and cardinal veins, occurs by vasculogenesis whereas the rest of the vasculature develops through angiogenesis,[39] although it has been presumed that blood vessels in early prenatal skin could also arise from angioblastic differentiation of dermal mesenchyme.[42]

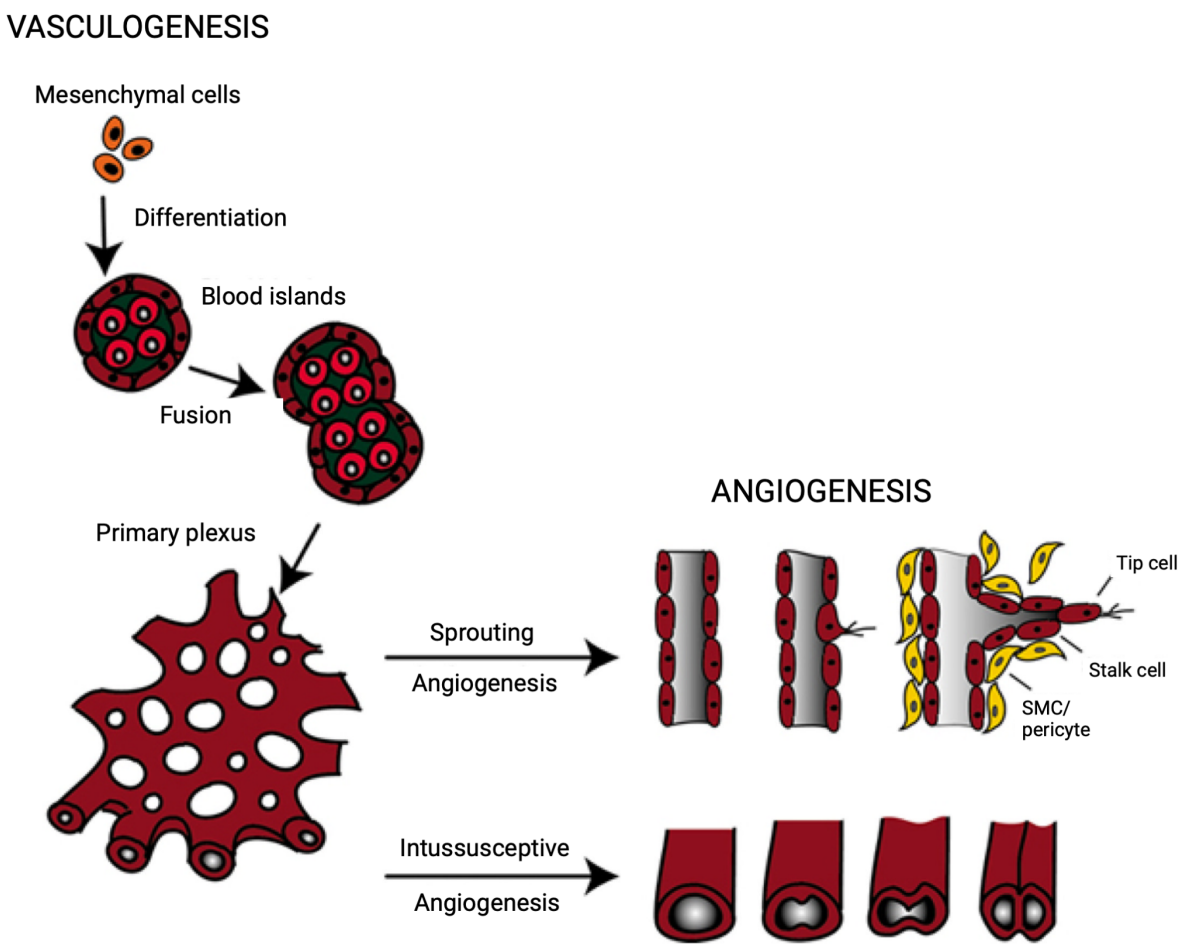

Figure 5.1. Mechanisms of vascular development.

Schematic representation of vasculogenesis which produces the primary vascular plexus from mesoderm precursor cells through angioblast formation and fusion; the early vascular plexus is then expanded and remodelled through sprouting and intussusceptive angiogenesis. SMC: smooth muscle cell. Taken from Heinke et al.[466]

In the developing skin, endothelial cells are apparent from around 6 PCW and join together to form discontinuous tube-like structures that are initially organised in a singular plane parallel to the epidermis.[49,96] These neo-vessels gradually evolve, increasing in density and complexity, to form longer, more continuous blood vessels of different calibres that situate in two planes by 8 PCW.[49,96] A vascular pattern resembling that of adult skin is already evident around the transition period from embryonic to foetal life, although vessel walls and basement membranes are still maturing.[49]

Whether immune cells such as macrophages, which were predicted to co-locate with vascular endothelial cells from the prenatal skin atlas (section 3.3.5), have a role in human cutaneous developmental angiogenesis has not been determined. In animal models, macrophages have been shown to contribute to vascularisation in various organs.[470] Depletion of macrophages led to formation of disorganised or unconnected blood vessels during organogenesis of mouse kidneys and testes.[471,472] Similarly, in mice deficient in microglia (the resident macrophages of the central nervous system), reduced volume and complexity of retinal vasculature have been observed,[473,474] indicating that macrophages are required for establishment of a normal vascular network during mouse embryogenesis.[475] In human development, macrophage subsets have been reported in close proximity to endothelial cells in yolk sac and gonads, and expressed gene profiles and signalling molecules involved in angiogenic pathways.[102,338] However, a study looking at the development of endothelial cells in human prenatal skin found that $CD45^+$ leukocytes were not specifically associated with either blood or lymphatic vessels in situ, but rather appeared randomly distributed in the dermis.[96] Findings from the new multi-omics atlas predicted otherwise, necessitating a re-evaluation of macrophage contribution to prenatal skin angiogenesis. Moreover, the lack of immune cells in the skin organoids coincided with a marked reduction in endothelial cells. This posed the question whether these two observations could be causally linked and whether vascularisation in the skin organoids could be rescued through supplementation with macrophages.

In addition to endothelial cells, macrophages, especially TML macrophages, were also predicted to co-locate with neural cells in the neurovascular microenvironments of prenatal skin (Figure 3.57, section 3.3.5). Neural cells, comprising neurons and surrounding glial Schwann cells, develop from the neural crest with nerve fibres identifiable in human embryonic skin as early as 6 PCW.[39,42,50] These nerves initially appear as thick trunks in the subepidermal region and gradually mature into adult-type beaded fibres that extend into the epidermis and form networks in the deeper dermis and around developing appendages.[42,50] Peripheral-nerve associated macrophages involved in neuroprotection, axonal growth and myelination have been demonstrated in postnatal mouse skin both under physiological condition and following nerve injury.[476–478] Some of these macrophages are prenatally seeded and their potential contribution to peripheral nerve development during mouse embryogenesis has been suggested.[476,479] It is not known whether macrophages can function similarly in human prenatal skin.

In this chapter, I explored the potential functional implications of macrophage co-localisation with neural cells and vascular endothelial cells in the predicted neurovascular microenvironments. The sparsity of endothelial cells in the skin organoid was further investigated by analysing different determinants of angiogenesis and comparing with prenatal skin. Based on the results, in vitro studies were then performed to confirm the identified role of macrophages in angiogenesis, using cultures of skin organoids to determine the suitability of the model to functionally validate in vivo findings.

5.2 Objectives

This chapter continues the address of the overall study aim started in the previous chapter which was to determine the contribution of immune cells to prenatal skin formation, focusing here on blood vessel and peripheral nerve development. Additionally, it follows on from the evaluation of the faithfulness of the hair-bearing skin organoid model to in vivo prenatal skin, which was conducted in chapter 3, to address the final study aim of determining the utility of skin organoids to functionally assess the role of immune cells in skin morphogenesis. These aims were achieved through the following chapter objectives:

1. Review the gene programmes and biological pathways enriched in prenatal skin macrophages and analyse their ligand-receptor interactions with co-locating neural and endothelial cells.

2. Compare the refined endothelial cell states between prenatal skin and skin organoids.

3. Assess differences in factors driving angiogenesis between prenatal skin and skin organoids.

4. Validate whether macrophages co-locate with endothelial cells and contribute to angiogenesis through immunofluorescence and in vitro culture assays.

5.3 Results

5.3.1 Macrophages and early neurocutaneous development

Co-location of macrophages with neural cells in early prenatal skin

Macrophages were predicted to co-locate with neural cells in tissue microenvironments in prenatal skin by NMF analysis (Figure 3.57, section 3.3.5). Specifically, TML macrophages co-localised with *PID*$^{+}$ Schwann cells in microenvironment 1 (early neurovascular microenvironment) which was also shared by neuron progenitors. TML macrophages were also predicted to share microenvironment 5 (late neurovascular microenvironment) with Schwann/Schwann precursors and myelinating Schwann cells. The outputs from correlation analysis of cell state abundances (section 2.5.3) were reviewed and further supported the co-location of TML macrophages with these neural cells, especially in the earlier stages of gestation (Figure 5.2).

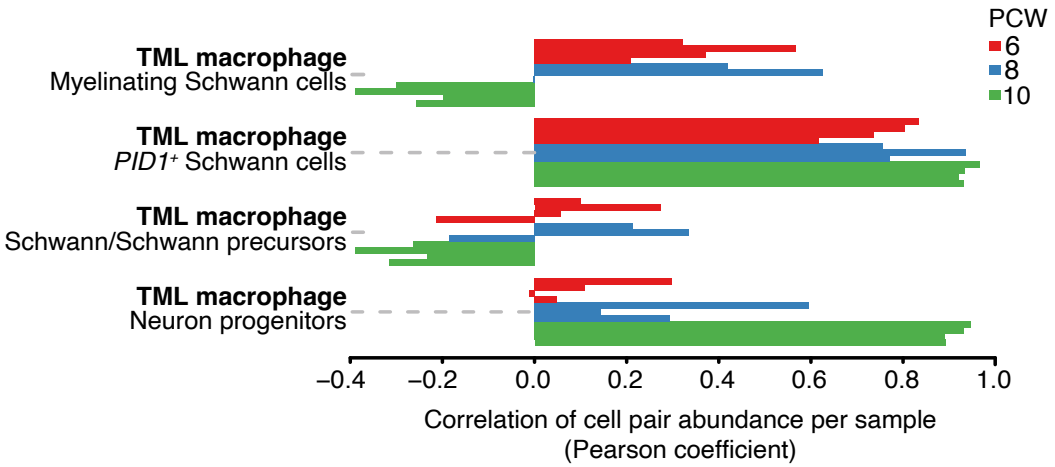

Figure 5.2. Co-location of macrophages and neural cells by correlation analysis.
Bar plot showing Pearson correlation coefficients between pairs of cell state abundances (normalised per spot) for TML macrophage and neural cell states in prenatal skin. Pearson correlation coefficients were calculated across all skin-covered spots of Visium samples; each sample is shown by an individual bar. TML macrophage: *TREM2*$^{+}$ microglia-like macrophage.

Enrichment of neural-related gene modules in TML macrophages

The transcriptional similarities between prenatal skin TML macrophages and microglia from the brain and microglia-like macrophages in other developmental tissues was discussed in section 3.3.1. Moreover, gene set enrichment analyses of the different macrophage subsets (section 2.4.7) revealed that TML macrophages expressed gene programmes related to cell migration, synapse pruning, neurogenesis, and myelination (Figure 5.3), mirroring functions undertaken by brain microglia and peripheral-nerve associated macrophages in mouse skin.[478–481]

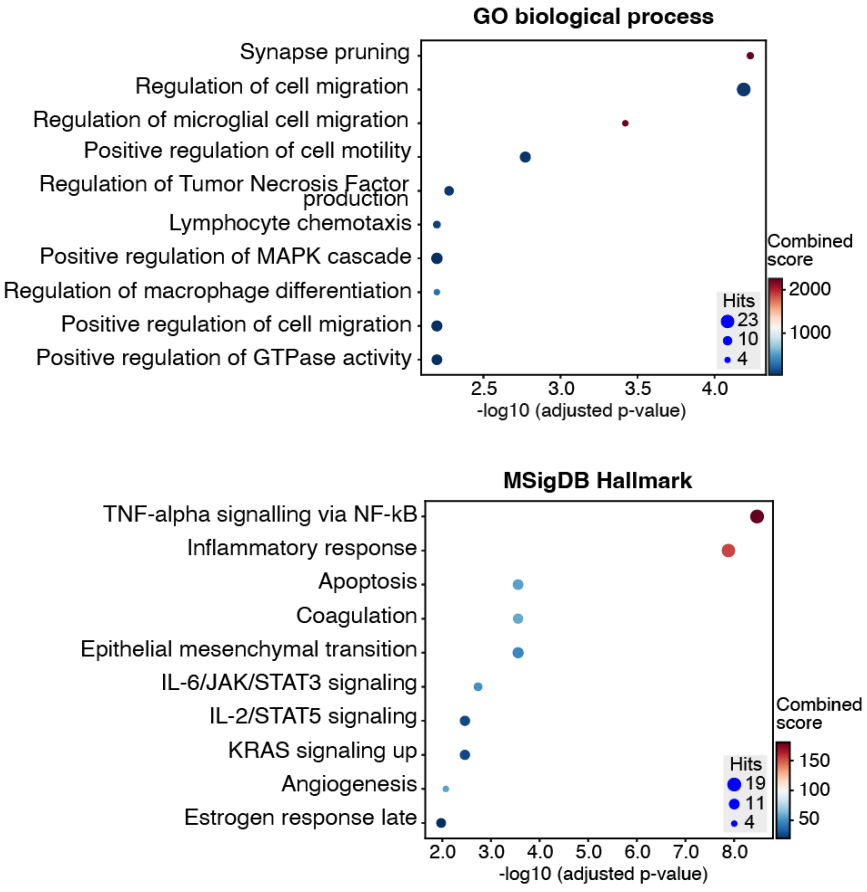

Figure 5.3. Gene set enrichment in TML macrophages.

Dot plots showing results of ORA for genes differentially expressed by TML macrophages compared to other myeloid cells in prenatal skin. The top 10 enriched gene sets (y-axis) from GOBP 2023 (top) and MSigDB Hallmark (bottom) and the degree of significance, calculated as the negative $\log_{10}$ of the adjusted p-value (from Fisher's exact test, Benjamini-Hochberg corrected for multiple testing) (x-axis), are shown in each plot; the colour scale indicates the combined score computed by Enrichr and the dot size is proportional to the number of genes associated with the gene set.

Accordingly, TML macrophages upregulated genes encoding the purinergic receptor P2Y12 (*P2RY12*) and podoplanin (*PDPN*) (Figure 5.4) which promote directed cellular migration and process extension in microglia.[482,483] They also expressed the complement *C3* and the fractalkine receptor *CX3CR1* which function in eliminating redundant synapses and regulating synapse maturation during neuronal development, including in peripheral nerves.[479,481,484] Expression of *TREM2*, known to be involved in activation and metabolic fitness of microglia and in maintenance of brain synaptic balance and neuronal wiring,[485] was increased in TML macrophages in prenatal skin (Figure 5.4). They additionally differentially expressed *BHLHE41*, a transcriptional regulator of neuronal cell differentiation,[486] and *JAM2* which modulates axonal myelination[487] (Figure 5.4). The enrichment of these gene modules suggested that TML macrophages may indeed contribute to early neural development in human prenatal skin.

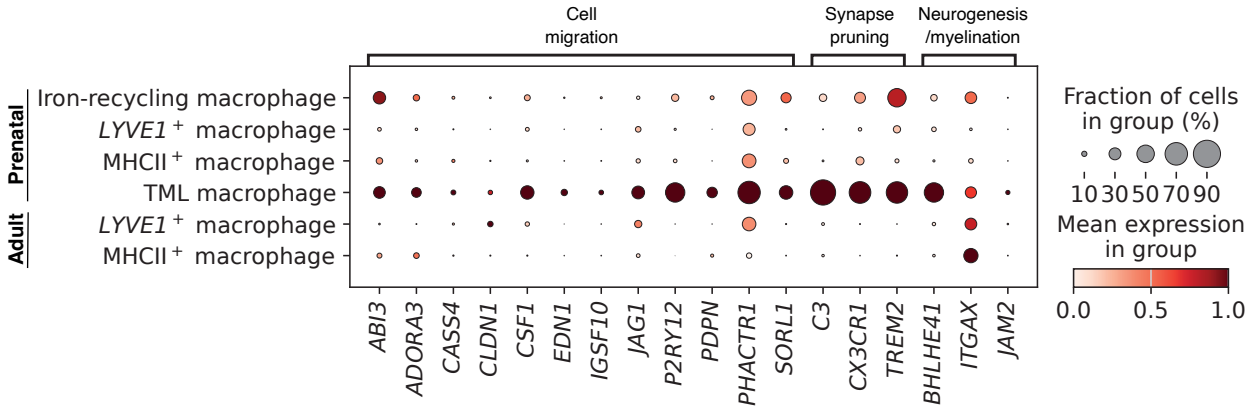

Figure 5.4. Neural-related gene modules enriched in TML macrophages.

Dot plot of selected genes (from ORA) differentially expressed by TML macrophages compared to other prenatal and adult skin macrophages; for a given gene, dot colour indicates normalised variance-scaled mean expression and dot size indicates the percentage of expressing cells in each category.

Cell-cell interactions between TML macrophages and neural cells

The predicted cellular crosstalk between co-locating TML macrophages and neural cells were therefore analysed. Several ligand-receptor interactions between TML macrophages and Schwann cells and neuron progenitors were identified that contribute to neural development (Figure 5.5). For instance, the interactions of *VEGFA*, expressed by TML macrophages, with neuropilins 1 and 2 (*NRP1* and *NRP2*) have been reported to guide nerve axon and cell bodies during

development.[488,489] TML macrophages were also predicted to signal through *GRN*, which can function as a neurotrophic factor,[490] to *NTRK1* receptors expressed on neuron progenitors and involved in neuron survival.[491] Additionally, the semaphorins, *SEMA3E* and *SEMA3C*, interacting with *PLXND1* and *NRP2* respectively (Figure 5.5), have been implicated in promoting axon growth and regulating the specificity of synapse formation.[492,493] These identified cell-cell communication further supported the potential role of TML macrophages in establishment of the early peripheral nervous system in prenatal skin.

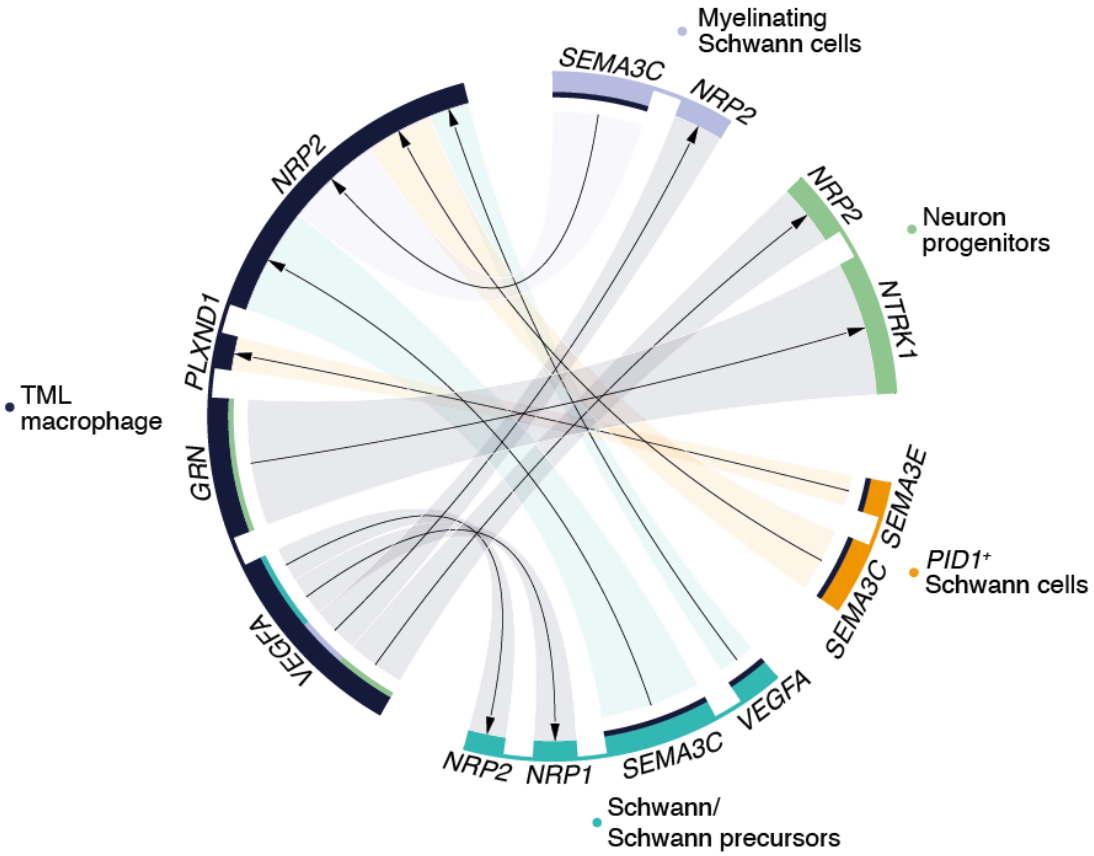

Figure 5.5. Cell-cell interactions between TML macrophages and neural cells.
Circos plot showing selected significant interactions predicted between TML macrophages and Schwann cells or neuron progenitors in prenatal skin. Arrows indicate directionality (ligand to receptor) and connection widths (shaded areas) are proportional to the mean expression values of ligand-receptors pairs; significance determined by permutation testing (adjusted p-value < 0.05) in CellPhoneDB.

5.3.2 Macrophages and vascular development in prenatal skin

Co-location of macrophages with endothelial cells in early prenatal skin

Macrophages were predicted to co-locate with vascular endothelial cells in early and late neurovascular microenvironments (Figure 3.57) based on NMF analysis as described in section 3.3.5. TML macrophages were predicted to co-localise with arterioles in microenvironment 1 (early neurovascular microenvironment) (Figure 3.57). TML macrophages also contributed to microenvironment 5 (late neurovascular microenvironment), alongside iron-recyling, *LYVE1*$^{+}$ and MHCII^{+} macrophages, a tissue microenvironment they shared with several endothelial cell states including capillaries, capillary arterioles, early endothelial cells, and post-capillary venules (Figure 3.57). This was further corroborated by the findings from correlation analysis of cell state abundances which demonstrated positive coefficients between different subsets of macrophages and vascular endothelial cells (Figure 3.58, section 3.3.5).

To confirm these computationally predicted co-locations, RNAscope smFISH and immunofluorescence assays were carried out using prenatal skin samples from two gestational ages - 8 and 10 PCW. Samples from the first trimester were tested, matching sampling undertaken for spatial transcriptomic data generation (sections 3.3.5) and for confirmation of in situ co-location of macrophages and fibroblasts (section 4.3.3) as previously discussed. Similar to immunostaining performed in section 4.3.3, markers for *LYVE1*$^{+}$ and TML macrophages, which were more abundant in early gestation (Figure 3.23), were purposefully selected to increase the likelihood of detecting macrophages on tissue sections.

Immunofluorescence examinations showed *LYVE1*$^{+}$ macrophages (CD45^{+}LYVE1^{+}) in close proximity to vascular endothelial cells (CD31^{+}) in early prenatal skin (Figure 5.6). For further orthogonal verification, additional in situ hybridisation was done using RNAscope probes against alternate markers for macrophages (*CD68*) and endothelial cells (*CDH5*). Macrophages (*CD68*$^{+}$), including TML macrophages (*P2RY12*$^{+}$), were seen adjacent to longitudinally sectioned blood vessels (*CDH5*$^{+}$) (Figure 5.7). These results validated the co-location of vascular endothelial cells with *LYVE1*$^{+}$ and TML macrophages in early prenatal skin.

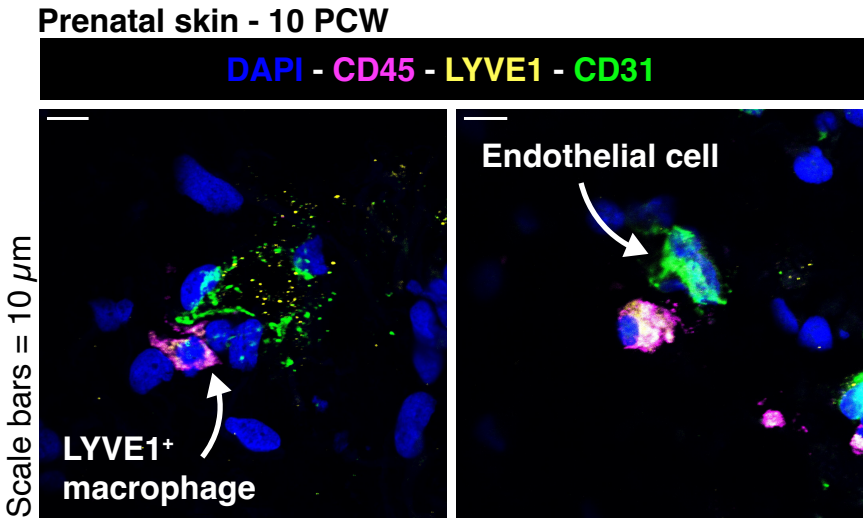

Figure 5.6. Immunofluorescence assay of perivascular macrophages.

Images of immunostained prenatal skin showing *LYVE1*$^{+}$ macrophages (LYVE1, yellow; CD45, magenta) next to endothelial cells (CD31, green) with DAPI (blue) nuclear staining. Representative image (10 PCW) shown from n=1 independent biological sample with 4 replicates. Scale bars, 10 μm.

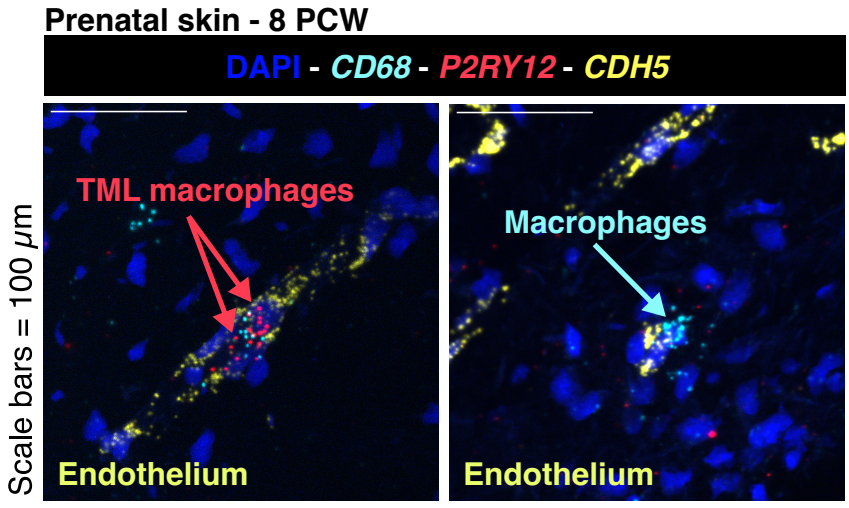

Figure 5.7. RNAscope FISH of perivascular macrophages.

RNAscope images showing macrophages (*CD68*, cyan) including TML macrophages (*P2RY12*, red) adjacent to vascular endothelium (*CDH5*, yellow) in prenatal skin with DAPI (blue) nuclear staining. Representative image (8 PCW) shown from n=3 independent biological samples. Scale bars,100 μm.

Enrichment of angiogenesis gene modules in macrophage subsets

The results of gene set enrichment analyses of the different macrophages subsets (section 2.4.7) showed that macrophages upregulated diverse gene programmes related to angiogenesis, such as sprouting angiogenesis, endothelial cell migration and proliferation, and blood vessel morphogenesis, with both positive and negative regulation (Appendix M). This suggested that macrophages tightly co-ordinate the various steps during formation of prenatal skin vasculature.

To investigate whether the individual prenatal macrophage subsets each contributed to specific angiogenic processes, different angiogenesis gene modules (Appendix G1) were scored in each macrophage population (section 2.4.8). The gene sets were obtained from the Enrichr database;[204] scores were calculated for each macrophage subset and visualised as a heatmap (Figure 5.8) following standardisation (section 2.4.8). This revealed that sprouting angiogenesis was positively regulated by *LYVE1*$^+$ and TML macrophages and endothelial cell migration by iron-recycling macrophages and TML macrophages (Figure 5.8). *LYVE1*$^+$ macrophages also promoted endothelial cell proliferation and blood vessel morphogenesis, in keeping with their close association with blood vessels on immunofluorescence microscopy (Figure 5.6).

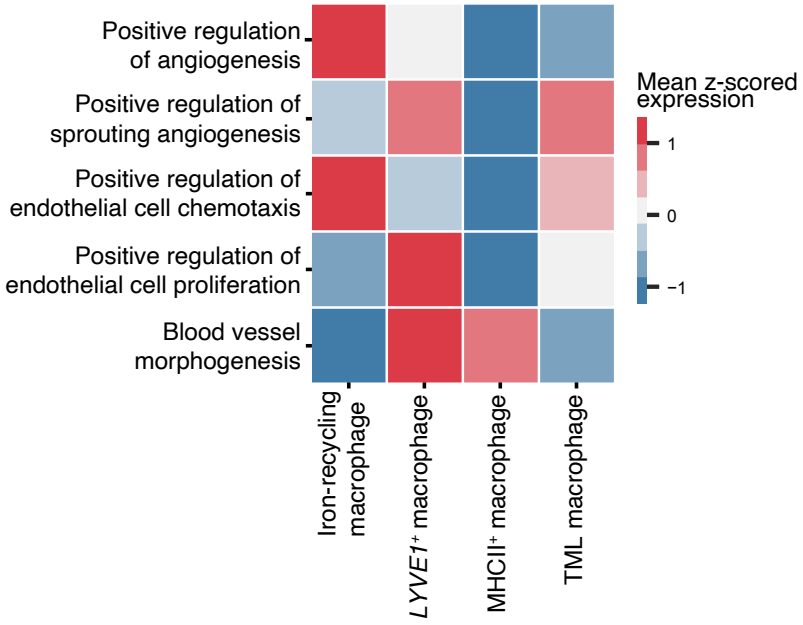

Figure 5.8. Angiogenesis gene module scores in macrophage subsets.

Heatmap of gene module scores of different angiogenesis gene sets in prenatal skin macrophages; colour scale indicates the normalised (z-scoring) mean score per macrophage population for each gene set.

Cellular crosstalk between macrophages and vascular endothelial cells

To identify the cell-cell communication potentially mediating the above immune support of angiogenesis, the predicted ligand-receptor interactions between vascular endothelial cells and co-locating macrophages (iron-recycling, *LYVE1*$^{+}$, MHCII^{+} and TML) were examined in prenatal skin. Macrophages expressed VEGFs (*VEFGA*, *VEGFB*), PDGFs (*PDGFC*), and chemokines (*CCL8*, *CXCL8*) which interacted with corresponding cell-surface receptors on endothelial cells, including neuropilins (*NRP1*, *NRP2*), tyrosine kinases (*KDR*, *FLT4*) and chemokine receptors (*ACKR1*), to promote or regulate angiogenesis (Figure 5.9).

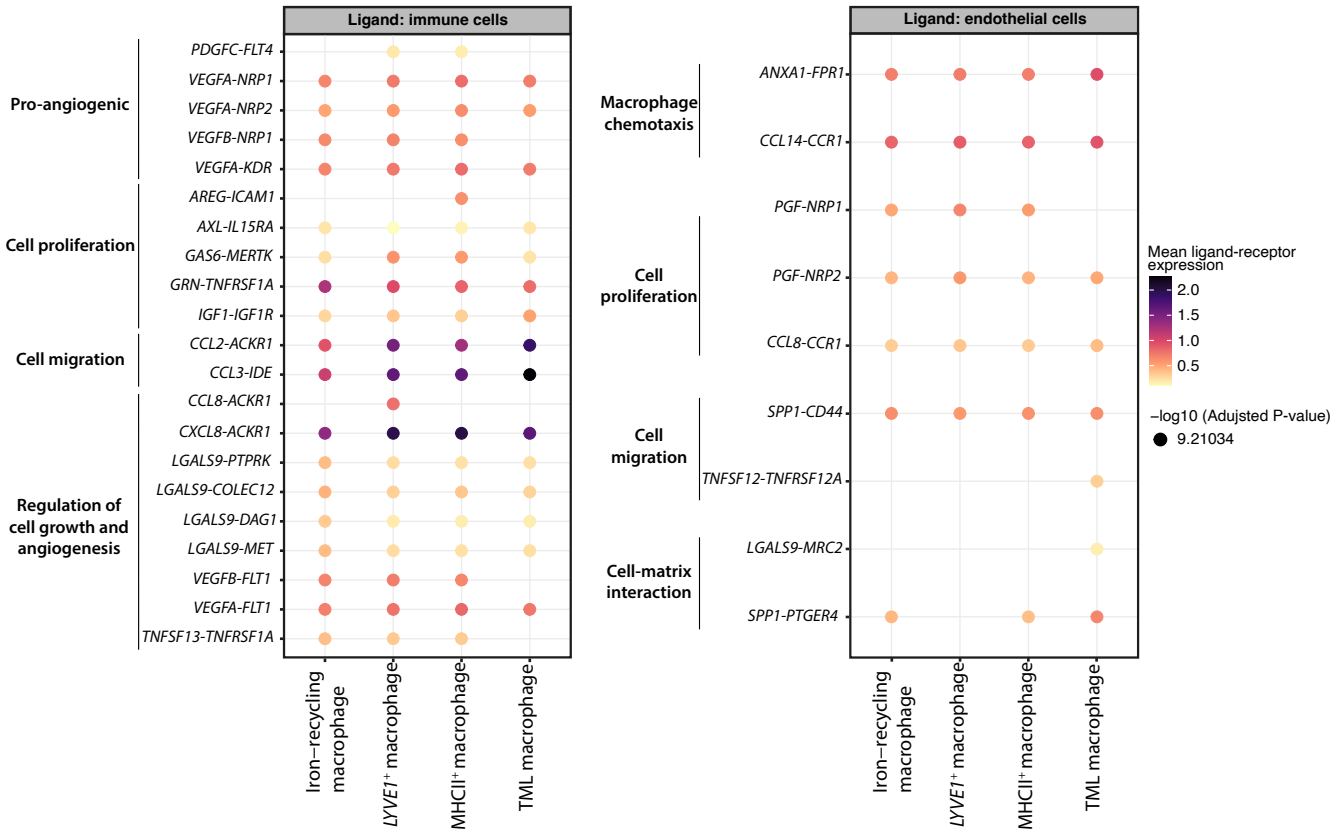

Figure 5.9. Cell-cell interactions between macrophages and endothelial cells.

Dot plots of selected significant interactions between macrophages and endothelial cells in prenatal skin grouped by function; ligand (first gene in each gene pair) is expressed by macrophages (left) or endothelial cells (right). Colour scale indicates the mean expression values for ligand-receptors pairs; significance determined by permutation testing (adjusted p-value < 0.05) in CellPhoneDB.

The analysis also showed that signalling involved in cellular proliferation (for example, *GRN-TNFRSF1A*, *IGF1-IGF1R*, *PGF-NRP1*, *PGF-NRP2*)[494–496] and cell chemotaxis and migration (for example, *CCL2-ACKR1*, *CCL14-CCR1*, *TNFSF12-TNFRSF12A*)[497,498] were reciprocal between macrophages and endothelial cells (Figure 5.9). This implied that, in fact, bi-directional regulation, from macrophages to endothelial cells and vice versa, carefully orchestrated the development of blood vessels in prenatal skin. Indeed, modulation of macrophage recruitment, infiltration and expansion by endothelial cells has previously been reported.[499–501]

Collectively, these results indicated that macrophages co-located and interacted with endothelial cells to contribute to distinct angiogenic processes during establishment of prenatal skin vascular network. Based on the findings from in vivo prenatal skin, whether the endothelial cells of the skin organoid were impacted by the deficiency of immune cells in this in vitro model was next investigated.

5.3.3 Endothelial cells of the skin organoid model

Comparison of endothelial cells between skin organoid and prenatal skin

Comparison of the skin organoid scRNA-seq dataset with prenatal and adult skin data (section 3.3.3) highlighted that the skin organoid lacked immune cells and had substantially reduced endothelial cells (Figure 3.26). To delineate the refined endothelial cell states present in the skin organoid compared to prenatal skin, the integration of the endothelium data subsets (section 2.4.2) was visualised within a combined embedding (Figure 5.10). This again showed a paucity of endothelial cells in the skin organoid and further revealed a lack of heterogeneity in this model: most skin organoid endothelial cells resembled prenatal skin capillary arterioles and lymphatic cells were completely absent (Figure 5.10).

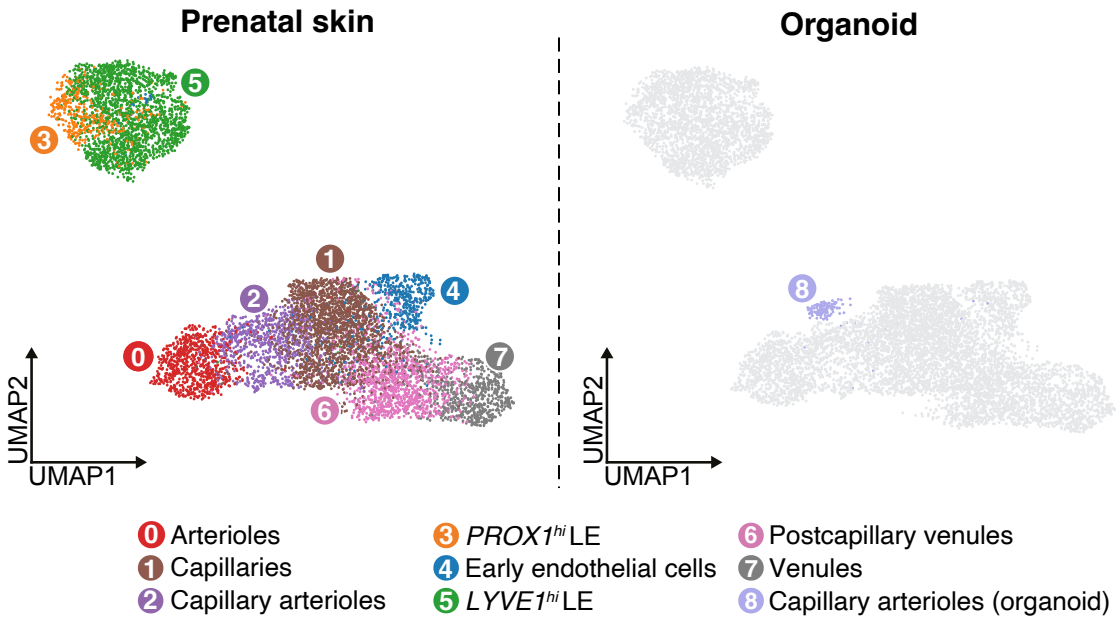

Figure 5.10. Refined endothelial cell states in integrated prenatal skin and skin organoid data.

UMAP visualisation of co-embedded prenatal skin (left) and skin organoid (right) endothelial clusters in the integrated scRNA-seq data; clusters are coloured by refined cell state annotations. LE: lymphatic endothelium.

To confirm the transcriptional identity of the endothelial cells present in the skin organoid, scores were derived for different categories (capillary, arteriole, venule and LE) using published marker genes[205–207] (Appendix G2) (section 2.4.8) and plotted across all endothelial cell states in prenatal skin and the skin organoid (Figure 5.11). The skin organoid capillary arterioles had increased capillary score, which was also high in prenatal skin capillary arterioles and capillaries, but low arteriole, venule and LE scores (Figure 5.11). In combination with the integration analyses above, these results corroborated skin organoid endothelial cells as capillary arterioles.

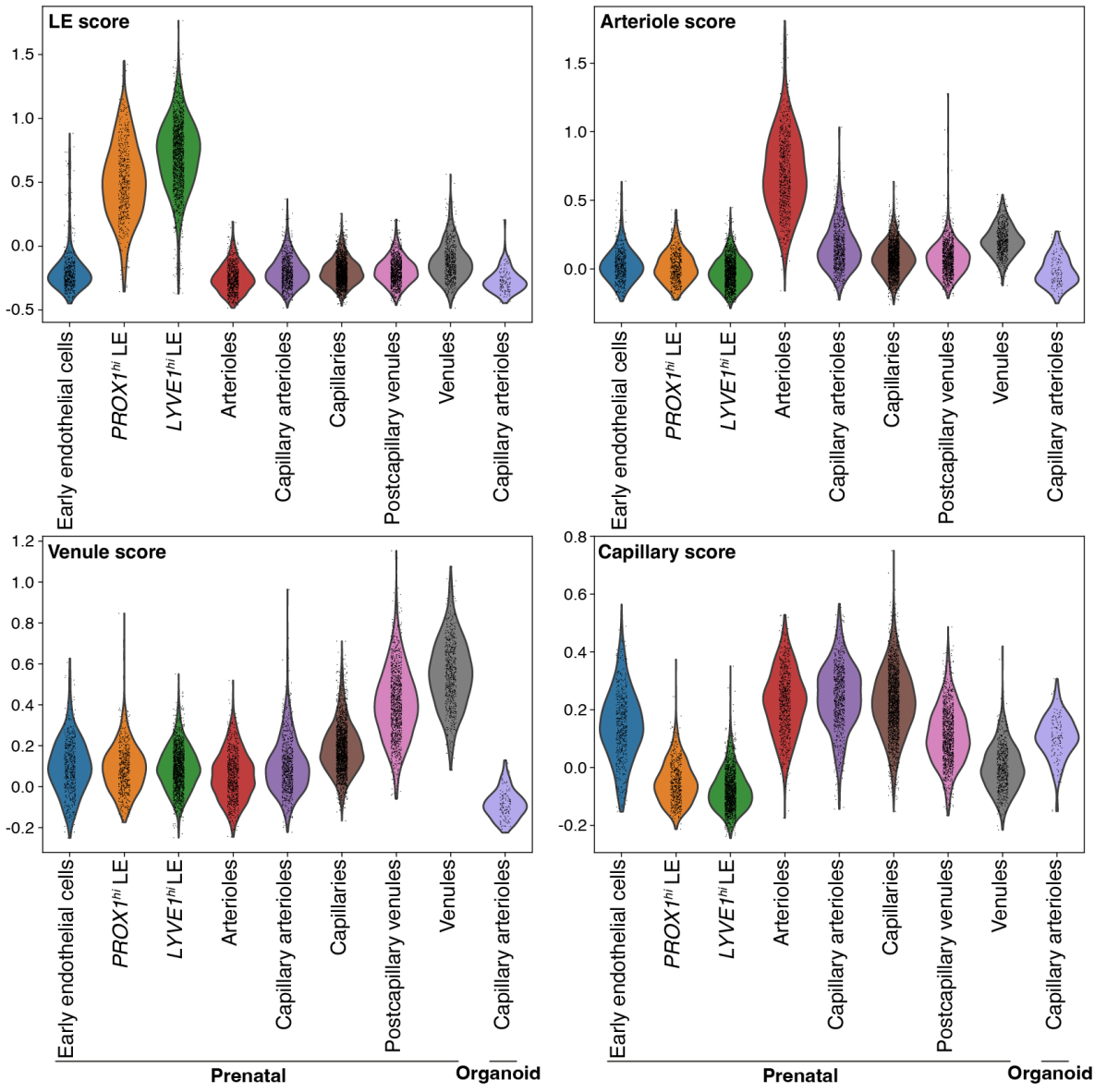

Figure 5.11. Module scoring of endothelial marker genes.

Violin plots of the distribution of endothelial gene module scores in prenatal skin and skin organoid vascular and lymphatic cells. LE: lymphatic endothelium.

Endothelial cell differentiation

Endothelial cell differentiation in in vivo prenatal skin

To better understand endothelial cell differentiation during development, and lack thereof in the skin organoid, inferred trajectory and pseudotime analysis of prenatal skin endothelial cells was carried out using CellRank[193,194] with scVelo[195] (section 2.4.5). Early endothelial cells were predicted to differentiate either along an 'arteriolar trajectory', which produced capillaries, capillary arterioles and arterioles, or along a 'venular trajectory', which gave rise to postcapillary venules and venules (Figure 5.12).

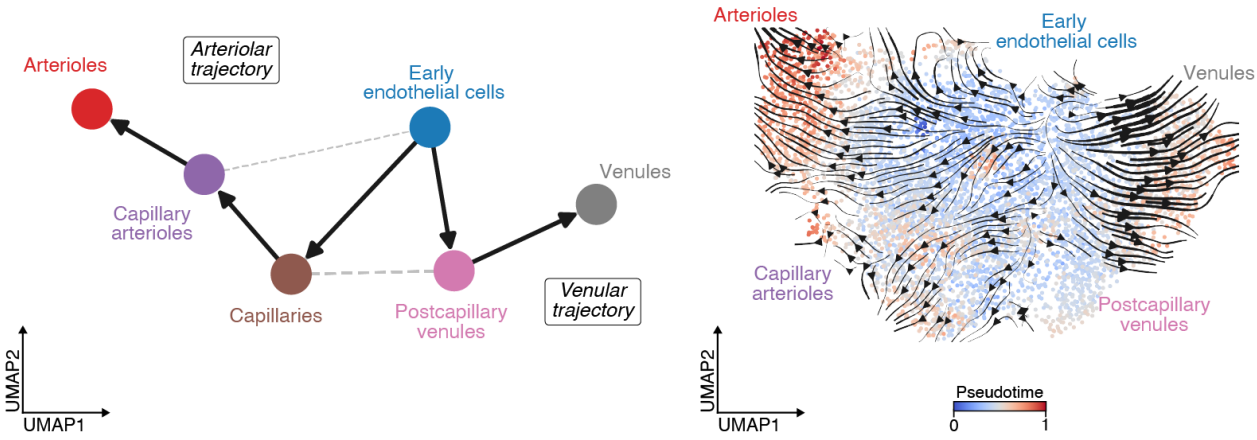

Figure 5.12. Inferred differentiation trajectory of endothelial cells.

Differentiation along 'Arteriolar' and 'Venular' trajectories of prenatal skin vascular endothelial cells. Inferred trajectories shown by PAGA plot (left) with weighted connectivities between nodes (coloured by cell states) and UMAP (right) overlaid with velocity-based directionality and coloured by pseudotime.

Accordingly, the bifurcating differentiation trajectories were characterised by the differential expression along their respective pseudotime of genes defining arteriolar (*AQP1*, *NOTCH4*, *SOX5*, *HEY1*, *FBLN5*, *GJA4*, *GJA5*) or venular (*SELE*, *VWF*, *ACKR1*, *PLVAP*, *CLU*) endothelial cells[205–207] (Figures 5.13 and 5.14). *NOTCH4* and *GJA4* were discussed earlier as indicators of arterial cell fate commitment and *SELE* as marker for postcapillary venule differentiation in prenatal skin[207,308] (section 3.3.1). In addition, the identified genes encoding transcriptional regulators (*SOX5*, *HEY1*), membrane channels (*AQP1*, *GJA5*) and an ECM molecule promoting adhesion of endothelial cells (*FBLN5*) have been reported as markers of arterioles, capillary arterioles and capillaries in adult

human skin and lung.[205–207] These reports also described genes encoding the haemostatic glycoprotein von Willebrand factor (*VWF)* and its modulator clusterin (*CLU*),[502] atypical chemokine receptor 1 (*ACKR1*), and the membrane molecule regulating microvascular permeability (*PLVAP*)[503] as denoting a venous signature,[205–207] thus corroborating the genes found along the venular pseudotime.

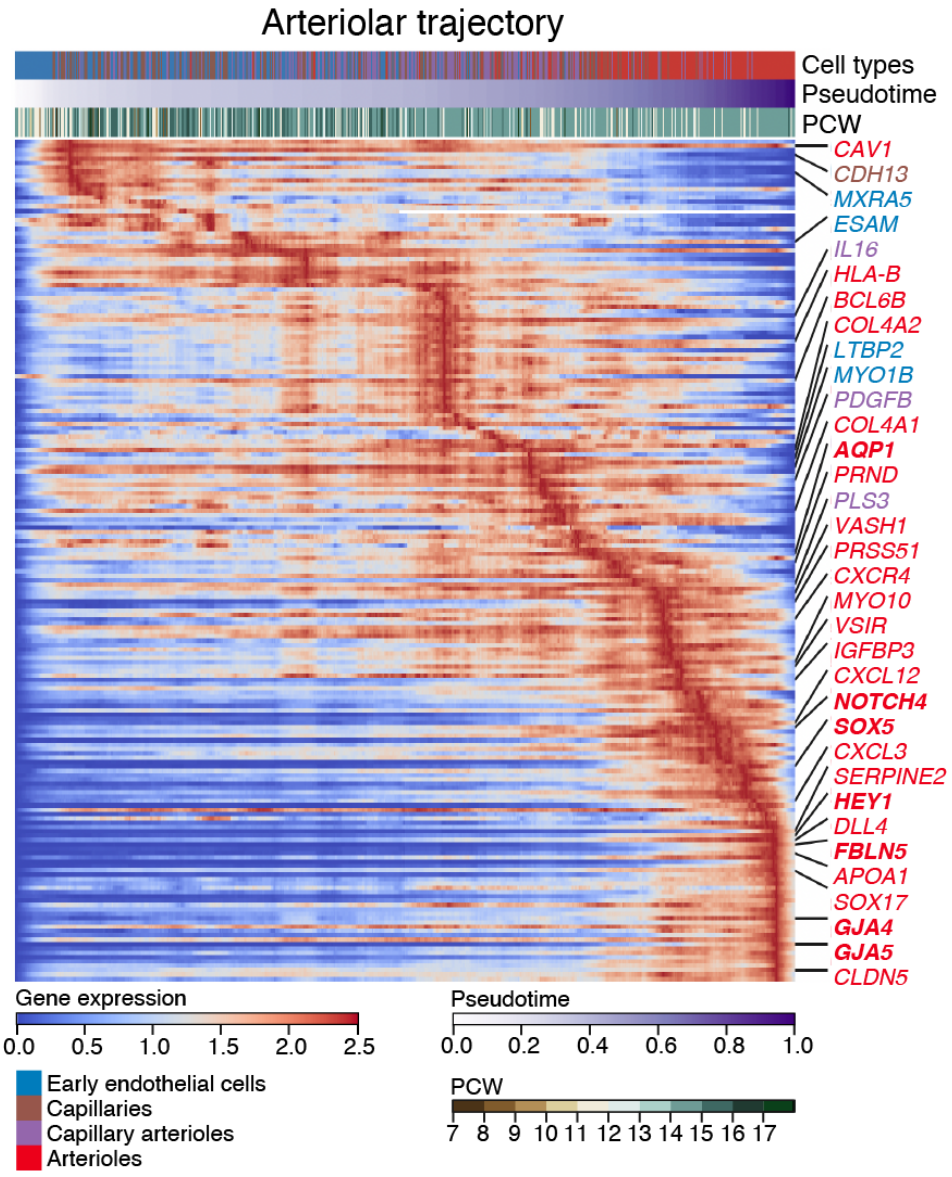

Figure 5.13. Driver genes along the arteriolar trajectory.

Heat map of genes (y-axis) differentially expressed across pseudotime (x-axis) along the arteriolar trajectory; corresponding prenatal skin endothelial cell states and gestational ages (PCW) are indicated alongside pseudotime and blue-red colour scale represents normalised gene expression.

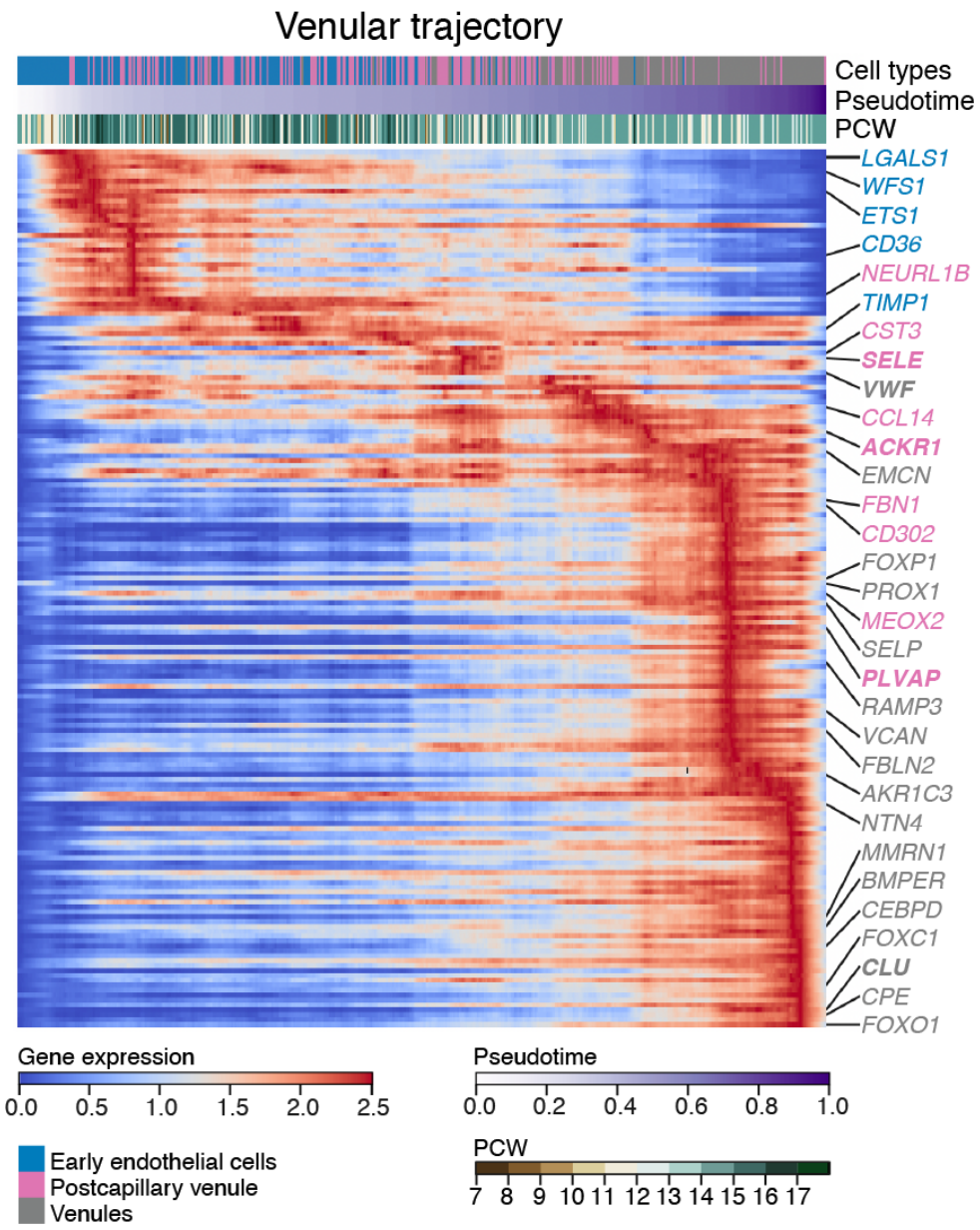

Figure 5.14. Driver genes along the venular trajectory.

Heat map of genes (y-axis) differentially expressed across pseudotime (x-axis) along the venular trajectory; corresponding prenatal skin endothelial cell states and gestational ages (PCW) are indicated alongside pseudotime and blue-red colour scale represents normalised gene expression.

Endothelial cell differentiation in in vitro models

The trajectory analysis inferred that prenatal skin capillary arteriole cells developed from early endothelial and capillary cells and further differentiated into arterioles. Except for capillary arteriole cells, the other endothelial cell states were absent in the skin organoid (Figure 5.10). This could be due to a number of factors: (1) all of the endothelial cells from the skin organoid were not captured during processing, or (2) the growth factors used to promote ectodermal differentiation for hair follicle formation in the skin organoid did not support angiogenesis, or (3) the heterogeneity of prenatal skin vasculature cannot be fully recapitulated in vitro.

To verify the latter two points, scRNA-seq data from a dedicated blood vessel organoid was compared with prenatal skin using LR analysis (section 2.4.3). In this organoid system, which was derived from human ES cells and iPS cells and lacked immune cells, the endothelial cells also failed to acquire definite arterial or venous identities.[190] This observation from the authors was reflected in the comparison to prenatal skin. Endothelial cells from the blood vessel organoid closely matched early endothelial, capillary and arteriole cells in prenatal skin (Figure 5.15), suggesting proclivity towards an arterial transcriptome. The alignment of prenatal skin postcapillary venules to combined endothelial and mural cells in the organoid (Figure 5.15) likely corresponded to an intermediate population with immature-venous and mural markers which was present in the blood vessel organoid.[190] Overall, these findings implied that even a mesoderm-geared blood vessel organoid model did not reproduce the full spectrum of endothelial diversity seen in vivo and that additional factors may contribute to the limited vascular differentiation observed in vitro.

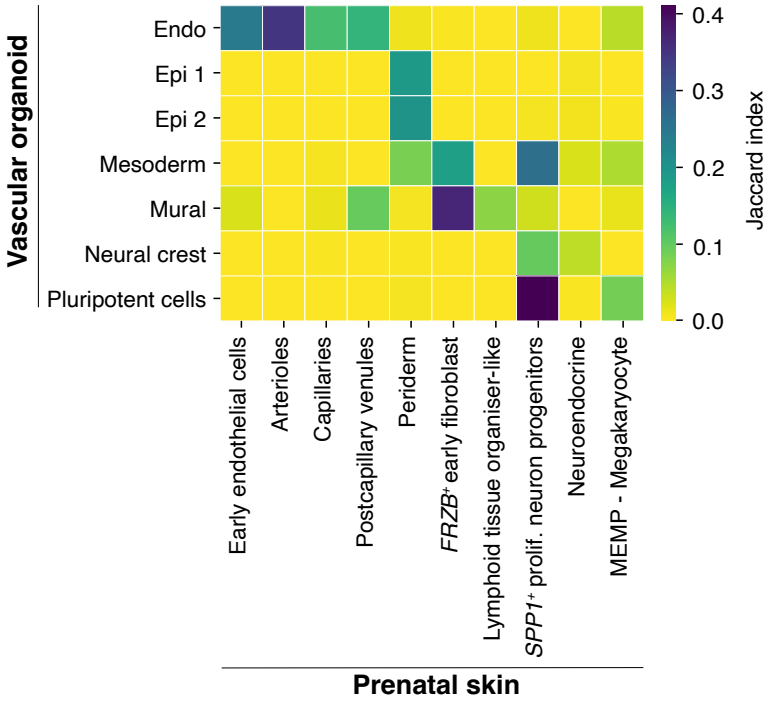

Figure 5.15. Alignment of blood vessel organoid to prenatal skin.

Heatmap showing degree of correspondence between prenatal skin and blood vessel organoid cell types; colour scale indicates the Jaccard index for blood vessel organoid labels (y-axis) from a logistic regression model trained on prenatal skin data (x-axis).

Mechanisms for limited endothelial cells in the skin organoid model

Additional potential mechanisms for the failure of skin organoid endothelial cells to expand and differentiate were therefore explored. Several recognised drivers of angiogenesis, including blood flow, tissue hypoxia, growth factors, potential for sprouting angiogenesis, pro-angiogenic signals, and transcription factors were examined.[504,505]

Blood flow, hypoxia, growth factors and sprouting potential

Laminar shear stress caused by blood flow can affect the transcriptomic signature and phenotype of endothelial cells.[506] The expressions of flow-responsive genes were compared between prenatal skin and skin organoid capillary arteriole cells (Figure 5.16). As expected, most of flow-induced genes (for example, *KLF2*, *KLF4* and *NRP1*) were upregulated in prenatal skin compared to the skin organoid whereas flow-suppressed genes (for example, *ANGPT2*, *APLN* and *THBS1*) were downregulated (Figure 5.16), in keeping with the absence of blood flow in the skin organoid.[506]

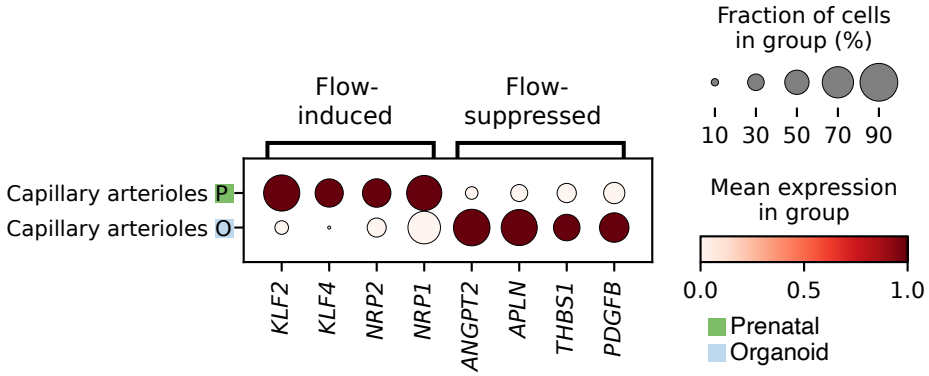

Figure 5.16. Expression of known flow-responsive genes.

Dot plot of expression of reported[506] flow-induced and flow-suppressed genes by prenatal skin and skin organoid capillary arteriole cells; for a given gene, dot colour indicates normalised variance-scaled mean expression and dot size indicates the percentage of expressing cells in each category.

Hypoxia triggers the expression of VEGFs (encoded by *VEGFA*, *VEGFB*, *VEGFC* and *VEGFD*) which in turn activate angiogenic programmes to enable sprouting angiogenesis. The nascent sprout is guided by the leading tip cells which process environmental cues to define the direction of growth while the tailing stalk cells proliferate and establish cellular junctions to form the new blood vessel[507] (section 5.1). The impact of hypoxia and potential for sprouting angiogenesis were assessed by gene module scoring of published gene sets[204,208] (Appendix G2), with tip and stalk scores representing sprouting potential (section 2.4.8).

The standardised hypoxia scores of all cell groups were decreased in the skin organoid relative to prenatal skin (Figure 5.17). Interestingly, despite the lower hypoxia scores in the skin organoid, its expression of VEGFs was generally higher than in prenatal skin for corresponding cell groups (Figure 5.18). However, while the tip scores were increased in both skin organoid and prenatal skin capillary arteriole cells, the stalk scores were reduced in the organoid endothelial cells compared to in vivo skin (Figure 5.19).

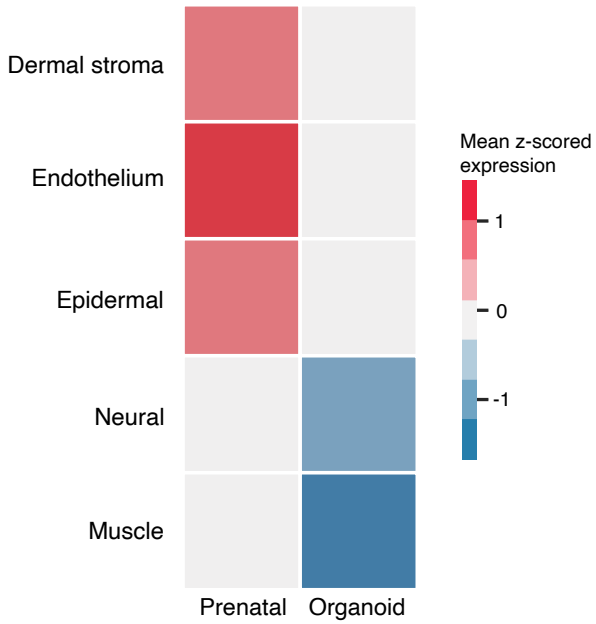

Figure 5.17. Hypoxia gene module scores.

Heatmap of gene module scores of the hypoxia gene set in prenatal skin and skin organoid broad cell groups; colour scale indicates the normalised (z-scoring) mean score per cell group in each dataset.

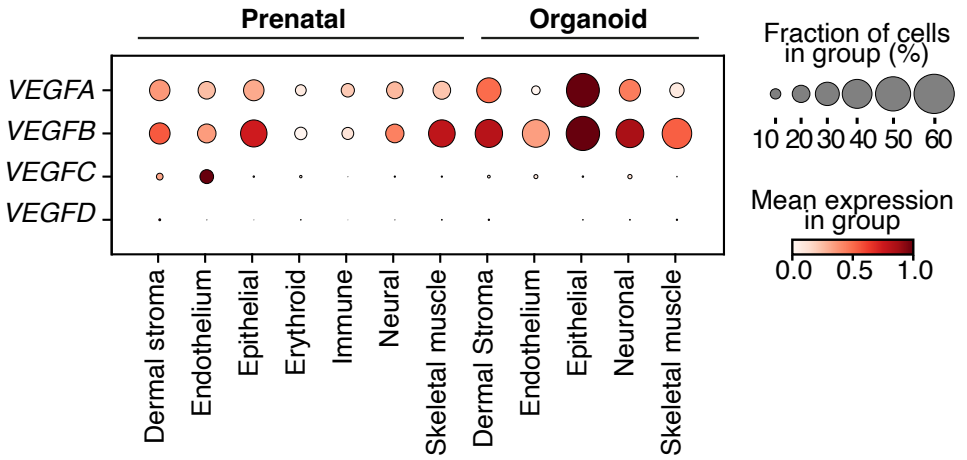

Figure 5.18. Expression of VEGFs.

Dot plot of expression of genes encoding VEGFs by prenatal skin and skin organoid broad cell groups; for a given gene, dot colour indicates normalised variance-scaled mean expression and dot size indicates the percentage of expressing cells in each category.

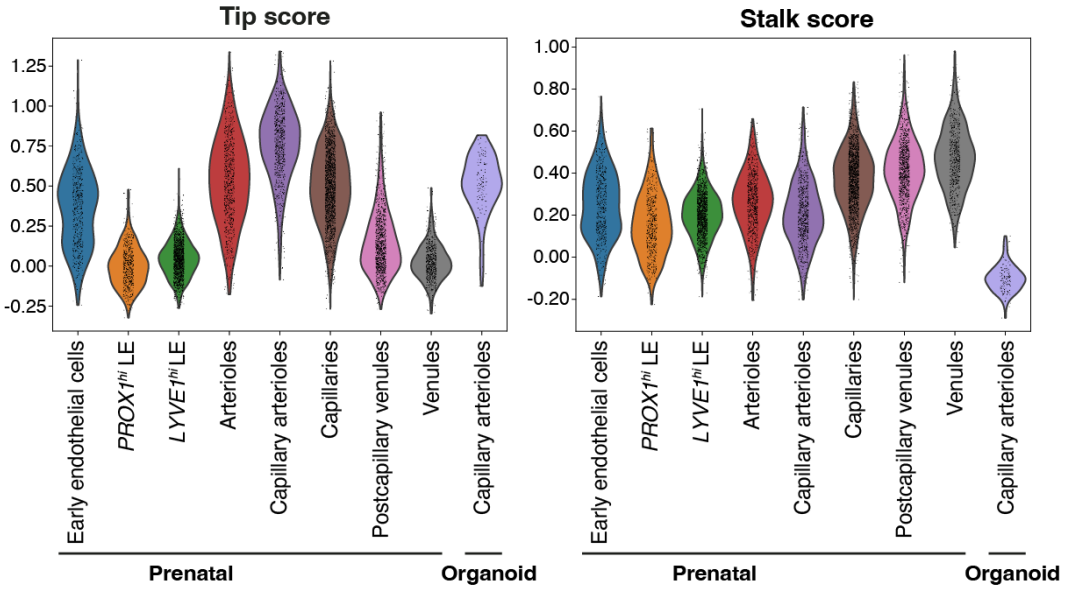

Figure 5.19. Module scoring of tip and stalk gene sets.

Violin plots of the distribution of endothelial tip and stalk gene module scores in prenatal skin and skin organoid vascular and lymphatic cells. LE: lymphatic endothelium.

These findings suggested that in spite of high expression of VEGFs in the skin organoid and adoption of a tip cell gene profile by its capillary arterioles, the stalk cell signature was attenuated which overall precluded endothelial cell expansion.

Angiogenic signals and regulon analysis

Angiogenesis-related genes were next investigated in the prenatal skin and skin organoids by first determining the differentially expressed genes between the two dataset which are known to encode secreted proteins involved in angiogenesis[209] and then identifying the cell states expressing these genes (section 2.4.8). This analysis revealed that pro-angiogenic signalling molecules (*TNF*, *ADM, CXCL8*)[508–510] were upregulated in prenatal skin relative to the skin organoid and were mainly expressed by myeloid cells including macrophages (Figure 5.20). Prenatal skin vascular endothelial cells also had higher expression of genes that regulate angiogenesis and vessel tubulogenesis (*EGFL7*, *LOXL2*, *TFPI*)[511–513] compared to skin organoid cells (Figure 5.20).

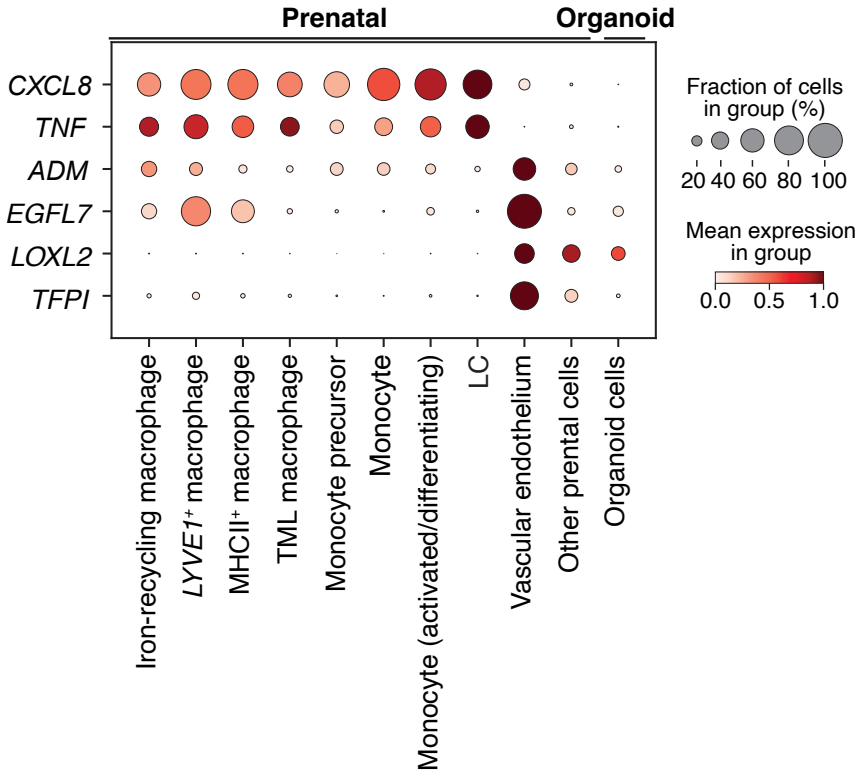

Figure 5.20. Comparison of angiogenic signals between prenatal skin and the skin organoid.

Dot plot of selected angiogenic factors differentially expressed by prenatal skin and skin organoid cells; for a given gene, dot colour indicates normalised variance-scaled mean expression and dot size indicates the percentage of expressing cells in each category. LC: Langerhans cell; TML: *TREM2*$^+$ microglia-like macrophage.

Additionally, the expression of the corresponding receptors (*TNFRSF1A*, *TNFRSF1B*, *RAMP2*, *ACKR1*) for the above pro-angiogenic molecules were assessed alongside VEGF receptors (*FLT1*, *KDR*). In comparison to prenatal skin endothelial cells, capillary arterioles in the skin organoid downregulated all tested receptors (Figure 5.21).

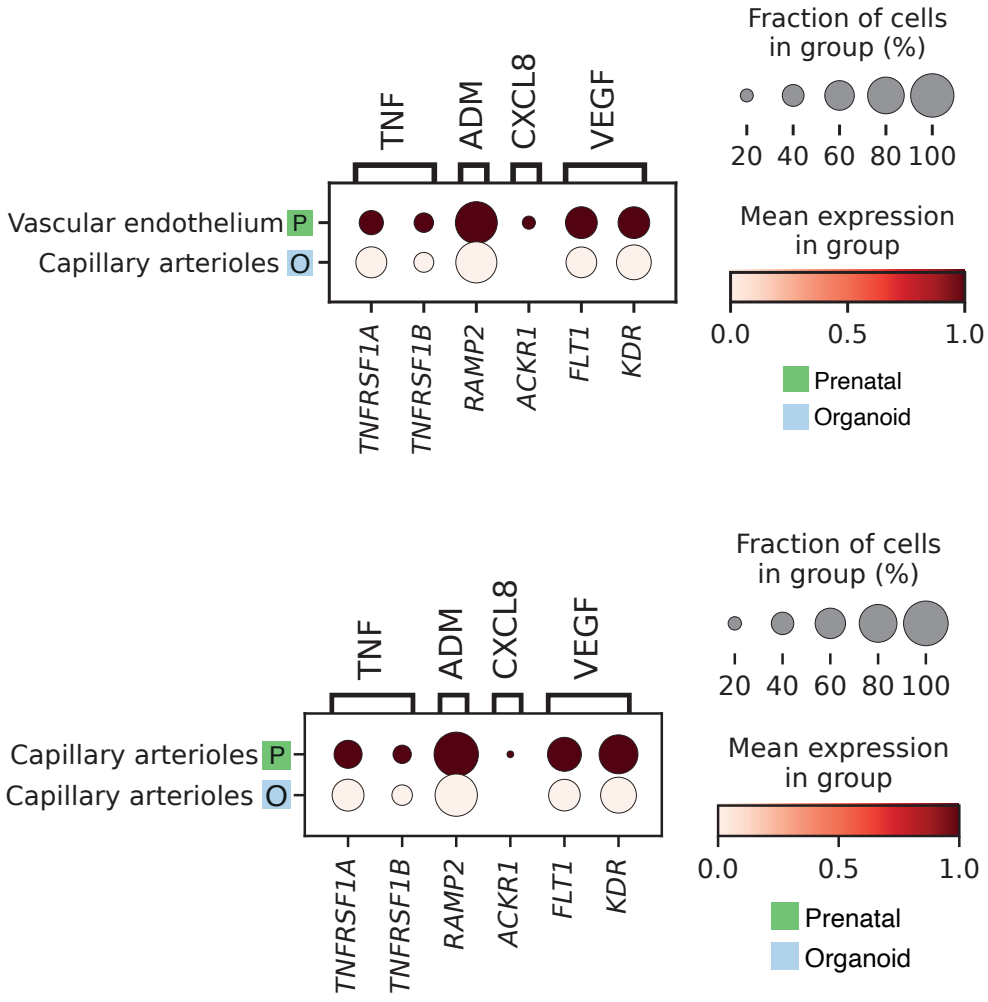

Figure 5.21. Expression of angiogenic receptors.

Dot plot of expression of pro-angiogenic receptor genes in prenatal skin and skin organoid vascular endothelial cells (top) and capillary arterioles (bottom); for a given gene, dot colour indicates normalised variance-scaled mean expression and dot size indicates the percentage of expressing cells in each category.

To explore the transcription factors potentially regulating the observed differences in expression of angiogenesis-related genes between prenatal skin and the skin organoid, regulon analysis was conducted using pySCENIC[210] (section 2.4.9). Several transcription factors implicated in endothelial cell biology and angiogenesis (*FOXP1*, *GATA1*, *GATA2*, *NFATC1*, *SOX7*)[514–521] were differentially regulated between the capillary arteriole cells of the prenatal skin and the skin organoid (Figure 5.22). Of those, *GATA2* is known to have a key role in developmental angiogenesis and to control VEGF-driven endothelial cell migration and sprouting in vitro.[522–524] The VEGF receptors (*KDR* and *FLT1*), which were found earlier to be downregulated in the skin organoid capillary arterioles, are also known downstream targets of *GATA2*.[523,525] *GATA1*, *FOXP1* and *NFATC1* mediate cellular migration, proliferation and tube morphogenesis of endothelial cells, with the latter two also involved in cardiovascular development, while *SOX7* regulates early specification of endothelial progenitors and hypoxia-induced angiogenesis.[514–521]

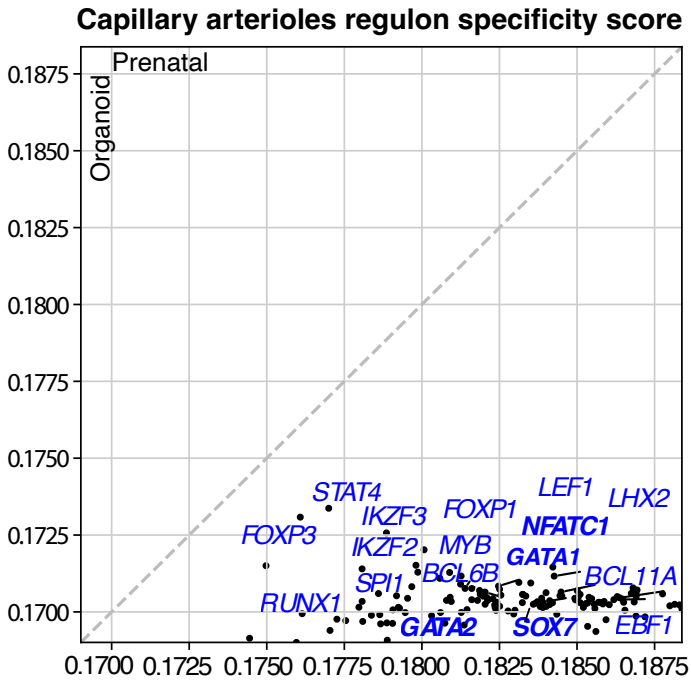

Figure 5.22. Comparison of regulon activity.

Scatter plot of transcription factors differentially regulated between prenatal skin (x-axis) and skin organoid (y-axis) capillary arteriole cells; assessed by regulon specificity score in pySCENIC.

The STRING database[211,212] was then used to construct a gene interaction network (Figure 5.23) including the identified transcription factors (section 2.4.9). *GATA2* and *NFATC1* appeared to regulate multiple genes (*ETS1*, *VWF*, *PVLAP* and *SELE*) which were differentially expressed along the venular pseudotime (Figure 5.14) and which also function in endothelial differentiation.[205] These target genes were mostly downregulated in the capillary arterioles of the skin organoids compared to prenatal skin (Figure 5.24), in keeping with the reduced activity of their upstream transcription factors, *GATA2* and *NFATC1*, in the skin organoids (Figure 5.22).

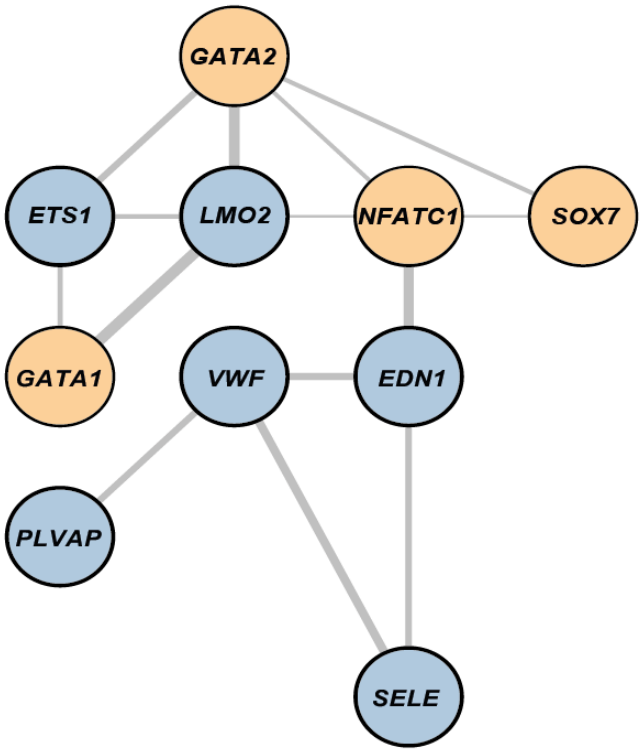

Figure 5.23. Gene interaction network.

Network graph showing interactions between transcription factors identified from regulon analysis (orange nodes) with selected target genes (blue nodes); edge (grey) widths are proportional to weighted connectivities from STRING.

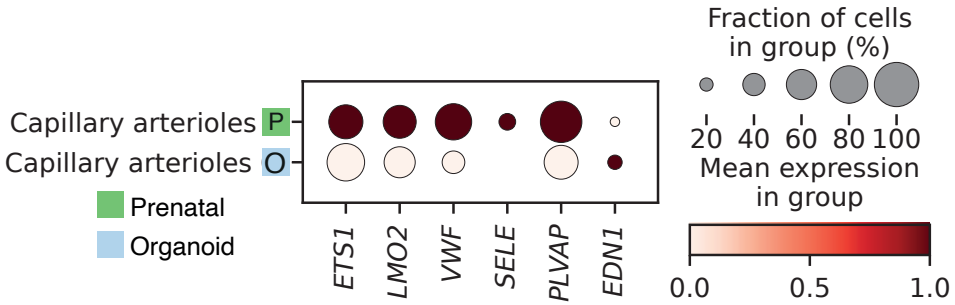

Figure 5.24. Expression of target genes.

Dot plot of expression of *GATA2* and *NFATC1* target genes in prenatal skin and organoid capillary arterioles; for a given gene, dot colour indicates normalised variance-scaled mean expression and dot size indicates the percentage of expressing cells in each category.

Finally, NicheNet[213] modelling was performed to infer the intercellular communication driving the differences in transcription factors and angiogenic genes between prenatal skin and the skin organoid (section 2.4.9). This analysis also predicted that macrophage-expressed pro-angiogenic molecules, including *TNF* and *IL1B*,[508,526] were potential ligands regulating the differential gene profiles between prenatal skin and skin organoid endothelial cells (Appendix H). Notably, *VEGFA* was also detected as one of the upstream ligands (Appendix H) and was linked to *GATA2* gene regulatory effects (Figure 5.25).

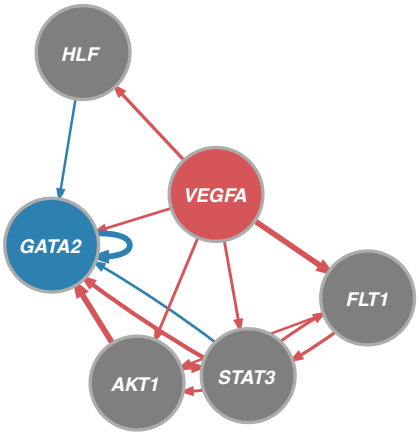

Figure 5.25. Ligand to target gene links.

Network graph showing interactions linking the selected ligand (*VEGFA*, red) and target gene (*GATA2*, blue) through signalling mediators (grey) identified from NicheNet; edge colours indicate nature of interaction as signalling (red) or gene regulatory (blue) and edge widths are proportional to weights of the represented interactions.

Collectively, these results (summarised in Figure 5.26) indicated that the elevated VEGF expression in the skin organoid was insufficient to compensate for the absence of macrophage-related factors to drive pro-angiogenic regulon activity, including *GATA2* and downstream VEGF receptor induction, and subsequent endothelial cell expansion and differentiation. This suggested that macrophages may be critical for adequate vascular endothelial development in the skin organoids, supporting earlier observations from in vivo prenatal skin (section 5.3.2).

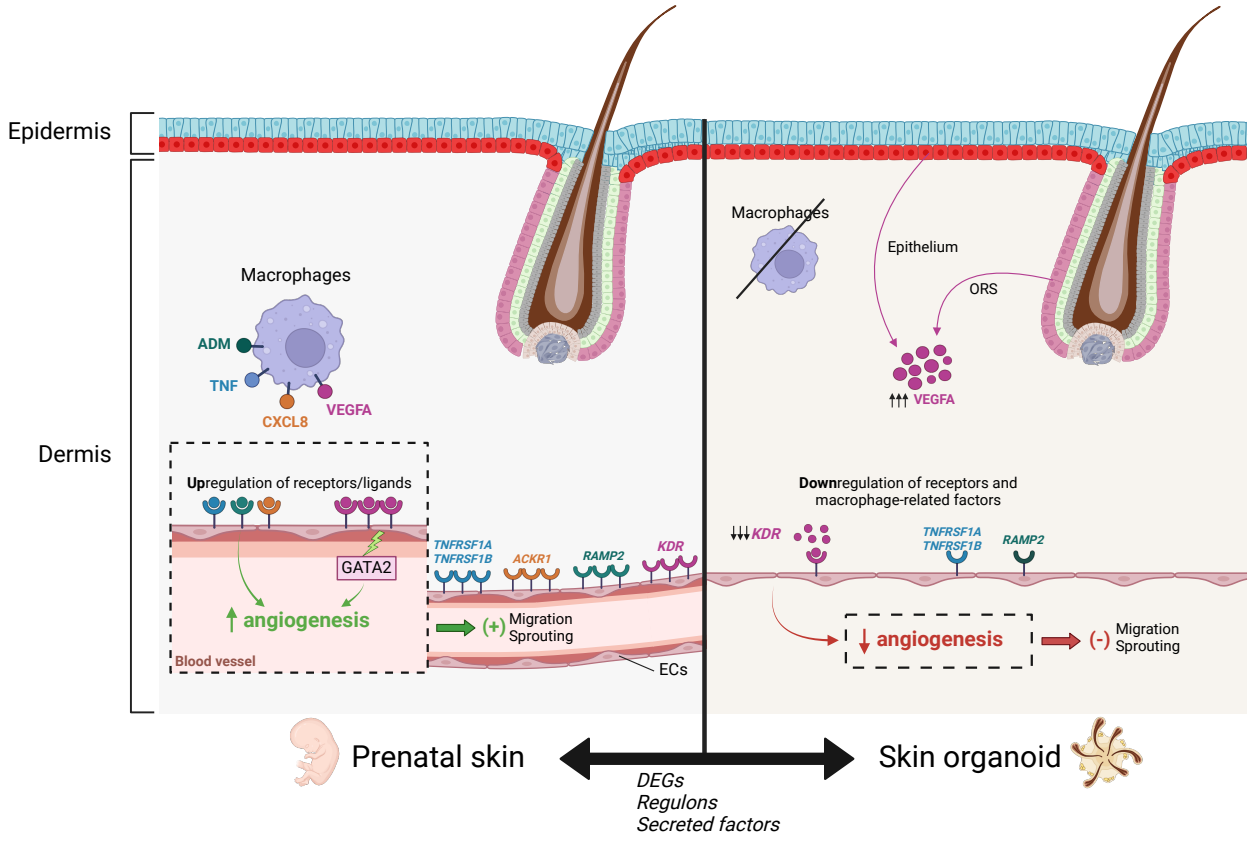

Figure 5.26. Angiogenesis in prenatal skin and skin organoids.

Schematic representation of factors contributing to differences in angiogenesis between in vivo prenatal skin and in vitro skin organoid model. DEGs: differentially expressed genes; ECs: endothelial cells; ORS: outer root sheath. Adapted from Gopee et al.[157]

5.3.4 Co-culture of skin organoids with macrophages

To determine whether addition of macrophages could improve vascularisation of the skin organoid and to validate the role of these immune cells in angiogenesis, in vitro co-culture experiments were carried out. Macrophages were derived from the same iPS cell line as the skin organoids, using a published protocol.[219] The cultured immune cells were analysed by flow cytometry to confirm their cell identity, using a combination of known macrophage markers (CD14, CD16 and CD206), and to exclude DCs (CD1C) (section 2.6.1) (Figure 5.27).

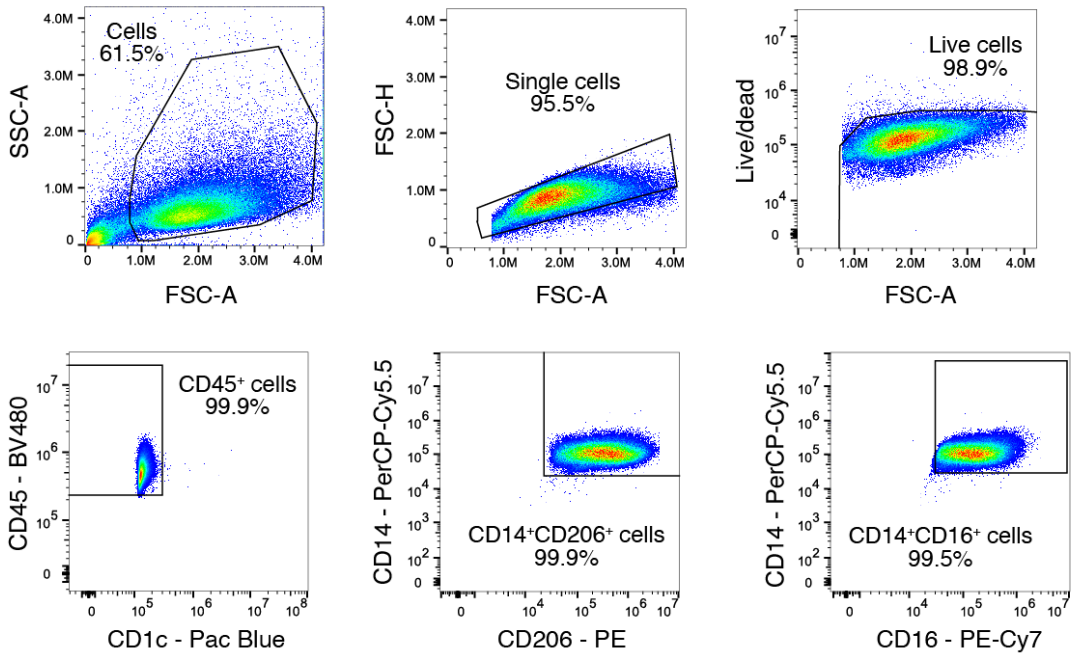

Figure 5.27. Phenotyping of iPS cell-derived macrophages.

Flow cytometry analysis of iPS cell-derived macrophages demonstrating cultured live single immune ($CD45^+$) cells comprised almost exclusively of macrophages without DCs based on markers for macrophages (CD14, CD16, CD206) and DCs (CD1C).

The autologous iPS cell-derived macrophages were introduced in the early stages of skin organoid differentiation (day 12) and the endothelial network was assayed on day 35 of co-culture using whole-mount immunofluorescence staining followed by spinning disc confocal imaging (sections 2.6.3 and 2.6.4). Given the macrophage culture essentially consisted of macrophages only (Figure 5.27), anti-CD45 antibody was used to detect macrophages and anti-CD31 to identify vascular endothelial cells. Marked differences were observed between the vasculature of the skin organoids cultured with and without macrophages (Figure 5.28).

In skin organoids co-cultured with macrophages, endothelial cells formed a refined and organised vascular network (Figure 5.28), with macrophages seen co-localising with blood vessels even after 5 weeks of culture as confirmed on cryosection images (Figure 5.29). In the absence of macrophages, endothelial cells aggregated into a dense mesh-like formation, reminiscent of a developing primitive vascular plexus (Figure 5.29). This disorganised mesh could be less amenable to dissociation, precluding isolation of endothelial cells and contributing to the paucity of endothelial cells noted in the skin organoid scRNA-seq data (Figure 5.10).

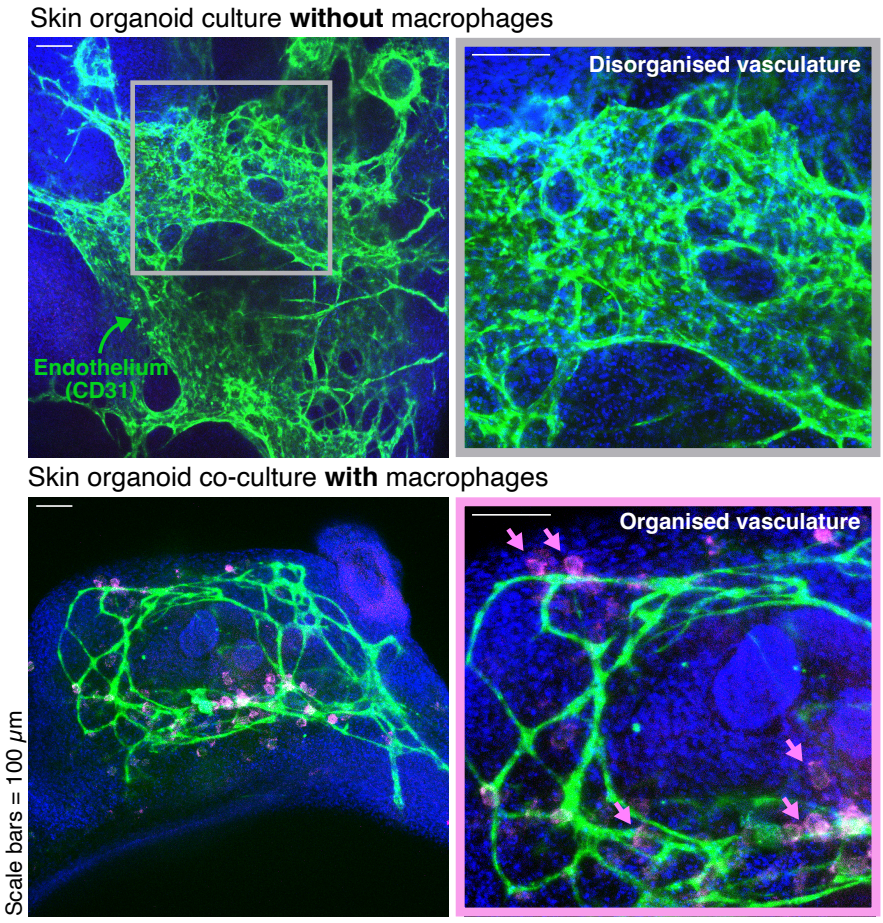

Figure 5.28. Vascular network in skin organoids cultured with and without macrophages. Images of whole-mount immunostained skin organoids cultured without (top) and with (bottom) autologous macrophages (CD45, magenta) demonstrating differences in network formation of vascular endothelial cells (CD31, green) with DAPI (blue) nuclear staining. Representative images shown from 10 independent samples (n=5 with macrophages, n=5 without macrophages). Scale bars, 100 μm.

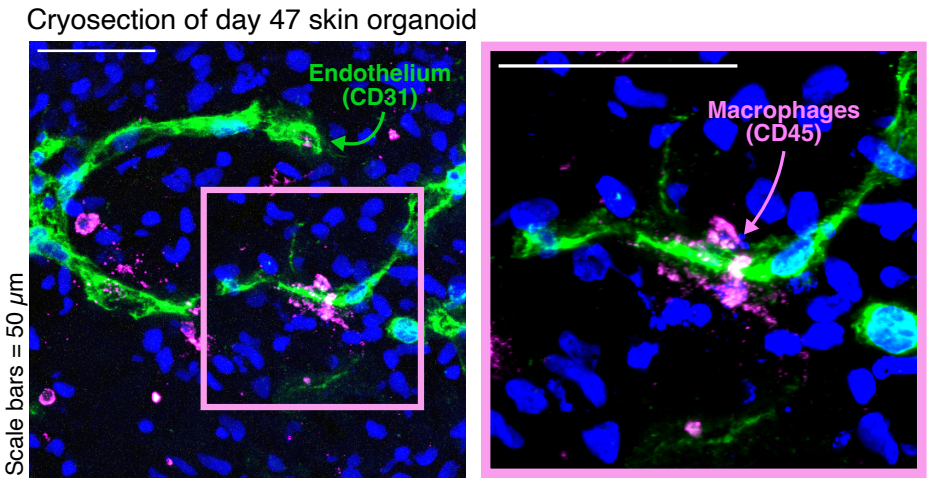

Figure 5.29. Immunofluorescence assay of macrophage and endothelial cell co-location in skin organoids.

Large-area (left) and magnified (right) images of immunostained skin organoid cryosections showing macrophages (CD45, magenta) in close proximity to endothelial cells (CD31, green) with DAPI (blue) nuclear staining. Representative images shown from n=2 independent samples. Scale bars, 50 μm.

To quantify differences in the vascular network and account for potential differences within and across skin organoids, the endothelial cell coverage was measured and normalised to the whole organoid area (section 2.6.5) to obtain the endothelial cell density in each skin organoid. Comparison of the average cell densities confirmed significantly decreased endothelial coverage in the skin organoids co-cultured with macrophages, corresponding to their more elaborate and pruned vascular networks (Figure 5.30). These observations demonstrated that macrophages indeed contributed to angiogenesis by closely associating with blood vessels and remodelling the vascular network and could be used to enhance vascularisation in the skin organoid model.

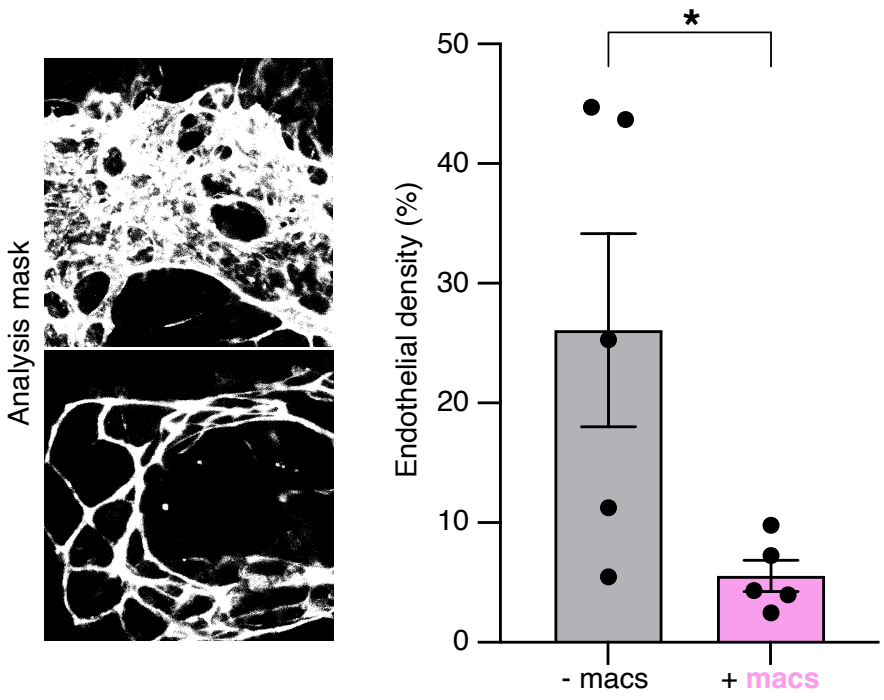

Figure 5.30. Assessing vascular network in skin organoids.

Endothelial cell coverage (quantified as percentage of endothelial density from vascular image segmentation masks) in skin organoids cultured without (grey) and with (pink) macrophages. Data from 10 independent samples (n=5 with macrophages, n=5 without macrophages) shown as mean percentage ± SD; *p = 0.0317 from unpaired t-test.

5.4 Section discussion

Blood vessels and nerves, including those that serve the skin, constitute some of the earliest structures that form during embryogenesis.[39,49] Yet, their morphogenesis in human prenatal skin remains incompletely characterised. In particular, whether macrophages, which have been implicated in developmental angiogenesis of non-integumentary organs in both animal models[470] and humans[100,338] and in cutaneous neurogenesis in mice,[479] play a role in the establishment of prenatal skin neurovasculature is not known. A previous study of human embryonic and foetal skin found no association between immune cells and blood or lymphatic vessels.[96] The predicted co-location of macrophages with endothelial and neural cells from the multi-omics atlas, together with the coincidental reduction of vascular endothelium in the immune deficient skin organoids, prompted a re-examination of these immune cells in neurovascular development of prenatal skin. In this section, I discuss the results of these investigations which exposed macrophages as key orchestrators of cutaneous angiogenesis and the translational implications to enhance organoid models and tissue engineering.

5.4.1 Support of prenatal cutaneous angiogenesis by macrophages

The validated co-location of macrophages with endothelial cells by multi-modal immunostaining, identification of their reciprocal cellular communication, and enrichment of pro-angiogenic gene programmes (section 5.3.2) confirmed the critical involvement of these innate immune cells in prenatal skin angiogenesis. These findings contradicted the previous reports that macrophages are randomly distributed in prenatal skin dermis and do not cluster around blood vessels.[96] However, a very recent prenatal immune cell atlas, published during the conduct of this research, also identified macrophages localising to the perivascular space across several foetal organs including skin, lung, heart, kidneys and female gonads.[458] These macrophages expressed pro-angiogenic gene modules and produced a supernatant in vitro which significantly induced tube formation by cultured human umbilical vein endothelial cells.[458] This corroborated the observations from the prenatal skin atlas and indicated that macrophages support angiogenesis in diverse tissues during gestation.

The prenatal skin atlas provided further insights and revealed that different subsets of macrophages potentially contributed to specific aspects of angiogenesis such as sprouting, endothelial cell chemotaxis, and blood vessel morphogenesis (section 5.3.2). This was uncovered by leveraging

the distinct macrophage cell states identified by scRNA-seq analysis for which angiogenesis gene modules were then computed (section 5.3.2). These results suggested that macrophage phenotype may be relevant to the intricate coordination of cutaneous angiogenesis by these immune cells. Similar observations have been made in tissue engineering studies that attempted to utilise macrophages to improve vascularisation and integration of biomaterial scaffolds.[527,528] The findings from the prenatal skin atlas could therefore be exploited for the strategic design of scaffolds that fully harness the different angiogenic capabilities of individual macrophage subsets. However, it should be acknowledged that there was a degree of overlap in the angiogenesis gene programmes across the macrophage subsets as well as in their cell-cell interactions with endothelial cells (section 5.3.2). This may reflect their plastic nature and warrants additional investigations and validation in future studies.

5.4.2 Vascularisation of tissue organoids

Addition of macrophages to the hair-bearing skin organoids improved formation of their vascular networks. Skin organoids co-cultured with macrophages displayed an elaborate and organised network of blood vessels that closely resembled the mature vascular pattern in prenatal skin (section 5.3.4). Conversely, a disorganised mesh-like aggregation of endothelial cells was observed in the absence of macrophages (section 5.3.4). This validated the macrophage support of angiogenesis identified in prenatal skin and demonstrated the utility of the skin organoid for functional assessments of the role of immune cells in skin development.

The vascularisation of organoid models to attain similar vascular complexity to in vivo tissues remains a major challenge.[529,530] Even dedicated blood vessel organoids derived from human ES and iPS cells cannot recapitulate the full heterogeneity of endothelial cells as discussed in section 5.3.3. However, improved organisation and maturation of blood vessels has been demonstrated in a neural organoid in the presence of macrophages where these immune cells were seen closely associating with endothelial cells.[531] Consistent with these findings, the skin organoid further demonstrates that addition of macrophages provides a potential avenue to enhance vascularisation of tissue organoids.[529,530] Interestingly, the iPS cell-derived macrophages in the current study persisted at least five weeks in skin organoid cultures, compared to 1-2 weeks in liquid cultures supplemented with macrophage colony-stimulating factor.[219] Increased macrophage viability was also previously observed when cultured with self-assembling skin equivalents,[532] underscoring the

requirement for tissue residency and environment in sustaining the longevity of macrophages in vitro.[157]

Notably, however, the refined vascular networks seen in the skin organoids were not transcriptionally compared to prenatal skin to verify whether they comprised the full spectrum of endothelial cell states identified in vivo. Additionally, whether the remodelled vessel-like structures formed tubes with patent lumens that course along their entire lengths should be investigated. Future studies generating scRNA-seq data of skin organoids cultured with and without macrophages together with additional visualisation techniques, such as three dimensional rendering, would be useful to determine to what extent the presence of macrophages support endothelial cell differentiation and tube morphogenesis in vitro.

5.4.3 Support of peripheral nerve development by yolk sac-derived macrophages

In addition to angiogenesis, macrophages also appeared to support development of the peripheral nerves in prenatal skin. In particular, yolk-sac derived TML macrophages were predicted to co-localise with neural cells and expressed gene programmes and signalling molecules supporting neuron survival, axon growth and guidance, synapse pruning, and regulation of myelination (section 5.3.1). Although these findings require further validation in human prenatal skin, similar functions have been reported in nerve-associated macrophages in mouse skin.[477–479] Intriguingly, these macrophages in adult mice are almost exclusively prenatally seeded and partially derived from yolk sac progenitors under physiological condition.[476,478] Following injury, other tissue resident macrophages can acquire the same phenotype as nerve-associated macrophages after populating the regenerating neurons and being shaped by the local nerve microenvironment.[476,478] TML macrophages in human prenatal skin, however, decline in later gestation and are not known, so far, to persist postnatally. Whether other subsets of macrophages associate with neural cells in late gestation prenatal skin and in adult skin and how their transcriptional and functional profiles overlap with or differ from TML macrophages require further exploration. This may provide insights into the neuro-immune crosstalk specific to de novo nerve formation during skin morphogenesis.

Chapter 6 . Conclusion and future directions

The key insights unravelled from the data generated and analysed as part of this thesis have been thoroughly reviewed at the end of each results chapter (sections 3.4, 4.4 and 5.4). The context of existing literature was considered, limitations were acknowledged and areas for further investigation were proposed. In this final chapter, I briefly recap these findings and discussions and then focus on assessing the overall strengths and weaknesses of the presented study and highlighting potential future research directions to address unresolved questions.

6.1 Overview

Skin, the largest organ in the human body, develops in utero from two juxtaposed primary germ layers (ectoderm and mesoderm) into an architecturally complex and strategically organised system which performs crucial roles postnatally, ranging from barrier functions, sensation to thermoregulation (sections 1.1 and 1.2). Its morphogenesis is underpinned by precise spatiotemporally distributed structural, cellular and molecular changes (sections 1.2 and 1.3.2). An in depth understanding of these developmental processes can yield invaluable information regarding the origins, natural history, and pathophysiology of cutaneous and trichological disorders.[42] Indeed, several inherited and congenital skin and hair diseases result from pathological alterations of normal integumentary development, for instance of the basal layer and BMZ in epidermolysis bullosa, of placodes in ectodermal dysplasias, and of epidermal differentiation in ichthyoses.[533–536] Additionally, co-optation of prenatal gene programmes has been demonstrated in several malignancies and in inflammatory dermatoses, where embryonic macrophage-venular capillary interactions were shown to re-emerge in psoriasis and eczema.[100,537–539] As such, comprehensive profiling of human prenatal skin presents an unparalleled resource for not only delineating its physiological development but also for identifying potential new therapeutic targets and creating a reference to guide strategies for skin and hair follicle regeneration.

The morphological transformations of structural and ultrastructural features that occur during human prenatal skin and hair follicle organogenesis have been documented in remarkable detail in earlier studies (section 1.2). An analogous systematic charting of the cellular and molecular dynamics during gestation remains wanting, hindered by the constrained availability of human foetal tissues and of techniques allowing unbiased profiling at scale (section 3.1). The wider

accessibility to commercial scRNA-seq and spatial platforms that permit whole transcriptome analysis on small tissue volumes (section 1.4) has provided an avenue to begin addressing these limitations. A variety of developmental tissues have been examined using these techniques within or outwith the HDCA initiative,[109] part of the Human Cell Atlas consortium where over 62 million cells have so far been profiled.[540] The few studies on human prenatal skin (section 1.4.4), however, have focused on its constituent immune cells, mainly examining their ontogeny or compositional shifts across trimesters.[98,101,148,149] Its non-immune components, including hair follicle appendage, or contributions of immune cells to broader skin development have not been adequately assessed.

This study aimed to address this knowledge gap, using integrated droplet-based scRNA-seq and spatial transcriptomics approaches combined with smFISH, immunofluorescence and in vitro culture assays, to generate a comprehensive multi-omics atlas of human prenatal skin and functionally assess the role of immune cells in skin morphogenesis. Comparative analyses were conducted with external datasets from adult healthy skin,[100] adult anagen hair follicles,[189] embryonic mouse hair follicles,[61] and reindeer skin[192] to investigate features specific to human prenatal skin and identify cross-species similarities or differences. In addition, a hair-bearing skin organoid system (section 1.5) was benchmarked against prenatal skin to determine its faithfulness in recapitulating in vivo skin and utility to study skin development and diseases. The results are summarised below.

6.2 Summary of findings and discussions

6.2.1 Prenatal skin multi-omics atlas reveals cellular crosstalk and immune cell co-location during de novo hair follicle formation

The multi-omics human prenatal skin atlas characterised 86 distinct granular immune and non-immune cell states grouped into 21 broad cell groups, mapped their spatial organisation in situ, and determined their recapitulation in a skin organoid model derived from hPSCs. This extensive resource, which can be interactively visualised and queried on a dedicated web portal (https://developmental.cellatlas.io/fetal-skin), revealed notable insights into human skin and hair follicle morphogenesis.

Inferred differentiation trajectories from epithelial (*POSTN*$^{+}$ basal) and mesenchymal progenitor cells (*HOXC5*$^{+}$ early fibroblasts) that give rise to terminal skin and hair follicle structures showed that the ontogenically debated CL,[376] formed along the same path as the ORS and not the IRS (section 3.4.3) while mesenchymal cells transitioned through an intermediate pre-Dc state before aggregating into the Dc as recently reported in mice[59] (section 3.3.4). These processes were orchestrated by mesenchymal-epithelial signalling, including *CXCL12-ACKR3* interactions which were newly shown to potentially mediate the migration of the pre-Dc cells towards the epidermis (section 3.3.4). Although several parallels were noted between human and mouse hair follicle development in the signalling pathways coordinating initiation and downgrowth, cross-species differences were also distinguished: the tempo of differentiation of hair follicle mesenchymal cells was faster in mice and and the expression of immune chemotactic genes were upregulated human prenatal skin (section 3.3.4). Indeed, immune cells appeared to be critically involved in de novo human hair follicle formation. Tregs accumulated peri-follicularly from 15 PCW and LTi and ILC3 cells were predicted to co-locate and interact with pre-Dc cells to promote their migration (section 3.3.4). These findings indicate the potential moonlighting functions of immune cells in hair follicle morphogenesis.

6.2.2 Early dermal fibroblasts and macrophages contribute to scarless healing potential of prenatal skin

The multi-omics human prenatal skin atlas uncovered tissue microenvironments where specific immune and non-immune cells were predicted to co-locate (section 3.3.5). Specifically, macrophages shared microenvironments with early prenatal skin fibroblasts and expressed gene programmes and ligands for cell-cell interactions which implicated them as crucial regulators of inflammation and promoters of fibroblast homeostasis and scarless repair (sections 4.3.3, 4.3.4, 4.3.5). In particular, TML macrophages emerged as key players in prenatal skin capacity for regeneration (section 4.3.3). The wider distribution of these yolk-sac derived microglia-like macrophages across tissues in early gestation, including testicular cords and heart, and their immunomodulatory and morphogenic functions are increasingly recognised.[102,338,458]

In addition to macrophages modulating the skin immune milieu, compositional and transcriptional shifts occurring in prenatal skin fibroblasts across gestation suggest that factors inherent to these cells also conduce to the regenerative properties of developing skin (discussed in section 4.4.1). In early gestation, progenitor fibroblasts (*HOXC5*$^{+}$ early fibroblasts) were abundant and genes promoting cell growth and immune suppression were upregulated (sections 4.3.1 and 4.3.2). Conversely, genes implicated in collagen deposition, ECM formation, immune activation and inflammatory priming were expressed by dermal fibroblasts in later gestation (sections 4.3.1 and 4.3.2). Accordingly, late gestation fibroblasts had a higher probability of matching to pro-inflammatory, non-regenerative fibroblasts from reindeer skin compared to early gestation fibroblasts (section 4.3.4). Although, these findings align with earlier studies which proposed foetal fibroblasts as the principal effectors of skin regeneration,[423,455] the overarching picture depicts critical bi-directional modulation between fibroblasts and macrophages that ultimately defines the phenotype of macrophages, the skin immune environment and scarless healing potential of prenatal skin (discussed in section 4.4.2).

6.2.3 Macrophages support neurogenesis and angiogenesis in prenatal skin

Macrophages also co-localised with neural and vascular endothelial cells in neurovascular microenvironments (sections 3.3.5, 5.3.1 and 5.3.2). Macrophages engaged in reciprocal cellular communication with the neurovasculature and expressed gene programmes related to proliferation, guidance and regulation of neurons and blood vessels, underscoring their critical involvement in prenatal skin neurogenesis and angiogenesis (sections 5.3.1, 5.3.2). This is in line with evidence from animal studies[470,477–479] and emerging findings from human prenatal tissues.[100,458]

Notably, comparison of the hair-bearing skin organoid model to prenatal skin highlighted a marked reduction in endothelial cells, both in terms of quantity and heterogeneity, in the immune deficient skin organoids despite faithful recapitulation of epidermal, dermal and neural components (sections 3.3.3 and 5.3.3). Formation of the latter structures was likely promoted by the timed supplementation of specific growth factors that direct skin and hair follicle development in the organoids (section 1.5.1). Vascular endothelial growth factor expression was increased in skin organoid cells but did not compensate for the absence of macrophage-related factors to drive endothelial cell expansion and differentiation (section 5.3.3). Addition of macrophages rescued vascularisation in the skin organoids: an elaborate and organised network of blood vessels formed when co-cultured with macrophages whereas a disorganised mesh-like aggregation of endothelial cells was observed in their absence (section 5.3.4). This validated the pro-angiogenic support by macrophages identified in prenatal skin and further demonstrated the utility of the skin organoid model for functional assessment of immune cells in skin development.

6.3 Strengths and weaknesses

6.3.1 Strengths of the current study

Breadth and depth of profiling

The scRNA-seq data generated in this project constitutes the largest dataset of human prenatal skin, totalling 433,961 cells after quality control and removal of low quality cells. The study from Suo et al.,[101] which included part of the data generated in this current work and explored primarily the cross-organ development of the human immune system (section 1.4.4.), contained 181,684 immune and non-immune cells from developing skin. Wang et al.[458] and Xu et al.[98] both analysed $CD45^+$ cells only, comprising 221,917 and 40,467 immune cells from prenatal skin respectively. Although a high cell count is not critical in scRNA-seq studies, at similar sequencing depths, it provides increased power to detect rarer cell states and to accurately identify DEGs for correct biological interpretation.[164,541] Consequently, the inclusion and thorough characterisation of both immune and non-immune cells enabled an unprecedented assessment of human hair follicle neogenesis at cellular and molecular resolution, including inference of differentiation trajectories and mesenchymal-epithelial cellular interactions (section 3.3.4).

Spatial contextualisation

This is the first study to specifically generate and examine spatial transcriptomic data (Visium platform) of human prenatal skin. While skin areas were included in a previous spatially-resolved cell atlas of whole embryonic hind limb, this study was largely focused on its musculoskeletal components.[141] The skin-related data from this publication was combined with data newly generated during the current work to provide a spatial transcriptomic dataset of human prenatal skin across three anatomical sites (limb, abdomen, face), the first of its kind. The integrated dataset was then applied to overcome one of the major drawbacks of isolated single-cell approaches, which is the loss of cellular spatial context upon tissue dissociation[113] (sections 1.4.1 and 1.4.2). This was achieved by spatial data decomposition to re-locate in situ the cell states identified in scRNA-seq data (section 3.3.5). This mapping enabled the discovery of tissue microenvironments where immune cells co-localise with non-immune cells and contribute to prenatal skin development (section 3.3.5, 4.3.3, 5.3.1 and 5.3.2), thereby expanding the non-canonical roles of immune cells and advancing our knowledge of skin morphogenesis.

Benchmarking of skin organoid model

Another strong point of this study is the novel analyses and applications of skin organoids. Although skin equivalents have been increasingly used in drug and cosmetic testing, disease modelling and as research tools (section 1.5), methodical benchmarking of skin organoids at molecular level against in vivo skin has not been undertaken. This study started to address this lacune by systematically comparing a hair-bearing skin organoid system to both prenatal and adult skin at cellular and transcriptome levels. A significant degree of convergence was demonstrated, underscoring the skin organoid as a functional model of developing skin. The analysis also identified important differences, such as paucity of endothelial cells in the organoids, and notably enabled translation of findings from prenatal skin to enhance vascularisation of skin organoids. This serves as a proof of concept that the multi-omics prenatal skin atlas can be wielded as a guide to fashion improved skin equivalents. By careful characterisation of the individual macrophage subsets, in terms of biological processes and ligand-receptor expression, it can potentially also accelerate tissue engineering of immunomodulatory biomaterials for wound healing and skin regeneration.[528]

6.3.2 Weaknesses of the current study

Sampling from late gestation stages

Although the single-cell prenatal skin atlas comprised samples from a wide range of developmental stages (7 to 17 PCW), later gestational ages were not represented. The implications for the detection of cell types that mature around or after 17 PCW (for example, sebaceous and apocrine cells) was discussed in section 3.4.1.

Late gestation samples are expectedly scarce (reduced termination rates in late pregnancy) and foetal tissues over 20 PCW are not available from HDBR in the UK.[109,156] Critically, this also limits enquiry into the factors conferring scarless healing potential as foetal skin loses its regenerative capacity around 24 weeks of gestation,[43,429,430] that is after the 17 PCW stage included in this study. Adult skin was used here to represent the scarring phenotype (section 4.3.2) but is potentially limited by confounding from exposure to ex utero conditions (for instance, microbiome). Direct comparison of samples before and after 24 weeks could reveal internally-controlled differences between the pro-regenerative and pro-fibrotic environments inherent to prenatal skin.

Spatial transcriptomic data was also generated only from first trimester samples. This was informed by observations from earlier studies of the uncoupling of MHCII gene expression by macrophages in early gestation (< 11 PCW).[101] Whether macrophages continue to co-localise with non-immune cells and function in skin morphogenesis in mid and late gestational stages was not assessed. The cell-cell interactions examined in section 5.3.2 and additional immunofluorescence assays (at 15 PCW) performed for the publication of this study[157] suggest they likely have a persistent role in skin development, at least in angiogenesis, but this remains to be fully investigated.

Non-myeloid immune cell contributions

The emphasis of this study has been on myeloid immune cells, particularly macrophages, in human prenatal skin development. This was predicated on the results of the unbiased NMF analysis which showed macrophage subsets co-locating with several non-immune cells, including vascular endothelial and neural cells, in tissue microenvironments (section 3.3.5) in conjunction with observations from earlier studies as mentioned above. However, other immune cell types, such as ILCs, mast cells and early B cells, were also predicted to co-localise with non-immune cutaneous components, such as early epidermis. Tregs were shown to accumulate around the developing hair follicles in prenatal skin and LTi and ILC3 cells were predicted to support pre-Dc migration (section 3.3.4). The contributions of non-macrophage immune cells to skin morphogenesis warrant further exploration.

Mechanistic investigations

A number of different approaches were employed to validate the findings that immune cells actively partake in prenatal skin development, including orthogonal computational analyses (for example, reindeer skin comparison and NicheNet), smFISH and immunofluorescence assays, and in vitro cell cultures (scratch wound and skin organoid experiments). However, it should be acknowledged that mechanistic studies to confirm how macrophages perform these roles and how critical they are to these functions - or whether redundant pathways exist - were beyond the scope of this study.

6.4 Future directions

Suggestions for future work were considered at the end of each results chapter. The points discussed below expands on some of these recommendations and proposes some new ideas in light of emerging technologies.

Hair follicle biology

The results from analysing de novo hair follicle formation in human prenatal skin revealed several interesting findings as described above (section 6.2.1). However, there are key questions in human hair follicle development that remain incompletely answered such as the orchestration of regionally variable hair follicle patterning, spatial coordination of matrix cells (IRS precursors) to produce the distinct layers of the IRS, and precise localisation of sebaceous gland along the hair follicle.[63] Innovative techniques that provide spatial transcriptome information at cellular resolution, such as Xenium[542] and Visium HD,[543] may provide the tools to untangle these developmental events. Placode and adjacent peri-placode epidermal cells (or earlier states identified in the prenatal skin atlas) could be distinguished and compared; spatially-defined transcriptional differences cross-sectionally in the hair matrix and longitudinally along the ORS (for sebaceous glands) could be assessed and contrasted with surrounding cells. Differences identified may hint to mechanisms at play that govern these biological events which could then be further validated using the hair-bearing skin organoid model. Information from the current prenatal skin atlas can indicate the appropriate gestational ages and anatomical sites to be sampled. With advances in computational methods, cross-modality data integration may provide augmented insights to progress our understanding of hair follicle biology.

Molecular roadmaps to scarless repair

Scarring competence is present in human prenatal skin fibroblasts (around 12 PCW) well before the transition from regenerative to reparative repair occurs (towards the end of the second trimester)[43,429,430] (sections 4.3.1). As argued in section 4.4.1, this implies that during the second trimester, skin fibroblasts balance between regenerative and fibrotic capabilities. This dual capacity appears to persist in adult mammalian tissues.[544] A study in mice demonstrated that cutaneous wounds reverted to healing scarlessly if specific mechanical signals (mediated by Yes-associated protein) were inhibited, indicating that postnatal skin fibroblasts retain a molecular capacity for regeneration.[461] Elucidating what precipitates the shift towards scarring in utero during normal skin

development may trace the molecular roadmap and switch(es) to unlocking latent regenerative potential in postanal fibroblasts.[544] This ideally requires skin samples from late gestational stages (> 24 PCW) as discussed in section 6.3.2. Existing human prenatal skin datasets, even combined, are insufficient to address this, being limited in terms of ages or cell types included. For instance, a recent study sampled prenatal skin up to 26 PCW but only isolated immune cells.[458] Future research directions should foster cross-centre collaborations, co-ordinated through the HDCA and its international data-sharing guidance,[109] to generate the necessary dataset that comprehensively profiles both immune and non-immune cells into the third trimester.

Future applications for skin organoids

The transcriptional regulatory networks involved in prenatal skin development and hair follicle differentiation, should be systematically assessed in future studies by using, for instance, regulon analysis. Identified regulons and transcription factors should also be compared to those activated in the skin organoids to better recognise divergent points between the in vivo and in vitro systems and further optimise the organoid model[411] (as discussed in section 3.4.2). Careful alignment of the skin organoid model to prenatal skin at transcription factor level, to complement the cellular and transcriptome mapping undertaken in this study, would further enhance its suitability for perturbation studies which could begin to address the lack of mechanistic investigations highlighted above (section 6.3.2).

Additionally, lineage tracing studies, to which in vivo human tissues are not amenable, may be feasible in the skin organoids as exemplified in other organoid models.[545–548] These studies leveraged advances in sequencing-based lineage tracing methods that enable mapping of clonal information onto single-cell and spatial transcriptomic data.[549] For instance, reporter barcodes combined with spatial transcriptomics were used to dynamically trace cell lineages in cerebral organoids, identifying that specific lineages became spatially restricted early during differentiation.[547] Similar experiments, or complementary approaches such as cell tracking,[550] could be undertaken using the skin organoids to map the organisational principles of developing hair follicles and deduce the unconfirmed origins of particular cell types such as CL or periderm cells.[545]

6.5 Conclusion

This study revealed novel insights into human skin and hair follicle development through comprehensive multi-omics profiling of prenatal skin. It characterised the early epithelial and mesenchymal cell states and interactions that form human hair follicles de novo and delineated the cellular differentiation trajectories followed. It uncovered that immune cells, notably macrophages, function outside of their conventional immune roles, exhibiting an intricate interplay with non-immune constituents to morph prenatal skin. Macrophages co-localised and interacted with fibroblasts, neural cells and endothelial cells to potentially promote prenatal skin scarless healing, neurogenesis and angiogenesis. Indeed, wound closure and vascular network formation were significantly improved following addition of autologous macrophages to cultures of fibroblasts and skin organoids respectively, supporting the role of immune cells in prenatal skin repair and morphogenesis.

In addition, this extensive cellular and transcriptomic atlas complements existing detailed morphological examinations of embryonic and foetal skin, offering an instrumental resource to advance understanding and treatment of cutaneous and trichological disorders. The molecular charting of prenatal skin physiological development establishes a backdrop to further study genesis, natural history, and potential therapeutic intervals of genetic skin and hair follicle diseases. The gene modules co-opted during oncofoetal reprogramming and inflammation can also be explored to develop new treatment paradigms. Finally, the systematic benchmarking of the hair-bearing skin organoid model alongside prenatal skin profiling provides a blueprint to guide future skin regeneration strategies and organoid tissue engineering.

References

1. McGrath JA, Uitto J. Structure and function of the skin [Internet]. Rook's Textbook of Dermatology. Wiley; 2024. p. 1–50. Available from: https://onlinelibrary.wiley.com/doi/10.1002/9781119709268.rook002

2. Kolarsick PAJ, Kolarsick MA, Goodwin C. Anatomy and physiology of the skin. J Dermatol Nurses Assoc. 2011 Jul;3(4):203–13.

3. Shen Z, Sun L, Liu Z, Li M, Cao Y, Han L, et al. Rete ridges: Morphogenesis, function, regulation, and reconstruction. Acta Biomater. 2023 Jan 1;155:19–34.

4. Deegan AJ, Wang RK. Microvascular imaging of the skin. Phys Med Biol. 2019 Mar 21;64(7):07TR01.

5. Boulais N, Misery L. The epidermis: a sensory tissue. Eur J Dermatol. 2008 Mar;18(2):119–27.

6. Kowalczyk AP, Green KJ. Structure, function, and regulation of desmosomes. Prog Mol Biol Transl Sci. 2013;116:95–118.

7. Holbrook KA. Biologic structure and function: Perspectives on morphologic approaches to the study of the granular layer keratinocyte. J Invest Dermatol. 1989 Apr;92(4):S84–104.

8. Matsui T, Amagai M. Dissecting the formation, structure and barrier function of the stratum corneum. Int Immunol. 2015 Jun;27(6):269–80.

9. Cichorek M, Wachulska M, Stasiewicz A, Tymińska A. Skin melanocytes: biology and development. Postepy Dermatol Alergol. 2013 Feb;30(1):30–41.

10. Boulais N, Misery L. Merkel cells. J Am Acad Dermatol. 2007 Jul;57(1):147–65.

11. Abraham J, Mathew S. Merkel Cells: A Collective Review of Current Concepts. Int J Appl Basic Med Res. 2019 Jan-Mar;9(1):9–13.

12. Roig-Rosello E, Rousselle P. The human epidermal basement membrane: A shaped and cell instructive platform that aging slowly alters. Biomolecules. 2020 Nov 27;10(12):1607.

13. McMillan JR, Akiyama M, Shimizu H. Epidermal basement membrane zone components: ultrastructural distribution and molecular interactions. J Dermatol Sci. 2003 May;31(3):169–77.

14. Uitto J, Olsen DR, Fazio MJ. Extracellular matrix of the skin: 50 years of progress. J Invest Dermatol. 1989 Apr;92(4):S61–77.

15. Pfisterer K, Shaw LE, Symmank D, Weninger W. The Extracellular Matrix in Skin Inflammation and Infection. Front Cell Dev Biol. 2021 Jul 6;9:682414.

16. Stunova A, Vistejnova L. Dermal fibroblasts-A heterogeneous population with regulatory function in wound healing. Cytokine Growth Factor Rev. 2018 Feb;39:137–50.

17. Wong R, Geyer S, Weninger W, Guimberteau JC, Wong JK. The dynamic anatomy and patterning of skin. Exp Dermatol. 2016 Feb;25(2):92–8.

18. Liu M, Lu F, Feng J. Aging and homeostasis of the hypodermis in the age-related deterioration of skin function. Cell Death Dis. 2024 Jun 24;15(6):443.

19. Avram AS, Avram MM, James WD. Subcutaneous fat in normal and diseased states: 2. Anatomy and physiology of white and brown adipose tissue. J Am Acad Dermatol. 2005 Oct;53(4):671–83.

20. Chen SX, Zhang LJ, Gallo RL. Dermal White Adipose Tissue: A Newly Recognized Layer of Skin Innate Defense. J Invest Dermatol. 2019 May;139(5):1002–9.

21. Kosaka K, Kubota Y, Adachi N, Akita S, Sasahara Y, Kira T, et al. Human adipocytes from the subcutaneous superficial layer have greater adipogenic potential and lower PPAR-γ DNA methylation levels than deep layer adipocytes. Am J Physiol Cell Physiol. 2016 Aug 1;311(2):C322–9.

22. Li Y, Long J, Zhang Z, Yin W. Insights into the unique roles of dermal white adipose tissue (dWAT) in wound healing. Front Physiol. 2024 Feb 23;15:1346612.

23. Paus R, Cotsarelis G. The biology of hair follicles. N Engl J Med. 1999 Aug 12;341(7):491–7.

24. Hardy MH. The secret life of the hair follicle. Trends Genet. 1992 Feb;8(2):55–61.

25. Joshi RS. The Inner Root Sheath and the Men Associated with it Eponymically. Int J Trichology. 2011 Jan;3(1):57–62.

26. Morioka K. Outer root sheath and companion layer. In: Hair Follicle: Differentiation Under the Electron Microscope - An Atlas. Tokyo: Springer-Verlag; 2006. p. 89–106.

27. Rothnagel JA, Roop DR. Hair follicle companion layer: reacquainting an old friend. J Invest Dermatol. 1995 May;104(5 Suppl):42S – 43S.

28. Schneider MR, Schmidt-Ullrich R, Paus R. The hair follicle as a dynamic miniorgan. Curr Biol. 2009 Feb 10;19(3):R132–42.

29. Shamloul G, Khachemoune A. An updated review of the sebaceous gland and its role in health and diseases Part 1: Embryology, evolution, structure, and function of sebaceous glands. Dermatol Ther. 2021 Jan;34(1):e14695.

30. Wilke K, Martin A, Terstegen L, Biel SS. A short history of sweat gland biology. Int J Cosmet Sci. 2007 Jun;29(3):169–79.

31. Lefèvre-Utile A, Braun C, Haftek M, Aubin F. Five functional aspects of the epidermal barrier. Int J Mol Sci. 2021 Oct 28;22(21):11676.

32. Elias PM. Skin barrier function. Curr Allergy Asthma Rep. 2008 Jul;8(4):299–305.

33. Brenner M, Hearing VJ. The protective role of melanin against UV damage in human skin. Photochem Photobiol. 2008 May;84(3):539–49.

34. Charkoudian N. Skin blood flow in adult human thermoregulation: how it works, when it does not, and why. Mayo Clin Proc. 2003 May;78(5):603–12.

35. Baker LB. Physiology of sweat gland function: The roles of sweating and sweat composition in human health. Temperature (Austin). 2019 Jul 17;6(3):211–59.

36. Mostafa WZ, Hegazy RA. Vitamin D and the skin: Focus on a complex relationship: A review. J Adv Res. 2015 Nov;6(6):793–804.

37. Tyser RCV, Srinivas S. Recent advances in understanding cell types during human gastrulation. Semin Cell Dev Biol. 2022 Nov;131:35–43.

38. Ghimire S, Mantziou V, Moris N, Martinez Arias A. Human gastrulation: The embryo and its models. Dev Biol. 2021 Jun;474:100–8.

39. Sadler TW. Langman's Medical Embryology. 15th ed. Baltimore, MD: Wolters Kluwer Health; 2023. 472 p.

40. Alshaiji J. The embryogenesis of the skin. In: Pediatric Dermatologic Surgery. Chichester, UK: John Wiley & Sons, Ltd; 2019. p. 1–11.

41. Bronner ME, LeDouarin NM. Development and evolution of the neural crest: an overview. Dev Biol. 2012 Jun 1;366(1):2–9.

42. Lee LW, Holbrook KA. Embryogenesis of the skin [Internet]. Harper's Textbook of Pediatric Dermatology. Wiley; 2019. p. 1–35. Available from: https://doi.org/10.1002/9781119142812.ch1

43. Hu MS, Borrelli MR, Hong WX, Malhotra S, Cheung ATM, Ransom RC, et al. Embryonic skin development and repair. Organogenesis. 2018 Jan 2;14(1):46–63.

44. Holbrook KA. Human epidermal embryogenesis. Int J Dermatol. 1979 Jun;18(5):329–56.

45. Eckhart L, Holthaus KB, Sachslehner AP. Cell differentiation in the embryonic periderm and in scaffolding epithelia of skin appendages. Dev Biol. 2024 Nov;515:60–6.

46. Holbrook KA, Underwood RA, Vogel AM, Gown AM, Kimball H. The appearance, density and distribution of melanocytes in human embryonic and fetal skin revealed by the anti-melanoma monoclonal antibody, HMB-45. Anat Embryol (Berl). 1989;180(5):443–55.

47. Kim DK, Holbrook KA. The appearance, density, and distribution of Merkel cells in human embryonic and fetal skin: their relation to sweat gland and hair follicle development. J Invest Dermatol. 1995 Mar;104(3):411–6.

48. Smith LT, Holbrook KA. Embryogenesis of the dermis in human skin. Pediatr Dermatol. 1986 Sep;3(4):271–80.

49. Johnson CL, Holbrook KA. Development of human embryonic and fetal dermal vasculature. J Invest Dermatol. 1989 Aug;93(2 Suppl):10S – 17S.

50. Terenghi G, Sundaresan M, Moscoso G, Polak JM. Neuropeptides and a neuronal marker in cutaneous innervation during human foetal development. J Comp Neurol. 1993 Feb 22;328(4):595–603.

51. Botting RA, Haniffa M. The developing immune network in human prenatal skin. Immunology. 2020 Jun;160(2):149–56.

52. Millar SE. Molecular mechanisms regulating hair follicle development. J Invest Dermatol. 2002 Feb;118(2):216–25.

53. Hardman MJ, Moore L, Ferguson MW, Byrne C. Barrier formation in the human fetus is patterned. J Invest Dermatol. 1999 Dec;113(6):1106–13.

54. Holbrook KA, Minami SI. Hair follicle embryogenesis in the human. Characterization of events in vivo and in vitro. Ann N Y Acad Sci. 1991 Dec 26;642:167–96.

55. Pinkus H. Embryology of hair. In: The Biology of Hair Growth. Elsevier; 1958. p. 1–32.

56. Holbrook KA, Smith LT, Kaplan ED, Minami SA, Hebert GP, Underwood RA. Expression of morphogens during human follicle development in vivo and a model for studying follicle morphogenesis in vitro. J Invest Dermatol. 1993 Jul;101(1 Suppl):39S – 49S.

57. Singh G, Archana G. Unraveling the mystery of vernix caseosa. Indian J Dermatol. 2008;53(2):54–60.

58. Saxena N, Mok KW, Rendl M. An updated classification of hair follicle morphogenesis. Exp Dermatol. 2019 Apr;28(4):332–44.

59. Mok KW, Saxena N, Heitman N, Grisanti L, Srivastava D, Muraro MJ, et al. Dermal Condensate Niche Fate Specification Occurs Prior to Formation and Is Placode Progenitor Dependent. Dev Cell. 2019 Jan;48(1):32–48.e5.

60. Joost S, Annusver K, Jacob T, Sun X, Dalessandri T, Sivan U, et al. The Molecular Anatomy of Mouse Skin during Hair Growth and Rest. Cell Stem Cell. 2020 Mar;26(3):441–57.e7.

61. Jacob T, Annusver K, Czarnewski P, Dalessandri T, Kalk C, Levra Levron C, et al. Molecular and spatial landmarks of early mouse skin development. Dev Cell. 2023 Oct 23;58(20):2140–62.e5.

62. Paus R, Müller-Röver S, Van Der Veen C, Maurer M, Eichmüller S, Ling G, et al. A comprehensive guide for the recognition and classification of distinct stages of hair follicle morphogenesis. J Invest Dermatol. 1999 Oct;113(4):523–32.

63. Bernard BA. The hair follicle enigma. Exp Dermatol. 2017 Jun;26(6):472–7.

64. Wong VW, Sorkin M, Glotzbach JP, Longaker MT, Gurtner GC. Surgical approaches to create murine models of human wound healing. J Biomed Biotechnol. 2011;2011(1):969618.

65. Medetgul-Ernar K, Davis MM. Standing on the shoulders of mice. Immunity. 2022 Aug 9;55(8):1343–53.

66. Nguyen AV, Soulika AM. The dynamics of the skin's immune system. Int J Mol Sci. 2019 Apr 12;20(8):1811.

67. Zhang C, Merana GR, Harris-Tryon T, Scharschmidt TC. Skin immunity: dissecting the complex biology of our body's outer barrier. Mucosal Immunol. 2022 Apr;15(4):551–61.

68. Clayton K, Vallejo AF, Davies J, Sirvent S, Polak ME. Langerhans cells-programmed by the epidermis. Front Immunol. 2017 Nov 29;8:1676.

69. Seneschal J, Clark RA, Gehad A, Baecher-Allan CM, Kupper TS. Human epidermal Langerhans cells maintain immune homeostasis in skin by activating skin resident regulatory T cells. Immunity. 2012 May 25;36(5):873–84.

70. Kashem SW, Haniffa M, Kaplan DH. Antigen-presenting cells in the skin. Annu Rev Immunol. 2017 Apr 26;35:469–99.

71. Haniffa M, Gunawan M, Jardine L. Human skin dendritic cells in health and disease. J Dermatol Sci. 2015 Feb;77(2):85–92.

72. Segura E. Human dendritic cell subsets: An updated view of their ontogeny and functional specialization. Eur J Immunol. 2022 Nov;52(11):1759–67.

73. Trompette A, Ubags ND. Skin barrier immunology from early life to adulthood. Mucosal Immunol. 2023 Apr;16(2):194–207.

74. Park MD, Silvin A, Ginhoux F, Merad M. Macrophages in health and disease. Cell. 2022 Nov 10;185(23):4259–79.

75. Lee SH, Sacks DL. Resilience of dermis resident macrophages to inflammatory challenges. Exp Mol Med. 2024 Oct;56(10):2105–12.

76. Yanez DA, Lacher RK, Vidyarthi A, Colegio OR. The role of macrophages in skin homeostasis. Pflugers Arch. 2017 Apr;469(3-4):455–63.

77. Mass E, Nimmerjahn F, Kierdorf K, Schlitzer A. Tissue-specific macrophages: how they develop and choreograph tissue biology. Nat Rev Immunol. 2023 Sep;23(9):563–79.

78. Mills CD, Kincaid K, Alt JM, Heilman MJ, Hill AM. M-1/M-2 macrophages and the Th1/Th2 paradigm. J Immunol. 2000 Jun 15;164(12):6166–73.

79. Liu C, Liu Z, Li Z, Wu Y. Molecular regulation of mast cell development and maturation. Mol Biol Rep. 2010 Apr;37(4):1993–2001.

80. Ramirez GA, Yacoub MR, Ripa M, Mannina D, Cariddi A, Saporiti N, et al. Eosinophils from physiology to disease: A comprehensive review. Biomed Res Int. 2018 Jan 28;2018:9095275.

81. Cruz MS, Diamond A, Russell A, Jameson JM. Human αβ and γδ T cells in skin immunity and disease. Front Immunol. 2018 Jun 6;9:1304.

82. Clark RA, Chong B, Mirchandani N, Brinster NK, Yamanaka KI, Dowgiert RK, et al. The vast majority of CLA+ T cells are resident in normal skin. J Immunol. 2006 Apr 1;176(7):4431–9.

83. Spits H. Development of alphabeta T cells in the human thymus. Nat Rev Immunol. 2002 Oct;2(10):760–72.

84. Watanabe R, Gehad A, Yang C, Scott LL, Teague JE, Schlapbach C, et al. Human skin is protected by four functionally and phenotypically discrete populations of resident and recirculating memory T cells. Sci Transl Med. 2015 Mar 18;7(279):279ra39.

85. Ali N, Zirak B, Rodriguez RS, Pauli ML, Truong HA, Lai K, et al. Regulatory T Cells in Skin Facilitate Epithelial Stem Cell Differentiation. Cell. 2017 Jun;169(6):1119–29.e11.

86. Hu Y, Hu Q, Li Y, Lu L, Xiang Z, Yin Z, et al. γδ T cells: origin and fate, subsets, diseases and immunotherapy. Signal Transduct Target Ther. 2023 Nov 22;8(1):434.

87. Nel I, Bertrand L, Toubal A, Lehuen A. MAIT cells, guardians of skin and mucosa? Mucosal Immunol. 2021 Jul;14(4):803–14.

88. Kobayashi T, Ricardo-Gonzalez RR, Moro K. Skin-resident innate lymphoid cells - cutaneous innate guardians and regulators. Trends Immunol. 2020 Feb;41(2):100–12.

89. Brüggen MC, Bauer WM, Reininger B, Clim E, Captarencu C, Steiner GE, et al. In situ mapping of innate lymphoid cells in human skin: Evidence for remarkable differences between normal and inflamed skin. J Invest Dermatol. 2016 Dec;136(12):2396–405.

90. Lerman I, Mitchell DC, Richardson CT. Human cutaneous B cells: what do we really know? Ann Transl Med. 2021 Mar;9(5):440.

91. Karaaslan S, Tomayko MM. A niche for plasma cells: The skin. J Invest Dermatol. 2019 Dec;139(12):2411–4.

92. Morgan D, Tergaonkar V. Unraveling B cell trajectories at single cell resolution. Trends Immunol. 2022 Mar;43(3):210–29.

93. Minges Wols HA. Plasma Cells. In: Encyclopedia of Life Sciences [Internet]. Chichester: John Wiley & Sons, Ltd; 2006. Available from: http://dx.doi.org/10.1038/npg.els.0004030

94. Wilson RP, McGettigan SE, Dang VD, Kumar A, Cancro MP, Nikbakht N, et al. IgM plasma cells reside in healthy skin and accumulate with chronic inflammation. J Invest Dermatol. 2019 Dec;139(12):2477–87.

95. Nihal M, Mikkola D, Wood GS. Detection of clonally restricted immunoglobulin heavy chain gene rearrangements in normal and lesional skin: analysis of the B cell component of the skin-associated lymphoid tissue and implications for the molecular diagnosis of cutaneous B cell lymphomas. J Mol Diagn. 2000 Feb;2(1):5–10.

96. Schuster C, Mildner M, Botta A, Nemec L, Rogojanu R, Beer L, et al. Development of blood and lymphatic endothelial cells in embryonic and fetal human skin. Am J Pathol. 2015 Sep;185(9):2563–74.

97. Walraven M, Talhout W, Beelen RHJ, van Egmond M, Ulrich MMW. Healthy human second-trimester fetal skin is deficient in leukocytes and associated homing chemokines. Wound Repair Regen. 2016 May;24(3):533–41.

98. Xu Y, Zhang J, Hu Y, Li X, Sun L, Peng Y, et al. Single-cell transcriptome analysis reveals the dynamics of human immune cells during early fetal skin development. Cell Rep. 2021 Aug;36(6):109524.

99. Popescu DM, Botting RA, Stephenson E, Green K, Webb S, Jardine L, et al. Decoding human fetal liver haematopoiesis. Nature. 2019 Oct;574(7778):365–71.

100. Reynolds G, Vegh P, Fletcher J, Poyner EFM, Stephenson E, Goh I, et al. Developmental cell programs are co-opted in inflammatory skin disease. Science. 2021 Jan;371(6527).

101. Suo C, Dann E, Goh I, Jardine L, Kleshchevnikov V, Park JE, et al. Mapping the developing human immune system across organs. Science. 2022 Jun;376(6597):eabo0510.

102. Goh I, Botting RA, Rose A, Webb S, Engelbert J, Gitton Y, et al. Yolk sac cell atlas reveals multiorgan functions during human early development. Science. 2023 Aug 18;381(6659):eadd7564.

103. Yamane T. Mouse yolk sac hematopoiesis. Front Cell Dev Biol. 2018 Jul 20;6:80.

104. Ivanovs A, Rybtsov S, Welch L, Anderson RA, Turner ML, Medvinsky A. Highly potent human hematopoietic stem cells first emerge in the intraembryonic aorta-gonad-mesonephros region. J Exp Med. 2011 Nov 21;208(12):2417–27.

105. Calvanese V, Capellera-Garcia S, Ma F, Fares I, Liebscher S, Ng ES, et al. Mapping human haematopoietic stem cells from haemogenic endothelium to birth. Nature. 2022 Apr;604(7906):534–40.

106. Farley AM, Morris LX, Vroegindeweij E, Depreter MLG, Vaidya H, Stenhouse FH, et al. Dynamics of thymus organogenesis and colonization in early human development.

Development. 2013 May;140(9):2015–26.

107. Masuda T, Amann L, Monaco G, Sankowski R, Staszewski O, Krueger M, et al. Specification of CNS macrophage subsets occurs postnatally in defined niches. Nature. 2022 Apr;604(7907):740–8.

108. Wu Y, Hirschi KK. Tissue-resident macrophage development and function. Front Cell Dev Biol. 2020;8:617879.

109. Haniffa M, Taylor D, Linnarsson S, Aronow BJ, Bader GD, Barker RA, et al. A roadmap for the Human Developmental Cell Atlas. Nature. 2021 Sep;597(7875):196–205.

110. Tang F, Barbacioru C, Wang Y, Nordman E, Lee C, Xu N, et al. mRNA-Seq whole-transcriptome analysis of a single cell. Nat Methods. 2009 May;6(5):377–82.

111. Kolodziejczyk AA, Kim JK, Svensson V, Marioni JC, Teichmann SA. The technology and biology of single-cell RNA sequencing. Mol Cell. 2015 May 21;58(4):610–20.

112. Kashima Y, Sakamoto Y, Kaneko K, Seki M, Suzuki Y, Suzuki A. Single-cell sequencing techniques from individual to multiomics analyses. Exp Mol Med. 2020 Sep;52(9):1419–27.

113. Williams CG, Lee HJ, Asatsuma T, Vento-Tormo R, Haque A. An introduction to spatial transcriptomics for biomedical research. Genome Med. 2022 Jun 27;14(1):68.

114. Valihrach L, Zucha D, Abaffy P, Kubista M. A practical guide to spatial transcriptomics. Mol Aspects Med. 2024 Jun;97(101276):101276.

115. Dubois A, Gopee N, Olabi B, Haniffa M. Defining the skin cellular community using single-cell genomics to advance precision medicine. J Invest Dermatol. 2021 Feb;141(2):255–64.

116. Vento-Tormo R, Efremova M, Botting RA, Turco MY, Vento-Tormo M, Meyer KB, et al. Single-cell reconstruction of the early maternal-fetal interface in humans. Nature. 2018 Nov;563(7731):347–53.

117. Durante MA, Rodriguez DA, Kurtenbach S, Kuznetsov JN, Sanchez MI, Decatur CL, et al. Single-cell analysis reveals new evolutionary complexity in uveal melanoma. Nat Commun. 2020 Jan 24;11(1):496.

118. Puram SV, Tirosh I, Parikh AS, Patel AP, Yizhak K, Gillespie S, et al. Single-cell transcriptomic analysis of primary and metastatic tumor ecosystems in head and neck cancer. Cell. 2017 Dec 14;171(7):1611–24.e24.

119. Tirosh I, Izar B, Prakadan SM, Wadsworth MH 2nd, Treacy D, Trombetta JJ, et al. Dissecting the multicellular ecosystem of metastatic melanoma by single-cell RNA-seq. Science. 2016 Apr 8;352(6282):189–96.

120. Stubbington MJT, Rozenblatt-Rosen O, Regev A, Teichmann SA. Single-cell transcriptomics to explore the immune system in health and disease. Science. 2017 Oct 6;358(6359):58–63.

121. Der E, Suryawanshi H, Morozov P, Kustagi M, Goilav B, Ranabothu S, et al. Tubular cell and keratinocyte single-cell transcriptomics applied to lupus nephritis reveal type I IFN and fibrosis relevant pathways. Nat Immunol. 2019 Jul;20(7):915–27.

122. Stephenson E, Reynolds G, Botting RA, Calero-Nieto FJ, Morgan MD, Tuong ZK, et al. Single-cell multi-omics analysis of the immune response in COVID-19. Nat Med. 2021 May;27(5):904–16.

123. Regev A, Teichmann SA, Lander ES, Amit I, Benoist C, Birney E, et al. The Human Cell Atlas. Elife [Internet]. 2017 Dec 5;6. Available from: http://dx.doi.org/10.7554/eLife.27041

124. See P, Lum J, Chen J, Ginhoux F. A single-cell sequencing guide for immunologists. Front Immunol. 2018 Oct 23;9:2425.

125. Ramsköld D, Luo S, Wang YC, Li R, Deng Q, Faridani OR, et al. Full-length mRNA-Seq from single-cell levels of RNA and individual circulating tumor cells. Nat Biotechnol. 2012 Aug;30(8):777–82.

126. Picelli S, Björklund ÅK, Faridani OR, Sagasser S, Winberg G, Sandberg R. Smart-seq2 for sensitive full-length transcriptome profiling in single cells. Nat Methods. 2013 Nov;10(11):1096–8.

127. Jaitin DA, Kenigsberg E, Keren-Shaul H, Elefant N, Paul F, Zaretsky I, et al. Massively parallel single-cell RNA-seq for marker-free decomposition of tissues into cell types. Science. 2014 Feb 14;343(6172):776–9.

128. Zheng GXY, Terry JM, Belgrader P, Ryvkin P, Bent ZW, Wilson R, et al. Massively parallel digital transcriptional profiling of single cells. Nat Commun. 2017 Jan 16;8(1):14049.

129. Chromium Single Cell [Internet]. 10x Genomics. [cited 2024 Dec 4]. Available from: https://www.10xgenomics.com/platforms/chromium

130. Cheng M, Jiang Y, Xu J, Mentis AFA, Wang S, Zheng H, et al. Spatially resolved transcriptomics: a comprehensive review of their technological advances, applications, and challenges. J Genet Genomics. 2023 Sep;50(9):625–40.

131. Lubeck E, Coskun AF, Zhiyentayev T, Ahmad M, Cai L. Single-cell in situ RNA profiling by sequential hybridization. Nat Methods. 2014 Apr;11(4):360–1.

132. Moffitt JR, Hao J, Wang G, Chen KH, Babcock HP, Zhuang X. High-throughput single-cell gene-expression profiling with multiplexed error-robust fluorescence in situ hybridization. Proc Natl Acad Sci U S A. 2016 Sep 27;113(39):11046–51.

133. Lee JH, Daugharthy ER, Scheiman J, Kalhor R, Yang JL, Ferrante TC, et al. Highly multiplexed subcellular RNA sequencing in situ. Science. 2014 Mar 21;343(6177):1360–3.

134. Kishi JY, Liu N, West ER, Sheng K, Jordanides JJ, Serrata M, et al. Light-Seq: light-directed in situ barcoding of biomolecules in fixed cells and tissues for spatially indexed sequencing. Nat Methods. 2022 Nov;19(11):1393–402.

135. Ståhl PL, Salmén F, Vickovic S, Lundmark A, Navarro JF, Magnusson J, et al. Visualization and analysis of gene expression in tissue sections by spatial transcriptomics. Science. 2016 Jul 1;353(6294):78–82.

136. Rodriques SG, Stickels RR, Goeva A, Martin CA, Murray E, Vanderburg CR, et al. Slide-seq: A scalable technology for measuring genome-wide expression at high spatial resolution. Science. 2019 Mar 29;363(6434):1463–7.

137. Stickels RR, Murray E, Kumar P, Li J, Marshall JL, Di Bella DJ, et al. Highly sensitive spatial transcriptomics at near-cellular resolution with Slide-seqV2. Nat Biotechnol. 2021 Mar;39(3):313–9.

138. Chen A, Liao S, Cheng M, Ma K, Wu L, Lai Y, et al. Spatiotemporal transcriptomic atlas of

mouse organogenesis using DNA nanoball-patterned arrays. Cell. 2022 May 12;185(10):1777–92.e21.

139. Visium Spatial Platform [Internet]. 10x Genomics. [cited 2024 Dec 4]. Available from: https://www.10xgenomics.com/platforms/visium

140. Garcia-Alonso L, Handfield LF, Roberts K, Nikolakopoulou K, Fernando RC, Gardner L, et al. Mapping the temporal and spatial dynamics of the human endometrium in vivo and in vitro. Nat Genet. 2021 Dec;53(12):1698–711.

141. Zhang B, He P, Lawrence JEG, Wang S, Tuck E, Williams BA, et al. A human embryonic limb cell atlas resolved in space and time. Nature [Internet]. 2023 Dec 6; Available from: http://dx.doi.org/10.1038/s41586-023-06806-x

142. Castillo RL, Sidhu I, Dolgalev I, Chu T, Prystupa A, Subudhi I, et al. Spatial transcriptomics stratifies psoriatic disease severity by emergent cellular ecosystems. Sci Immunol. 2023 Jun 8;8(84):eabq7991.

143. Cross AR, de Andrea CE, Villalba-Esparza M, Landecho MF, Cerundolo L, Weeratunga P, et al. Spatial transcriptomic characterization of COVID-19 pneumonitis identifies immune circuits related to tissue injury. JCI Insight [Internet]. 2023 Jan 24;8(2). Available from: http://dx.doi.org/10.1172/jci.insight.157837

144. Ji AL, Rubin AJ, Thrane K, Jiang S, Reynolds DL, Meyers RM, et al. Multimodal analysis of composition and spatial architecture in human squamous cell carcinoma. Cell. 2020 Jul 23;182(2):497–514.e22.

145. Visium Spatial Gene Expression Reagent Kits User Guide, Document Number CG000239 Rev H [Internet]. 10x Genomics. [cited 2024 Nov 8]. Available from: https://cdn.10xgenomics.com/image/upload/v1723742999/support-documents/CG000239_Visium_Spatial_Gene_Expression_User_Guide_RevH.pdf

146. Marx V. Method of the Year: spatially resolved transcriptomics. Nat Methods. 2021 Jan;18(1):9–14.

147. Kleshchevnikov V, Shmatko A, Dann E, Aivazidis A, King HW, Li T, et al. Cell2location

maps fine-grained cell types in spatial transcriptomics. Nat Biotechnol. 2022 May;40(5):661–71.

148. Reitermaier R, Krausgruber T, Fortelny N, Ayub T, Vieyra-Garcia PA, Kienzl P, et al. αβγδ T cells play a vital role in fetal human skin development and immunity. J Exp Med. 2021 Apr;218(4).

149. Bian Z, Gong Y, Huang T, Lee CZW, Bian L, Bai Z, et al. Deciphering human macrophage development at single-cell resolution. Nature. 2020 Jun;582(7813):571–6.

150. Choudhury S, Das A. Advances in generation of three-dimensional skin equivalents: pre-clinical studies to clinical therapies. Cytotherapy. 2021 Jan;23(1):1–9.

151. Riabinin A, Pankratova M, Rogovaya O, Vorotelyak E, Terskikh V, Vasiliev A. Ideal living skin equivalents, from old technologies and models to advanced ones: The prospects for an integrated approach. Biomed Res Int. 2024 Aug 16;2024(1):9947692.

152. Hirsch T, Rothoeft T, Teig N, Bauer JW, Pellegrini G, De Rosa L, et al. Regeneration of the entire human epidermis using transgenic stem cells. Nature. 2017 Nov 16;551(7680):327–32.

153. Lee J, Böscke R, Tang PC, Hartman BH, Heller S, Koehler KR. Hair follicle development in mouse pluripotent stem cell-derived skin organoids. Cell Rep. 2018 Jan 2;22(1):242–54.

154. Lee J, Rabbani CC, Gao H, Steinhart MR, Woodruff BM, Pflum ZE, et al. Hair-bearing human skin generated entirely from pluripotent stem cells. Nature. 2020 Jun;582(7812):399–404.

155. Lee J, van der Valk WH, Serdy SA, Deakin C, Kim J, Le AP, et al. Generation and characterization of hair-bearing skin organoids from human pluripotent stem cells. Nat Protoc. 2022 May;17(5):1266–305.

156. Human Developmental Biology Resource [Internet]. HDBR. [cited 2024 Nov 28]. Available from: https://www.hdbr.org/

157. Gopee NH, Winheim E, Olabi B, Admane C, Foster AR, Huang N, et al. A prenatal skin atlas reveals immune regulation of human skin morphogenesis. Nature [Internet]. 2024 Oct 16; Available from: http://dx.doi.org/10.1038/s41586-024-08002-x

158. Chromium Single Cell 5' Reagent Kits User Guide (v2 Chemistry Dual Index), Document Number CG000331 Rev F [Internet]. 10x Genomics. [cited 2024 Nov 8]. Available from: https://cdn.10xgenomics.com/image/upload/v1722286172/support-documents/CG000331_Chromium_Next_GEM_Single_Cell_5_v2_UserGuide_RevF.pdf

159. Chromium Single Cell 3' Reagent Kits User Guide (v3.1 Chemistry Dual Index), Document Number CG000315 Rev F [Internet]. 10x Genomics. [cited 2024 Nov 8]. Available from: https://cdn.10xgenomics.com/image/upload/v1722285481/support-documents/CG000315_ChromiumNextGEMSingleCell3__GeneExpression_v3.1_DualIndex__RevF.pdf

160. Methanol Fixation, H&E Staining & Imaging for Visium Spatial Protocols, Document Number CG000160 Rev D [Internet]. 10x Genomics. [cited 2024 Nov 29]. Available from: https://cdn.10xgenomics.com/image/upload/v1695417730/support-documents/CG000160_DemonstratedProtocol_MethanolFixationandHEStaining_RevD.pdf

161. Visium Spatial Tissue Optimization Reagents Kits User Guide, Document Number CG000238 Rev F [Internet]. 10x Genomics. [cited 2024 Nov 8]. Available from: https://cdn.10xgenomics.com/image/upload/v1723743003/support-documents/CG000238_VisiumSpatialTissueOptimizationUserGuide_RevF.pdf

162. Lun ATL, Riesenfeld S, Andrews T, Dao TP, Gomes T, participants in the 1st Human Cell Atlas Jamboree, et al. EmptyDrops: distinguishing cells from empty droplets in droplet-based single-cell RNA sequencing data. Genome Biol. 2019 Mar 22;20(1):63.

163. Wolf FA, Angerer P, Theis FJ. SCANPY: large-scale single-cell gene expression data analysis. Genome Biol. 2018 Feb 6;19(1):15.

164. Haque A, Engel J, Teichmann SA, Lönnberg T. A practical guide to single-cell RNA-sequencing for biomedical research and clinical applications. Genome Med. 2017 Aug 18;9(1):75.

165. Luecken MD, Theis FJ. Current best practices in single-cell RNA-seq analysis: a tutorial. Mol Syst Biol. 2019 Jun 19;15(6):e8746.

166. Xi NM, Li JJ. Benchmarking computational doublet-detection methods for single-cell RNA

sequencing data. Cell Syst. 2021 Feb 17;12(2):176–94.e6.

167. Wolock SL, Lopez R, Klein AM. Scrublet: Computational Identification of Cell Doublets in Single-Cell Transcriptomic Data. Cell Syst. 2019 Apr;8(4):281–91.e9.

168. Lun ATL, McCarthy DJ, Marioni JC. A step-by-step workflow for low-level analysis of single-cell RNA-seq data with Bioconductor. F1000Res. 2016 Aug 31;5:2122.

169. Bais AS, Kostka D. scds: computational annotation of doublets in single-cell RNA sequencing data. Bioinformatics. 2020 Feb 15;36(4):1150–8.

170. McGinnis CS, Patterson DM, Winkler J, Conrad DN, Hein MY, Srivastava V, et al. MULTI-seq: sample multiplexing for single-cell RNA sequencing using lipid-tagged indices. Nat Methods. 2019 Jul;16(7):619–26.

171. Ilicic T, Kim JK, Kolodziejczyk AA, Bagger FO, McCarthy DJ, Marioni JC, et al. Classification of low quality cells from single-cell RNA-seq data. Genome Biol. 2016 Feb 17;17(1):29.

172. Griffiths JA, Scialdone A, Marioni JC. Using single-cell genomics to understand developmental processes and cell fate decisions. Mol Syst Biol. 2018 Apr 16;14(4):e8046.

173. Heaton H, Talman AM, Knights A, Imaz M, Gaffney DJ, Durbin R, et al. Souporcell: robust clustering of single-cell RNA-seq data by genotype without reference genotypes. Nat Methods. 2020 Jun;17(6):615–20.

174. Nayak R, Hasija Y. A hitchhiker's guide to single-cell transcriptomics and data analysis pipelines. Genomics. 2021 Mar;113(2):606–19.

175. Vallejos CA, Risso D, Scialdone A, Dudoit S, Marioni JC. Normalizing single-cell RNA sequencing data: challenges and opportunities. Nat Methods. 2017 Jun;14(6):565–71.

176. Lopez R, Regier J, Cole MB, Jordan MI, Yosef N. Deep generative modeling for single-cell transcriptomics. Nat Methods. 2018 Dec;15(12):1053–8.

177. Gayoso A, Lopez R, Xing G, Boyeau P, Valiollah Pour Amiri V, Hong J, et al. A Python library for probabilistic analysis of single-cell omics data. Nat Biotechnol. 2022

Feb;40(2):163–6.

178. Luecken MD, Büttner M, Chaichoompu K, Danese A, Interlandi M, Mueller MF, et al. Benchmarking atlas-level data integration in single-cell genomics. Nat Methods. 2022 Jan;19(1):41–50.

179. Luke Z, Malte L. Single-cell best practices: Data integration - Batch-aware feature selection [Internet]. [cited 2024 Nov 29]. Available from: https://www.sc-best-practices.org/cellular_structure/integration.html#batch-aware-feature-selection

180. Xiang R, Wang W, Yang L, Wang S, Xu C, Chen X. A comparison for dimensionality reduction methods of single-cell RNA-seq data. Front Genet. 2021 Mar 23;12:646936.

181. Pearson K. LIII. On lines and planes of closest fit to systems of points in space. Lond Edinb Dublin Philos Mag J Sci. 1901 Nov;2(11):559–72.

182. Traag VA, Waltman L, van Eck NJ. From Louvain to Leiden: guaranteeing well-connected communities. Sci Rep. 2019 Mar 26;9(1):5233.

183. McInnes L, Healy J, Melville J. UMAP: Uniform Manifold Approximation and Projection for Dimension Reduction [Internet]. arXiv [stat.ML]. 2018. Available from: https://doi.org/10.48550/arXiv.1802.03426

184. Single Cell analysis Tool Kit [Internet]. Github; [cited 2024 Nov 30]. Available from: https://github.com/Teichlab/sctk?tab=readme-ov-file

185. Dann E, Henderson NC, Teichmann SA, Morgan MD, Marioni JC. Differential abundance testing on single-cell data using k-nearest neighbor graphs. Nat Biotechnol. 2022 Feb;40(2):245–53.

186. Korsunsky I, Millard N, Fan J, Slowikowski K, Zhang F, Wei K, et al. Fast, sensitive and accurate integration of single-cell data with Harmony. Nat Methods. 2019 Dec;16(12):1289–96.

187. Tran HTN, Ang KS, Chevrier M, Zhang X, Lee NYS, Goh M, et al. A benchmark of batch-effect correction methods for single-cell RNA sequencing data. Genome Biol. 2020 Jan 16;21(1):12.

188. Jardine L, Webb S, Goh I, Quiroga Londoño M, Reynolds G, Mather M, et al. Blood and immune development in human fetal bone marrow and Down syndrome. Nature. 2021 Oct;598(7880):327–31.

189. Takahashi R, Grzenda A, Allison TF, Rawnsley J, Balin SJ, Sabri S, et al. Defining Transcriptional Signatures of Human Hair Follicle Cell States. J Invest Dermatol. 2020 Apr;140(4):764–73.e4.

190. Nikolova MT, He Z, Wimmer RA, Seimiya M, Nikoloff JM, Penninger JM, et al. Fate and state transitions during human blood vessel organoid development. 2022.

191. Domínguez Conde C, Xu C, Jarvis LB, Rainbow DB, Wells SB, Gomes T, et al. Cross-tissue immune cell analysis reveals tissue-specific features in humans. Science. 2022 May 13;376(6594):eabl5197.

192. Sinha S, Sparks HD, Labit E, Robbins HN, Gowing K, Jaffer A, et al. Fibroblast inflammatory priming determines regenerative versus fibrotic skin repair in reindeer. Cell. 2022 Dec 8;185(25):4717–36.e25.

193. Lange M, Bergen V, Klein M, Setty M, Reuter B, Bakhti M, et al. CellRank for directed single-cell fate mapping. Nat Methods. 2022 Feb;19(2):159–70.

194. Weiler P, Lange M, Klein M, Pe'er D, Theis F. CellRank 2: unified fate mapping in multiview single-cell data. Nat Methods. 2024 Jul;21(7):1196–205.

195. Bergen V, Lange M, Peidli S, Wolf FA, Theis FJ. Generalizing RNA velocity to transient cell states through dynamical modeling. Nat Biotechnol. 2020 Dec;38(12):1408–14.

196. Kaminow B, Yunusov D, Dobin A. STARsolo: accurate, fast and versatile mapping/quantification of single-cell and single-nucleus RNA-seq data [Internet]. bioRxiv. bioRxiv; 2021. Available from: http://dx.doi.org/10.1101/2021.05.05.442755

197. Setty M, Kiseliovas V, Levine J, Gayoso A, Mazutis L, Pe'er D. Characterization of cell fate probabilities in single-cell data with Palantir. Nat Biotechnol. 2019 Apr;37(4):451–60.

198. Efremova M, Vento-Tormo M, Teichmann SA, Vento-Tormo R. CellPhoneDB: inferring cell-cell communication from combined expression of multi-subunit ligand-receptor complexes.

Nat Protoc. 2020 Apr;15(4):1484–506.

199. Gu Z, Gu L, Eils R, Schlesner M, Brors B. circlize Implements and enhances circular visualization in R. Bioinformatics. 2014 Oct;30(19):2811–2.

200. Chen EY, Tan CM, Kou Y, Duan Q, Wang Z, Meirelles GV, et al. Enrichr: interactive and collaborative HTML5 gene list enrichment analysis tool. BMC Bioinformatics. 2013 Apr;14:128.

201. Kuleshov MV, Jones MR, Rouillard AD, Fernandez NF, Duan Q, Wang Z, et al. Enrichr: a comprehensive gene set enrichment analysis web server 2016 update. Nucleic Acids Res. 2016 Jul 8;44(W1):W90–7.

202. Xie Z, Bailey A, Kuleshov MV, Clarke DJB, Evangelista JE, Jenkins SL, et al. Gene set knowledge discovery with Enrichr. Curr Protoc. 2021 Mar;1(3):e90.

203. Fang Z, Liu X, Peltz G. GSEApy: a comprehensive package for performing gene set enrichment analysis in Python. Bioinformatics [Internet]. 2023 Jan 1;39(1). Available from: http://dx.doi.org/10.1093/bioinformatics/btac757

204.Chen EY. Enrichr [Internet]. [cited 2024 Nov 15]. Available from: https://maayanlab.cloud/Enrichr/#libraries

205. Li Q, Zhu Z, Wang L, Lin Y, Fang H, Lei J, et al. Single-cell transcriptome profiling reveals vascular endothelial cell heterogeneity in human skin. Theranostics. 2021 Apr;11(13):6461–76.

206. Schupp JC, Adams TS, Cosme C Jr, Raredon MSB, Yuan Y, Omote N, et al. Integrated Single-Cell Atlas of Endothelial Cells of the Human Lung. Circulation. 2021 Jul;144(4):286–302.

207. He Y, Tacconi C, Dieterich LC, Kim J, Restivo G, Gousopoulos E, et al. Novel Blood Vascular Endothelial Subtype-Specific Markers in Human Skin Unearthed by Single-Cell Transcriptomic Profiling. Cells. 2022 Mar;11(7).

208. Chen W, Xia P, Wang H, Tu J, Liang X, Zhang X, et al. The endothelial tip-stalk cell selection and shuffling during angiogenesis. J Cell Commun Signal. 2019 Sep;13(3):291–301.

209. Human Protein Atlas: proteinatlas.org [Internet]. protein_class:Predicted secreted proteins. [cited 2023 Jun 19]. Available from: https://www.proteinatlas.org/search/protein_class%3APredicted+secreted+proteins

210. Van de Sande B, Flerin C, Davie K, De Waegeneer M, Hulselmans G, Aibar S, et al. A scalable SCENIC workflow for single-cell gene regulatory network analysis. Nat Protoc. 2020 Jul;15(7):2247–76.

211. Szklarczyk D, Gable AL, Nastou KC, Lyon D, Kirsch R, Pyysalo S, et al. The STRING database in 2021: customizable protein-protein networks, and functional characterization of user-uploaded gene/measurement sets. Nucleic Acids Res. 2021 Jan 8;49(D1):D605–12.

212. Szklarczyk D, Kirsch R, Koutrouli M, Nastou K, Mehryary F, Hachilif R, et al. The STRING database in 2023: protein-protein association networks and functional enrichment analyses for any sequenced genome of interest. Nucleic Acids Res. 2023 Jan 6;51(D1):D638–46.

213. Browaeys R, Saelens W, Saeys Y. NicheNet: modeling intercellular communication by linking ligands to target genes. Nat Methods. 2020 Feb;17(2):159–62.

214. Li B, Zhang W, Guo C, Xu H, Li L, Fang M, et al. Benchmarking spatial and single-cell transcriptomics integration methods for transcript distribution prediction and cell type deconvolution. Nat Methods. 2022 Jun;19(6):662–70.

215. Gaujoux R, Seoighe C. A flexible R package for nonnegative matrix factorization. BMC Bioinformatics. 2010 Jul;11:367.

216. Brunet JP, Tamayo P, Golub TR, Mesirov JP. Metagenes and molecular pattern discovery using matrix factorization. Proc Natl Acad Sci U S A. 2004 Mar;101(12):4164–9.

217. Streeter I, Harrison PW, Faulconbridge A, The HipSci Consortium, Flicek P, Parkinson H, et al. The human-induced pluripotent stem cell initiative-data resources for cellular genetics. Nucleic Acids Res. 2017 Jan 4;45(D1):D691–7.

218.Hipsci.org [Internet]. [cited 2024 Nov 10]. Available from: https://www.hipsci.org/#/lines/HPSI0114i-kolf_2

219. Alsinet C, Primo MN, Lorenzi V, Bello E, Kelava I, Jones CP, et al. Robust temporal map of

human in vitro myelopoiesis using single-cell genomics. Nat Commun. 2022 May 24;13(1):2885.

220. Hörl D, Rojas Rusak F, Preusser F, Tillberg P, Randel N, Chhetri RK, et al. BigStitcher: reconstructing high-resolution image datasets of cleared and expanded samples. Nat Methods. 2019 Sep;16(9):870–4.

221. Rueden CT, Schindelin J, Hiner MC, DeZonia BE, Walter AE, Arena ET, et al. ImageJ2: ImageJ for the next generation of scientific image data. BMC Bioinformatics. 2017 Nov 29;18(1):529.

222. Suarez-Arnedo A, Torres Figueroa F, Clavijo C, Arbeláez P, Cruz JC, Muñoz-Camargo C. An image J plugin for the high throughput image analysis of in vitro scratch wound healing assays. PLoS One. 2020 Jul 28;15(7):e0232565.

223. Bankhead P, Loughrey MB, Fernández JA, Dombrowski Y, McArt DG, Dunne PD, et al. QuPath: Open source software for digital pathology image analysis. Sci Rep. 2017 Dec 4;7(1):16878.

224. de Groot SC, Ulrich MMW, Gho CG, Huisman MA. Back to the Future: From Appendage Development Toward Future Human Hair Follicle Neogenesis. Front Cell Dev Biol. 2021 Apr;9:661787.

225. Mestas J, Hughes CCW. Of mice and not men: differences between mouse and human immunology. J Immunol. 2004 Mar 1;172(5):2731–8.

226. Semple BD, Blomgren K, Gimlin K, Ferriero DM, Noble-Haeusslein LJ. Brain development in rodents and humans: Identifying benchmarks of maturation and vulnerability to injury across species. Prog Neurobiol. 2013 Jul;106-107:1–16.

227. Zhou Z, Pan Y, Zhou S, Wang S, Zhang D, Cao Y, et al. Single-cell analysis reveals specific neuronal transition during mouse corticogenesis. Front Cell Dev Biol. 2023 Nov 6;11:1209320.

228. Ihrie RA, Marques MR, Nguyen BT, Horner JS, Papazoglu C, Bronson RT, et al. Perp is a p63-regulated gene essential for epithelial integrity. Cell. 2005 Mar 25;120(6):843–56.

229. Watt B, van Niel G, Raposo G, Marks MS. PMEL: a pigment cell-specific model for functional amyloid formation. Pigment Cell Melanoma Res. 2013 May;26(3):300–15.

230. De Mazière AM, Muehlethaler K, van Donselaar E, Salvi S, Davoust J, Cerottini JC, et al. The melanocytic protein Melan-A/MART-1 has a subcellular localization distinct from typical melanosomal proteins. Traffic. 2002 Sep;3(9):678–93.

231. Lin HH, Bell E, Uwanogho D, Perfect LW, Noristani H, Bates TJD, et al. Neuronatin promotes neural lineage in ESCs via Ca(2+) signaling. Stem Cells. 2010 Nov;28(11):1950–60.

232. Day INM, Thompson RJ. UCHL1 (PGP 9.5): Neuronal biomarker and ubiquitin system protein. Prog Neurobiol. 2010 Mar;90(3):327–62.

233. Wolbert J, Li X, Heming M, Mausberg AK, Akkermann D, Frydrychowicz C, et al. Redefining the heterogeneity of peripheral nerve cells in health and autoimmunity. Proc Natl Acad Sci U S A. 2020 Apr 28;117(17):9466–76.

234. Iozzo RV. The family of the small leucine-rich proteoglycans: key regulators of matrix assembly and cellular growth. Crit Rev Biochem Mol Biol. 1997;32(2):141–74.

235. Aprile M, Ambrosio MR, D'Esposito V, Beguinot F, Formisano P, Costa V, et al. PPARG in human adipogenesis: Differential contribution of canonical transcripts and dominant negative isoforms. PPAR Res. 2014 Mar 23;2014:537865.

236. Merkel M, Eckel RH, Goldberg IJ. Lipoprotein lipase: genetics, lipid uptake, and regulation. J Lipid Res. 2002 Dec;43(12):1997–2006.

237. Roberds SL, Anderson RD, Ibraghimov-Beskrovnaya O, Campbell KP. Primary structure and muscle-specific expression of the 50-kDa dystrophin-associated glycoprotein (adhalin). J Biol Chem. 1993 Nov 15;268(32):23739–42.

238. Yu S, Zheng L, Trinh DK, Asa SL, Ezzat S. Distinct transcriptional control and action of fibroblast growth factor receptor 4 in differentiating skeletal muscle cells. Lab Invest. 2004 Dec;84(12):1571–80.

239. Siekmann AF. Biology of vascular mural cells. Development [Internet]. 2023 Aug 15;150(16). Available from: http://dx.doi.org/10.1242/dev.200271

240. Hsieh TB, Jin JP. Evolution and function of calponin and transgelin. Front Cell Dev Biol. 2023 Jun 8;11:1206147.

241. Yuan SM. A-smooth muscle actin and ACTA2 gene expressions in vasculopathies. Braz J Cardiovasc Surg. 2015 Nov;30(6):644–9.

242. Lertkiatmongkol P, Liao D, Mei H, Hu Y, Newman PJ. Endothelial functions of platelet/endothelial cell adhesion molecule-1 (CD31). Curr Opin Hematol. 2016 May;23(3):253–9.

243. Harris ES, Nelson WJ. VE-cadherin: at the front, center, and sides of endothelial cell organization and function. Curr Opin Cell Biol. 2010 Oct;22(5):651–8.

244. Li J, Li E, Czepielewski RS, Chi J, Guo X, Han YH, et al. Neurotensin is an anti-thermogenic peptide produced by lymphatic endothelial cells. Cell Metab. 2021 Jul 6;33(7):1449–65.e6.

245. Vaahtomeri K, Brown M, Hauschild R, De Vries I, Leithner AF, Mehling M, et al. Locally triggered release of the chemokine CCL21 promotes dendritic cell transmigration across lymphatic endothelia. Cell Rep. 2017 May 2;19(5):902–9.

246. Barresi V, Di Bella V, Lo Nigro L, Privitera AP, Bonaccorso P, Scuderi C, et al. Temporary serine protease inhibition and the role of SPINK2 in human bone marrow. iScience. 2023 Jun 16;26(6):106949.

247. Shah SN, Kerr C, Cope L, Zambidis E, Liu C, Hillion J, et al. HMGA1 reprograms somatic cells into pluripotent stem cells by inducing stem cell transcriptional networks. PLoS One. 2012 Nov 15;7(11):e48533.

248. Alkon N, Bauer WM, Krausgruber T, Goh I, Griss J, Nguyen V, et al. Single-cell analysis reveals innate lymphoid cell lineage infidelity in atopic dermatitis. J Allergy Clin Immunol. 2022 Feb;149(2):624–39.

249. Hashemi E, McCarthy C, Rao S, Malarkannan S. Transcriptomic diversity of innate lymphoid cells in human lymph nodes compared to BM and spleen. Commun Biol. 2024 Jun 25;7(1):769.

250. Menon AP, Moreno B, Meraviglia-Crivelli D, Nonatelli F, Villanueva H, Barainka M, et al.

Modulating T cell responses by targeting CD3. Cancers (Basel) [Internet]. 2023 Feb 13;15(4). Available from: http://dx.doi.org/10.3390/cancers15041189

251. Tkachenko A, Kupcova K, Havranek O. B-cell receptor signaling and beyond: The role of igα (CD79a)/Igβ (CD79b) in normal and malignant B cells. Int J Mol Sci [Internet]. 2023 Dec 19;25(1). Available from: http://dx.doi.org/10.3390/ijms25010010

252. Schröder B. The multifaceted roles of the invariant chain CD74--More than just a chaperone. Biochim Biophys Acta. 2016 Jun;1863(6 Pt A):1269–81.

253. Horowitz A, Yu H, Pandey S, Mishra B, Sahoo D. C1QA is an invariant biomarker for tissue macrophages [Internet]. bioRxivorg. 2024. Available from: http://dx.doi.org/10.1101/2024.01.26.577475

254. Rőszer T. Understanding the mysterious M2 macrophage through activation markers and effector mechanisms. Mediators Inflamm. 2015 May 18;2015(1):816460.

255. Chistiakov DA, Killingsworth MC, Myasoedova VA, Orekhov AN, Bobryshev YV. CD68/macrosialin: not just a histochemical marker. Lab Invest. 2017 Jan;97(1):4–13.

256. Xue D, Tabib T, Morse C, Yang Y, Domsic RT, Khanna D, et al. Expansion of Fcγ receptor IIIa-positive macrophages, ficolin 1-positive monocyte-derived dendritic cells, and plasmacytoid dendritic cells associated with severe skin disease in systemic sclerosis. Arthritis Rheumatol. 2022 Feb;74(2):329–41.

257. Wong ETL, Jenne DE, Zimmer M, Porter SD, Gilks CB. Changes in chromatin organization at the neutrophil elastase locus associated with myeloid cell differentiation. Blood. 1999 Dec 1;94(11):3730–6.

258. Rizo-Téllez SA, Sekheri M, Filep JG. Myeloperoxidase: Regulation of neutrophil function and target for therapy. Antioxidants (Basel). 2022 Nov 21;11(11):2302.

259. Atiakshin D, Kostin A, Trotsenko I, Samoilova V, Buchwalow I, Tiemann M. Carboxypeptidase A3-A key component of the protease phenotype of mast cells. Cells. 2022 Feb 6;11(3):570.

260. Jiang J, Faiz A, Berg M, Carpaij OA, Vermeulen CJ, Brouwer S, et al. Gene signatures from

scRNA-seq accurately quantify mast cells in biopsies in asthma. Clin Exp Allergy. 2020 Dec;50(12):1428–31.

261. Liu Y, Zuo X, Chen P, Hu X, Sheng Z, Liu A, et al. Deciphering transcriptome alterations in bone marrow hematopoiesis at single-cell resolution in immune thrombocytopenia. Signal Transduct Target Ther. 2022 Oct 7;7(1):347.

262. Zhang W, Yan C, Liu X, Yang P, Wang J, Chen Y, et al. Global characterization of megakaryocytes in bone marrow, peripheral blood, and cord blood by single-cell RNA sequencing. Cancer Gene Ther. 2022 Nov;29(11):1636–47.

263. Nandakumar SK, Ulirsch JC, Sankaran VG. Advances in understanding erythropoiesis: evolving perspectives. Br J Haematol. 2016 Apr;173(2):206–18.

264. Hammond NL, Dixon J, Dixon MJ. Periderm: Life-cycle and function during orofacial and epidermal development. Semin Cell Dev Biol. 2019 Jul;91:75–83.

265. Moll R, Moll I, Wiest W. Changes in the pattern of cytokeratin polypeptides in epidermis and hair follicles during skin development in human fetuses. Differentiation. 1982;23(2):170–8.

266. Kopan R, Fuchs E. A new look into an old problem: keratins as tools to investigate determination, morphogenesis, and differentiation in skin. Genes Dev. 1989 Jan;3(1):1–15.

267. Bragulla HH, Homberger DG. Structure and functions of keratin proteins in simple, stratified, keratinized and cornified epithelia. J Anat. 2009 Apr;214(4):516–59.

268. Moll R, Divo M, Langbein L. The human keratins: biology and pathology. Histochem Cell Biol. 2008 Jun;129(6):705–33.

269. Kalabusheva EP, Shtompel AS, Rippa AL, Ulianov SV, Razin SV, Vorotelyak EA. A Kaleidoscope of Keratin Gene Expression and the Mosaic of Its Regulatory Mechanisms. Int J Mol Sci [Internet]. 2023 Mar 15;24(6). Available from: http://dx.doi.org/10.3390/ijms24065603

270. Qian Z, Okuhara D, Abe MK, Rosner MR. Molecular cloning and characterization of a mitogen-activated protein kinase-associated intracellular chloride channel. J Biol Chem. 1999 Jan 15;274(3):1621–7.

271. Money TT, King RG, Wong MH, Stevenson JL, Kalionis B, Erwich JJHM, et al. Expression and cellular localisation of chloride intracellular channel 3 in human placenta and fetal membranes. Placenta. 2007 May-Jun;28(5-6):429–36.

272. Hardardottir H, Parmley TH 2nd, Quirk JG Jr, Sanders MM, Miller FC, O'Brien TJ. Distribution of CA 125 in embryonic tissues and adult derivatives of the fetal periderm. Am J Obstet Gynecol. 1990 Dec;163(6 Pt 1):1925–31.

273. Van Agtmael T, Bruckner-Tuderman L. Basement membranes and human disease. Cell Tissue Res. 2010 Jan;339(1):167–88.

274. Walker JT, McLeod K, Kim S, Conway SJ, Hamilton DW. Periostin as a multifunctional modulator of the wound healing response. Cell Tissue Res. 2016 Sep;365(3):453–65.

275. Wang S, Drummond ML, Guerrero-Juarez CF, Tarapore E, MacLean AL, Stabell AR, et al. Single cell transcriptomics of human epidermis identifies basal stem cell transition states. Nat Commun. 2020 Aug 25;11(1):4239.

276. McGowan KM, Coulombe PA. Keratin 17 expression in the hard epithelial context of the hair and nail, and its relevance for the pachyonychia congenita phenotype. J Invest Dermatol. 2000 Jun;114(6):1101–7.

277. Ma L, Liu J, Wu T, Plikus M, Jiang TX, Bi Q, et al. "Cyclic alopecia" in Msx2 mutants: defects in hair cycling and hair shaft differentiation. Development. 2003 Jan;130(2):379–89.

278. Langbein L, Rogers MA, Praetzel-Wunder S, Böckler D, Schirmacher P, Schweizer J. Novel type I hair keratins K39 and K40 are the last to be expressed in differentiation of the hair: completion of the human hair keratin catalog. J Invest Dermatol. 2007 Jun;127(6):1532–5.

279. Langbein L, Schweizer J. Keratins of the human hair follicle. Int Rev Cytol. 2005;243:1–78.

280. Nakano K, Kanai-Azuma M, Kanai Y, Moriyama K, Yazaki K, Hayashi Y, et al. Cofilin phosphorylation and actin polymerization by NRK/NESK, a member of the germinal center kinase family. Exp Cell Res. 2003 Jul 15;287(2):219–27.

281. Huang Y, Guzy R, Ma SF, Bonham CA, Jou J, Schulte JJ, et al. Central lung gene expression associates with myofibroblast features in idiopathic pulmonary fibrosis. BMJ Open Respir

Res [Internet]. 2023 Feb;10(1). Available from: http://dx.doi.org/10.1136/bmjresp-2022-001391

282. Garrett SM, Hsu E, Thomas JM, Pilewski JM, Feghali-Bostwick C. Insulin-like growth factor (IGF)-II- mediated fibrosis in pathogenic lung conditions. PLoS One. 2019 Nov 25;14(11):e0225422.

283. Emont MP, Jacobs C, Essene AL, Pant D, Tenen D, Colleluori G, et al. A single-cell atlas of human and mouse white adipose tissue. Nature. 2022 Mar;603(7903):926–33.

284. Cawthorn WP, Scheller EL, MacDougald OA. Adipose tissue stem cells meet preadipocyte commitment: going back to the future. J Lipid Res. 2012 Feb;53(2):227–46.

285. Rivera-Gonzalez G, Shook B, Horsley V. Adipocytes in skin health and disease. Cold Spring Harb Perspect Med. 2014 Mar 1;4(3):a015271–a015271.

286. Whytock KL, Sun Y, Divoux A, Yu G, Smith SR, Walsh MJ, et al. Single cell full-length transcriptome of human subcutaneous adipose tissue reveals unique and heterogeneous cell populations. iScience. 2022 Aug 19;25(8):104772.

287. Huang Y, Hu D, Huang C, Nichols CG. Genetic discovery of ATP-sensitive K+ channels in cardiovascular diseases. Circ Arrhythm Electrophysiol. 2019 May;12(5):e007322.

288. Bondjers C, He L, Takemoto M, Norlin J, Asker N, Hellström M, et al. Microarray analysis of blood microvessels from PDGF-B and PDGF-Rbeta mutant mice identifies novel markers for brain pericytes. FASEB J. 2006 Aug;20(10):1703–5.

289. Kumar A, D'Souza SS, Moskvin OV, Toh H, Wang B, Zhang J, et al. Specification and diversification of pericytes and smooth muscle cells from mesenchymoangioblasts. Cell Rep. 2017 May 30;19(9):1902–16.

290. Muhl L, Mocci G, Pietilä R, Liu J, He L, Genové G, et al. A single-cell transcriptomic inventory of murine smooth muscle cells. Dev Cell. 2022 Oct 24;57(20):2426–43.e6.

291. Sincennes MC, Brun CE, Lin AYT, Rosembert T, Datzkiw D, Saber J, et al. Acetylation of PAX7 controls muscle stem cell self-renewal and differentiation potential in mice. Nat Commun. 2021 May 31;12(1):3253.

292. Zammit PS. Function of the myogenic regulatory factors Myf5, MyoD, Myogenin and MRF4 in skeletal muscle, satellite cells and regenerative myogenesis. Semin Cell Dev Biol. 2017 Dec;72:19–32.

293. Schmidt M, Schüler SC, Hüttner SS, von Eyss B, von Maltzahn J. Adult stem cells at work: regenerating skeletal muscle. Cell Mol Life Sci. 2019 Jul;76(13):2559–70.

294. Laing NG, Dye DE, Wallgren-Pettersson C, Richard G, Monnier N, Lillis S, et al. Mutations and polymorphisms of the skeletal muscle Î±-actin gene (*ACTA1*). Hum Mutat. 2009 Sep;30(9):1267–77.

295. Wang L, Geist J, Grogan A, Hu LYR, Kontrogianni-Konstantopoulos A. Thick filament protein network, functions, and disease association. Compr Physiol. 2018 Mar 13;8(2):631–709.

296. Bushby KM. Making sense of the limb-girdle muscular dystrophies. Brain. 1999 Aug;122 (Pt 8):1403–20.

297. Perrone-Bizzozero N, Bird CW. Role of HuD in nervous system function and pathology. Front Biosci (Schol Ed). 2013 Jan 1;5(2):554–63.

298. Cederquist GY, Luchniak A, Tischfield MA, Peeva M, Song Y, Menezes MP, et al. An inherited TUBB2B mutation alters a kinesin-binding site and causes polymicrogyria, CFEOM and axon dysinnervation. Hum Mol Genet. 2012 Dec 15;21(26):5484–99.

299. Choy B, LaLonde A, Que J, Wu T, Zhou Z. MCM4 and MCM7, potential novel proliferation markers, significantly correlated with Ki-67, Bmi1, and cyclin E expression in esophageal adenocarcinoma, squamous cell carcinoma, and precancerous lesions. Hum Pathol. 2016 Nov;57:126–35.

300. Boudjadi S, Chatterjee B, Sun W, Vemu P, Barr FG. The expression and function of PAX3 in development and disease. Gene. 2018 Aug 5;666:145–57.

301. Li S, Jakobs TC. Secreted phosphoprotein 1 slows neurodegeneration and rescues visual function in mouse models of aging and glaucoma. Cell Rep. 2022 Dec 27;41(13):111880.

302. Fricker LD, McKinzie AA, Sun J, Curran E, Qian Y, Yan L, et al. Identification and

characterization of proSAAS, a granin-like neuroendocrine peptide precursor that inhibits prohormone processing. J Neurosci. 2000 Jan 15;20(2):639–48.

303. Ha CM, Choi J, Choi EJ, Costa ME, Lee BJ, Ojeda SR. NELL2, a neuron-specific EGF-like protein, is selectively expressed in glutamatergic neurons and contributes to the glutamatergic control of GnRH neurons at puberty. Neuroendocrinology. 2008 Jun 12;88(3):199–211.

304. Jin Y, Li JL. Olfactomedin-like 3: possible functions in embryonic development and tumorigenesis. Chin Med J (Engl). 2019 Jul 20;132(14):1733–8.

305. Raimondi C, Brash JT, Fantin A, Ruhrberg C. NRP1 function and targeting in neurovascular development and eye disease. Prog Retin Eye Res. 2016 May;52:64–83.

306. Alemany S, Vilor-Tejedor N, Bustamante M, Pujol J, Macià D, Martínez-Vilavella G, et al. A Genome-wide Association Study of attention function in a population-based sample of children. PLoS One. 2016 Sep 22;11(9):e0163048.

307. Li L, Liu Z, Yang H, Li Y, Zeng Q, Chen L, et al. Investigation of novel de novo KCNC2 variants causing severe developmental and early-onset epileptic encephalopathy. Seizure. 2022 Oct;101:218–24.

308. Villa N, Walker L, Lindsell CE, Gasson J, Iruela-Arispe ML, Weinmaster G. Vascular expression of Notch pathway receptors and ligands is restricted to arterial vessels. Mech Dev. 2001 Oct;108(1-2):161–4.

309. Geldhof V, de Rooij LPMH, Sokol L, Amersfoort J, De Schepper M, Rohlenova K, et al. Single cell atlas identifies lipid-processing and immunomodulatory endothelial cells in healthy and malignant breast. Nat Commun. 2022 Sep 20;13(1):5511.

310. Han Z, Ni J, Smits P, Underhill CB, Xie B, Chen Y, et al. Extracellular matrix protein 1 (ECM1) has angiogenic properties and is expressed by breast tumor cells. FASEB J. 2001 Apr;15(6):988–94.

311. Ng A, Wong M, Viviano B, Erlich JM, Alba G, Pflederer C, et al. Loss of glypican-3 function causes growth factor-dependent defects in cardiac and coronary vascular development. Dev Biol. 2009 Nov 1;335(1):208–15.

312. Wilting J, Papoutsi M, Christ B, Nicolaides KH, von Kaisenberg CS, Borges J, et al. The transcription factor Prox1 is a marker for lymphatic endothelial cells in normal and diseased human tissues. FASEB J. 2002 Aug;16(10):1271–3.

313. Wigle JT, Oliver G. Prox1 function is required for the development of the murine lymphatic system. Cell. 1999 Sep 17;98(6):769–78.

314. Kong LL, Yang NZ, Shi LH, Zhao GH, Zhou W, Ding Q, et al. The optimum marker for the detection of lymphatic vessels. Mol Clin Oncol. 2017 Oct;7(4):515–20.

315. Gutierrez-Miranda L, Yaniv K. Cellular origins of the lymphatic endothelium: Implications for cancer lymphangiogenesis. Front Physiol. 2020 Sep 24;11:577584.

316. Banerji S, Ni J, Wang SX, Clasper S, Su J, Tammi R, et al. LYVE-1, a new homologue of the CD44 glycoprotein, is a lymph-specific receptor for hyaluronan. J Cell Biol. 1999 Feb 22;144(4):789–801.

317. Kulkarni RM, Greenberg JM, Akeson AL. NFATc1 regulates lymphatic endothelial development. Mech Dev. 2009 May;126(5-6):350–65.

318. Heger L, Balk S, Lühr JJ, Heidkamp GF, Lehmann CHK, Hatscher L, et al. CLEC10A is a specific marker for human CD1c+ dendritic cells and enhances their toll-like receptor 7/8-induced cytokine secretion. Front Immunol. 2018 Apr 27;9:744.

319. Salaun B, de Saint-Vis B, Pacheco N, Pacheco Y, Riesler A, Isaac S, et al. CD208/dendritic cell-lysosomal associated membrane protein is a marker of normal and transformed type II pneumocytes. Am J Pathol. 2004 Mar;164(3):861–71.

320. Banga R, Procopio FA, Lana E, Gladkov GT, Roseto I, Parsons EM, et al. Lymph node dendritic cells harbor inducible replication-competent HIV despite years of suppressive ART. Cell Host Microbe. 2023 Oct 11;31(10):1714–31.e9.

321. Villani AC, Satija R, Reynolds G, Sarkizova S, Shekhar K, Fletcher J, et al. Single-cell RNA-seq reveals new types of human blood dendritic cells, monocytes, and progenitors. Science [Internet]. 2017 Apr 21;356(6335). Available from: http://dx.doi.org/10.1126/science.aah4573

322. Valladeau J, Dezutter-Dambuyant C, Saeland S. Langerin/CD207 sheds light on formation of birbeck granules and their possible function in Langerhans cells. Immunol Res. 2003;28(2):93–107.

323. Mizumoto N, Takashima A. CD1a and langerin: acting as more than Langerhans cell markers. J Clin Invest. 2004 Mar;113(5):658–60.

324. Xia C, Braunstein Z, Toomey AC, Zhong J, Rao X. S100 proteins as an important regulator of macrophage inflammation. Front Immunol. 2017;8:1908.

325. Bunbury A, Potolicchio I, Maitra R, Santambrogio L. Functional analysis of monocyte MHC class II compartments. FASEB J. 2009 Jan;23(1):164–71.

326. Zhu Y, Tang X, Xu Y, Wu S, Liu W, Geng L, et al. RNASE2 mediates age-associated B cell expansion through monocyte derived IL-10 in patients with systemic lupus erythematosus. Front Immunol. 2022 Feb 21;13:752189.

327. Zhang T, Fu JN, Chen GB, Zhang X. Plac8-ERK pathway modulation of monocyte function in sepsis. Cell Death Discov. 2024 Jul 3;10(1):308.

328. Montaldo E, Lusito E, Bianchessi V, Caronni N, Scala S, Basso-Ricci L, et al. Cellular and transcriptional dynamics of human neutrophils at steady state and upon stress. Nat Immunol. 2022 Oct;23(10):1470–83.

329. Read CB, Kuijper JL, Hjorth SA, Heipel MD, Tang X, Fleetwood AJ, et al. Cutting Edge: identification of neutrophil PGLYRP1 as a ligand for TREM-1. J Immunol. 2015 Feb 15;194(4):1417–21.

330. Ning DS, Zhou ZQ, Zhou SH, Chen JM. Identification of macrophage differentiation related genes and subtypes linking atherosclerosis plaque processing and metabolic syndrome via integrated bulk and single-cell sequence analysis. Heliyon. 2024 Jul 30;10(14):e34295.

331. Kahles F, Findeisen HM, Bruemmer D. Osteopontin: A novel regulator at the cross roads of inflammation, obesity and diabetes. Mol Metab. 2014 Jul;3(4):384–93.

332. Lim HY, Lim SY, Tan CK, Thiam CH, Goh CC, Carbajo D, et al. Hyaluronan receptor LYVE-1-expressing macrophages maintain arterial tone through hyaluronan-mediated regulation of

smooth muscle cell collagen. Immunity. 2018 Aug 21;49(2):326–41.e7.

333. Kieu TQ, Tazawa K, Kawashima N, Noda S, Fujii M, Nara K, et al. Kinetics of LYVE-1-positive M2-like macrophages in developing and repairing dental pulp in vivo and their pro-angiogenic activity in vitro. Sci Rep. 2022 Mar 25;12(1):5176.

334. Recalcati S, Locati M, Cairo G. Systemic and cellular consequences of macrophage control of iron metabolism. Semin Immunol. 2012 Dec;24(6):393–8.

335. Baitsch D, Bock HH, Engel T, Telgmann R, Müller-Tidow C, Varga G, et al. Apolipoprotein E induces antiinflammatory phenotype in macrophages. Arterioscler Thromb Vasc Biol. 2011 May;31(5):1160–8.

336. Jurga AM, Paleczna M, Kuter KZ. Overview of general and discriminating markers of differential microglia phenotypes. Front Cell Neurosci. 2020 Aug 6;14:198.

337. Haage V, Semtner M, Vidal RO, Hernandez DP, Pong WW, Chen Z, et al. Comprehensive gene expression meta-analysis identifies signature genes that distinguish microglia from peripheral monocytes/macrophages in health and glioma. Acta Neuropathol Commun. 2019 Feb 14;7(1):20.

338. Garcia-Alonso L, Lorenzi V, Mazzeo CI, Alves-Lopes JP, Roberts K, Sancho-Serra C, et al. Single-cell roadmap of human gonadal development. Nature. 2022 Jul;607(7919):540–7.

339. Zeng Y, Liu C, Gong Y, Bai Z, Hou S, He J, et al. Single-cell RNA sequencing resolves spatiotemporal development of pre-thymic lymphoid progenitors and thymus organogenesis in human embryos. Immunity. 2019 Nov 19;51(5):930–48.e6.

340. Stehling-Sun S, Dade J, Nutt SL, DeKoter RP, Camargo FD. Regulation of lymphoid versus myeloid fate “choice” by the transcription factor Mef2c. Nat Immunol. 2009 Mar;10(3):289–96.

341. Herglotz J, Unrau L, Hauschildt F, Fischer M, Kriebitzsch N, Alawi M, et al. Essential control of early B-cell development by Mef2 transcription factors. Blood. 2016 Feb 4;127(5):572–81.

342. Szabo PA, Levitin HM, Miron M, Snyder ME, Senda T, Yuan J, et al. Single-cell transcriptomics of human T cells reveals tissue and activation signatures in health and disease.

Nat Commun. 2019 Oct 17;10(1):4706.

343. Rajendeeran A, Tenbrock K. Regulatory T cell function in autoimmune disease. J Transl Autoimmun. 2021 Oct 30;4(100130):100130.

344. Rebuffet L, Melsen JE, Escalière B, Basurto-Lozada D, Bhandoola A, Björkström NK, et al. High-dimensional single-cell analysis of human natural killer cell heterogeneity. Nat Immunol. 2024 Aug;25(8):1474–88.

345. Lane PJL, Gaspal FM, McConnell FM, Withers DR, Anderson G. Lymphoid tissue inducer cells: pivotal cells in the evolution of CD4 immunity and tolerance? Front Immunol. 2012 Feb 29;3:24.

346. Mazzurana L, Czarnewski P, Jonsson V, Wigge L, Ringnér M, Williams TC, et al. Tissue-specific transcriptional imprinting and heterogeneity in human innate lymphoid cells revealed by full-length single-cell RNA-sequencing. Cell Res. 2021 May;31(5):554–68.

347. van de Pavert SA. Layered origins of lymphoid tissue inducer cells. Immunol Rev. 2023 May;315(1):71–8.

348. Ito T, Carson WF 4th, Cavassani KA, Connett JM, Kunkel SL. CCR6 as a mediator of immunity in the lung and gut. Exp Cell Res. 2011 Mar 10;317(5):613–9.

349. Lee RD, Munro SA, Knutson TP, LaRue RS, Heltemes-Harris LM, Farrar MA. Single-cell analysis identifies dynamic gene expression networks that govern B cell development and transformation. Nat Commun. 2021 Nov 25;12(1):6843.

350. Ohmori H, Hikida M. Expression and function of recombination activating genes in mature B cells. Crit Rev Immunol. 1998;18(3):221–35.

351. Reth M, Nielsen P. Signaling circuits in early B-cell development. Adv Immunol. 2014;122:129–75.

352. Sun B, Mallampati S, Gong Y, Wang D, Lefebvre V, Sun X. Sox4 is required for the survival of pro-B cells. J Immunol. 2013 Mar 1;190(5):2080–9.

353. Christian SL, Cambridge G. Editorial: CD24 in the regulation of cellular development and

disease. Front Immunol. 2024 Feb 27;15:1374701.

354. Leandro MJ. B-cell subpopulations in humans and their differential susceptibility to depletion with anti-CD20 monoclonal antibodies. Arthritis Res Ther. 2013 Mar 25;15 Suppl 1(Suppl 1):S3.

355. Gilbert SF. The Neural Crest. In: Developmental Biology 6th edition. Sinauer Associates; 2000.

356. Hill MA. Embryology [Internet]. Neural Crest Development. [cited 2024 Aug 25]. Available from: https://embryology.med.unsw.edu.au/embryology/index.php/Neural_Crest_Development

357. Palis J, Segel GB. Developmental biology of erythropoiesis. Blood Rev. 1998 Jun;12(2):106–14.

358.Palis J. Erythropoiesis in the mammalian embryo. Exp Hematol. 2024 Aug;136(104283):104283.

359. Driskell RR, Watt FM. Understanding fibroblast heterogeneity in the skin. Trends Cell Biol. 2015 Feb;25(2):92–9.

360. Direder M, Wielscher M, Weiss T, Laggner M, Copic D, Klas K, et al. The transcriptional profile of keloidal Schwann cells. Exp Mol Med. 2022 Nov;54(11):1886–900.

361. Legué E, Nicolas JF. Hair follicle renewal: organization of stem cells in the matrix and the role of stereotyped lineages and behaviors. Development. 2005 Sep;132(18):4143–54.

362. Daszczuk P, Mazurek P, Pieczonka TD, Olczak A, Boryń ŁM, Kobielak K. An intrinsic oscillation of gene networks inside hair follicle stem cells: An additional layer that can modulate hair stem cell activities. Front Cell Dev Biol. 2020 Dec 10;8:595178.

363. Fan SMY, Tsai CF, Yen CM, Lin MH, Wang WH, Chan CC, et al. Inducing hair follicle neogenesis with secreted proteins enriched in embryonic skin. Biomaterials. 2018 Jun;167:121–31.

364. Ngcungcu T, Oti M, Sitek JC, Haukanes BI, Linghu B, Bruccoleri R, et al. Duplicated

enhancer region increases expression of CTSB and segregates with keratolytic winter erythema in South African and Norwegian families. Am J Hum Genet. 2017 May 4;100(5):737–50.

365. Egberts F, Heinrich M, Jensen JM, Winoto-Morbach S, Pfeiffer S, Wickel M, et al. Cathepsin D is involved in the regulation of transglutaminase 1 and epidermal differentiation. J Cell Sci. 2004 May 1;117(Pt 11):2295–307.

366. Shimomura Y, Wajid M, Kurban M, Sato N, Christiano AM. Mutations in the keratin 85 (KRT85/hHb5) gene underlie pure hair and nail ectodermal dysplasia. J Invest Dermatol. 2010 Mar;130(3):892–5.

367. Lee HT, Liu SP, Lin CH, Lee SW, Hsu CY, Sytwu HK, et al. A Crucial Role of CXCL14 for Promoting Regulatory T Cells Activation in Stroke. Theranostics. 2017 Feb;7(4):855–75.

368. Wang H, Shi P, Shi X, Lv Y, Xie H, Zhao H. Surprising magic of CD24 beyond cancer. Front Immunol. 2023;14:1334922.

369. Dhariwala MO, Karthikeyan D, Vasquez KS, Farhat S, Weckel A, Taravati K, et al. Developing Human Skin Contains Lymphocytes Demonstrating a Memory Signature. Cell Rep Med. 2020 Nov;1(8):100132.

370. Gopee NH, Huang N, Olabi B, Admane C, Botting RA, Foster AR, et al. A human prenatal skin cell atlas reveals immune cell regulation of skin morphogenesis [Internet]. bioRxiv. 2023. Available from: http://dx.doi.org/10.1101/2023.10.12.556307

371. Vidal VPI, Chaboissier MC, Lützkendorf S, Cotsarelis G, Mill P, Hui CC, et al. Sox9 is essential for outer root sheath differentiation and the formation of the hair stem cell compartment. Curr Biol. 2005 Aug 9;15(15):1340–51.

372. Feinstein Y, Borrell V, Garcia C, Burstyn-Cohen T, Tzarfaty V, Frumkin A, et al. F-spondin and mindin: two structurally and functionally related genes expressed in the hippocampus that promote outgrowth of embryonic hippocampal neurons. Development. 1999 Aug;126(16):3637–48.

373. Jia W, Li H, He YW. The extracellular matrix protein mindin serves as an integrin ligand and

is critical for inflammatory cell recruitment. Blood. 2005 Dec;106(12):3854–9.

374. Martisova A, Sommerova L, Krejci A, Selingerova I, Kolarova T, Zavadil Kokas F, et al. Identification of AGR2 Gene-Specific Expression Patterns Associated with Epithelial-Mesenchymal Transition. Int J Mol Sci. 2022 Sep;23(18).

375. Delom F, Mohtar MA, Hupp T, Fessart D. The anterior gradient-2 interactome. Am J Physiol Cell Physiol. 2020 Jan;318(1):C40–7.

376. Sequeira I, Nicolas JF. Redefining the structure of the hair follicle by 3D clonal analysis. Development. 2012 Oct;139(20):3741–51.

377. Mesler AL, Veniaminova NA, Lull MV, Wong SY. Hair Follicle Terminal Differentiation Is Orchestrated by Distinct Early and Late Matrix Progenitors. Cell Rep. 2017 Apr;19(4):809–21.

378. McGrath JA, McMillan JR, Shemanko CS, Runswick SK, Leigh IM, Lane EB, et al. Mutations in the plakophilin 1 gene result in ectodermal dysplasia/skin fragility syndrome. Nat Genet. 1997 Oct;17(2):240–4.

379. Dardour L, Cosyns K, Devriendt K. A novel missense variant in the PVRL4 gene underlying ectodermal dysplasia-syndactyly syndrome in a Turkish child. Mol Syndromol. 2017 Dec;9(1):22–4.

380. Khan AK, Muhammad N, Aziz A, Khan SA, Shah K, Nasir A, et al. A novel mutation in homeobox DNA binding domain of HOXC13 gene underlies pure hair and nail ectodermal dysplasia (ECTD9) in a Pakistani family. BMC Med Genet. 2017 Apr 12;18(1):42.

381. Ito T, Shimomura Y, Farooq M, Suzuki N, Sakabe JI, Tokura Y. Trichorhinophalangeal syndrome with low expression of TRPS1 on epidermal and hair follicle epithelial cells. J Dermatol. 2013 May;40(5):396–8.

382. Fujimoto A, Farooq M, Fujikawa H, Inoue A, Ohyama M, Ehama R, et al. A missense mutation within the helix initiation motif of the keratin K71 gene underlies autosomal dominant woolly hair/hypotrichosis. J Invest Dermatol. 2012 Oct;132(10):2342–9.

383. Shimomura Y, Wajid M, Petukhova L, Kurban M, Christiano AM. Autosomal-dominant

woolly hair resulting from disruption of keratin 74 (KRT74), a potential determinant of human hair texture. Am J Hum Genet. 2010 Apr 9;86(4):632–8.

384. Al-Owain M, Wakil S, Shareef F, Al-Fatani A, Hamadah E, Haider M, et al. Novel homozygous mutation in DSP causing skin fragility-woolly hair syndrome: report of a large family and review of the desmoplakin-related phenotypes. Clin Genet. 2011 Jul;80(1):50–8.

385. Jackson A, Moss C, Chandler KE, Balboa PL, Bageta ML, Petrof G, et al. Biallelic TUFT1 variants cause woolly hair, superficial skin fragility and desmosomal defects. Br J Dermatol. 2023 Jan 23;188(1):75–83.

386. Ü Basmanav FB, Cau L, Tafazzoli A, Méchin MC, Wolf S, Romano MT, et al. Mutations in three genes encoding proteins involved in hair shaft formation cause uncombable hair syndrome. Am J Hum Genet. 2016 Dec 1;99(6):1292–304.

387. Li CF, Chen JY, Ho YH, Hsu WH, Wu LC, Lan HY, et al. Snail-induced claudin-11 prompts collective migration for tumour progression. Nat Cell Biol. 2019 Feb;21(2):251–62.

388. Dillenburg-Pilla P, Patel V, Mikelis CM, Zárate-Bladés CR, Doçi CL, Amornphimoltham P, et al. SDF-1/CXCL12 induces directional cell migration and spontaneous metastasis via a CXCR4/Gαi/mTORC1 axis. FASEB J. 2015 Mar;29(3):1056–68.

389. Biggs LC, Mäkelä OJ, Myllymäki SM, Das Roy R, Närhi K, Pispa J, et al. Hair follicle dermal condensation forms via Fgf20 primed cell cycle exit, cell motility, and aggregation. Elife. 2018 Jul;7.

390. Cescon M, Gattazzo F, Chen P, Bonaldo P. Collagen VI at a glance. J Cell Sci. 2015 Oct 1;128(19):3525–31.

391. Andreeva A, Lee J, Lohia M, Wu X, Macara IG, Lu X. PTK7-Src signaling at epithelial cell contacts mediates spatial organization of actomyosin and planar cell polarity. Dev Cell. 2014 Apr 14;29(1):20–33.

392. Hagner A, Shin W, Sinha S, Alpaugh W, Workentine M, Abbasi S, et al. Transcriptional Profiling of the Adult Hair Follicle Mesenchyme Reveals R-spondin as a Novel Regulator of Dermal Progenitor Function. iScience. 2020 Apr;23(4):101019.

393. Hu B, Lefort K, Qiu W, Nguyen BC, Rajaram RD, Castillo E, et al. Control of hair follicle cell fate by underlying mesenchyme through a CSL-Wnt5a-FoxN1 regulatory axis. Genes Dev. 2010 Jul;24(14):1519–32.

394. Belmadani A, Jung H, Ren D, Miller RJ. The chemokine SDF-1/CXCL12 regulates the migration of melanocyte progenitors in mouse hair follicles. Differentiation. 2009 Apr;77(4):395–411.

395. Kral M, Klimek C, Kutay B, Timelthaler G, Lendl T, Neuditschko B, et al. Covalent dimerization of interleukin-like epithelial-to-mesenchymal transition (EMT) inducer (ILEI) facilitates EMT, invasion, and late aspects of metastasis. FEBS J. 2017 Oct;284(20):3484–505.

396. Yin S, Chen F, Ye P, Yang G. Overexpression of FAM3C protein as a novel biomarker for epithelial-mesenchymal transition and poor outcome in gastric cancer. Int J Clin Exp Pathol. 2018 Aug;11(8):4247–56.

397. Nunan R, Campbell J, Mori R, Pitulescu ME, Jiang WG, Harding KG, et al. Ephrin-BS drive junctional downregulation and actin stress fiber disassembly to enable wound re-epithelialization. Cell Rep. 2015 Nov 17;13(7):1380–95.

398. Song Y, Miao Z, Brazma A, Papatheodorou I. Benchmarking strategies for cross-species integration of single-cell RNA sequencing data. Nat Commun. 2023 Oct 14;14(1):6495.

399. Wang N, Zhang WD, Zhong ZY, Zhou XB, Shi XR, Wang X. FGF7 secreted from dermal papillae cell regulates the proliferation and differentiation of hair follicle stem cell1. J Integr Agric [Internet]. 2023 Oct; Available from: http://dx.doi.org/10.1016/j.jia.2023.10.012

400. Mii S, Murakumo Y, Asai N, Jijiwa M, Hagiwara S, Kato T, et al. Epidermal hyperplasia and appendage abnormalities in mice lacking CD109. Am J Pathol. 2012 Oct;181(4):1180–9.

401. Kageyama T, Miyata H, Seo J, Nanmo A, Fukuda J. In vitro hair follicle growth model for drug testing. Sci Rep. 2023 Mar 24;13(1):4847.

402. Hudson R, Taniguchi-Sidle A, Boras K, Wiggan O, Hamel PA. Alx-4, a transcriptional activator whose expression is restricted to sites of epithelial-mesenchymal interactions. Dev

Dyn. 1998 Oct;213(2):159–69.

403. Rahmani W, Sinha S, Biernaskie J. Immune modulation of hair follicle regeneration. NPJ Regen Med. 2020 May 11;5(1):9.

404. Luissint AC, Nusrat A, Parkos CA. JAM-related proteins in mucosal homeostasis and inflammation. Semin Immunopathol. 2014 Mar;36(2):211–26.

405. Mallipattu SK, Estrada CC, He JC. The critical role of Krüppel-like factors in kidney disease. Am J Physiol Renal Physiol. 2017 Feb 1;312(2):F259–65.

406. Di Gregoli K, Somerville M, Bianco R, Thomas AC, Frankow A, Newby AC, et al. Galectin-3 identifies a subset of macrophages with a potential beneficial role in atherosclerosis. Arterioscler Thromb Vasc Biol. 2020 Jun;40(6):1491–509.

407. Ghersi G, Zhao Q, Salamone M, Yeh Y, Zucker S, Chen WT. The protease complex consisting of dipeptidyl peptidase IV and seprase plays a role in the migration and invasion of human endothelial cells in collagenous matrices. Cancer Res. 2006 May;66(9):4652–61.

408. Fu X, Li J, Sun X, Sun T, Sheng Z. Epidermal stem cells are the source of sweat glands in human fetal skin: evidence of synergetic development of stem cells, sweat glands, growth factors, and matrix metalloproteinases. Wound Repair Regen. 2005 Jan;13(1):102–8.

409. Martino PA, Heitman N, Rendl M. The dermal sheath: An emerging component of the hair follicle stem cell niche. Exp Dermatol. 2021 Apr;30(4):512–21.

410. Weber EL, Lai YC, Lei M, Jiang TX, Chuong CM. Human Fetal Scalp Dermal Papilla Enriched Genes and the Role of R-Spondin-1 in the Restoration of Hair Neogenesis in Adult Mouse Cells. Front Cell Dev Biol. 2020 Nov;8:583434.

411. Sumanaweera D, Suo C, Cujba AM, Muraro D, Dann E, Polanski K, et al. Gene-level alignment of single-cell trajectories. Nat Methods [Internet]. 2024 Sep 19; Available from: http://dx.doi.org/10.1038/s41592-024-02378-4

412. Ito M. The innermost cell layer of the outer root sheath in anagen hair follicle: light and electron microscopic study. Arch Derm Res. 1986;279(2):112–9.

413. Pinkus H, Iwasaki T, Mishima Y. Outer root sheath keratinization in anagen and catagen of the mammalian hair follicle. A seventh distinct type of keratinization in the hair follicle: trichilemmal keratinization. J Anat. 1981 Aug;133(Pt 1):19–35.

414. Gu LH, Coulombe PA. Keratin expression provides novel insight into the morphogenesis and function of the companion layer in hair follicles. J Invest Dermatol. 2007 May;127(5):1061–73.

415. Zhang YV, Cheong J, Ciapurin N, McDermitt DJ, Tumbar T. Distinct self-renewal and differentiation phases in the niche of infrequently dividing hair follicle stem cells. Cell Stem Cell. 2009 Sep 4;5(3):267–78.

416. Winter H, Langbein L, Praetzel S, Jacobs M, Rogers MA, Leigh IM, et al. A novel human type II cytokeratin, K6hf, specifically expressed in the companion layer of the hair follicle. J Invest Dermatol. 1998 Dec;111(6):955–62.

417. Iwata R, Vanderhaeghen P. Tempus fugit: How time flies during development. Science. 2020 Sep;369(6510):1431–2.

418. Halley AC. The Tempo of Mammalian Embryogenesis: Variation in the Pace of Brain and Body Development. Brain Behav Evol. 2022 Feb;97(1-2):96–107.

419. Carter AM. Animal models of human pregnancy and placentation: alternatives to the mouse. Reproduction. 2020 Dec;160(6):R129–43.

420. Wynn TA, Vannella KM. Macrophages in tissue repair, regeneration, and fibrosis. Immunity. 2016 Mar;44(3):450–62.

421. Krzyszczyk P, Schloss R, Palmer A, Berthiaume F. The role of macrophages in acute and chronic wound healing and interventions to promote pro-wound healing phenotypes. Front Physiol. 2018 May 1;9:419.

422. Davis FM, Tsoi LC, Wasikowski R, denDekker A, Joshi A, Wilke C, et al. Epigenetic regulation of the PGE2 pathway modulates macrophage phenotype in normal and pathologic wound repair. JCI Insight [Internet]. 2020 Sep 3;5(17). Available from: http://dx.doi.org/10.1172/jci.insight.138443

423. Lorenz HP, Lin RY, Longaker MT, Whitby DJ, Adzick NS. The fetal fibroblast: the effector cell of scarless fetal skin repair. Plast Reconstr Surg. 1995 Nov;96(6):1251–9.

424. Longaker MT, Adzick NS. The biology of fetal wound healing: a review. Plast Reconstr Surg. 1991 Apr;87(4):788–98.

425. Rowlatt U. Intrauterine wound healing in a 20 week human fetus. Virchows Arch A Pathol Anat Histol. 1979 Mar 23;381(3):353–61.

426. Somasundaram K, Prathap K. Intra-uterine healing of skin wounds in rabbit foetuses. J Pathol. 1970 Feb;100(2):81–6.

427. Dixon JB. Inflammation in the fœtal and neonatal rat: The local reactions to skin burns. J Pathol Bacteriol. 1960 Jul;80(1):73–82.

428. Harrison MR, Adzick NS, Longaker MT, Goldberg JD, Rosen MA, Filly RA, et al. Successful repair in utero of a fetal diaphragmatic hernia after removal of herniated viscera from the left thorax. N Engl J Med. 1990 May 31;322(22):1582–4.

429. Larson BJ, Longaker MT, Lorenz HP. Scarless fetal wound healing: a basic science review. Plast Reconstr Surg. 2010 Oct;126(4):1172–80.

430. Cass DL, Bullard KM, Sylvester KG, Yang EY, Longaker MT, Adzick NS. Wound size and gestational age modulate scar formation in fetal wound repair. J Pediatr Surg. 1997 Mar;32(3):411–5.

431. Satish L, Kathju S. Cellular and molecular characteristics of scarless versus fibrotic wound healing. Dermatol Res Pract. 2010 Dec 27;2010(1):790234.

432. Ulrich MMW. Fetal Wound Healing. In: Téot L, Mustoe TA, Middelkoop E, Gauglitz GG, editors. Textbook on Scar Management. Cham: Springer International Publishing; 2020. p. 3–9.

433. Shao A, Owens DM. The immunoregulatory protein CD200 as a potentially lucrative yet elusive target for cancer therapy. Oncotarget. 2023 Feb 4;14:96–103.

434. Koyama T, Ochoa-Callejero L, Sakurai T, Kamiyoshi A, Ichikawa-Shindo Y, Iinuma N, et al.

Vascular endothelial adrenomedullin-RAMP2 system is essential for vascular integrity and organ homeostasis. Circulation. 2013 Feb 19;127(7):842–53.

435. Neumaier EE, Rothhammer V, Linnerbauer M. The role of midkine in health and disease. Front Immunol. 2023 Nov 30;14:1310094.

436. Sosne G, Qiu P, Christopherson PL, Wheater MK. Thymosin beta 4 suppression of corneal NFkappaB: a potential anti-inflammatory pathway. Exp Eye Res. 2007 Apr;84(4):663–9.

437. Ascensión AM, Fuertes-Álvarez S, Ibañez-Solé O, Izeta A, Araúzo-Bravo MJ. Human Dermal Fibroblast Subpopulations Are Conserved across Single-Cell RNA Sequencing Studies. J Invest Dermatol. 2021 Jul;141(7):1735–44.e35.

438. Solé-Boldo L, Raddatz G, Schütz S, Mallm JP, Rippe K, Lonsdorf AS, et al. Single-cell transcriptomes of the human skin reveal age-related loss of fibroblast priming. Commun Biol. 2020 Apr;3(1):188.

439. Gur C, Wang SY, Sheban F, Zada M, Li B, Kharouf F, et al. LGR5 expressing skin fibroblasts define a major cellular hub perturbed in scleroderma. Cell. 2022 Apr;185(8):1373–88.e20.

440. Deng CC, Hu YF, Zhu DH, Cheng Q, Gu JJ, Feng QL, et al. Single-cell RNA-seq reveals fibroblast heterogeneity and increased mesenchymal fibroblasts in human fibrotic skin diseases. Nat Commun. 2021 Jun;12(1):3709.

441. Liu J, Wu Q, Shi J, Guo W, Jiang X, Zhou B, et al. LILRB4, from the immune system to the disease target. Am J Transl Res. 2020 Jul 15;12(7):3149–66.

442. Munday J, Kerr S, Ni J, Cornish AL, Zhang JQ, Nicoll G, et al. Identification, characterization and leucocyte expression of Siglec-10, a novel human sialic acid-binding receptor. Biochem J. 2001 Apr 15;355(Pt 2):489–97.

443. Lee M, Lee Y, Song J, Lee J, Chang SY. Tissue-specific Role of CXCR1 Expressing Immune Cells and Their Relationships with Human Disease. Immune Netw. 2018 Feb;18(1):e5.

444. Du C, Wang Y, Zhang F, Yan S, Guan Y, Gong X, et al. Synaptotagmin-11 inhibits cytokine secretion and phagocytosis in microglia. Glia. 2017 Oct;65(10):1656–67.

445. Mathur N, Mehdi SF, Anipindi M, Aziz M, Khan SA, Kondakindi H, et al. Ghrelin as an Anti-Sepsis Peptide: Review. Front Immunol. 2020;11:610363.

446. Waseem T, Duxbury M, Ito H, Ashley SW, Robinson MK. Exogenous ghrelin modulates release of pro-inflammatory and anti-inflammatory cytokines in LPS-stimulated macrophages through distinct signaling pathways. Surgery. 2008 Mar;143(3):334–42.

447. Buechler MB, Fu W, Turley SJ. Fibroblast-macrophage reciprocal interactions in health, fibrosis, and cancer. Immunity. 2021 May;54(5):903–15.

448. Ma F, Li Y, Jia L, Han Y, Cheng J, Li H, et al. Macrophage-stimulated cardiac fibroblast production of IL-6 is essential for TGF β/Smad activation and cardiac fibrosis induced by angiotensin II. PLoS One. 2012 May 4;7(5):e35144.

449. Henn D, Chen K, Fehlmann T, Trotsyuk AA, Sivaraj D, Maan ZN, et al. Xenogeneic skin transplantation promotes angiogenesis and tissue regeneration through activated Trem2 macrophages. Sci Adv. 2021 Dec;7(49):eabi4528.

450. Liechty KW, Adzick NS, Crombleholme TM. Diminished interleukin 6 (IL-6) production during scarless human fetal wound repair. Cytokine. 2000 Jun;12(6):671–6.

451. Denton CP, Ong VH, Xu S, Chen-Harris H, Modrusan Z, Lafyatis R, et al. Therapeutic interleukin-6 blockade reverses transforming growth factor-beta pathway activation in dermal fibroblasts: insights from the faSScinate clinical trial in systemic sclerosis. Ann Rheum Dis. 2018 Sep;77(9):1362–71.

452. Alivernini S, MacDonald L, Elmesmari A, Finlay S, Tolusso B, Gigante MR, et al. Distinct synovial tissue macrophage subsets regulate inflammation and remission in rheumatoid arthritis. Nat Med. 2020 Aug;26(8):1295–306.

453. Ortmayr G, Brunnthaler L, Pereyra D, Huber H, Santol J, Rumpf B, et al. Immunological Aspects of AXL/GAS-6 in the Context of Human Liver Regeneration. Hepatol Commun. 2022 Mar;6(3):576–92.

454. Peng CK, Wu CP, Lin JY, Peng SC, Lee CH, Huang KL, et al. Gas6/Axl signaling attenuates alveolar inflammation in ischemia-reperfusion-induced acute lung injury by up-regulating

SOCS3-mediated pathway. PLoS One. 2019 Jul;14(7):e0219788.

455. Lorenz HP, Longaker MT, Perkocha LA, Jennings RW, Harrison MR, Adzick NS. Scarless wound repair: a human fetal skin model. Development. 1992 Jan;114(1):253–9.

456. Liechty KW, Crombleholme TM, Cass DL, Martin B, Adzick NS. Diminished interleukin-8 (IL-8) production in the fetal wound healing response. J Surg Res. 1998 Jun;77(1):80–4.

457. Braga TT, Agudelo JSH, Camara NOS. Macrophages during the fibrotic process: M2 as friend and foe. Front Immunol. 2015 Nov 25;6:602.

458. Wang Z, Wu Z, Wang H, Feng R, Wang G, Li M, et al. An immune cell atlas reveals the dynamics of human macrophage specification during prenatal development. Cell. 2023 Sep 28;186(20):4454–71.e19.

459. desJardins-Park HE, Mascharak S, Chinta MS, Wan DC, Longaker MT. The spectrum of scarring in craniofacial wound repair. Front Physiol. 2019 Mar 29;10:322.

460. Cho DI, Kim MR, Jeong HY, Jeong HC, Jeong MH, Yoon SH, et al. Mesenchymal stem cells reciprocally regulate the M1/M2 balance in mouse bone marrow-derived macrophages. Exp Mol Med. 2014 Jan 10;46(1):e70.

461. Mascharak S, desJardins-Park HE, Davitt MF, Griffin M, Borrelli MR, Moore AL, et al. Preventing Engrailed-1 activation in fibroblasts yields wound regeneration without scarring. Science [Internet]. 2021 Apr 23;372(6540). Available from: http://dx.doi.org/10.1126/science.aba2374

462. Aarabi S, Bhatt KA, Shi Y, Paterno J, Chang EI, Loh SA, et al. Mechanical load initiates hypertrophic scar formation through decreased cellular apoptosis. FASEB J. 2007 Oct;21(12):3250–61.

463. Longaker MT, Rohrich RJ, Greenberg L, Furnas H, Wald R, Bansal V, et al. A randomized controlled trial of the embrace advanced scar therapy device to reduce incisional scar formation. Plast Reconstr Surg. 2014 Sep;134(3):536–46.

464. Yang Y, Huang J, Zeng A, Long X, Yu N, Wang X. The role of the skin microbiome in wound healing. Burns Trauma. 2024 Mar 4;12:tkad059.

465. Canesso MCC, Vieira AT, Castro TBR, Schirmer BGA, Cisalpino D, Martins FS, et al. Skin wound healing is accelerated and scarless in the absence of commensal microbiota. J Immunol. 2014 Nov 15;193(10):5171–80.

466. Heinke J, Patterson C, Moser M. Life is a pattern: vascular assembly within the embryo. Front Biosci (Elite Ed). 2012 Jan 1;4(6):2269–88.

467. Risau W, Flamme I. Vasculogenesis. Annu Rev Cell Dev Biol. 1995;11(1):73–91.

468. Risau W. Mechanisms of angiogenesis. Nature. 1997 Apr 17;386(6626):671–4.

469. Carmeliet P. Mechanisms of angiogenesis and arteriogenesis. Nat Med. 2000 Apr;6(4):389–95.

470. Gu X, Li SY, DeFalco T. Immune and vascular contributions to organogenesis of the testis and ovary. FEBS J. 2022 May;289(9):2386–408.

471. DeFalco T, Bhattacharya I, Williams AV, Sams DM, Capel B. Yolk-sac-derived macrophages regulate fetal testis vascularization and morphogenesis. Proc Natl Acad Sci U S A. 2014 Jun 10;111(23):E2384–93.

472. Munro DAD, Wineberg Y, Tarnick J, Vink CS, Li Z, Pridans C, et al. Macrophages restrict the nephrogenic field and promote endothelial connections during kidney development. Elife [Internet]. 2019 Feb 13;8. Available from: http://dx.doi.org/10.7554/eLife.43271

473. Kubota Y, Takubo K, Shimizu T, Ohno H, Kishi K, Shibuya M, et al. M-CSF inhibition selectively targets pathological angiogenesis and lymphangiogenesis. J Exp Med. 2009 May 11;206(5):1089–102.

474. Fantin A, Vieira JM, Gestri G, Denti L, Schwarz Q, Prykhozhij S, et al. Tissue macrophages act as cellular chaperones for vascular anastomosis downstream of VEGF-mediated endothelial tip cell induction. Blood. 2010 Aug;116(5):829–40.

475. Zhao X, Eyo UB, Murugan M, Wu LJ. Microglial interactions with the neurovascular system in physiology and pathology. Dev Neurobiol. 2018 Jun;78(6):604–17.

476. Kolter J, Feuerstein R, Zeis P, Hagemeyer N, Paterson N, d'Errico P, et al. A subset of skin

macrophages contributes to the surveillance and regeneration of local nerves. Immunity. 2019 Jun 18;50(6):1482–97.e7.

477. Stratton JA, Holmes A, Rosin NL, Sinha S, Vohra M, Burma NE, et al. Macrophages Regulate Schwann Cell Maturation after Nerve Injury. Cell Rep. 2018 Sep;24(10):2561–72.e6.

478. Wang PL, Yim AKY, Kim KW, Avey D, Czepielewski RS, Colonna M, et al. Peripheral nerve resident macrophages share tissue-specific programming and features of activated microglia. Nat Commun. 2020 May 21;11(1):2552.

479. Kolter J, Kierdorf K, Henneke P. Origin and Differentiation of Nerve-Associated Macrophages. J Immunol. 2020 Jan;204(2):271–9.

480. Ding Z, Guo S, Luo L, Zheng Y, Gan S, Kang X, et al. Emerging roles of microglia in neuro-vascular unit: Implications of microglia-neurons interactions. Front Cell Neurosci. 2021 Oct 12;15:706025.

481. Szepesi Z, Manouchehrian O, Bachiller S, Deierborg T. Bidirectional Microglia-Neuron Communication in Health and Disease. Front Cell Neurosci. 2018 Sep;12:323.

482. Moore CS, Ase AR, Kinsara A, Rao VTS, Michell-Robinson M, Leong SY, et al. P2Y12 expression and function in alternatively activated human microglia. Neurol Neuroimmunol Neuroinflamm. 2015 Apr;2(2):e80.

483. Astarita JL, Acton SE, Turley SJ. Podoplanin: emerging functions in development, the immune system, and cancer. Front Immunol. 2012 Sep 12;3:283.

484. Wolf Y, Yona S, Kim KW, Jung S. Microglia, seen from the CX3CR1 angle. Front Cell Neurosci. 2013 Mar 18;7:26.

485.Pocock J, Vasilopoulou F, Svensson E, Cosker K. Microglia and TREM2. Neuropharmacology. 2024 Oct 1;257(110020):110020.

486. Bret C, Desmots-Loyer F, Moreaux J, Fest T. BHLHE41, a transcriptional repressor involved in physiological processes and tumor development. Cell Oncol [Internet]. 2024 Sep 10; Available from: http://dx.doi.org/10.1007/s13402-024-00973-3

487. Follis RM, Carter BD. Myelin avoids the JAM. Neuron. 2016 Aug 17;91(4):713–6.

488. Erskine L, François U, Denti L, Joyce A, Tillo M, Bruce F, et al. VEGF-A and neuropilin 1 (NRP1) shape axon projections in the developing CNS via dual roles in neurons and blood vessels. Development. 2017 Jul 1;144(13):2504–16.

489. Cariboni A, Hickok J, Rakic S, Andrews W, Maggi R, Tischkau S, et al. Neuropilins and their ligands are important in the migration of gonadotropin-releasing hormone neurons. J Neurosci. 2007 Feb 28;27(9):2387–95.

490. Van Damme P, Van Hoecke A, Lambrechts D, Vanacker P, Bogaert E, van Swieten J, et al. Progranulin functions as a neurotrophic factor to regulate neurite outgrowth and enhance neuronal survival. J Cell Biol. 2008 Apr 7;181(1):37–41.

491. Hechtman JF. NTRK insights: best practices for pathologists. Mod Pathol. 2022 Mar;35(3):298–305.

492. Koncina E, Roth L, Gonthier B, Bagnard D. Role of Semaphorins during Axon Growth and Guidance. Landes Bioscience; 2013.

493. Ding JB, Oh WJ, Sabatini BL, Gu C. Semaphorin 3E-Plexin-D1 signaling controls pathway-specific synapse formation in the striatum. Nat Neurosci. 2011 Dec 18;15(2):215–23.

494. Toh H, Cao M, Daniels E, Bateman A. Expression of the growth factor progranulin in endothelial cells influences growth and development of blood vessels: a novel mouse model. PLoS One. 2013 May 31;8(5):e64989.

495. Bach LA. Endothelial cells and the IGF system. J Mol Endocrinol. 2015 Feb;54(1):R1–13.

496. Ziche M, Maglione D, Ribatti D, Morbidelli L, Lago CT, Battisti M, et al. Placenta growth factor-1 is chemotactic, mitogenic, and angiogenic. Lab Invest. 1997 Apr;76(4):517–31.

497. Peng Z, Pang H, Wu H, Peng X, Tan Q, Lin S, et al. CCL2 promotes proliferation, migration and angiogenesis through the MAPK/ERK1/2/MMP9, PI3K/AKT, Wnt/β-catenin signaling pathways in HUVECs. Exp Ther Med. 2023 Feb;25(2):77.

498. Li Y, Zheng Y, Li T, Wang Q, Qian J, Lu Y, et al. Chemokines CCL2, 3, 14 stimulate

macrophage bone marrow homing, proliferation, and polarization in multiple myeloma. Oncotarget. 2015 Sep 15;6(27):24218–29.

499. He H, Xu J, Warren CM, Duan D, Li X, Wu L, et al. Endothelial cells provide an instructive niche for the differentiation and functional polarization of M2-like macrophages. Blood. 2012 Oct 11;120(15):3152–62.

500. Saunders DC, Aamodt KI, Richardson TM, Hopkirk AJ, Aramandla R, Poffenberger G, et al. Coordinated interactions between endothelial cells and macrophages in the islet microenvironment promote β cell regeneration. NPJ Regen Med. 2021 Apr 6;6(1):22.

501. Amersfoort J, Eelen G, Carmeliet P. Immunomodulation by endothelial cells - partnering up with the immune system? Nat Rev Immunol. 2022 Sep;22(9):576–88.

502. Cox AA, Liu A, Ng CJ. Clusterin knockdown has effects on intracellular and secreted von Willebrand factor in human umbilical vein endothelial cells. PLoS One. 2024 Feb 16;19(2):e0298133.

503. Denzer L, Muranyi W, Schroten H, Schwerk C. The role of PLVAP in endothelial cells. Cell Tissue Res. 2023 May;392(2):393–412.

504. Campinho P, Vilfan A, Vermot J. Blood flow forces in shaping the vascular system: A focus on endothelial cell behavior. Front Physiol. 2020 Jun 5;11:552.

505. Marziano C, Genet G, Hirschi KK. Vascular endothelial cell specification in health and disease. Angiogenesis. 2021 May;24(2):213–36.

506. Helle E, Ampuja M, Antola L, Kivelä R. Flow-induced transcriptomic remodeling of endothelial cells derived from human induced pluripotent stem cells. Front Physiol. 2020 Oct 15;11:591450.

507. Blanco R, Gerhardt H. VEGF and Notch in tip and stalk cell selection. Cold Spring Harb Perspect Med. 2013 Jan 1;3(1):a006569.

508. Fajardo LF, Kwan HH, Kowalski J, Prionas SD, Allison AC. Dual role of tumor necrosis factor-alpha in angiogenesis. Am J Pathol. 1992 Mar;140(3):539–44.

509. Ribatti D, Nico B, Spinazzi R, Vacca A, Nussdorfer GG. The role of adrenomedullin in angiogenesis. Peptides. 2005 Sep;26(9):1670–5.

510. Cambier S, Gouwy M, Proost P. The chemokines CXCL8 and CXCL12: molecular and functional properties, role in disease and efforts towards pharmacological intervention. Cell Mol Immunol. 2023 Mar;20(3):217–51.

511. Holroyd EW, Delacroix S, Larsen K, Harbuzariu A, Psaltis PJ, Wang L, et al. Tissue factor pathway inhibitor blocks angiogenesis via its carboxyl terminus. Arterioscler Thromb Vasc Biol. 2012 Mar;32(3):704–11.

512. Usuba R, Pauty J, Soncin F, Matsunaga YT. EGFL7 regulates sprouting angiogenesis and endothelial integrity in a human blood vessel model. Biomaterials. 2019 Mar;197:305–16.

513. de Jong OG, van der Waals LM, Kools FRW, Verhaar MC, van Balkom BWM. Lysyl oxidase-like 2 is a regulator of angiogenesis through modulation of endothelial-to-mesenchymal transition. J Cell Physiol. 2019 Jul;234(7):10260–9.

514. Suehiro JI, Kanki Y, Makihara C, Schadler K, Miura M, Manabe Y, et al. Genome-wide approaches reveal functional vascular endothelial growth factor (VEGF)-inducible nuclear factor of activated T cells (NFAT) c1 binding to angiogenesis-related genes in the endothelium. J Biol Chem. 2014 Oct 17;289(42):29044–59.

515. Fan C, Ouyang P, Timur AA, He P, You SA, Hu Y, et al. Novel roles of GATA1 in regulation of angiogenic factor AGGF1 and endothelial cell function. J Biol Chem. 2009 Aug 28;284(35):23331–43.

516. Yang L, Guan H, He J, Zeng L, Yuan Z, Xu M, et al. VEGF increases the proliferative capacity and eNOS/NO levels of endothelial progenitor cells through the calcineurin/NFAT signalling pathway. Cell Biol Int. 2012 Jan;36(1):21–7.

517. Grundmann S, Lindmayer C, Hans FP, Hoefer I, Helbing T, Pasterkamp G, et al. FoxP1 stimulates angiogenesis by repressing the inhibitory guidance protein semaphorin 5B in endothelial cells. PLoS One. 2013 Sep 2;8(9):e70873.

518. Wang D, Liu B, Xiong T, Yu W, Yang H, Wang J, et al. Transcription factor Foxp1 stimulates

angiogenesis in adult rats after myocardial infarction. Cell Death Discov. 2022 Sep 10;8(1):381.

519. Lilly AJ, Mazan A, Scott DA, Lacaud G, Kouskoff V. SOX7 expression is critically required in FLK1-expressing cells for vasculogenesis and angiogenesis during mouse embryonic development. Mech Dev. 2017 Aug;146:31–41.

520. Klomp J, Hyun J, Klomp JE, Pajcini K, Rehman J, Malik AB. Comprehensive transcriptomic profiling reveals SOX7 as an early regulator of angiogenesis in hypoxic human endothelial cells. J Biol Chem. 2020 Apr 10;295(15):4796–808.

521. Zhang Y, Liu J, Lin J, Zhou L, Song Y, Wei B, et al. The transcription factor GATA1 and the histone methyltransferase SET7 interact to promote VEGF-mediated angiogenesis and tumor growth and predict clinical outcome of breast cancer. Oncotarget. 2016 Mar 1;7(9):9859–75.

522. Khandekar M, Brandt W, Zhou Y, Dagenais S, Glover TW, Suzuki N, et al. A Gata2 intronic enhancer confers its pan-endothelia-specific regulation. Development. 2007 May;134(9):1703–12.

523. Coma S, Allard-Ratick M, Akino T, van Meeteren LA, Mammoto A, Klagsbrun M. GATA2 and Lmo2 control angiogenesis and lymphangiogenesis via direct transcriptional regulation of neuropilin-2. Angiogenesis. 2013 Oct;16(4):939–52.

524. De Val S, Black BL. Transcriptional control of endothelial cell development. Dev Cell. 2009 Feb;16(2):180–95.

525. Mammoto A, Connor KM, Mammoto T, Yung CW, Huh D, Aderman CM, et al. A mechanosensitive transcriptional mechanism that controls angiogenesis. Nature. 2009 Feb;457(7233):1103–8.

526. Carmi Y, Voronov E, Dotan S, Lahat N, Rahat MA, Fogel M, et al. The role of macrophage-derived IL-1 in induction and maintenance of angiogenesis. J Immunol. 2009 Oct 1;183(7):4705–14.

527. Nolfi AL, Behun MN, Yates CC, Brown BN, Kulkarni M. Beyond growth factors: Macrophage-centric strategies for angiogenesis. Curr Pathobiol Rep. 2020 Dec;8(4):111–20.

528. Spiller KL, Anfang RR, Spiller KJ, Ng J, Nakazawa KR, Daulton JW, et al. The role of macrophage phenotype in vascularization of tissue engineering scaffolds. Biomaterials. 2014 May;35(15):4477–88.

529. Yip S, Wang N, Sugimura R. Give them vasculature and immune cells: How to fill the gap of organoids. Cells Tissues Organs. 2023 Jan 30;212(5):369–82.

530. Strobel HA, Moss SM, Hoying JB. Vascularized tissue organoids. Bioengineering (Basel). 2023 Jan 17;10(2):124.

531. Wörsdörfer P, Dalda N, Kern A, Krüger S, Wagner N, Kwok CK, et al. Generation of complex human organoid models including vascular networks by incorporation of mesodermal progenitor cells. Sci Rep. 2019 Oct 30;9(1):15663.

532. Huang M, Smith A, Watson M, Bhandari R, Baugh LM, Ivanovska I, et al. Self-assembled human skin equivalents model macrophage activation of cutaneous fibrogenesis in systemic sclerosis. Arthritis Rheumatol. 2022 Jul;74(7):1245–56.

533. Dermitzakis I, Chatzi D, Kyriakoudi SA, Evangelidis N, Vakirlis E, Meditskou S, et al. Skin development and disease: A molecular perspective. Curr Issues Mol Biol. 2024 Jul 30;46(8):8239–67.

534. Has C, Bauer JW, Bodemer C, Bolling MC, Bruckner-Tuderman L, Diem A, et al. Consensus reclassification of inherited epidermolysis bullosa and other disorders with skin fragility. Br J Dermatol. 2020 Oct;183(4):614–27.

535. Gutiérrez-Cerrajero C, Sprecher E, Paller AS, Akiyama M, Mazereeuw-Hautier J, Hernández-Martín A, et al. Ichthyosis. Nat Rev Dis Primers. 2023 Jan 19;9(1):2.

536. Itin PH. Etiology and pathogenesis of ectodermal dysplasias. Am J Med Genet A. 2014 Oct;164A(10):2472–7.

537. Sharma A, Blériot C, Currenti J, Ginhoux F. Oncofetal reprogramming in tumour development and progression. Nat Rev Cancer. 2022 Oct;22(10):593–602.

538. Balachandran S, Narendran A. The developmental origins of cancer: A review of the genes expressed in embryonic cells with implications for tumorigenesis. Genes (Basel) [Internet].

2023 Feb 28;14(3). Available from: http://dx.doi.org/10.3390/genes14030604

539. Phillips HS, Kharbanda S, Chen R, Forrest WF, Soriano RH, Wu TD, et al. Molecular subclasses of high-grade glioma predict prognosis, delineate a pattern of disease progression, and resemble stages in neurogenesis. Cancer Cell. 2006 Mar;9(3):157–73.

540. Human Cell Atlas [Internet]. HCA: Data portal. [cited 2024 Dec 1]. Available from: https://data.humancellatlas.org/

541. Liu Y, Huang J, Pandey R, Liu P, Therani B, Qiu Q, et al. Robustness of single-cell RNA-seq for identifying differentially expressed genes. BMC Genomics. 2023 Jul 3;24(1):371.

542. Xenium In Situ Platform [Internet]. 10x Genomics. [cited 2024 Dec 3]. Available from: https://www.10xgenomics.com/platforms/xenium#panels

543. HD Products: Visium HD Spatial Gene Expression [Internet]. 10x Genomics. [cited 2024 Dec 3]. Available from: https://www.10xgenomics.com/products/visium-hd-spatial-gene-expression

544. McKinley KL, Longaker MT, Naik S. Emerging frontiers in regenerative medicine. Science. 2023 May 26;380(6647):796–8.

545. Nathans JF, Ayers JL, Shendure J, Simpson CL. Genetic tools for cell lineage tracing and profiling developmental trajectories in the skin. J Invest Dermatol. 2024 May;144(5):936–49.

546. Lindenhofer D, Haendeler S, Esk C, Littleboy JB, Brunet Avalos C, Naas J, et al. Cerebral organoids display dynamic clonal growth and tunable tissue replenishment. Nat Cell Biol. 2024 May;26(5):710–8.

547. He Z, Maynard A, Jain A, Gerber T, Petri R, Lin HC, et al. Lineage recording in human cerebral organoids. Nat Methods. 2022 Jan;19(1):90–9.

548. Bury LAD, Fu S, Wynshaw-Boris A. Neuronal lineage tracing from progenitors in human cortical organoids reveals mechanisms of neuronal production, diversity, and disease. Cell Rep. 2024 Oct 22;43(10):114862.

549. Wagner DE, Klein AM. Lineage tracing meets single-cell omics: opportunities and challenges.

Nat Rev Genet. 2020 Jul;21(7):410–27.

550. Betjes MA, Zheng X, Kok RNU, van Zon JS, Tans SJ. Cell tracking for organoids: Lessons from developmental biology. Front Cell Dev Biol. 2021 Jun 3;9:675013.

Appendices

Appendix A. Ethical approval for prenatal skin tissue acquisition.

A1: Ethical approval for HDBR.

NHS
Health Research Authority

North East - Newcastle & North Tyneside 1 Research Ethics Committee
2nd Floor, 2 Redman Place
Stratford
London
E20 1JQ

Telephone: 0207 104 8241

14 July 2023

Prof Deborah J Henderson
Newcastle University
Newcastle University Biosciences Institute
International Centre for Life
Times Square
NE1 3BZ

Dear Prof Henderson

Title of the Research Tissue Bank:	**The Human Developmental Biology Resource 2023**
REC reference:	**23/NE/0135**
Designated Individual:	**Dr Chris Morris**
IRAS project ID:	**330783**

The Research Ethics Committee reviewed the above application at the meeting held on 11 July 2023. Thank you for attending to discuss the application.

Ethical Opinion

The members of the Committee present gave a favourable ethical opinion of the above research tissue bank on the basis described in the application form and supporting documentation, subject to the conditions specified below.

The Committee has also confirmed that the favourable ethical opinion applies to all research projects conducted in the UK using tissue or data supplied by the tissue bank, provided that the release of the tissue or data complies with the attached conditions. It will not be necessary for these researchers to make project-based applications for ethical approval. They will be deemed to have ethical approval from this committee. You should provide the researcher with a copy of this letter as confirmation of this. The Committee should be notified of all projects receiving tissue and data from the tissue bank by means of an annual report.

This application was for the renewal of a Research Tissue Bank application. The previous REC Reference number for this application was 18/NE/0290.

Research Governance

Under the UK Policy Framework for Health and Social Care Research, there is no requirement for NHS research permission for the establishment of research tissue banks in the NHS. Applications to NHS R&D offices through IRAS are not required as all NHS organisations are expected to have included management review in the process of establishing the research tissue bank.

Research permission is also not required by collaborators at tissue collection centres (TCCs) who provide tissue or data under the terms of a supply agreement between the organisation and the research tissue bank. TCCs are not research sites for the purposes of the RGF.

Research tissue bank managers are advised to provide R&D offices at all TCCs with a copy of the REC application for information, together with a copy of the favourable opinion letter when available. All TCCs should be listed in Part C of the REC application.

NHS researchers undertaking specific research projects using tissue or data supplied by the research tissue bank must apply for permission to R&D offices at all organisations where the research is conducted, whether or not the research tissue bank has ethical approval.

Assessment of site suitability is not a requirement for ethical review of research tissue banks.

Registration of Research Tissue Banks

It is a condition of the ethical approval that all Research Tissue Banks are registered on the UK Clinical Research Collaboration (UKCRC) Tissue Directory. The Research Tissue Bank should be registered no later than 6 weeks after the date of this favourable ethical opinion letter or 6 weeks after the Research Tissue Bank holds tissue with the intention to provide for research purposes. Please use the following link to register the Research Tissue Bank on the UKCRC Directory: https://directory.biobankinguk.org/Register/Biobank Registration is defined as having added details of the types of tissue samples held in the tissue bank.

There is no requirement to separately notify the REC but you should do so at the earliest opportunity e.g. when submitting an amendment or when submitting an annual progress report. We will monitor the registration details as part of the annual progress reporting process.

Publication of Your Research Summary

We will publish your research summary for the above study on the research summaries section of our website, together with your contact details, no earlier than three months from the date of this favourable opinion letter.

Should you wish to provide a substitute contact point, make a request to defer, or require further information, please visit:
https://www.hra.nhs.uk/planning-and-improving-research/application-summaries/research-summaries/

N.B. If your study is related to COVID-19 we will aim to publish your research summary within 3 days rather than three months.

During this public health emergency, it is vital that everyone can promptly identify all relevant research related to COVID-19 that is taking place globally. If you haven't already done so, please register your study on a public registry as soon as possible and provide the HRA with the

registration detail, which will be posted alongside other information relating to your project. We are also asking sponsors not to request deferral of publication of research summary for any projects relating to COVID-19. In addition, to facilitate finding and extracting studies related to COVID-19 from public databases, please enter the WHO official acronym for the coronavirus disease (COVID-19) in the full title of your study. Approved COVID-19 studies can be found at: https://www.hra.nhs.uk/covid-19-research/approved-covid-19-research/

Duration of Ethical Opinion

The favourable opinion has been renewed for five years from the end of the previous five year period provided that you comply with the standard conditions of ethical approval for Research Tissue Banks set out in the attached document. You are advised to study the conditions carefully. The opinion may be renewed for a further period of up to five years on receipt of a fresh application. It is suggested that the fresh application is made 3-6 months before the 5 years expires, to ensure continuous approval for the research tissue bank.

Research Tissue Bank Renewals

The previous five-year period ran from 10/12/2018 to 10/12/2023. This Research Tissue Bank may be renewed for further periods of five years at a time by following the process described in the above paragraph.

Approved Documents

The documents reviewed and approved at the meeting were:

Document	*Version*	*Date*
Covering letter on headed paper [Covering letter]	N/A	15 June 2023
Human Tissue Authority licence [HTA licence 12534]	1	06 July 2016
IRAS Checklist XML [Checklist_22062023]		22 June 2023
Other [HDBR Tissue Access Policy]	1	03 August 2018
Other [HDBR Terms of Reference]	1	03 August 2018
Other [SOP - Recruitment of HDBR donors]	4	15 June 2023
Other [SOP - Collection of consented material]	4	15 June 2023
Other [HDBR Sample Sign Out form]	2	01 February 2018
Other [HDBR Participant Data Questionnaire]	1	03 August 2018
Other [RE annual report 2021]	N/A	12 August 2022
Other [Chief Investigator CV]	N/A	14 June 2023
Other [Ethics amendment to PIS]	N/A	30 September 2021
Other [Overview of HDBR PRES survey results April 2021]	1	30 April 2021
Other [BSACP conference abstract]	N/A	07 October 2021
Participant consent form [F18 Consent Form_V5_2707_2018.pdf]	5	27 July 2018
Participant information sheet (PIS) [F16_HDBR_Participant_Information_Sheet_V7.0_300921]	7	03 August 2018
Protocol for management of the tissue bank [Protcol for management of tissue bank]	1	15 June 2023
REC Application Form [RTB_Form_22062023]		22 June 2023

Summary of research programme(s) [Research Summary]	1	15 June 2023

Licence from the Human Tissue Authority

Thank you for providing a copy of the above licence.

Membership of the Committee

The members of the Ethics Committee who were present at the meeting are listed on the attached sheet.

Statement of Compliance

The Committee is constituted in accordance with the Governance Arrangements for Research Ethics Committees and complies fully with the Standard Operating Procedures for Research Ethics Committees in the UK.

After ethical review: Reporting requirements

The attached standard conditions give detailed guidance on reporting requirements for research tissue banks with a favourable opinion, including:

- Notifying substantial amendments
- Submitting Annual Progress reports

The latest guidance on these topics can be found at
https://www.hra.nhs.uk/approvals-amendments/managing-your-approval/.

User Feedback

The Health Research Authority is continually striving to provide a high quality service to all applicants and sponsors. You are invited to give your view of the service you have received and the application procedure. If you wish to make your views known please use the feedback form available on the HRA website:
http://www.hra.nhs.uk/about-the-hra/governance/quality-assurance/

HRA Learning

We are pleased to welcome researchers and research staff to our HRA Learning Events and online learning opportunities– see details at:
https://www.hra.nhs.uk/planning-and-improving-research/learning/

IRAS project ID: 330783	**Please quote this number on all correspondence**

Yours sincerely

PP
Mr Paddy Stevenson
Chair

E-mail: newcastlenorthtyneside1.rec@hra.nhs.uk

Enclosures: List of names and professions of members who were present at the meeting and those who submitted written comments

Research Tissue Bank – Conditions of Approval

Copy to: Dr Chris Morris, Newcastle University

North East - Newcastle & North Tyneside 1 Research Ethics Committee

Attendance at Committee meeting on 11 July 2023

Committee Members:

Name	*Profession*	*Present*	*Notes*
Dr Chien-Yi Chang	Lecturer	No	
Professor Tim Cheetham	Professor of Clinical Paediatric Endocrinology and Honorary Consultant Paediatrician	No	
Mr Jeremy Dearling	Former Registered Nurse	Yes	
Mrs Emma Ginn	Specialist Pharmacy Officer Quality Assurance	Yes	
Reverend Nigel Goodfellow	Retired Head of Chaplaincy	Yes	
Dr Charles Kelly	Consultant Clinical Oncologist	Yes	
Dr Vrinda Nair	Consultant Neonatologist	Yes	
Mrs Bijal Patel	Research Study Coordinator	No	
Mrs Sue Phillips	Clinical Lead Pharmacist	Yes	
Dr Philip Ryan	Retired Occupational Health Physician	Yes	Chair
Miss Miryam Vermaat	Volunteer	Yes	
Mr Mike Wyatt	Consultant Vascular Surgeon	Yes	

Also in Attendance:

Name	*Position (or reason for attending)*
Ms Nicola Beazley-Long	Approvals Officer
Mr Ali Hussain	Approvals Administrator
Mr z. Mark Sidaway	Approvals Specialist

CONDITIONS OF REC FAVOURABLE OPINION

Research Ethics Committee:	North East - Newcastle & North Tyneside 1 Research Ethics Committee
Research Tissue Bank:	The Human Developmental Biology Resource 2023
REC reference number:	23/NE/0135
Name of applicant:	Prof Deborah J Henderson
Date of approval:	14 July 2023
IRAS project ID:	330783

A REC Favourable Opinion has been given to the Research Tissue Bank ("RTB") by the Research Ethics Committee ("the Committee") subject to the following conditions.

1. Further communications with the Committee

1.1 Further communications with the Committee are the personal responsibility of the applicant.

2. Duration of approval

2.1 Approval is given for a period of 5 years, which may be renewed on consideration of a new application by the Committee, taking account of developments in legislation, policy and guidance in the interim. New applications should include relevant changes of policy or practice made by the RTB, including any substantial amendments approved, since the original approval together with any proposed new developments.

3. Licensing

3.1 A copy of the Licence from the Human Tissue Authority (HTA) should be provided when available (if not already submitted).

3.2 The Committee should be notified if the Authority renews the licence, varies the licensing conditions or revokes the Licence, or of any change of Designated Individual. If the Licence is revoked, the REC favourable opinion would be terminated.

3.3 It is a condition of the REC favourable opinion that all Research Tissue Banks are registered on the UK Clinical Research Collaboration (UKCRC) Tissue Directory

4. Generic ethical approval for projects receiving tissue

4.1 Samples of human tissue or other biological material may be supplied and used in research projects to be conducted in accordance with the following conditions.

4.1.1 The research project should be within the fields of medical or biomedical research described in the approved application form.

4.1.2 The RTB should be satisfied that the research has been subject to scientific critique, is appropriately designed in relation to its objectives and (with the exception of student research below doctoral level) is likely to add something useful to existing knowledge.

4.1.3 Where tissue samples have been donated with informed consent for use in future research ("broad consent"), the RTB should be satisfied that the use of the samples complies with the terms of the donor consent.

4.1.4 All samples and any associated clinical information must be non-identifiable to the researcher at the point of release (i.e. anonymised or linked anonymised).

4.1.5 Samples will not be released to any project requiring further data or tissue from donors or involving any other research procedures. Any contact with donors must be confined to ethically approved arrangements for the feedback of clinically significant information.

4.1.6 A supply agreement must be in place with the researcher to ensure storage, use and disposal of the samples in accordance with the HTA Codes of Practice, the terms of the ethical approval and any other conditions required by the RTB.

4.2 A research project in the UK using tissue provided by a RTB in accordance with these conditions will be considered to have ethical approval from the Committee under the terms of this approval. In England, Wales and Northern Ireland this means that the researcher will not require a licence from the Human Tissue Authority for storage of the tissue for use in relation to this project.

4.3 The RTB may require any researcher to seek specific ethical review for their project. Where this applies an application should be prepared and submitted for ethical review.

4.4 A substantial amendment should be submitted to seek the Committee's agreement to change the conditions of generic approval.

5. Records

5.1 The Bank should maintain a record of all research projects to which tissue has been supplied. The record should contain at least the full title of the project, a summary of its purpose, the name of the Chief Investigator, the sponsor, the location of the research, the date on which the project was approved by the RTB, details of the

tissue released and any relevant reference numbers.

5.2 The Committee may request access to these records at any time.

6. Annual reports

6.1 An annual report should be provided to the Committee listing all projects for which tissue has been released in the previous year. The list should give the full title of each project, the name of the Chief Investigator, the sponsor, the location of the research and the date of approval by the RTB. The report is due on the anniversary of the date on which ethical approval for the RTB was given.

6.2 The Committee may request additional reports on the management of the RTB at any time.

7. Substantial amendments

7.1 Substantial amendments should be notified to the Committee and a favourable ethical opinion obtained before implementing the amendment. A substantial amendment generally means any significant change to the arrangements for the management of the RTB as described in the application to the Committee and supporting documentation.

7.2 A substantial amendment should be generated by accessing the original application form on the Integrated Research Application System (IRAS).

7.3 The following changes should always be notified as substantial amendments:

7.3.1 Any significant change to the policy for use of the tissue in research, including changes to the types of research to be undertaken or supported by the RTB.

7.3.2 Any significant change to the types of biological material to be collected and stored, or the circumstances of collection.

7.3.3 Any significant change to informed consent arrangements, including new/modified information sheets and consent forms.

7.3.4 Request for approval to release tissue to researchers (if not sought as part of the initial application), or changes to the terms of the approval;

7.3.4 A change to the conditions of generic approval

7.3.5 Appointment of a new tissue bank manager (i.e. the person making the application and responsible for further reporting to the REC);

7.3.6 Any other significant change to the governance of the RTB.

8. Serious Adverse Events

8.1 The Committee should be notified as soon as possible of any serious adverse event or

reaction, any serious breach of security or confidentiality, or any other incident that could undermine public confidence in the ethical management of the tissue. The criteria for notifying the Committee will be the same as those for notifying the Human Tissue Authority in the case of research tissue RTBs in England, Wales and Northern Ireland.

9. Other information to be notified

9.1 The Committee should be notified of any change in the contact details for the applicant or where the applicant hands over responsibility for communication with the Committee to another person at the establishment.

10. Closure of the RTB

10.1 Any plans to close the RTB should be notified to the Committee and the HTA as early as possible and at least two months before closure. The Committee should be informed what arrangements are to be made for disposal of the tissue or transfer to another research tissue RTB.

10.2 Where tissue is transferred to another RTB, the ethical approval for the RTB is not transferable. Where the second RTB is ethically approved, it should notify the responsible Research Ethics Committee by submitting an amendment. The terms of its own ethical approval would apply to any tissue it receives.

11. Breaches of approval conditions

11.1 The Committee should be notified as soon as possible of any breach of these approval conditions.

11.2 Where serious breaches occur, the Committee may review its ethical opinion l and may, exceptionally, suspend or terminate the approval.

A2: Ethical approval for Cambridge University Hospitals.

NHS
Health Research Authority

East of England - Cambridge Central Research Ethics Committee

Royal Standard Place
Nottingham
NG1 6FS

Please note: This is the favourable opinion of the REC only and does not allow the amendment to be implemented at NHS sites in England until the outcome of the HRA assessment has been confirmed.

21 February 2018

Dr Rachel Kyd
Research and Development Department
Cambridge University Hospitals NHS Foundation Trust
Cambridge Biomedical Campus
Cambridge
CB2 0QQ

Dear Dr Kyd

Study title:	**Invitro studies of postmortem human foetal neural tissue**
REC reference:	**96/085**
Amendment number:	**16**
Amendment date:	**16 January 2018**
IRAS project ID:	**95602**

The above amendment was reviewed on 19 February 2018 by the Sub-Committee in correspondence.

Ethical opinion

The members of the Committee taking part in the review gave a favourable ethical opinion of the amendment on the basis described in the notice of amendment form and supporting documentation.

The Sub-Committee were in agreement that the Substantial Amendment did not raise any material ethical issues.

Approved documents

The documents reviewed and approved at the meeting were:

Document	*Version*	*Date*
Covering letter on headed paper [Cover Letter 19.01.2018.pdf]		19 January 2018
Notice of Substantial Amendment (non-CTIMP) [SKMBT_C45218011911060.pdf]	16	16 January 2018
Other [lay summary 31012018 JFD.DOCX]		31 January 2018
Participant consent form [ICF v9.0 160118.doc]	9	16 January 2018

Participant information sheet (PIS) [PIS v9.0 160118.doc]	9	16 January 2018
Research protocol or project proposal [Ethics tissue protocol V11 160118 clean.docx]	11	16 January 2018
Research protocol or project proposal [Ethics tissue protocol V11 160118 tracked.docx]	11	16 January 2018

Membership of the Committee

The members of the Committee who took part in the review are listed on the attached sheet.

Working with NHS Care Organisations

Sponsors should ensure that they notify the R&D office for the relevant NHS care organisation of this amendment in line with the terms detailed in the categorisation email issued by the lead nation for the study.

Statement of compliance

The Committee is constituted in accordance with the Governance Arrangements for Research Ethics Committees and complies fully with the Standard Operating Procedures for Research Ethics Committees in the UK.

We are pleased to welcome researchers and R & D staff at our Research Ethics Committee members' training days – see details at http://www.hra.nhs.uk/hra-training/

96/085:	**Please quote this number on all correspondence**

Yours sincerely

P.P

Revd Dr Derek Fraser
Chair

E-mail: NRESCommittee.EastofEngland-CambridgeCentral@nhs.net

Enclosures: *List of names and professions of members who took part in the review*

Copy to: *Professor Roger A Barker, Cambridge Centre for Brain Repair*

East of England - Cambridge Central Research Ethics Committee

Attendance at Sub-Committee of the REC meeting on 19 February 2018

Committee Members:

Name	*Profession*	*Present*	*Notes*
Revd Dr Derek Fraser (Chair)	Chaplain	Yes	
Mr David Lewin	Retired Research Officer	Yes	

Also in attendance:

Name	*Position (or reason for attending)*
Teagan Allen	REC Assistant

Appendix B. Metadata for prenatal skin specimens.

B1: Prenatal skin specimens included in scRNA-seq dataset.

specimen_id	age (PCW)	sex	sort strategy	technology	chemistry
F16	8	male	$CD45^-$	10X_scRNAseq	3prime
F16	8	male	$CD45^+$	10X_scRNAseq	3prime
F17	9	male	$CD45^-$	10X_scRNAseq	3prime
F17	9	male	$CD45^+$	10X_scRNAseq	3prime
F17	9	male	Total	10X_scRNAseq	3prime
F19	10	female	$CD45^-$	10X_scRNAseq	3prime
F19	10	female	$CD45^+$	10X_scRNAseq	3prime
F32	8 (CS22)	female	$CD45^-$	10X_scRNAseq	3prime
F32	8 (CS22)	female	$CD45^+$	10X_scRNAseq	3prime
F33	9	female	$CD45^-$	10X_scRNAseq	3prime
F33	9	female	$CD45^+$	10X_scRNAseq	3prime
F34	8	female	$CD45^-$	10X_scRNAseq	3prime
F34	8	female	$CD45^+$	10X_scRNAseq	3prime
F35	8 (CS23)	female	$CD45^-$	10X_scRNAseq	3prime
F35	8 (CS23)	female	$CD45^+$	10X_scRNAseq	3prime
F38	13	male	$CD45^-$	10X_scRNAseq	3prime
F38	13	male	$CD45^+$	10X_scRNAseq	3prime
F41	16	female	$CD45^-$	10X_scRNAseq	3prime
F41	16	female	$CD45^+$	10X_scRNAseq	3prime
F45	12	female	$CD45^-$	10X_scRNAseq	3prime
F45	12	female	$CD45^+$	10X_scRNAseq	3prime
F45	12	female	$CD45^+$	10X_scRNAseq	5GEX
F50	15	female	$CD45^-$	10X_scRNAseq	5GEX
F50	15	female	$CD45^+$	10X_scRNAseq	5GEX
F51	15	female	$CD45^-$	10X_scRNAseq	5GEX
F51	15	female	$CD45^+$	10X_scRNAseq	5GEX
F61	7 (CS18)	male	$CD45^-$	10X_scRNAseq	5GEX
F61	7 (CS18)	male	$CD45^+$	10X_scRNAseq	5GEX
F69	11	female	$CD45^-$	10X_scRNAseq	5GEX

F69	11	female	$CD45^{+}$	10X_scRNAseq	5GEX
F69	11	female	CD45en	10X_scRNAseq	5GEX
F71	14	female	$CD45^{-}$	10X_scRNAseq	5GEX
F71	14	female	$CD45^{+}$	10X_scRNAseq	5GEX
F71	14	female	CD45en	10X_scRNAseq	5GEX
F217	17	female	Total	10X_scRNAseq	5GEX
F220	17	female	$CD45^{-}CD34^{-}$	10X_scRNAseq	5GEX
F220	17	female	$CD45^{-}CD34^{+}$	10X_scRNAseq	5GEX
F220	17	female	$CD45^{+}$	10X_scRNAseq	5GEX
F221	14	female	$CD45^{-}CD34^{-}$	10X_scRNAseq	5GEX
F221	14	female	$CD45^{-}CD34^{+}$	10X_scRNAseq	5GEX
F221	14	female	$CD45^{+}$	10X_scRNAseq	5GEX

B2: Prenatal skin specimens included in spatial transcriptomic dataset.

Embryonic limb skin data (*) was obtained from a publicly available dataset from Zhang et al.[141] (E-MTAB-11341).

specimen_id	age (PCW)	sex	replicate sample_id	technology	site
Fspatial1	10	male	HCA_rFSKI13460601	10X_Visium	abdominal
Fspatial1	10	male	HCA_rFSKI13460602	10X_Visium	abdominal
Fspatial2	10	male	HCA_rFSKI13460603	10X_Visium	facial
Fspatial2	10	male	HCA_rFSKI13460604	10X_Visium	facial
Flimb1*	8	male	WSSS_THYst9383359	10X_Visium	limb
Flimb1*	8	male	WSSS_THYst9383361	10X_Visium	limb
Flimb1*	8	male	WSSS_THYst9383362	10X_Visium	limb
Flimb2*	6	female	WSSS_THYst9699523	10X_Visium	limb
Flimb2*	6	female	WSSS_THYst9699524	10X_Visium	limb
Flimb3*	6	female	WSSS_THYst9699525	10X_Visium	limb
Flimb3*	6	female	WSSS_THYst9699526	10X_Visium	limb

Appendix C: FACS-sorted cell proportions.

speci_id	sample_id	age (PCW)	sort strategy	count	total live events	parent multiplier
F16	4834STDY7002879	8	$CD45^+$	12939	385631	0.0335528
F16	4834STDY7002880	8	$CD45^-$	371538	385631	0.9634547
F17	4834STDY7038752	9	$CD45^+$	11514	517311	0.0222574
F17	4834STDY7038753	9	$CD45^-$	505206	517311	0.97660015
F19	FCAImmP7241241	10	$CD45^-$	22826	919270	0.024830572
F19	FCAImmP7241240	10	$CD45^+$	895669	919270	0.974326368
F32	FCAImmP7316896	8 (CS22)	$CD45^+$	317	8903	0.035605976
F32	FCAImmP7316897	8 (CS22)	$CD45^-$	8586	8903	0.964394024
F33	FCAImmP7316886	9	$CD45^+$	77153	1474021	0.052341859
F33	FCAImmP7316887	9	$CD45^+$	77153	1474021	0.052341859
F33	FCAImmP7316888	9	$CD45^-$	1396868	1474021	0.947658141
F34	FCAImmP7352189	8	$CD45^+$	237	7293	0.032496915
F34	FCAImmP7352190	8	$CD45^-$	7056	7293	0.967503085
F34	FCAImmP7352191	8	$CD45^-$	7056	7293	0.967503085
F35	FCAImmP7462240	8 (CS23)	$CD45^+$	1175	83036	0.014150489
F35	FCAImmP7462241	8 (CS23)	$CD45^-$	81861	83036	0.985849511
F38	FCAImmP7528290	13	$CD45^+$	294	10886	0.027007165
F38	FCAImmP7528291	13	$CD45^-$	10592	10886	0.972992835
F38	FCAImmP7528296	13	$CD45^+$	294	10886	0.027007165
F41	FCAImmP7555848	16	$CD45^-$	65	5188	0.012528913
F41	FCAImmP7555858	16	$CD45^+$	5123	5188	0.987471087
F45	FCAImmP7579212	12	$CD45^+$	138	5178	0.026651217
F45	FCAImmP7579213	12	$CD45^-$	5040	5178	0.973348783
F45	FCAImmP7579224	12	$CD45^+$	138	5178	0.026651217
F50	FCAImmP7803024	15	$CD45^+$	15293	1410218	0.010844423
F50	FCAImmP7803025	15	$CD45^+$	15293	1410218	0.010844423
F50	FCAImmP7803026	15	$CD45^-$	1394925	1410218	0.989155577
F50	FCAImmP7803027	15	$CD45^-$	1394925	1410218	0.989155577
F51	FCAImmP7803034	14	$CD45^+$	81785	1795901	0.045539815

F51	FCAImmP7803035	14	$CD45^+$	81785	1795901	0.045539815
F51	FCAImmP7803042	14	$CD45^-$	1714116	1795901	0.954460185
F51	FCAImmP7803043	14	$CD45^-$	1714116	1795901	0.954460185
F61	FCAImmP7862094	7 (CS18)	$CD45^+$	63	1472	0.042798913
F61	FCAImmP7862095	7 (CS18)	$CD45^-$	1409	1472	0.957201087
F61	FCAImmP7862096	7 (CS18)	$CD45^-$	1409	1472	0.957201087
F69	FCAImmP7964502	11	$CD45^+$	24386	1248592	0.019530799
F69	FCAImmP7964503	11	$CD45^-$ $CD34^+$	1224206	1248592	0.980469201
F69	FCAImmP7964504	11	$CD45^-$	1224206	1248592	0.980469201
F69	FCAImmP7964505	11	CD45en	1224206	1248592	0.980469201
F71	FCAImmP7964506	14	$CD45^+$	39796	1481874	0.02685519
F71	FCAImmP7964507	14	$CD45^+$	39796	1481874	0.02685519
F71	FCAImmP7964508	14	$CD45^-$	1442078	1481874	0.97314482
F71	FCAImmP7964509	14	$CD45^-$ $CD34^+$	1442078	1481874	0.97314482
F71	FCAImmP7964510	14	CD45en	1442078	1481874	0.97314482
F220	HCA_rFSKI14449635	17	$CD45^+$	26290	1562035	0.01683061
F220	HCA_rFSKI14449636	17	$CD45^-$ $CD34^-$	339393	1562035	0.21727618
F220	HCA_rFSKI14449637	17	$CD45^-$ $CD34^-$	339393	1562035	0.21727618
F220	HCA_rFSKI14449638	17	$CD45^-$ $CD34^+$	1196352	1562035	0.76589321
F220	HCA_rFSKI14449639	17	$CD45^+$	60243	2003643	0.03006673
F220	HCA_rFSKI14449640	17	$CD45^-$ $CD34^-$	1180906	2003643	0.58937945
F220	HCA_rFSKI14449641	17	$CD45^-$ $CD34^-$	1180906	2003643	0.58937945
F220	HCA_rFSKI14449642	17	$CD45^-$ $CD34^+$	762494	2003643	0.38055382
F221	HCA_rFSKI14539490	14	$CD45^+$	20854	1059047	0.01969129

F221	HCA_rFSKI14539491	14	$CD45^-$ $CD34^-$	338193	1059047	0.3193371
F221	HCA_rFSKI14539492	14	$CD45^-$ $CD34^-$	338193	1059047	0.3193371
F221	HCA_rFSKI14539493	14	$CD45^-$ $CD34^+$	700000	1059047	0.66097161
F221	HCA_rFSKI14539494	14	$CD45^+$	25300	371906	0.06802794
F221	HCA_rFSKI14539495	14	$CD45^-$ $CD34^-$	53883	371906	0.14488338
F221	HCA_rFSKI14539496	14	$CD45^-$ $CD34^-$	53883	371906	0.14488338
F221	HCA_rFSKI14539497	14	$CD45^-$ $CD34^+$	292723	371906	0.78708867
F221	HCA_rFSKI14539498	14	$CD45^+$	20847	1086301	0.01919081
F221	HCA_rFSKI14539499	14	$CD45^-$ $CD34^-$	249439	1086301	0.22962236
F221	HCA_rFSKI14539500	14	$CD45^-$ $CD34^-$	249439	1086301	0.22962236
F221	HCA_rFSKI14539501	14	$CD45^-$ $CD34^+$	816015	1086301	0.75118683

Appendix D. 10x Genomics Chromium Controller channel metadata.

Metadata for each sample loaded on the 10x Genomics Chromium Controller.

channel	specimen_id	age (PCW)	sex	sort strategy	sample_id
1	F16	8	male	$CD45^+$	4834STDY7002879
2	F16	8	male	$CD45^-$	4834STDY7002880
3	F17	9	male	Total	4834STDY7002883
4	F17	9	male	$CD45^+$	4834STDY7038752
5	F17	9	male	$CD45^-$	4834STDY7038753
6	F19	10	female	$CD45^+$	FCAImmP7241240
7	F19	10	female	$CD45^-$	FCAImmP7241241
8	F33	9	female	$CD45^+$	FCAImmP7316886
9	F33	9	female	$CD45^+$	FCAImmP7316887
10	F33	9	female	$CD45^-$	FCAImmP7316888
11	F32	8 (CS22)	female	$CD45^+$	FCAImmP7316896
12	F32	8 (CS22)	female	$CD45^-$	FCAImmP7316897
13	F34	8	female	$CD45^+$	FCAImmP7352189
14	F34	8	female	$CD45^-$	FCAImmP7352190
15	F34	8	female	$CD45^-$	FCAImmP7352191
16	F35	8 (CS23)	female	$CD45^+$	FCAImmP7462240
17	F35	8 (CS23)	female	$CD45^-$	FCAImmP7462241
18	F38	13	male	$CD45^+$	FCAImmP7528290
19	F38	13	male	$CD45^-$	FCAImmP7528291
20	F38	13	male	$CD45^+$	FCAImmP7528296
21	F41	16	female	$CD45^-$	FCAImmP7555848
22	F41	16	female	$CD45^+$	FCAImmP7555858
23	F45	12	female	$CD45^+$	FCAImmP7579212
24	F45	12	female	$CD45^-$	FCAImmP7579213
25	F45	12	female	$CD45^+$	FCAImmP7579224
26	F50	15	female	$CD45^+$	FCAImmP7803024
27	F50	15	female	$CD45^+$	FCAImmP7803025
28	F50	15	female	$CD45^-$	FCAImmP7803026

29	F50	15	female	$CD45^-$	FCAImmP7803027
30	F51	15	female	$CD45^+$	FCAImmP7803034
31	F51	15	female	$CD45^+$	FCAImmP7803035
32	F51	15	female	$CD45^-$	FCAImmP7803042
33	F51	15	female	$CD45^-$	FCAImmP7803043
34	F61	7 (CS18)	male	$CD45^+$	FCAImmP7862094
35	F61	7 (CS18)	male	$CD45^-$	FCAImmP7862095
36	F61	7 (CS18)	male	$CD45^-$	FCAImmP7862096
37	F69	11	female	$CD45^+$	FCAImmP7964502
38	F69	11	female	$CD45^-CD34^+$	FCAImmP7964503
39	F69	11	female	$CD45^-$	FCAImmP7964504
40	F69	11	female	CD45en	FCAImmP7964505
41	F71	14	female	$CD45^+$	FCAImmP7964506
42	F71	14	female	$CD45^+$	FCAImmP7964507
43	F71	14	female	$CD45^-$	FCAImmP7964508
44	F71	14	female	$CD45^-CD34^+$	FCAImmP7964509
45	F71	14	female	CD45en	FCAImmP7964510
46	F217	17	female	Total	WS_wEMB13942138
47	F217	17	female	Total	WS_wEMB13942139
48	F217	17	female	Total	WS_wEMB13942141
49	F217	17	female	Total	WS_wEMB13942142
50	F217	17	female	Total	WS_wEMB13942143
51	F217	17	female	Total	WS_wEMB13942144
52	F217	17	female	Total	WS_wEMB13942145
53	F217	17	female	Total	WS_wEMB13942146
54	F217	17	female	Total	WS_wEMB13942147
55	F217	17	female	Total	WS_wEMB13942148
56	F217	17	female	Total	WS_wEMB13942149
57	F217	17	female	Total	WS_wEMB13942150
58	F217	17	female	Total	WS_wEMB13942151
59	F217	17	female	Total	WS_wEMB13942152

60	F217	17	female	Total	WS_wEMB13942153
61	F220	17	female	$CD45^{+}$	HCA_rFSKI14449635
62	F220	17	female	$CD45^{-}CD34^{-}$	HCA_rFSKI14449636
63	F220	17	female	$CD45^{-}CD34^{-}$	HCA_rFSKI14449637
64	F220	17	female	$CD45^{-}CD34^{+}$	HCA_rFSKI14449638
65	F220	17	female	$CD45^{+}$	HCA_rFSKI14449639
66	F220	17	female	$CD45^{-}CD34^{-}$	HCA_rFSKI14449640
67	F220	17	female	$CD45^{-}CD34^{-}$	HCA_rFSKI14449641
68	F220	17	female	$CD45^{-}CD34^{+}$	HCA_rFSKI14449642
69	F221	14	female	$CD45^{+}$	HCA_rFSKI14539490
70	F221	14	female	$CD45^{-}CD34^{-}$	HCA_rFSKI14539491
71	F221	14	female	$CD45^{-}CD34^{-}$	HCA_rFSKI14539492
72	F221	14	female	$CD45^{-}CD34^{+}$	HCA_rFSKI14539493
73	F221	14	female	$CD45^{+}$	HCA_rFSKI14539494
74	F221	14	female	$CD45^{-}CD34^{-}$	HCA_rFSKI14539495
75	F221	14	female	$CD45^{-}CD34^{-}$	HCA_rFSKI14539496
76	F221	14	female	$CD45^{-}CD34^{+}$	HCA_rFSKI14539497
77	F221	14	female	$CD45^{+}$	HCA_rFSKI14539498
78	F221	14	female	$CD45^{-}CD34^{-}$	HCA_rFSKI14539499
79	F221	14	female	$CD45^{-}CD34^{-}$	HCA_rFSKI14539500
80	F221	14	female	$CD45^{-}CD34^{+}$	HCA_rFSKI14539501

Appendix E. Differentially expressed genes for broad cell types in prenatal skin.

The top 25 DEGs are shown from differential gene expression testing (two-sided Wilcoxon rank-sum, Benjamini-Hochberg adjusted) between broad cell types in prenatal skin scRNA-seq dataset.

	Adipocyte	B cell	DC	Erythroid	Fibroblast
0	FABP5	CD74	CD74	HBG2	COL1A2
1	SRPX	HLA-DRA	HLA-DRA	HBA2	COL1A1
2	LPL	CD79A	HLA-DPA1	HBA1	LUM
3	APOE	CD37	HLA-DRB1	HBG1	COL3A1
4	CFD	IGHM	HLA-DPB1	SLC25A37	COL6A2
5	COL12A1	HLA-B	CST3	ALAS2	DCN
6	PTX3	B2M	HLA-DMA	HBM	COL6A1
7	PPARG	HLA-DRB1	HLA-DQB1	SNCA	FSTL1
8	FABP4	CD79B	HLA-DRB5	AHSP	COL5A2
9	KCTD12	VPREB3	LSP1	SLC25A39	MFAP4
10	IGFBP4	HLA-DPA1	HLA-DQA1	HBZ	MFAP2
11	HSPB6	CD52	GPR183	GYPC	COL5A1
12	SERPINF1	PTMA	SRGN	BLVRB	CTSK
13	ASS1	LAPTM5	AIF1	AC104389.5	MEST
14	TGFBR3	HLA-DPB1	PFN1	HBQ1	GPC3
15	VCAN	HLA-C	FCER1G	GYPB	CRABP2
16	SOX9	CXCR4	LCP1	HBB	VIM
17	CD81	HLA-DQB1	VAMP8	PRDX2	OLFML3
18	RAMP2	LTB	CD37	FECH	FBLN1
19	MGST1	ARHGDIB	ACTB	SMIM1	ISLR
20	MGST3	CD69	SAMHD1	SLC4A1	LAPTM4A
21	IGFBP3	TCL1A	CORO1A	STRADB	SFRP2
22	NUPR1	LIMD2	B2M	FAM210B	PCOLCE
23	MMP2	MS4A1	LST1	HEMGN	PDGFRA
24	HAS2	CD24	HLA-DMB	ADIPOR1	TCF4

	Haem progenitor	ILC	Keratinocyte	Lymphatic endothelium	Macrophage
0	HMGA1	KLRB1	KRT17	TFF3	FTL
1	ARHGDIB	B2M	PERP	TFPI	AIF1
2	PRSS57	SRGN	S100A14	NTS	RNASE1
3	FXYD5	IFITM1	KRT5	CCL21	C1QA
4	RAC2	NKG7	DSP	RAMP2	C1QC
5	SERPINB1	HLA-B	LGALS7	ECSCR	TYROBP
6	GIHCG	ARHGDIB	SFN	MMRN1	LYVE1
7	ITGA4	CTSW	KRT15	GNG11	FOLR2
8	GATA2	IL2RG	KRT14	S100A10	CST3
9	SRGN	CD7	MIR205HG	CLDN5	CCL4
10	VAMP8	HLA-C	SPINT2	TMSB10	FCER1G
11	SPN	PTPRC	BCAM	ATP5F1E	STAB1
12	LAPTM5	PFN1	TRIM29	B2M	CD14
13	GMFG	TMSB4X	EFNA1	IGFBP7	NPC2
14	SPINT2	CD69	CD9	PROX1	CSF1R
15	NFE2	GZMA	TP63	HLA-B	DAB2
16	LIMD2	TRBC1	DSC3	CAVIN2	CCL3
17	ELF1	CORO1A	S100A2	RAB11A	TMSB4X
18	PFN1	HLA-A	CD24	S100A16	F13A1
19	AIF1	HCST	PLP2	PECAM1	NEAT1
20	CD37	CST7	KRT19	EGFL7	CD36
21	PTPN7	RAC2	EPCAM	ARL4A	FCGRT
22	ABRACL	IFITM2	DAPL1	ANXA2	MAF
23	SLC39A3	CD247	KRT8	HLA-A	C1QB
24	TAGLN2	KLRC1	LGALS7B	HLA-C	SAT1

	Mast cell	Megakaryocyte	Melanocyte	Monocyte	Mural cell
0	CPA3	GP9	PMEL	LYZ	CALD1
1	HPGDS	MPIG6B	TYRP1	S100A9	IGFBP7
2	TPSAB1	RGS18	MLANA	TYROBP	MYL9
3	TPSB2	PPBP	DCT	SRGN	MT2A
4	HPGD	OAZ1	GPNMB	FCN1	ACTA2
5	ANXA1	RGS10	NSG1	LST1	BGN
6	SLC18A2	TMEM40	CAPN3	IFI30	COL4A1
7	HDC	CAVIN2	MITF	S100A4	CPE
8	FCER1G	PF4	QPCT	FCER1G	TPM2
9	CLIC1	PDLIM1	IGFBP7	SH3BGRL3	CAV1
10	RHEX	TUBB1	KIT	MNDA	PDLIM1
11	PRDX1	RAP1B	SAT1	FTL	SEPTIN7
12	KIT	MAX	SDCBP	SOD2	TINAGL1
13	SRGN	MYL12A	C3orf79	S100A8	COL4A2
14	IL1RL1	TUBA4A	SNCA	PLAUR	TAGLN
15	FXYD5	LAT	EDNRB	CTSS	TPM1
16	CTSG	CLEC1B	TYR	AIF1	NR2F2
17	GATA2	CCND3	DBI	OAZ1	NDUFA4L2
18	ARHGDIB	CMTM5	GSTP1	FTH1	KCNJ8
19	RAC2	YWHAZ	TFAP2A	S100A11	TFPI
20	VWA5A	STXBP2	SPTSSA	NAMPT	SULT1E1
21	CAPG	NRGN	TSPO	LSP1	IFITM3
22	ALOX5AP	SNCA	CD59	CD74	PDGFRB
23	ARHGAP18	LIMS1	CDH3	SAT1	NOTCH3
24	AL157895.1	ITGA2B	PDLIM3	BCL2A1	MCAM

	Neuronal cells	Neutrophil	Schwann cell	Skeletal muscle	T cell	Vascular endothelium
0	NNAT	LYZ	S100B	SGCA	CD52	PECAM1
1	UCHL1	RETN	EGFL8	MYF5	LTB	RAMP2
2	TUBA1A	S100A9	MPZ	DLK1	B2M	GNG11
3	MARCKSL1	TSPO	NRXN1	FGFR4	CD3D	CAV1
4	TUBB2B	S100P	PLP1	SPATS2L	CD3E	CLDN5
5	PRDX2	S100A8	GFRA3	CDH15	ARHGDIB	TM4SF1
6	STMN1	MNDA	OLFML2A	C1QTNF3	HLA-B	ECSCR
7	TUBB3	STXBP2	CADM1	CD82	SARAF	EGFL7
8	H3F3A	SRGN	GPM6B	RAPSN	IFITM1	A2M
9	GAPDH	LST1	MOXD1	CHODL	PTPRC	CDH5
10	YWHAQ	LCP1	EDNRB	JSRP1	IL32	CRIP2
11	RAN	CORO1A	ITGA6	TSPAN12	IL7R	SPARCL1
12	HSBP1	TMSB4X	PEBP1	CDKN1C	CORO1A	ESAM
13	CKB	NKG7	CDH19	PDLIM3	RAC2	ICAM2
14	PCSK1N	TKT	MIA	NPY	HLA-C	PRCP
15	TUBB	OAZ1	TGFBR2	CRYAB	TMSB4X	PLVAP
16	TMSB15A	ARHGDIB	PMP22	PDLIM4	CD7	S100A16
17	BEX1	CYBA	DST	CHRNA1	CD69	CD34
18	LDHB	PFN1	CRABP1	TNNT1	LEPROTL1	IGFBP7
19	ZNF428	GCA	ZEB2	IGF2	IL2RG	EMCN
20	JPT1	HCST	ERBB3	MATN2	CYTIP	SELENOW
21	YWHAE	ATP5F1E	MAL	RACK1	PFN1	CAVIN2
22	SRP9	SERPINB1	CNN3	AC132217.2	EEF1B2	HSPG2
23	ACTG1	FCER1G	PRSS23	PPP1R14B	FYB1	MYL12A
24	PKM	EMB	APOD	ALDOA	LIMD2	TMSB10

Appendix F. Differentially expressed genes for refined cell states in prenatal skin.

F1: Epithelial cell states

The top 25 DEGs are shown from differential gene expression testing (two-sided Wilcoxon rank-sum, Benjamini-Hochberg adjusted) between epithelial cell states in prenatal skin scRNA-seq dataset.

	Companion layer	**Cuticle/cortex**	***DPYSL2*$^{+}$ basal**	**Immature basal**	**Immature suprabasal**	**Inner root sheath**
0	PERP	KRT85	FRZB	STMN1	KRT1	KRT25
1	LGALS7B	HSPB1	TM4SF1	TUBB	DMKN	HSPB1
2	DMKN	ID3	RARRES2	HMGN2	KRT10	KRT28
3	KRTDAP	MT4	DAPL1	HMGB1	FABP5	ID3
4	DBI	DUSP2	CREB5	TUBA1B	KRTDAP	GATA3
5	LGALS7	ACTG1	ACTG1	PTMA	PERP	SCEL
6	DSP	KRT35	PHGDH	PCLAF	KRT13	HOPX
7	LYPD3	MSX1	TMEM98	GSTP1	LGALS7B	KRT71
8	DSG1	GPNMB	CLDN1	HMGB2	LYPD3	DNAJB1
9	AQP3	YBX3	COL14A1	BEX3	DSP	APOE
10	JUP	AOPEP	EGR2	HINT1	DSC3	DUSP2
11	PKP1	KRT25	LHX2	NUSAP1	S100A11	SBSN
12	KRT10	SAT1	KRT17	CENPK	SFN	MSX2
13	TMEM45A	DNAJB1	PTMA	CDK1	CLDN4	FABP5
14	TACSTD2	ODC1	FHL2	H2AFZ	LGALS7	HSP90AA1
15	NUPR1	APOE	GJB6	MIF	DSG1	CUX1
16	DSC3	GJA1	TBX1	TYMS	DBI	TACSTD2
17	CLDN1	TACSTD2	GAPDH	CKS1B	H19	PERP
18	CALML5	ASS1	NFIB	UBE2C	CTSC	STK17A
19	LRATD1	BAMBI	HMGN2	TMSB10	LDHB	LGALS7
20	CYB5A	HOXC13	NRP2	PKMYT1	TACSTD2	CTSC
21	KRT1	HSPA1B	ASS1	PFN1	LY6D	DLX3
22	SBSN	CAMK2N1	FXYD6	RRM2	PDCD4	DSP
23	SULT2B1	STK17A	SOX9	H19	ZNF750	SULT2B1
24	GLTP	ID1	CARD16	CENPW	MAP1B	LYPD3

	Matrix	Outer root sheath	*POSTN*$^{+}$ basal	Periderm	Placode	Suprabasal IFE
0	EEF1B2	APOE	ABRACL	KRT8	WIF1	S100B
1	PTCH2	LGALS7B	POSTN	KRT19	MME	VIM
2	MSX2	LGALS7	DCN	CLIC3	SHH	ZEB2
3	KRT85	CYB5A	IGFBP2	KRT18	SPOCK1	COL1A2
4	CUX1	APOC1	CXCL14	KRT4	WNT10B	PLP1
5	PABPC1	DMKN	IGFBP6	CLDN4	ABI3BP	CST3
6	NRP2	MSMO1	KRT14	TMSB4X	PTCH2	LGALS1
7	SNHG29	CSTB	KRT19	ANXA2	KCNMA1	MARCKS
8	AOPEP	ALDH2	MIR205HG	S100A10	FAM210B	NRXN1
9	HMGA1	PLIN2	KREMEN2	S100A11	SMOC2	EGFL8
10	NME2	MGST1	CRIP1	IGFL2	EPCAM	MPZ
11	NPM1	SCD	WNT3	C19orf33	ASCL4	CRABP1
12	SLC25A5	ALDOA	LEF1	S100A6	SLC7A2	GFRA3
13	RACK1	CERS4	PLAU	LGALS3	CDH3	COL1A1
14	GAPDH	CALML5	IGF2	H19	CXCL14	CDH19
15	EEF1G	PPDPF	LINC00514	PRDX6	ROBO1	PMP22
16	BTF3	TMEM91	NPR3	AC110619.1	SEMA3D	COL3A1
17	HNRNPA1	DHCR7	COL17A1	ANXA1	SCUBE3	GPM6B
18	SEPTIN11	HMGCS1	SOX6	VAMP8	ALCAM	OLFML2A
19	HSPB1	EMP2	MEG3	TACSTD2	POLR1D	FN1
20	STK17A	DHCR24	H19	C4orf3	SNCAIP	TGFBR2
21	ID3	KRT79	GPNMB	ELF3	APCDD1	LAMA4
22	KIF21A	FDFT1	IGFBP5	MAL	PRXL2A	NR4A2
23	MIF	ECHDC1	ODC1	NDRG2	COMMD10	TIMP1
24	EEF1A1	FDPS	COL7A1	CD24	SEPTIN11	MIA

F2: Stromal cell states.

The top 25 DEGs are shown from differential gene expression testing (two-sided Wilcoxon rank-sum, Benjamini-Hochberg adjusted) between stromal cell states in prenatal skin scRNA-seq dataset.

	Dermal condensate	**Dermal papilla**	**Early adipocytes**	**Early myocytes**	***FRZB*$^{+}$ early fibroblast**
0	COX6C	RSPO3	FABP5	SGCA	RBP1
1	SOX4	EDNRA	LPL	CHRNA1	MDK
2	PTMA	STMN1	SRPX	NACA	PTN
3	TCF4	H3F3A	CFD	PDLIM3	NREP
4	PTH1R	CRYM	APOE	FITM1	VCAN
5	MFAP4	BMP7	PPARG	CDH15	FRZB
6	TRPS1	CYTL1	FABP4	ACTC1	SLC1A3
7	MEF2C	TPD52	PTX3	PFN1	ARHGAP29
8	TWIST2	SPON1	SOX9	PPP1R14B	CYP1B1
9	EDNRA	INHBA	KCTD12	RASSF4	ISLR
10	CTSK	S100A4	IGFBP4	GAPDH	ELOB
11	LOX	S100A6	HSPB6	RAPSN	SVIL
12	F2R	PHLDA1	TGFBR3	DES	PLTP
13	H3F3B	PAPPA2	MGST1	CD82	SLC6A13
14	PMEPA1	CENPW	ASS1	SIX1	ACTG1
15	GJA1	CXCR4	RAMP2	SIRT2	CXCL12
16	CYYR1	H3F3B	COL12A1	KLHL41	GPRC5B
17	MAFB	SH3BGRL3	CD81	JSRP1	LRRC17
18	CD55	CKB	SERPINF1	CDKN1C	ZIC1
19	HSPA1A	ALPL	ADAMTS18	ZNF106	FLRT2
20	TWIST1	CXCL14	VCAN	ALDOA	TSPAN7
21	HSPB1	SOX2	NUPR1	MEGF10	TPM1
22	SLC26A7	PTMA	MGST3	TPM2	ATP1A2
23	H1F0	LAMC3	HAS2	SPATS2L	TUBB
24	LMNA	DCXR	IGFBP3	POPDC3	TLE1

	HOXC5^{+} early fibroblast	LMCD1+ mural cell	Lymphoid tissue organiser-like	Myelinating Schwann cells	Myoblasts
0	EEF1G	TAGLN	SULT1E1	S100B	MYF5
1	CRABP1	ACTA2	CFH	EGFL8	SGCA
2	LINC02381	CALD1	COLEC11	GFRA3	C1QTNF3
3	ECRG4	MYL9	CEBPD	MPZ	DLK1
4	WIF1	TPM2	NR2F1	PLP1	FGFR4
5	APCDD1	CAV1	PCDH9	NRXN1	CD82
6	SNHG32	TPM1	ITGA8	GPM6B	NPY
7	TGFBI	ACTG2	IFITM3	MIA	CHODL
8	MEG3	OLFML2B	APOD	ITGA6	SPATS2L
9	CLDN11	TINAGL1	IFITM1	CDH19	MATN2
10	NOP53	COL4A1	TMSB4X	MAL	TSPAN12
11	SLC25A6	PDLIM1	IER3	NR4A2	TAGLN2
12	TCF4	TPM4	SOCS3	ARHGAP15	CDH15
13	LINC01116	SEPTIN7	CDH11	CRABP1	IGFBP2
14	EFNA5	NR2F2	NPR3	OLFML2A	CDKN1C
15	SNRPE	JAG1	NDUFA4	PMP22	PDLIM4
16	CBX6	EPS8	NR2F2	ARPC1B	COL15A1
17	HNRNPA1	TMSB4X	NFKBIZ	DST	RAPSN
18	EIF3E	COL4A2	C11orf96	CADM1	SPARCL1
19	LSAMP	SDC2	PROS1	ANXA2	JSRP1
20	NAP1L1	LMCD1	LIFR	APOA1	TNNT1
21	INHBA	PPP1R14A	ADAMTS1	CST3	CLCN5
22	GAS5	ID4	C7	SEMA3B	LDOC1
23	CCBE1	LMOD1	JUND	TTYH1	AC132217.2
24	FABP7	CCL2	CPE	MOXD1	PAX7

	Myocytes	Myofibroblasts	Neuroendocrine	Neuron progenitors	*PEAR1*$^{+}$ fibroblast
0	ACTA1	ITM2A	PCSK1N	TUBB3	IGFBP7
1	TPM2	DLK1	NELL2	TAGLN3	NR2F2
2	MYLPF	OGN	AK1	TUBB2B	OGN
3	ACTC1	CAPN6	CKB	STMN1	PTCH2
4	MYL1	NRK	PLTP	NNAT	APOE
5	TNNC2	H19	RBP1	TUBA1A	TIMP1
6	CKM	IGF2	CA2	MARCKSL1	IGF2
7	TNNI2	ISLR	LY6H	BEX1	EGFL6
8	TNNT3	EGFL6	HSBP1	TMSB4X	SLC2A3
9	SLN	MGP	SOX2	JPT1	LTBP4
10	MYL4	DCN	CLU	CD24	MEOX2
11	DES	PLAGL1	CCN2	MLLT11	CCDC102B
12	TPM1	PDGFRL	SPINT2	ELAVL4	UROD
13	TNNI1	SPARCL1	MSX1	H3F3A	SULT1E1
14	ENO3	PCOLCE	CDO1	TUBB	H19
15	KLHL41	SMOC2	WLS	DCX	PROCR
16	AK1	IGFBP6	BSG	STMN2	SERPINE2
17	ACTN2	IGFBP4	UCHL1	PTMA	NRP1
18	MYOZ2	ASPN	SLC22A17	CCNI	COL3A1
19	COX6A2	POSTN	ISYNA1	UCHL1	PLAC9
20	GAPDH	PLAC9	TCTEX1D2	SOX11	LDB2
21	MYH3	SERPINE2	C4orf48	NEUROD1	BGN
22	SELENOW	NUPR1	CFAP126	CRMP1	BNC2
23	HSPB2	MEST	SLC9A3R1	ACTG1	ZFP36
24	TNNT2	ANGPTL1	DNALI1	PRDX2	JUNB

	PID1^{+} Schwann cells	*PLN*$^{+}$ mural cell	Pericytes	Pre-adipocytes	Pre-dermal condensate
0	S100B	ACTA2	MT2A	TYROBP	VIM
1	NRXN1	MYL9	IGFBP7	FTL	TWIST2
2	APOD	TAGLN	CALD1	AIF1	TCF4
3	GPM6B	IGFBP7	TMSB4X	RNASE1	SFRP2
4	EDNRB	CRIP1	COL4A1	CCL3	PTK7
5	MPZ	TPM2	MYL9	LYVE1	CD9
6	COL20A1	CALD1	BGN	CD36	CXCL14
7	ITIH5	CAV1	CPE	FCER1G	CDC42EP3
8	PTPRZ1	PDLIM1	NDUFA4L2	C1QA	LGALS1
9	MIA	MYL6	FABP4	CCL4	COL6A2
10	SOX10	TPM1	IFITM3	SRGN	CAV1
11	RGCC	RGS5	ACTA2	NEAT1	IGFBP3
12	CDH19	BGN	PDLIM1	CD14	COL5A1
13	BCAN	ISYNA1	TINAGL1	F13A1	APCDD1
14	SCRG1	ADIRF	KCNJ8	C1QC	LUM
15	GAS7	SEPTIN4	COL4A2	STAB1	COX6C
16	ALCAM	SULT1E1	SEPTIN7	DAB2	CTSK
17	CADM1	TINAGL1	CAV1	FOLR2	ROBO2
18	PRSS23	MCAM	TFPI	CST3	COL3A1
19	CNPY2	MYLK	MYO1B	CD68	COL6A1
20	FOXD3-AS1	MEF2C	A2M	HCST	ARL4C
21	ERBB3	MT2A	ABCC9	MRC1	COL5A2
22	TUBA1A	SPARCL1	FABP5	CSF1R	ABI3BP
23	POU3F1	ACTG2	NR2F2	C1QB	ZNF385D
24	HSBP1	CRIP2	PDGFRB	AGR2	SEPTIN11

	***SPP1*$^{+}$ proliferating neuron progenitors**	**Schwann/Schwann precursors**	***WNT2*$^{+}$ fibroblast**
0	GAPDH	S100B	POSTN
1	MARCKSL1	EGFL8	DCN
2	RAN	MPZ	COL1A2
3	H2AFZ	NRXN1	ITM2A
4	HMGA1	PLP1	COL1A1
5	TTYH1	GFRA3	MGP
6	STMN1	OLFML2A	PLAC9
7	TMSB15A	CADM1	FSTL1
8	H3F3A	EDNRB	PCOLCE
9	HMGB1	MOXD1	OGN
10	HNRNPA1	APOD	COL3A1
11	TUBA1B	TGFBR2	ASPN
12	CFL1	ITGA6	COL14A1
13	PKM	GFRA1	GPC3
14	TUBB2B	S100A10	COL12A1
15	PARP1	ZEB2	DLK1
16	PCBP2	NR4A2	H19
17	LDHB	PEBP1	SPARC
18	SPP1	PRSS23	PDGFRL
19	NNAT	GPM6B	FNDC1
20	ERH	ERBB3	FBN1
21	TUBB	CDH19	COL5A2
22	PPIA	SPTBN1	CCDC80
23	PRDX2	HSBP1	LUM
24	RANBP1	DST	AKAP12

F3: Endothelial cell states.

The top 25 DEGs are shown from differential gene expression testing (two-sided Wilcoxon rank-sum, Benjamini-Hochberg adjusted) between endothelial cell states in prenatal skin scRNA-seq dataset.

	Arterioles	Capillaries	Capillary arterioles	Early endothelial cells
0	IGFBP3	FABP4	COL15A1	COL1A2
1	H19	RGCC	RGCC	COL5A2
2	EGFL8	CAV1	IL32	COL3A1
3	PRND	H19	COL4A1	COL1A1
4	IGF2	CD34	C1orf54	SLC3A2
5	ICAM2	IGF2	CAV1	GPC3
6	EFCAB14	CD36	FABP4	COL6A1
7	MYO10	SPARCL1	CD36	MEST
8	ACTG1	COL15A1	COL4A2	COL6A2
9	GJA4	RBP7	APLNR	ZEB2
10	TSPAN2	A2M	CD34	THY1
11	A2M	IGFBP2	SPARCL1	DCN
12	HEY1	CLIC1	ARHGAP18	S100A4
13	PODXL	ACTG1	LXN	RGS10
14	CALM1	ESAM	CAV2	LUM
15	ESAM	C1orf54	TM4SF18	ITM2A
16	CLDN5	AQP1	FSCN1	NME4
17	SELENOW	COL4A2	ESAM	CRABP2
18	CXCR4	ACTB	MEG3	APCDD1
19	NOTCH4	PLVAP	ACTB	CXCL14
20	DLL4	IL32	OIT3	SERPINF1
21	UNC5B	TAGLN2	SH3BP5	VCAN
22	GPIHBP1	COL4A1	CTNNBIP1	EEF1A1
23	RNASE1	CTNNBIP1	IGFBP2	SPATS2L
24	VSIR	IGFBP3	MYADM	CD248

	LYVE1^{hi} LE	PROX1^{hi} LE	Postcapillary venules	Venules
0	TFF3	NTS	ITM2A	FBLN2
1	NTS	TFF3	FSTL1	EDN1
2	CCL21	CCL21	SPARC	VCAN
3	TFPI	PROX1	SELE	FBN1
4	ATP5F1E	TFPI	PLVAP	CLU
5	FTH1	CLU	CST3	ITM2B
6	PROX1	DKK3	IFI27	FSTL1
7	S100A10	ALDH2	MCTP1	CTSC
8	LYVE1	PTPRE	DUSP23	MMRN1
9	MMRN1	NFATC1	AHR	CPE
10	STAB2	LAPTM5	VWF	ACKR1
11	POLR2L	NUPR1	ANXA1	PDIA5
12	NR2F1	PLSCR4	SPARCL1	PLVAP
13	NUPR1	TSPAN5	PRCP	ARL4A
14	PTX3	PPFIBP1	ACKR1	DUSP23
15	LAPTM5	MFAP2	IFITM1	ELN
16	RAB11A	CTSL	IL33	CYP1B1
17	PPFIBP1	ADD3	CTSC	NR2F2
18	ARL4A	CD47	FBN1	TGM2
19	ABI3BP	PLAAT3	EMCN	JUNB
20	CLU	MMRN1	KCTD12	THBD
21	PLSCR4	FTH1	JAM2	AKR1C1
22	IGF1	PCBD1	NREP	ENTPD1
23	RELN	CD9	CLEC3B	CEBPD
24	ADD3	STXBP6	SAT1	HMCN1

F4: Myeloid cell states.

The top 25 DEGs are shown from differential gene expression testing (two-sided Wilcoxon rank-sum, Benjamini-Hochberg adjusted) between myeloid cell states in prenatal skin scRNA-seq dataset.

	ASDC	DC1	DC2	Inflammatory DC	Iron-recycling macrophage
0	PLAC8	C1orf54	HLA-DPA1	BIRC3	CD74
1	C12orf75	CD74	CLEC10A	B2M	APOC1
2	CCDC50	HLA-DPA1	HLA-DRA	LAMP3	NPC2
3	SCT	HLA-DPB1	HLA-DPB1	MARCKSL1	CD68
4	SPIB	S100B	CD74	TXN	HLA-DPA1
5	IGKC	HLA-DQB1	HLA-DRB1	RGS1	HLA-DMA
6	MYL12A	CLEC9A	HLA-DQA1	CRIP1	HLA-DRA
7	TSPAN13	SNX3	HLA-DQB1	CCR7	HLA-DRB1
8	PLP2	HLA-DRA	HLA-DRB5	TMSB10	HLA-DPB1
9	TCF4	HLA-DQA1	CD1C	IL32	C1QC
10	CRIP1	HLA-DRB1	HLA-DMA	LSP1	APOE
11	IRF7	ACTB	CST3	GSTP1	TREM2
12	SEC61B	EEF1B2	FCER1A	GABARAPL2	CTSB
13	IL3RA	CST3	S100A10	IL7R	HLA-DRB5
14	PPIA	PSMB9	CRIP1	CD83	CTSD
15	IRF8	CPVL	EEF1B2	CD74	PSAP
16	UGCG	IRF8	GPAT3	SYNGR2	FABP5
17	TPM2	CPNE3	ACTB	VOPP1	HLA-DQB1
18	JCHAIN	HLA-DRB5	VIM	NCCRP1	LIPA
19	CD7	S100A10	TAGLN2	BTG1	ITM2B
20	PPP1R14A	IDO1	ANXA2	HLA-DQA1	ATP6V1F
21	TAGLN2	TAGLN2	LSP1	GPX4	GPNMB
22	APP	HLA-DMA	CYTIP	FSCN1	HLA-DQA1
23	HERPUD1	LGALS2	LMNA	HLA-B	TYROBP
24	PLD4	DNASE1L3	HLA-DMB	TAGLN2	B2M

	LC	*LYVE1*$^{+}$ macrophage	MHCII^{+} macrophage	Monocyte	Monocyte (activated/ differentiating)
0	FCER1A	DAB2	STAB1	S100A6	HLA-DRA
1	CD74	RNASE1	MAF	S100A9	HLA-DRB1
2	HLA-DPA1	LYVE1	ZFP36L1	S100A8	TIMP1
3	HLA-DRB1	SELENOP	MS4A7	FCN1	CST3
4	HLA-DPB1	F13A1	RNASE1	LYZ	CD74
5	RGS1	C1QA	TPT1	S100A11	HLA-DPA1
6	HLA-DRA	SPP1	FOS	S100A4	HLA-DPB1
7	HLA-DQB1	FTL	SNX6	G0S2	FCN1
8	HLA-DQA1	FOLR2	MRC1	CTSS	IFI30
9	GPR183	LGMN	CSF1R	CD52	HLA-DRB5
10	ALOX5AP	PLTP	FOSB	MNDA	HLA-DMA
11	HLA-DMA	CD36	EGR1	VCAN	HLA-DQB1
12	HLA-DRB5	FCGRT	HCST	BCL2A1	B2M
13	S100B	MRC1	MS4A4A	S100A12	SH3BGRL3
14	CAPG	C1QB	LYVE1	TSPO	CFP
15	PKIB	BLVRB	AGR2	IFI30	HLA-B
16	LITAF	EGFL7	KLF6	CSTA	IL1B
17	CD207	STAB1	NR4A2	CD55	FAU
18	CST3	C1QC	CCL3	SOD2	SERPINA1
19	CTSH	GYPC	C1QC	SH3BGRL3	CFD
20	HLA-DMB	MAF	C1QA	LSP1	CD48
21	CD83	NPC2	CCL4	NAMPT	TSPO
22	SGK1	AGR2	DAB2	PLAUR	C1orf162
23	CD1E	LILRB5	FOLR2	FTH1	S100A4
24	ACTB	CD14	CD163	HLA-B	CSTA

	Monocyte precursor	Neutrophil1	Neutrophil2	TML macrophage	pDC
0	LYZ	MPO	S100A8	C3	JCHAIN
1	RETN	AZU1	PGLYRP1	RGS1	PLAC8
2	S100A8	PRTN3	S100A9	ITM2B	GZMB
3	S100A9	SNHG29	LTF	OLFML3	SEC61B
4	TSPO	MS4A3	CAMP	LINC02712	CCDC50
5	RNASE2	CTSG	TSPO	FCGR3A	MZB1
6	LGALS1	CLEC11A	LCN2	CKB	IRF7
7	FCN1	PLAC8	S100P	CCL3	C12orf75
8	S100A4	SRGN	RETN	C12orf75	IGKC
9	S100A6	GIHCG	MYL6	IFNGR1	TCF4
10	CSTA	LYZ	MNDA	BIN1	ITM2C
11	TKT	ELANE	LYZ	TMSB4X	UGCG
12	VCAN	DEFA4	NCF1	SPP1	SERPINF1
13	MNDA	RETN	CD24	RNASET2	LTB
14	NKG7	PRSS57	S100A12	CX3CR1	IRF8
15	PLAC8	NUCB2	CDA	TREM2	TAGLN2
16	GAPDH	SERPINB1	GCA	C1QC	PLP2
17	CAPG	NKG7	PADI4	CCL3L1	NACA
18	STXBP2	RNASE2	CRISP3	OLR1	CD7
19	S100A12	P4HB	S100A6	ALOX5AP	CLIC3
20	FLNA	S100P	HP	P2RY12	LIME1
21	HMGB2	RASGRP2	ARG1	CSF2RA	TPM2
22	SERPINB1	CST7	UGCG	RGS10	MYL12A
23	COX8A	SSR4	STXBP2	NAA20	PTCRA
24	PFN1	RNASE3	NKG7	BHLHE41	SPCS1

F5: Lymphoid cell states.

The top 25 DEGs are shown from differential gene expression testing (two-sided Wilcoxon rank-sum, Benjamini-Hochberg adjusted) between lymphoid cell states in prenatal skin scRNA-seq dataset.

	B cell	CD4 T cell	CD8 T cell	ILC2	ILC3
0	CD74	LDHB	TPT1	S100A6	LST1
1	MS4A1	RGS10	RGS10	S100A4	LTB
2	HLA-DRA	SELL	LDHB	IL32	HSPB1
3	HLA-DRB1	LEF1	LEF1	KLRB1	IL4I1
4	CD79A	IL7R	AIF1	VIM	S100A4
5	HLA-DPA1	TCF7	FYB1	ANXA1	CD52
6	HLA-DQB1	SARAF	EEF1B2	LGALS1	TRBC1
7	HLA-DPB1	NOSIP	SELL	FXYD5	KIT
8	IGHM	CAMK4	CD3D	HPGDS	HNRNPA1
9	CD37	CD3E	NOSIP	GATA3	ZBTB16
10	HLA-DQA1	FYB1	NACA	LMNA	LINC00299
11	CD83	CD27	TMSB10	MYL6	GAPDH
12	HLA-DRB5	CD3D	TCF7	S100A11	EEF1G
13	HERPUD1	CD3G	IL7R	PRNP	SNHG29
14	TCL1A	ICOS	RGCC	EMP3	MAP3K8
15	HLA-DMA	LEPROTL1	TNFAIP3	S100A10	ID2
16	CD79B	ITM2A	CD3E	PHLDA1	SEC11A
17	RALGPS2	AIF1	KLF2	PLP2	NAA38
18	SMIM14	CCR7	LEPROTL1	TSPO	IL7R
19	VPREB3	TPT1	SNHG8	KRT1	TEX30
20	SPIB	BCL11B	RGS1	TIMP1	MPG
21	NCF1	CD2	BCL11B	TAGLN2	SLC16A3
22	IFI30	SMC4	CCR7	SH3BGRL3	ITM2C
23	NIBAN3	EEF1B2	PASK	CKLF	TPI1
24	IGKC	CORO1B	CAMK4	PPIB	MIF

	Innate T type1	Innate T type3	LTi	Lymphoid progenitor	NK cell
0	IL32	S100A4	IL7R	JCHAIN	NKG7
1	TNFAIP3	IL32	LST1	MEF2C	TYROBP
2	CD3E	ANXA1	S100A4	HNRNPA1	CST7
3	IL7R	S100A10	KIT	SOX4	CMC1
4	GZMK	IL7R	ZBTB16	AIF1	GZMA
5	DUSP2	LTB	KLRB1	LST1	CCL4
6	CD3D	S100A6	PRNP	NAP1L1	CTSW
7	CD8A	FXYD5	S100A6	H2AFY	KLRB1
8	ZFP36L2	VIM	LTB	STMN1	FCER1G
9	AIF1	CD52	EML4	SNHG29	CCL5
10	HCST	CD3E	TRBC1	PTMA	HCST
11	CTSW	S100A11	CD44	HMGN1	SRGN
12	CD27	CRIP1	MAP3K8	GSTP1	KLRD1
13	GZMM	SH3BGRL3	FXYD5	ZFAS1	XCL1
14	IFITM1	EMP3	GAPDH	NPM1	KLRC1
15	CXCR4	RGCC	SRGN	TXN	XCL2
16	NKG7	TAGLN2	TPT1	NREP	CLIC3
17	ARAP2	EEF1A1	TMIGD2	H3F3A	GZMM
18	TC2N	NOSIP	TSPO	YWHAE	IFITM2
19	RGCC	ZFP36L2	CCR6	SNHG6	PRF1
20	RGS10	FTH1	PHLDA1	IGLL1	GZMB
21	CNN2	CD3D	JAML	RNASEH2B	HOPX
22	LEPROTL1	FLT3LG	TPI1	ESD	CCL3
23	CD44	LEPROTL1	LMNA	HDAC2	CD7
24	GUK1	TPT1	ANXA1	EIF3E	GNLY

	Pre B cell	Pre pro B cell	Pro B cell	Treg
0	HLA-DRA	HMGB1	VPREB1	IL32
1	CD79B	STMN1	VPREB3	S100A4
2	CD74	HMGN2	PTMA	CD27
3	IGHM	PTMA	IGLL1	CD3E
4	VPREB3	H2AFZ	CD79B	FXYD5
5	TCL1A	TUBA1B	HLA-DRA	S100A10
6	CD37	HMGB2	HMGB1	CTLA4
7	CD79A	PCLAF	TCF4	DUSP4
8	PTMA	TUBB	CD74	LTB
9	IGLC1	IGLL1	CD24	CD2
10	CD24	TYMS	RCSD1	ARHGDIB
11	NIBAN3	VPREB1	MZB1	CD3D
12	AFF3	DUT	AKAP12	B2M
13	MZB1	H2AFY	STMN1	TMSB10
14	HLA-DPB1	UHRF1	SOX4	HLA-A
15	H3F3A	HIST1H4C	SSBP2	SH3BGRL3
16	HLA-DRB1	PRDX1	CD79A	ACTB
17	BACH2	NUCKS1	MME	RGS1
18	LAPTM5	RANBP1	ARPP21	GBP2
19	HLA-DPA1	PPIA	HMGN2	TNFRSF1B
20	RCSD1	VPREB3	LAPTM5	CD52
21	SPIB	TCF4	H3F3A	IL2RA
22	YBX3	DEK	RAG1	RAC2
23	NCF1	SUMO2	HMGB2	SPOCK2
24	RUBCNL	HMGA1	MEF2C	TMSB4X

Appendix G. Gene lists for gene module scoring

G1: Angiogenesis gene sets

positive regulation of angiogenesis (GO:0045766)		positive regulation of sprouting angiogenesis (GO:1903672)	positive regulation of endothelial cell chemotaxis (GO:2001028)	positive regulation of endothelial cell proliferation (GO:0001938)		blood vessel morphogenesis (GO:0048514)
S100A1	BRCA1	ITGA5	SEMA5A	CCL26	NRP2	TGFB1
WNT5A	HSPB1	PDPK1	FGF2	FGFBP1	ECM1	EGFL7
RUNX1	MTDH	S100A1	HSPB1	EGF	CCL11	CAV1
HIPK2	HK2	SMAD1	VEGFA	CCL24	FLT4	TGFBR1
ISL1	PIK3R6	FUT1	FGF18	EGFL7	ITGB3	TGFBR2
JMJD8	MDK	FGF1	TMSB4X	ITGA4	PDGFB	VEGFA
HIPK1	APELA	FGF2	FGF16	WNT5A	EMC10	TGFBR3
PDCL3	RRAS	DLL1	P2RX4	PPP1R16B	PIK3CD	RASA1
SFRP2	CTSH	JMJD8	SMOC2	VEGFC	NRARP	WT1
STIM1	CD34	KLF4	FGFR1	SIRT6	FGF2	ID1
NINJ1	CCR3	VEGFA	PRKD1	VEGFD	HIF1A	APLNR
TEK	PTGIS	PKM	LGMN	SIRT1	GATA2	NF1
APLNR	NOS3	TJP1	KDR	TGFBR1	NR4A1	CCM2
ADM2	PDPK1	BMPER	MET	APLN	THBS4	SLC1A1
EPHA1	TIE1	JAK1	PRKD2	VEGFA	MYDGF	ADM
SEMA5A	ADAM12			VEGFB	HMOX1	LRP5

SERPINE1	VASH2			BMP4	TNFSF12	RASIP1
CHRNA7	F3			PDCL3	PLCG1	EFNB2
PDCD6	KLF4			SP1	STAT5A	SHH
DLL1	PKM			BMP2	ZNF580	APELA
AQP1	TJP1			TEK	PDPK1	CDH2
CDH5	SMOC2			APLNR	PROX1	HAS2
BMPER	ANGPTL4			PLXNB3	ARNT	TGFBR3L
KDR	ANGPTL3			AGTR1	GDF2	TBX20
CYP1B1	RAMP2			JCAD	VASH2	KDR
ZNF304	AGGF1			SCG2	IGF2	CYP1B1
PAK4	ECM1			VIP	PRKCA	HOXA1
SASH1	ITGB1			BMPR2	F3	HES1
XBP1	FLT1			SEMA5A	PGF	STRA6
SMAD1	GRN			PDCD6	ADAM17	NKX2-5
GDF2	EMC10			HMGB1	CDH13	TBX1
PRKCB	THBS1			HTR2B	FGFR1	CCBE1
PRKCA	PIK3CD			HMGB2	PRKD1	GLMN
PGF	HYAL1			NRAS	ANG	SYK
FGF18	ITGAX			MDK	PRKD2	SERPINF2
PRKD1	ITGB8			APELA	AGGF1	PROX1
PRKD2	JAK1			AKT3	NRP1	GDF2
RLN2	HMGA2			AKT1		SMAD7

NODAL	GAB1			KDR		COL4A1
GATA6	SIRT6			EGR3		LOX
TWIST1	VEGFD					ANGPTL3
GATA4	SIRT1					ENG
FGF1	RHOB					RAMP2
FGF2	VEGFA					AGGF1
ETS1	VEGFB					NRP1
HIF1A	IL1A					FLT1
GATA2	IL1B					CUL7
MYDGF	SP1					FLT4
ZC3H12A	TMIGD2					LAMA1
HMOX1	AGO2					RBPJ
TNFSF12	RAPGEF3					SOX18
PLCG1	CHI3L1					HEY2
ANGPT4	CXCL8					SOX17
ANXA3	FOXC2					GJA5
ITGA5	CD40					TNNI3
JUP	BTG1					ITGB8
SPHK1	HSPB6					
VEGFC	FUT1					

G2: Endothelial and hypoxia gene sets

Tip score	Stalk score	Arterioles	Capillaries	Venules	LE	Hypoxia			
ADM	ACKR1	EFNB2	CA4	NR2F2	PROX1	ADM	DCN	HK1	NDST2
ANKRD37	AQP1	SOX17	PRX	VCAM1	FLT4	ADORA2B	DDIT3	HK2	NEDD4L
C1QTNF6	C1QTNF9	BMX	RGCC	ACKR1	PDPN	AK4	DDIT4	HMOX1	NFIL3
DLL4	CD36	SEMA3G	SPARC	SELP	CCL21	AKAP12	DPYSL4	HOXB9	NR3C1
COL4A2	CSRP2	HEY1	SGK1	SELE	SEMA3A	ALDOA	DTNA	HS3ST1	P4HA1
EDNRB	EHD4	LTBP4	CYB5A	ADAMTS9	SEMA3D	ALDOB	DUSP1	HSPA5	P4HA2
FSCN1	FBLN5	FBLN5	ACVRL1	IGFBP7	TBX1	ALDOC	EDN2	IDS	PAM
GPIHBP1	HSPB1	GJA5	TMEM100	HDAC9	HOXD3	AMPD3	EFNA1	IER3	PCK1
HSPG2	LIGP1	GJA4	ADGRF5	RORA	NR2F1	ANGPTL4	EFNA3	IGFBP1	PDGFB
IGFBP3	IL6ST	FBLIM1	ADGRL2	ACTN1	NR2F2	ANKZF1	EGFR	IGFBP3	PDK1
INHBB	JAM2	FBLN2	F2RL3	LDLRAD3	KDR	ANXA2	ENO1	IL6	PDK3
KCNE3	LGALS3	MGP	IFNGR1	LDLRAD4	TEK	ATF3	ENO2	ILVBL	PFKFB3
LAMA4	LRG1	BGN	VIPR1	LRRC1	TFF3	ATP7A	ENO3	INHA	PFKL
LXN	MEOX2	LTBP1	ARHGAP6	MCTP1	TM4SF18	B3GALT6	ERO1L	IRS2	PFKP
MCAM	PLSCR2	FN1	IFI27	VWF	SNCG	B4GALNT2	ERRFI1	ISG20	PGAM2
MEST	SDPR	SERPINE2	PREX1	COL15A1	SCN3B	BCAN	ETS1	JMJD6	PGF
NID2	SELP	CPAMD8	PRKCE	ZNF385D	RELN	BCL2	EXT1	JUN	PGK1
NOTCH4	SPINT2	CXCL12	SH2D3C	EBF1	KLHL4	BGN	F3	KDELR3	PGM1
PTN	TGFBI	VEGFA	SORBS1	TSHZ2		BHLHE40	FAM162A	KDM3A	PGM2
RBP1	TGM2	DKK2	EMP2	FLRT2		BNIP3L	FBP1	KIF5A	PHKG1

RGCC	TMEM176A	DLL4	ITGA1	OLFM1		BRS3	FOS	KLF6	PIM1
UNC5B	TMEM176B	SOX5	SLC9A3R2	CPXM2		BTG1	FOSL2	KLF7	PKLR
	TMEM252	HES4	AFF3	PLVAP		CA12	FOXO3	KLHL24	PKP1
	TSPAN7	PRDM16	MEIS1	PDE7B		CASP6	GAA	LALBA	PLAC8
	VEGFR1	IGFBP3	BTNL9	VWA1		CAV1	GALK1	LARGE	PLAUR
	VWF	SRGN	KIAA1217	SPRY1		CCNG2	GAPDH	LDHA	PLIN2
		SAT1	FCN3	CLU		CCRN4L	GAPDHS	LDHC	PNRC1
		SLC9A3R2	IL7R	MGP		CDKN1A	GBE1	LOX	PPARGC1A
		RHOB	CD36	IER3		CDKN1B	GCK	LXN	PPFIA4
		BST2	NRXN3	PERP		CDKN1C	GCNT2	MAFF	PPP1R15A
		JAG1	SLC6A4	EDN1		CHST2	GLRX	MAP3K1	PPP1R3C
			GPIHBP1	FBLN2		CHST3	GPC1	MIF	PRDX5
			ARHGAP18	LYST		CITED2	GPC3	MT1E	PRKCA
			IL18R1			COL5A1	GPC4	MT2A	PRKCDBP
						CP	GPI	MXI1	PTRF
						CSRP2	GRHPR	MYH9	PYGM
						CTGF	GYS1	NAGK	RBPJ
						CXCR4	HAS1	NCAN	RORA
						CXCR7	HDLBP	NDRG1	RRAGD
						CYR61	HEXA	NDST1	S100A4
						SAP30	TGFBI		
						SCARB1	TGM2		

						SDC2	TIPARP		
						SDC3	TKTL1		
						SDC4	TMEM45A		
						SELENBP1	TNFAIP3		
						SERPINE1	TPBG		
						SIAH2	TPD52		
						SLC25A1	TPI1		
						SLC2A1	TPST2		
						SLC2A3	UGP2		
						SLC2A5	VEGFA		
						SLC37A4	VHL		
						SLC6A6	VLDLR		
						SRPX	WISP2		
						STBD1	WSB1		
						STC1	XPNPEP1		
						STC2	ZFP36		
						SULT2B1	ZNF292		
						TES			
						TGFB3			

Appendix H. Prioritised ligands from NicheNet analysis.

The top 20 prioritised ligands are shown from NicheNet analysis, ranked based on ligand activity scores.

test_ligand	auroc	aupr	aupr_corrected	pearson	rank
TGFB1	0.576430921	0.220353823	0.07288708	0.143363209	1
IL1B	0.56782945	0.217381343	0.0699146	0.135580626	2
TNF	0.574838203	0.219865685	0.072398943	0.134935328	3
IL1A	0.573395796	0.219412398	0.071945656	0.130386669	4
BMP2	0.571427502	0.219030906	0.071564164	0.128804121	5
CCL2	0.573684947	0.220171172	0.07270443	0.127385025	6
ITGAM	0.579561951	0.222682333	0.075215591	0.126394163	7
ADAM17	0.577283556	0.216691632	0.06922489	0.125858808	8
YARS	0.586423181	0.218267678	0.070800936	0.125007562	9
GMFB	0.579517821	0.221140497	0.073673755	0.123980706	10
SELPLG	0.573850153	0.220041537	0.072574794	0.123590569	11
MMP9	0.575636513	0.217743501	0.070276759	0.123134658	12
SEMA4D	0.57430666	0.2227015	0.075234757	0.121477141	13
VEGFA	0.569375569	0.21461514	0.067148397	0.120232016	14
PLXNB2	0.576334776	0.220558173	0.073091431	0.119977315	15
VCAM1	0.579089592	0.218340388	0.070873646	0.119018684	16
CCL5	0.569166871	0.213916607	0.066449865	0.117562274	17
NMB	0.570801726	0.218289276	0.070822534	0.116980374	18
APOE	0.581105202	0.220609658	0.073142916	0.116900765	19
POMC	0.568884889	0.216345194	0.068878451	0.116332752	20

Appendix I. Primary and secondary antibodies used in immunofluorescence assays.

Primary antibodies					
Antibody	**Vendor**	**Clonality**	**Clone**	**Dilution**	**Antibody application**
CD45	Thermo Fisher Scientific	monoclonal	YAML501.4	1 in 100	IF prenatal skin section, IF SkO section
CD31	DAKO	monoclonal	JC70A	1 in 100	IF SkO section
CD31	Thermo Fisher Scientific	monoclonal	HEC7	1 in 100	IF prenatal skin section
LYVE1	Abcam	monoclonal	EPR21857	1 in 1000	IF penatal skin section
VIM	Santa Cruz Biotech	monoclonal	V9	1 in 100	IF prenatal skin section
FOXP3	Thermo Fisher Scientific	monoclonal	PCH101	1 in 50	IF prenatal skin section
SOX2	BD Biosciences	monoclonal	O30-678	1 in 100	IF prenatal skin section
KRT14	Abcam	monoclonal	LL002	1 in 100	IF prenatal skin section
KRT14	Vector Labs	monoclonal	LL002	1 in 100	IF prenatal skin section
Plectin	Santa Cruz Biotech	monoclonal	7A8	1 in 200	IF prenatal skin section
BP180 (Type XVII collagen)	obtained from PMID: 8514739	monoclonal	HD4-233	1 in 100	IF prenatal skin section
Laminin-332	Novus Biologicals	monoclonal	GB3	1 in 100	IF prenatal skin section
Type VII collagen	Abcam	monoclonal	LH7.2	1 in 2	IF prenatal skin section
KRT1	Vector Labs	monoclonal	34bB4	1 in 50	IF prenatal skin section

Secondary antibodies						
Host species	**Target species**	**Isotype**	**Conjugate**	**Vendor**	**Cat no**	**Dilution**
Goat	anti-mouse	IgG1	Alexa Fluor 488	Thermo Fisher Scientific	A-21121	1 in 1000
Goat	anti-rat	IgG(H+L)	Alexa Fluor 647	Thermo Fisher Scientific	A-21247	1 in 1000
Goat	anti-mouse	IgG1	Alexa Fluor 568	Thermo Fisher Scientific	A-21124	1 in 1000
Goat	anti-rabbit	IgG(H+L)	Alexa Fluor plus 488	Thermo Fisher Scientific	A-32731	1 in 1000
Goat	anti-mouse	IgG2a	Alexa Fluor 488	Thermo Fisher Scientific	A-21131	1 in 1000
Goat	anti-rat	IgG(H+L)	Alexa Fluor 488	Thermo Fisher Scientific	A-11006	1 in 1000
Goat	anti-mouse	IgG1	Alexa Fluor 568	Thermo Fisher Scientific	A-21124	1 in 1000
Alpaca	anti-mouse	IgG3	Alexa Fluor 647	Thermo Fisher Scientific	SMS3AF647-1-100	1 in 1000
Goat	anti-rabbit	IgG(H+L)	Alexa Fluor plus 594	Thermo Fisher Scientific	A-32740	1 in 1000

Appendix J. Experimental values for scratch wound assays

The quantified scratch width closure are shown in fibroblasts cultured with and without macrophages.

Fibroblasts only						
	Experiment 1			Experiment 2		
Time (hours)	**well 1**	**well 2**	**well 3**	**well 1**	**well 2**	**well 3**
0	0	0	0	0	0	0
6	30.83609	14.72145	11.87084	18.63826	20.29867	14.66346
12	43.49573	30.33047	35.72603	28.55922	32.89581	30.18586
18	49.41372	41.00629	47.67484	39.71653	43.89523	49.44098
24	51.4128	49.50328	49.23658	42.29936	43.50084	50.99264
30	62.40065	47.70606	50.31082	42.29796	47.5458	59.04266
36	51.84288	52.48815	53.45583	47.14424	37.52552	57.69571
42	57.24386	56.62786	51.78199	43.75445	36.00446	57.23264
48	37.62527	45.51682	50.0672	44.28687	42.40032	56.05495
54	41.02148	53.20525	57.31772	44.48742	40.91987	62.17796
60	45.76903	57.64416	56.42298	46.27136	39.96108	48.07478
66	38.54111	54.27302	53.1156	44.38032	41.14593	49.92531
72	42.44111	49.40384	51.91539	47.59708	48.72209	63.02922

Fibroblasts only						
	Experiment 3			Experiment 4		
Time (hours)	**well 1**	**well 2**	**well 3**	**well 1**	**well 2**	**well 3**
0	0	0	0	0	0	0
6	19.4697	11.23723	33.77385	17.14451	20.29161	20.70906
12	25.69378	20.85211	31.88113	29.8531	34.91983	33.012
18	43.11964	29.79495	50.38163	39.19073	44.3508	40.18601
24	48.80397	39.86883	42.71991	46.14131	47.75807	47.50859
30	29.38679	48.78713	38.38126	43.71425	48.35193	51.80783
36	27.49792	49.44271	42.07609	41.74354	58.84048	47.69234
42	33.91005	29.80131	54.22856	40.36943	43.91305	47.51351
48	25.59395	53.46135	54.31005	43.26546	49.40206	43.17147
54	30.57107	42.06795	47.82207	46.42622	38.23619	59.4187
60	30.34617	52.05349	58.05753	45.96734	42.6159	58.6478
66	28.8656	52.27172	53.9388	45.80251	50.68622	92.2809
72	29.30118	52.98475	64.78669	43.97331	56.65435	54.85675

Fibroblasts + macrophages						
	Experiment 1			Experiment 2		
Time (hours)	**well 1**	**well 2**	**well 3**	**well 1**	**well 2**	**well 3**
0	0	0	0	0	0	0
6	18.08302	11.55883	3.090146	17.03712	11.04731	11.28183
12	24.52024	22.06273	14.41298	28.44209	27.89482	21.56434
18	26.09258	21.84878	30.31457	35.95996	40.73343	28.64785
24	18.05038	27.99113	37.56807	43.38715	49.31105	34.24828
30	35.18821	34.48199	47.3456	31.91826	57.80413	40.52443
36	32.94627	39.62936	52.13341	71.45021	64.94129	34.28459
42	26.3805	52.49633	38.2233	73.58566	55.01708	37.56757
48	22.72543	53.88626	61.15613	75.91501	57.43413	40.02433
54	39.88973	56.80885	46.86473	62.68328	63.8611	46.93808
60	63.71156	53.16598	49.44878	59.31082	63.48268	57.85233
66	82.90997	58.15225	57.89751	68.22008	63.36683	48.7366
72	81.32131	57.41652	72.36316	82.60467	75.12796	82.03236

Fibroblasts + macrophages						
	Experiment 3			Experiment 4		
Time (hours)	well 1	well 2	well 3	well 1	well 2	well 3
0	0	0	0	0	0	0
6	24.83972	14.24944	13.87649	11.40792	9.769269	22.10265
12	31.77521	11.18928	23.99311	17.46995	19.83171	34.11822
18	37.20641	35.63671	33.22453	19.32319	21.83592	37.65154
24	43.31392	42.9428	42.7454	37.1151	33.22912	42.0832
30	50.91761	45.72435	44.53591	41.2389	33.93787	35.6882
36	48.91629	39.88843	40.06262	62.20751	36.38193	71.41447
42	24.63741	41.39794	51.09244	56.24204	39.96578	84.14122
48	53.2567	56.42651	57.94683	52.4862	42.24772	35.16565
54	42.96096	58.24603	57.74925	54.84585	48.71823	43.62623
60	53.94009	29.78952	56.9714	62.99784	51.19795	98.94905
66	79.08847	71.3923	64.30332	64.62592	47.60345	97.38963
72	66.39439	59.16477	66.97849	72.18529	53.45086	63.72219

Appendix K. Gene set enrichment analysis results for *WNT2*$^{+}$ prenatal skin fibroblasts

K1: Early *WNT2*$^{+}$ fibroblasts

The top 5 selected terms are shown with associated ranking and statistics calculated in Enrichr; p values provided from Fisher exact test, adjusted using Benjamini-Hochberg correction, and ranked by combined score.

Rank	Term – GOBP 2023	Overlap	P-value	Adjusted P-value	Odds Ratio	Combined Score
7	Macromolecule Biosynthetic Process (GO:0009059)	19/183	1.4268378402585E-05	0.004844327	3.389294359	37.8159324
14	Peptide Biosynthetic Process (GO:0043043)	16/158	8.99146047568849E-05	0.017377496	3.285072135	30.60586788
15	Positive Regulation Of Cell Differentiation (GO:0045597)	23/283	9.64800989546306E-05	0.017480988	2.590795226	23.95494294
16	Positive Regulation Of Macromolecule Metabolic Process (GO:0010604)	27/364	0.00011711	0.019970643	2.351427956	21.28606571
22	Regulation Of Cell Differentiation (GO:0045595)	17/193	0.000300236	0.03784284	2.815397122	22.83551822

K2: Late *WNT2*$^{+}$ fibroblasts

The top 5 selected terms are shown with associated ranking and statistics calculated in Enrichr; p values provided from Fisher exact test, adjusted using Benjamini-Hochberg correction, and ranked by combined score.

Rank	Term – GOBP 2023	Overlap	P-value	Adjusted P-value	Odds Ratio	Combined Score
1	Extracellular Matrix Organization (GO:0030198)	15/176	1.03718988651342E-07	7.1390359177699E-05	6.188997338	99.52885969
3	Extracellular Structure Organization (GO:0043062)	11/109	1.00270725893077E-06	0.00042289	7.37991371	101.9373234
6	Cellular Response To Transforming Growth Factor Beta Stimulus (GO:0071560)	10/96	2.33854473387663E-06	0.000642766	7.624251381	98.85590411
16	Collagen Fibril Organization (GO:0030199)	6/42	4.2551881083659E-05	0.004815872	10.81133113	108.8137396
25	Supramolecular Fiber Organization (GO:0097435)	15/316	0.000128266	0.009491713	3.286663503	29.45311045

Appendix L. Gene set enrichment analysis results for TML macrophages.

Selected terms are shown with associated ranking and statistics calculated in Enrichr; p values provided from Fisher exact test, adjusted using Benjamini-Hochberg correction, and ranked by combined score.

Rank	Term – GOBP 2023	Overlap	P-value	Adjusted P-value	Odds Ratio	Combined Score
13	Negative Regulation Of Tumor Necrosis Factor Production (GO:0032720)	6/47	5.02095075421161E-05	0.007087879	10.39499868	102.9032744
23	Inflammatory Response (GO:0006954)	12/236	0.000144299	0.011777731	3.853386927	34.07788837
26	Negative Regulation Of Interleukin-2 Production (GO:0032703)	4/21	0.000194256	0.014223848	16.61395741	141.9884331
31	Negative Regulation Of Cytokine Production (GO:0001818)	10/178	0.000231889	0.014326422	4.262384441	35.67295947
101	Regulation Of Endothelial Cell Proliferation (GO:0001936)	6/93	0.002073981	0.040198631	4.887339724	30.19537935
108	Regulation Of Chemokine Production (GO:0032642)	4/41	0.002633036	0.045176823	7.625690206	45.2936851
219	Regulation Of Monooxygenase Activity (GO:0032768)	2/12	0.011991532	0.103856807	14.02633452	62.04625559
229	Negative Regulation Of Interleukin-6 Production (GO:0032715)	3/34	0.012135014	0.103856807	6.803917051	30.01657071

Appendix M. Angiogenesis-related gene set enrichment analysis results for macrophages.

Selected terms relating to angiogenesis are shown with associated ranking and statistics calculated in Enrichr for the different macrophage subsets; p values provided from Fisher exact test, adjusted using Benjamini-Hochberg correction, and ranked by combined score.

Rank	Macrophage subset	Term	Overlap	P-value	Adjusted P-value	Odds Ratio	Combined Score
150	Iron-recycling macrophage	Positive Regulation Of Vascular Endothelial Growth Factor Production (GO:0010575)	2/24	0.00432243	0.028311872	22.60909091	123.0824771
158	Iron-recycling macrophage	Regulation Of Vascular Endothelial Growth Factor Production (GO:0010574)	2/26	0.005062892	0.031516505	20.72291667	109.537552475707
12	*LYVE1*$^+$ macrophage	Regulation Of Angiogenesis (GO:0045765)	19/205	4.1587507487940 2E-06	0.000829191	3.705890691	45.91708198
13	*LYVE1*$^+$ macrophage	Regulation Of Vascular Endothelial Cell Proliferation (GO:1905562)	6/18	5.8940647154749 4E-06	0.001026176	17.86580882	215.1322928
34	*LYVE1*$^+$ macrophage	Positive Regulation Of Angiogenesis (GO:0045766)	12/119	0.000108848	0.00774651	4.032171768	36.79580202
43	*LYVE1*$^+$ macrophage	Regulation Of Endothelial Cell Migration (GO:0010594)	10/88	0.000150276	0.008826452	4.599240266	40.48729271
61	*LYVE1*$^+$ macrophage	Positive Regulation Of Vascular Endothelial Cell Proliferation (GO:1905564)	4/12	0.000234861	0.009818703	17.8040293	148.7796713

78	*LYVE1*$^{+}$ macrophage	Negative Regulation Of Endothelial Cell Proliferation (GO:0001937)	6/37	0.000473597	0.01553879	6.909037002	52.88973523
82	*LYVE1*$^{+}$ macrophage	Positive Regulation Of Endothelial Cell Migration (GO:0010595)	9/85	0.000542197	0.016932223	4.24083082	31.89054401
83	*LYVE1*$^{+}$ macrophage	Negative Regulation Of Angiogenesis (GO:0016525)	9/86	0.0005911	0.01823966	4.185539045	31.11330993
127	*LYVE1*$^{+}$ macrophage	Regulation Of Sprouting Angiogenesis (GO:1903670)	5/33	0.001938221	0.03894472	6.363695937	39.74754763
128	*LYVE1*$^{+}$ macrophage	Vasculogenesis (GO:0001570)	5/33	0.001938221	0.03894472	6.363695937	39.74754763
8	*LYVE1*$^{+}$ macrophage	Angiogenesis (MSigDB Hallmark)	7/36	4.7785796380942 E-05	0.000249548	8.633199975	85.88982545
152	MHCII^{+} macrophage	Blood Vessel Diameter Maintenance (GO:0097746)	1/36	0.0712728	0.142545599	14.23142857	37.58862573
222	MHCII^{+} macrophage	Negative Regulation Of Blood Vessel Morphogenesis (GO:2000181)	1/77	0.146417326	0.200913461	6.540460526	12.56614975
230	MHCII^{+} macrophage	Negative Regulation Of Angiogenesis (GO:0016525)	1/86	0.162100378	0.214730371	5.845294118	10.63574365
101	TML macrophage	Regulation Of Endothelial Cell Proliferation (GO:0001936)	6/93	0.002073981	0.040198631	4.887339724	30.19537935

145	TML macrophage	Positive Regulation Of Vascular Endothelial Growth Factor Production (GO:0010575)	3/24	0.004552975	0.061652272	10.04897959	54.18384076
163	TML macrophage	Regulation Of Vascular Endothelial Growth Factor Production (GO:0010574)	3/26	0.005728287	0.069053803	9.174223602	47.36044967
8	TML macrophage	Angiogenesis (MSigDB Hallmark)	4/36	0.001618554	0.008452447	8.819444444	56.67571049

Appendix N. Additional outputs during PhD

N1: Related publications

1. **A prenatal skin atlas reveals immune regulation of human skin morphogenesis. Nature 635, 679–689 (2024).**

   ***Gopee NH**, *Winheim E, *Olabi B, Admane C, Foster AR, Huang N, Botting RA, Torabi F, Sumanaweera D, Le AP, Kim J, Verger L, Stephenson E, Adão D, Ganier C, Gim KY, Serdy SA, Deakin C, Goh I, Steele L, Annusver K, Miah MU, Tun WM, Moghimi P, Kwakwa KA, Li T, Basurto Lozada D, Rumney B, Tudor CL, Roberts K, Chipampe NJ, Sidhpura K, Englebert J, Jardine L, Reynolds G, Rose A, Rowe V, Pritchard S, Mulas I, Fletcher J, Popescu DM, Poyner E, Dubois A, Guy A, Filby A, Lisgo S, Barker RA, Glass IA, Park JE, Vento-Tormo R, Nikolova MT, He P, Lawrence JEG, Moore J, Ballereau S, Hale CB, Shanmugiah V, Horsfall D, Rajan N, McGrath JA, O'Toole EA, Treutlein B, Bayraktar O, Kasper M, Progatzky F, Mazin P, Lee J, Gambardella L, Koehler KR, Teichmann SA, Haniffa M.

2. **Cutaneous T cell lymphoma atlas reveals malignant TH2 cells supported by a B cell-rich tumor microenvironment. Nat Immunol 25, 2320–2330 (2024).**

   Li R, Strobl J, Poyner EFM, Balbaa A, Torabi F, Mazin PV, Chipampe NJ, Stephenson E, Ramírez-Suástegi C, Shanmugiah VBM, Gardner L, Olabi B, Coulthard R, Botting RA, Zila N, Prigmore E, **Gopee NH**, Chroscik MA, Kritikaki E, Engelbert J, Goh I, Chan HM, Johnson HF, Ellis J, Rowe V, Tun W, Reynolds G, Yang D, Foster AR, Gambardella L, Winheim E, Admane C, Rumney B, Steele L, Jardine L, Nenonen J, Pickard K, Lumley J, Hampton P, Hu S, Liu F, Liu X, Horsfall D, Basurto-Lozada D, Grimble L, Bacon CM, Weatherhead SC, Brauner H, Wang Y, Bai F, Reynolds NJ, Allen JE, Jonak C, Brunner PM, Teichmann SA, Haniffa M.

3. **Spatiotemporal single-Cell roadmap of human skin wound healing. Cell Stem Cell, in press.**

   Liu Z, Li D, Bian X, Luo L, Björklund AK, Li L, Zhang L, Chen Y, Guo L, Gao J, Cao C, Wang J, He W, Xiao Y, Zhu L, Annusver K, **Gopee H**, Bennett CL, Kasper M, Haniffa M, Sommar P, Landén NX.

4. **Defining the Skin Cellular Community Using Single-Cell Genomics to Advance Precision Medicine. J Invest Dermatol 141(2), 255-264 (2021).**

   *Dubois A, ***Gopee N**, *Olabi B, Haniffa M.

5. **Obesity is associated with attenuated tissue immunity in COVID-19. Am J Respir Crit Care Med 207(5), 566-576 (2023).**

Guo SA, Bowyer GS, Ferdinand JR, Maes M, Tuong ZK, Gillman E, Liao M, Lindeboom RGH, Yoshida M, Worlock K, **Gopee H**, Stephenson E, Gao CA, Lyons PA, Smith KGC, Haniffa M, Meyer KB, Nikolić MZ, Zhang Z, Wunderink RG, Misharin AV, Dougan G, Navapurkar V, Teichmann SA, Conway Morris A, Clatworthy MR.

6. **Single-cell multi-omics analysis of the immune response in COVID-19. Nat Med 27, 904–916 (2021).**

Stephenson E, Reynolds G, Botting RA, Calero-Nieto FJ, Morgan MD, Tuong ZK, Bach K, Sungnak W, Worlock KB, Yoshida M, Kumasaka N, Kania K, Engelbert J, Olabi B, Spegarova JS, Wilson NK, Mende N, Jardine L, Gardner LCS, Goh I, Horsfall D, McGrath J, Webb S, Mather MW, Lindeboom RGH, Dann E, Huang N, Polanski K, Prigmore E, Gothe F, Scott J, Payne RP, Baker KF, Hanrath AT, Schim van der Loeff ICD, Barr AS, Sanchez-Gonzalez A, Bergamaschi L, Mescia F, Barnes JL, Kilich E, de Wilton A, Saigal A, Saleh A, Janes SM, Smith CM, **Gopee N**, Wilson C, Coupland P, Coxhead JM, Kiselev VY, van Dongen S, Bacardit J, King HW; Cambridge Institute of Therapeutic Immunology and Infectious Disease-National Institute of Health Research COVID-19 BioResource Collaboration; Rostron AJ, Simpson AJ, Hambleton S, Laurenti E, Lyons PA, Meyer KB, Nikolić MZ, Duncan CJA, Smith KGC, Teichmann SA, Clatworthy MR, Marioni JC, Göttgens B, Haniffa M.

N2: Presentations

- **Immune cell regulation of skin morphogenesis.**
  Oral presentation at the Sanger Institute Cellular Genetics programme retreat (Cambridge, UK, 2023).
- **Role of immune cells in skin morphogenesis and skin tumour microenvironment.**
  Oral presentation at the Tissue Type 2 immunity meeting (Venice, 2022).
- **Lessons from the skin Development Cell Atlas.**
  Oral presentation at the 102nd British Association of Dermatologists (BAD) meeting (Glasgow, UK, 2022).

- **Immune cells moonlight as regulators of skin morphogenesis: findings from a multi-omics prenatal skin atlas.**
  Poster presentation at the European Society for Dermatological Research (ESDR) meeting (Lisbon, 2024).
- **Immune cell regulation of skin morphogenesis.**
  Poster presentation NIHR Newcastle BRC Celebration of Research Excellence meeting (Newcastle, UK, 2024).
- **IL-17A and IL-17F in the pathogenesis of hidradenitis suppurativa: insights from early and chronic lesions.**
  Co-investigator and co-author of oral presentation at the International Societies of Dermatology (ISID) meeting (Japan, 2023).

- **Atlas of the human skin: Mapping cells across life course and disease.**
  Oral presentation as finalist in the Newcastle University Insights Public lecture series.